

# Modeling and simulation of the plasma discharge in a radiofrequency thruster

by

Jiewei ZHOU

*in partial fulfillment of the requirements  
for the degree of Doctor in Mecánica de Fluidos Programa Interuniversitario*

Universidad Carlos III de Madrid

Advisor 1:

Eduardo AHEDO GALILEA

Advisor 2:

Pablo FAJARDO PEÑA

Tutor:

Eduardo AHEDO GALILEA

April, 2021

Esta tesis se distribuye bajo licencia “Creative Commons **Reconocimiento – No Comercial – Sin Obra Derivada**”.



## *Acknowledgements*

First of all, I would like to thank my thesis advisors Eduardo Ahedo and Pablo Farjardo. I still remember the day I met you in the office and you proposed me the thesis project. At that time, I had several other options for PhD and I was confused, but now, I know that I did the right choice. During these years, you guided me and I learnt so much from you. Thanks also to Mario Merino and Gonzalo Sánchez-Arriaga, Jesus Ramos and Manuel Martínez-Sánchez, who also guided me in research. Here, I would like to do a special mention to Gonzalo Sánchez-Arriaga for developing the simulation tool VLASMAN, which I used to produce a part of the results for my thesis; and Jesus Ramos and Manuel Martínez-Sánchez for helping in the analysis and interpretation of the results obtained with VLASMAN.

Many thanks to my PhD colleagues. Daniel introduced the basis of a electron fluid model, which I worked on afterwards. Adrian and Filippo are the masters of particle-in-cell models and supported me to have the simulation tool HYPHEN working for helicon plasma thrusters. Alvaro and Pedro established the plasma-wave interaction models and made possible fully couple simulations.

Many thanks to Francesco Taccogna for receiving me at CNR in Bari. During the stay, your guidance made possible HYPHEN to simulate for complex alternative propellants. I enjoyed much the stay, and I still remember our conversations together with Pierpaolo Minelli about football during the lunches. Although you guys do not like Real Madrid, I must to say that recently we beat Juventus several times in Champions League.

Of course, my thanks to my parents and brother for supporting me and trying to give me the best education, from primary school to PhD. During these years, when I was doing my PhD, we have faced many challenges, but together we have overcome the problems. Moreover, we have received a new member in our family, little Shihan, who was besides me and brought me so much fun (but also bother me) during the last stressful months of thesis.

My thanks to Huimin, for staying with me these years and bringing me often food when I was working overtime so that I do not starve. I am proud that, currently, we are initiating the project GC EDUCATION, together with our friend Leilei, to promote high performance education among the next generation of young Chinese people in Spain.

This thesis received funding mainly from Airbus Defense and Space, contract number CW240050. The last year of thesis was supported by the HIPATIA project of HORIZON 2020 (European Commission), grant number GA870542.

Finally, I am writing this after the revision of the thesis by the international experts, Manuel Martínez-Sánchez (Emeritus Professor from MIT) and Francesco Taccogna (Permanent Researcher from CNR). Thanks to them, the quality and clarity of the thesis was improved.

Jiewei ZHOU  
Universidad Carlos III de Madrid  
February 8, 2021





# Published and Submitted Content

## REFERRED JOURNALS:

- [1] G. Sánchez-Arriaga, **J. Zhou**, E. Ahedo, M. Martínez-Sánchez and J.J. Ramos, “Kinetic features and non-stationary electron trapping in paraxial magnetic nozzles”, *Plasma Sources Science and Technology*, 27 (2018) 035002. DOI: 10.1088/1361-6595/aaad7f.

G. Sánchez-Arriaga was the original developer of the simulation tool VLASMAN. J. Zhou implemented some additional elements. J. Zhou ran and processed all the simulations, and carried out the analysis of the results and the writing for a part of the paper. In the tasks, he was helped by the rest of the authors. Those contents of the paper done mainly by J. Zhou are adapted and included in this thesis as Chapter 5. Whenever material from this source is included in this thesis, it is singled out with typographic means and explicit reference.

- [2] **J. Zhou**, D. Pérez-Grande, P. Fajardo and E. Ahedo, “Numerical treatment of a magnetized electron fluid model within an electromagnetic plasma thruster simulation code”, *Plasma Sources Science and Technology*, 28 (2019) 115004. DOI: 10.1088/1361-6595/ab4bd3.

A formulation of the numerical treatment was provided by D. Pérez-Grande. J. Zhou, with the aid and advice of his supervisors, is the author of the whole paper tasks: identification of important numerical issues of the formulation, implementation of improved algorithms, production and analysis of the results, and writing of the paper. The contents of the paper are adapted and included in this thesis as Chapter 2. Whenever material from this source is included in this thesis, it is singled out with typographic means and explicit reference.

- [3] A. Sánchez-Villar, **J. Zhou**, E. Ahedo and M. Merino, “Coupled plasma transport and electromagnetic wave simulation of an ECR thruster”, *Plasma Sources Science and Technology*, *accepted for publication*. DOI: 10.1088/1361-6595/abde20.

This paper is within the framework of the thesis by A. Sánchez-Villar. The production of the results required the simulation tool prepared in this thesis by J. Zhou. Some figures of the paper are included in Appendix B of this thesis for illustrating the contributions. Whenever material from this source is included in this thesis, it is singled out with typographic means and explicit reference.

- [4] **J. Zhou**, G. Sánchez-Arriaga and E. Ahedo, “Time-dependent expansion of a weakly-collisional plasma beam in a paraxial magnetic nozzle”, *Plasma Sources Science and Technology*, *under the final process of the revision*.

G. Sánchez-Arriaga implemented the collision operator in the simulation tool VLASMAN, and J. Zhou tested and validated the implementation. J. Zhou, with the advice and supervision of the two co-authors, is the author of the whole paper tasks. The contents of the paper are adapted and included in this thesis as Chapter 6. Whenever material from this source is included in this thesis, it is singled out with typographic means and explicit reference.

# Other Research Merits

## CONFERENCE PROCEEDINGS:

- [1] D. Pérez-Grande, **J. Zhou**, A. Domínguez-Vázquez, P. Fajardo and E. Ahedo, "Development of a fully two-dimensional electron fluid model for plasma thrusters", 35th International Electric Propulsion Conference, Atlanta, USA, 2017.
- [2] G. Sánchez-Arriaga, **J. Zhou**, E. Ahedo, M. Martínez-Sánchez and J.J. Ramos, "One-dimensional direct vlasov simulations of non-stationary plasma expansion in magnetic nozzle", 35th International Electric Propulsion Conference, Atlanta, USA, 2017.
- [3] **J. Zhou**, G. Sánchez-Arriaga, E. Ahedo, M. Martínez-Sánchez and J.J. Ramos, "Collisional effects in non-stationary plasma expansions along convergent-divergent magnetic nozzles", Space Propulsion Conference 2018, Seville, Spain, 2018.
- [4] **J. Zhou**, A. Domínguez-Vázquez, D. Pérez-Grande, P. Fajardo and E. Ahedo, "An axisymmetric hybrid model for the plasma transport in a helicon plasma thruster", Space Propulsion Conference 2018, Seville, Spain, 2018.
- [5] E. Ahedo, P. Fajardo, M. Merino, J. Navarro-Cavallé, A. Sánchez-Villar, M. Wijnen and **J. Zhou**, "Helicon and ecr plasma sources for space propulsion, simulation and testing", ICEAA - IEEE APWC 2019, Granada, Spain, 2019.
- [6] A. Sánchez-Villar, **J. Zhou**, M. Merino and E. Ahedo, "PIC/fluid/wave simulations of the plasma discharge in an ecr plasma thruster", 36th International Electric Propulsion Conference, Vienna, Austria, 2019.
- [7] A. Domínguez-Vázquez, **J. Zhou**, P. Fajardo and E. Ahedo, "Analysis of the plasma discharge in a hall thruster via a hybrid 2D code", 36th International Electric Propulsion Conference, Vienna, Austria, 2019.
- [8] **J. Zhou**, P. Jiménez, M. Merino, P. Fajardo and E. Ahedo, "Numerical simulations of the plasma discharge in a helicon plasma thruster", 36th International Electric Propulsion Conference, Vienna, Austria, 2019.

## PRESENTATIONS IN CONFERENCES:

- [1] A. Domínguez-Vázquez, D. Pérez-Grande, A. Sánchez-Villar, B. Tian, **J. Zhou**, P. Fajardo, M. Merino and E. Ahedo, “Hyphen: a multi-thruster simulation platform”, *EPIC 2018*, London, UK, 2018.
- [2] A. Domínguez-Vázquez, **J. Zhou**, A. Sánchez-Villar, M. Merino, P. Fajardo and E. Ahedo: “Hyphen: a simulation platform for space plasma thrusters”, *EUCASS 2019*, Madrid, Spain, 2019.



# Abstract

In the current electric propulsion industry for space applications, two of the main issues are the lifetime limitation of the mature technologies, Hall effect thrusters and gridded ion thrusters, due to the erosion of their electrodes; and the search for alternative propellants due to the scarcity of xenon. Electrodeless thrusters with magnetic nozzles, in particular the helicon plasma thruster and the electron cyclotron resonance thruster, are disruptive electric propulsion concepts that offer prolonged lifetime and tolerance for a wide variety of propellants. These thrusters are still under development, and further research is necessary for them to become competitive in terms of propulsive performances.

This thesis is focused on the modeling and simulation of the plasma discharge in electrodeless thrusters with two codes. HYPHEN, a two-dimensional axisymmetric hybrid code, is used for full simulations of the thrusters. This code was extended from Hall effect thrusters to electrodeless thrusters, within the objective of developing a multi-thruster simulation platform valid for many types of electromagnetic thrusters. VLASMAN, a one-dimensional kinetic code, is used for simulations of the plasma expansion along the magnetic nozzles.

The hybrid formulation of HYPHEN offers a good trade-off between computational cost and reliability of the results for full simulations, with a particle-in-cell model for heavy species and a fluid model for electrons. The particle model was ready for use from previous works, while the fluid model, with the basis established, was incomplete from the numerical point of view. The fluid model is solved on a magnetic field aligned mesh given the anisotropic character of the strongly magnetized electrons. However, the mesh, for realistic magnetic field topologies, can be highly irregular and the preliminary numerical algorithms were leading to inaccurate results. Thus, in this thesis, the numerical treatment of the fluid model is investigated, and solid numerical algorithms are found allowing to solve even complex magnetic topologies with singular points. Once the electron fluid model is completed, simulations coupled with the particle model are run for the helicon plasma thruster prototype HPT05M. The simulations are focused on the plasma transport assuming a known power deposition map from the helicon antenna. The thruster performances and profiles of plasma magnitudes are studied. The prototype is partially optimized, in terms of some design parameters, but the thrust efficiencies obtained are within the state-of-art. The main limitations for a full optimization beyond the state-of-art are identified and solutions are proposed.

Furthermore, HYPHEN was initially developed to simulate xenon and other atomic propellants. In this thesis, as many candidates for alternative propellants usually have more complex chemistry, the code is implemented with the main collisions for diatomic substances. Simulations are run with air as propellant for HPT05M testing successfully the implementation. The results have allowed also to evaluate the air-breathing concept in helicon plasma thrusters.

The kinetic formulation of VLASMAN is used for deeper studies of the plasma expansion along the magnetic nozzles. In the expansion, the plasma becomes very rarefied, and more accurate simulations than those from HYPHEN are required. Other one-dimensional steady state models were used in previous works, however they were not able to solve self-consistently a subpopulation of electrons trapped along the expansion. VLASMAN models the mechanisms responsible for the trapping of electrons, the transient and collisional processes. Simulations with VLASMAN are run to study the trapped electrons in terms of the transient history and collisionality. The solution of the subpopulation, and that

of the whole plasma, reached in the steady state is found dependent on the transient history. Once the collisions are added, even if rare, the transient history is erased and the steady state solution becomes unique. The amount of trapped electrons is found important on the electron cooling and on the balances of electron momentum and energy. Furthermore, some studies focused on the extraction of results for implementation in macroscopic models are conducted.

# Resumen

En la industria actual de la propulsión eléctrica para aplicaciones espaciales, dos de los principales problemas son la limitación de la vida útil de las tecnologías maduras, propulsores de efecto Hall y propulsores iónicos con rejillas, debido a la erosión de sus electrodos; y la búsqueda de propulsores alternativos debido a la escasez del xenón. Los propulsores sin electrodos con tobera magnéticas, en particular el propulsor Helicón y el propulsor cicloelectrónico, son conceptos de propulsión eléctrica disruptivos que ofrecen una vida útil prolongada y tolerancia a una amplia variedad de propulsores. Estos propulsores aún están en desarrollo y se necesita más investigación para que sean competitivos en términos de actuaciones propulsivas.

Esta tesis se centra en el modelado y simulación de la descarga de plasma en propulsores sin electrodos con dos códigos. HYPHEN, un código híbrido axisimétrico bidimensional, se usa para simulaciones completas de los propulsores. Este código es extendido de los propulsores de efecto Hall a los propulsores sin electrodos, bajo el objetivo de desarrollar una plataforma de simulación multipropulsor válido para muchos tipos de propulsores electromagnéticos. VLASMAN, un código cinético unidimensional, se usa para simulaciones de la expansión del plasma a lo largo de las toberas magnéticas.

La formulación híbrida de HYPHEN ofrece un buen punto intermedio entre el coste computacional y la fiabilidad de los resultados para simulaciones completas, con un modelo de partículas para especies pesadas y un modelo fluido para electrones. El modelo de partículas estaba ya listo para su uso de trabajos anteriores, mientras que el modelo fluido, con la base establecida, estaba incompleto desde el punto de vista numérico. El modelo fluido se resuelve en una malla alineada con el campo magnético dado el carácter anisotrópico de los electrones fuertemente magnetizados. Sin embargo, la malla, para topologías de campos magnéticos realistas, puede ser muy irregular y los algoritmos numéricos preliminares llevaban a resultados inexactos. En esta tesis, se investiga el tratamiento numérico del modelo fluido y se encuentran algoritmos numéricos sólidos que permiten resolver incluso topologías magnéticas complejas con puntos singulares. Una vez que se completa el modelo fluido, se llevan a cabo simulaciones junto con el modelo de partículas para el prototipo de propulsor Helicón HPT05M. Las simulaciones se centran en el transporte de plasma asumiendo un mapa conocido de deposición de potencia de la antena Helicón. Se estudian las actuaciones del propulsor y perfiles de las magnitudes del plasma. El prototipo se optimiza parcialmente, en términos de algunos parámetros de diseño, pero las eficiencias de empuje obtenidas están dentro del estado de arte. Se identifican las principales limitaciones para una optimización total más allá del estado de arte y se proponen soluciones.

Además, HYPHEN se desarrolló inicialmente para simular xenón y otros propulsores atómicos. En esta tesis, como muchos candidatos a propulsores alternativos suelen tener una química más compleja, el código se implementa con las principales colisiones de sustancias diatómicas. Simulaciones se llevan a cabo con aire como propulsante para el HPT05M testeando con éxito la implementación. Los resultados también han permitido evaluar el concepto de air-breathing en los propulsores Helicón.

La formulación cinética de VLASMAN se utiliza para estudiar con mayor profundidad la expansión del plasma a lo largo de las toberas magnéticas. En la expansión, el plasma se vuelve muy enrarecido y se requieren simulaciones más precisas que las de HYPHEN. En trabajos anteriores se utilizaron otros modelos unidimensionales estacionarios, sin embargo, no pudieron resolver de manera



autoconsistente una subpoblación de electrones atrapados a lo largo de la expansión. VLASMAN modela los mecanismos responsables del atrapado de electrones: los procesos transitorios y colisionales. Simulaciones con VLASMAN se llevan a cabo para estudiar los electrones atrapados en términos del transitorio y colisionalidad. La solución de la subpoblación, y la de todo el plasma, alcanzada en el estacionario depende del transitorio. Una vez que se incluyen las colisiones, incluso si son poco frecuentes, se borra el transitorio y la solución estacionaria colapsa en una única. Se descubre que la cantidad de electrones atrapados es importante en el enfriamiento y en el balance de momento y energía de los electrones. Además, se realizan algunos estudios enfocados a la extracción de resultados para su implementación en modelos macroscópicos.



# Contents

<b>Acknowledgements</b>	<b>iii</b>
<b>Published and Submitted Content</b>	<b>v</b>
<b>Other Research Merits</b>	<b>vii</b>
<b>List of Figures</b>	<b>xix</b>
<b>List of Tables</b>	<b>xxiii</b>
<b>1 Introduction</b>	<b>1</b>
1.1 Thesis scope and objectives . . . . .	5
1.2 Thesis outline . . . . .	6
<b>2 Hybrid simulation model: numerical treatment (i)</b>	<b>7</b>
2.1 Introduction . . . . .	7
2.2 Problem formulation . . . . .	8
2.2.1 Geometric and magnetic topologies . . . . .	8
2.2.2 Electron fluid model . . . . .	9
2.3 Numerical treatment . . . . .	11
2.3.1 Problem discretization . . . . .	11
2.3.2 Gradient reconstruction methods . . . . .	13
2.3.3 Magnitudes at the boundary faces . . . . .	14
2.4 Simulation results . . . . .	16
2.4.1 Performances . . . . .	16
2.4.2 2D plasma profiles . . . . .	17
2.4.3 Assessment of the momentum equation terms . . . . .	20
2.4.4 On current ambipolarity and plume extension . . . . .	22
2.4.5 Effects of mesh refinement . . . . .	24
2.5 Conclusions . . . . .	25
2.A Testing gradient reconstruction methods . . . . .	25
2.B Performance indicators . . . . .	27
<b>3 Hybrid simulation model: numerical treatment (ii) and parametric analysis for HPTs</b>	<b>29</b>
3.1 Introduction . . . . .	29
3.2 Model formulation . . . . .	30
3.2.1 General aspects . . . . .	30
3.2.2 Electron module . . . . .	32

3.3	Numerical treatment for E-module . . . . .	35
3.4	Results . . . . .	36
3.4.1	2D plasma profiles . . . . .	37
3.4.2	Performances . . . . .	41
3.4.3	On the thrust generation . . . . .	42
3.5	Conclusions . . . . .	44
<b>4</b>	<b>Hybrid simulation model: modeling of chemistry and alternative propellants for HPTs</b>	<b>47</b>
4.1	Introduction . . . . .	47
4.2	Modeling of collisions . . . . .	47
4.2.1	Type of collisions . . . . .	47
4.2.2	Implementation in HYPHEN . . . . .	50
4.3	Results . . . . .	51
4.3.1	2D plasma profiles . . . . .	51
4.3.2	Performances . . . . .	55
4.4	Conclusions . . . . .	56
<b>5</b>	<b>Kinetic study of magnetic nozzles: transient process</b>	<b>57</b>
5.1	Introduction . . . . .	57
5.2	Magnetic nozzle model based on guiding center theory . . . . .	58
5.2.1	Plasma model . . . . .	58
5.2.2	Evolution of macroscopic quantities . . . . .	60
5.2.3	Simulation domain and boundary conditions . . . . .	61
5.2.4	Direct Vlasov solver . . . . .	62
5.3	Stationary solution and parametric analysis . . . . .	63
5.4	Conclusions . . . . .	67
5.A	Effect of the convergent segment . . . . .	68
<b>6</b>	<b>Kinetic study of magnetic nozzles: collisions</b>	<b>69</b>
6.1	Introduction . . . . .	69
6.2	Magnetic nozzle model . . . . .	69
6.2.1	Physical model and boundary conditions . . . . .	69
6.3	Kinetic features . . . . .	73
6.3.1	Basic concepts . . . . .	73
6.3.2	Effect of collisions on trapped-electron subpopulation . . . . .	75
6.4	Macroscopic response . . . . .	77
6.4.1	Spatial profiles . . . . .	77
6.4.2	Momentum and energy balances . . . . .	79
6.5	On closure laws for electron heat flux . . . . .	81
6.6	On the total potential drop . . . . .	84
6.7	Conclusions . . . . .	85
6.A	Numerical scheme . . . . .	86
6.B	A density-dependent collision frequency . . . . .	87
<b>7</b>	<b>Conclusions and future work</b>	<b>89</b>

7.1	Conclusions . . . . .	90
7.1.1	Full simulations with HYPHEN . . . . .	90
7.1.2	Kinetic simulations of magnetic nozzle with VLASMAN . . . . .	92
7.2	Future work . . . . .	93
<b>A</b>	<b>Fully coupled simulations of two HPT prototypes</b>	<b>95</b>
<b>B</b>	<b>Fully coupled simulations of an ECRT prototype</b>	<b>103</b>
	<b>Bibliography</b>	<b>105</b>



# List of Figures

1.1	Pictures of (left) the HPT prototype HPT05M and (right) the vacuum chamber in the facilities of EP2. . . . .	5
2.1	(a) Scheme of the mini-HPT plasma domain to be simulated. The vessel length and radius are 3 cm and 1 cm, respectively. The injector radius is 0.75cm. (b) Conventional magnetic field to be used in cases C1A (and in case C1B with double strength). (c) Magnetic field with a null point used in case C2. . . . .	8
2.2	Sketch of cells and faces in a MFAM. The three crosses ( $\times$ ) are examples of the three types of faces. For each one, the circles surrounding them constitute the stencil considered for gradient reconstruction. The FDM is considered for an inner face. The WLSM is used for the non-inner faces with stencils constituted by two levels of adjacency. . . . .	11
2.3	Relative errors in computing magnitudes at the boundary faces with WLSM(1) and WLSM(2). The coordinate $l$ is an arc length parameter that begins at point $(0,0)$ and increases clockwise along the boundary walls $W1$ , $W2$ , and $W3$ . . . . .	15
2.4	2D maps of main plasma magnitudes for case C1A. The electron fluid model algorithms are responsible of determining $\phi$ and $j_e$ . The I-module provides $n_e$ and $j_i$ . Plots of plasma properties in this and subsequent figures correspond to a time average of the last 100 timesteps (which correspond to $5\mu s$ with the time step used) of the stationary solution. . . . .	18
2.5	Same than Fig. 2.4 for case C1B. . . . .	19
2.6	Same than Fig. 2.4 for case C2. The null magnetic point is indicated with a white dot. . . . .	20
2.7	Additional 2D maps of case C1A for the analysis of the terms in the electron momentum equation. Upper and lower bounds have been imposed to the color scale to highlight main features. . . . .	21
2.8	Electric current densities inside the chamber for case C2: (a) the FDM is used in inner faces, (b) the WLSM is used in all faces. The white dot indicates the location of the magnetic null point. . . . .	22
2.9	Electric current densities inside the chamber for same magnetic field than case C1A but with $T_{e0} = 16eV$ (i.e. doubling the $T_e$ map). Numerical algorithms on the electron momentum equation are applied directly on (a) $\Phi$ or (b) $\phi$ . . . . .	22
2.10	(a)-(b) Ion and electric current densities for a case identical to C1A except that the plume axial length is 4.5cm instead of 3cm. For easier comparison with same currents in Fig. 2.4, plots have been restricted to $z \leq 6cm$ . (c) Ion and electron currents for plume axial lengths of 3cm, 4.5cm and 6cm, at the mean $r$ of each $z = \text{const}$ section. . . . .	23

2.11	Panels (a) and (b) correspond to the same cases than Fig. 2.9 but using 4800 cells/mesh instead of 1200 in the simulations. Panel (c) plots the cuts of the electric current density at the chamber exit section, $z = 3\text{cm}$ , for the 1200, 2400 and 4800 cells/mesh cases and the two numerical strategies followed to compute $\phi$ . The percentages shown in the inserts of panel (c) correspond to the mean deviation $\delta$ (defined in the main text) with respect to $ \vec{j} $ for 4800 cells and $\Phi$ as unknown. . . . .	24
2.12	Scheme of the stencils used by each GRM when testing with an analytical function. Panel (left) corresponds to FDM and (right) to WLSM. GRM is done for a particular face of a hypothetical MFAM, which is represented by a cross and located at $(x_{\parallel}, x_{\perp})$ . The surrounding cells, whose centers are marked by a circle, constitute the stencils. The main text defines the trial function and explains the different configurations of the stencils. . .	26
3.1	(a) Sketch of the thruster and (b)-(d) 3 possible applied magnetic fields generated by the set of coils. . . . .	30
3.2	Structure of the code. . . . .	31
3.3	(a) Cartesian mesh of I-module and (b) MFAM mesh of E-module for a particular simulation case. . . . .	31
3.4	2D maps of plasma magnitudes for C0. . . . .	38
3.5	2D maps of plasma magnitudes for C1A. . . . .	39
3.6	2D maps of plasma magnitudes for C1B. . . . .	39
3.7	2D maps of plasma magnitudes for C2A. . . . .	40
3.8	2D maps of plasma magnitudes for C2B. . . . .	40
3.9	1D $z$ -profiles at a mean $r$ , about 75% of domain radius at each $z = \text{constant}$ section, of (a) azimuthal current density, (b) magnetic field angle, (c) magnetic field strength and (d) magnetic thrust per unit volume for C0 (—), C1B (----) and C2B (·····). . . .	43
3.10	(a) Pressure force per unit area of the plasma on (a) back wall and (b) lateral wall of the vessel for C0 (—), C1B (----) and C2B (·····). . . . .	44
4.1	Reaction rates of air substances, $Xe$ is shown for comparison. . . . .	49
4.2	2D maps of plasma magnitudes for $N_2$ . . . . .	52
4.3	2D maps of plasma magnitudes for $O$ . . . . .	53
4.4	2D maps of plasma magnitudes for $Xe$ . . . . .	54
4.5	Electron azimuthal current density and total collision frequency for $N_2$ (first column), $O$ (second column), and $Xe$ (third column). . . . .	55
5.1	Net current-to-magnetic field ratio $j/B$ versus the total potential drop ( $\phi_M$ ) and the one between the throat and $z_M$ ( $\phi_{TM}$ ) for several expansion rates and box sizes. The curves practically overlap, also for the case $r_L = 100$ (not shown). . . . .	63
5.2	(a), (b) and (d) Respectively, the normalized space charge, $\phi$ versus $z$ and $n_i$ versus $1/B$ for $r_L = 50$ and several $z_M$ . (c) $\phi$ versus $1/B$ for $z_M = 800$ and several expansion rates. . .	64
5.3	Stationary, spatial profiles of inertial, pressure, and electric forces of ions and electrons for $r_L = 50$ and $z_M = 800$ . . . . .	65
5.4	(a), (b) The perpendicular temperature of the electrons and the ions, respectively. (c) Their parallel temperatures and (d) the mean kinetic energy of the ions. $z_M = 800$ and solid, dashed, and dot-dash lines correspond to $r_L = 100, 50$ , and $25$ , respectively. . . .	66



5.5	Axial profiles of the heat fluxes [panel (a)] and their relative rates versus the pressure fluxes [panel (b)] $r_L = 50$ and $z_M = 800$ . . . . .	67
5.6	(a), (b) The charge densities and potential profiles for simulations with lengths of the convergent segment equal to $z_0 = -50$ (solid black), $z_0 = -25$ (dashed blue) and $z_0 = -12.5$ (red dashed-dotted). The curves practically overlap. . . . .	68
6.1	Sketch of the magnetic nozzle (left) and the external magnetic field $B$ (right). Plasma is injected from a source and expands from $z_0$ to $z_D$ with the nozzle throat M at $z = 0$ . . . .	70
6.2	Cases of maximum magnetic moment $\mu_m$ curves for electrons. Each panel represents a specific energy. The vertical dash-dot lines represent the position of the MN throat, and the horizontal dashed lines separate the subpopulation regions. Examples of trajectory of individual electrons shown are for the absence of collisions. . . . .	74
6.3	Steady-state electron VDF $\hat{f}_e$ and target Maxwellian VDF $\hat{f}_{Me}$ in the $\mu$ - $z$ plane for the cases of $\tilde{v}_e = 0, 0.01$ and $0.1$ . Results are for $E/T_{e0} = 2.85$ . . . . .	75
6.4	1D profiles of $\hat{f}_e^\pm$ and $\hat{f}_{Me}^\pm$ extracted from 2D profiles of Fig. 6.3 (c) and (f) [case $\tilde{v}_e = 0.1$ and $E/T_{e0} = 2.85$ ]: (a) $\mu$ -profiles at $\hat{z} = 300$ , and (c) $z$ -profiles at $\hat{\mu} = 3$ ; (b) and (d) are zooms of (a) and (c), respectively. . . . .	76
6.5	Steady-state density percentages of the three electron subpopulations for two cases of $\tilde{v}_e$ . . . . .	77
6.6	Steady-state spatial profiles of macroscopic plasma magnitudes. Curves correspond to three cases of $\tilde{v}_e$ : 0 (-.-.-.), 0.01 (- - -) and 0.1 (—). . . . .	78
6.7	Parallel and perpendicular electron temperatures for each electron subpopulation [case $\tilde{v}_e = 0.1$ ]. Notice that, locally, free and reflected electrons have practically the same ratio $T_\perp/T_\parallel$ . . . . .	79
6.8	Balances of (a)-(b) momentum and (c)-(d) energy ‘per particle’ for $\tilde{v}_e = 0.1$ . Units in (a)-(b) are referred to $T_{e0}/\lambda_{De0}$ and in (c)-(d) to $T_{e0}$ . Momentum and energy corresponds to Eqs. (6.20) and (6.21), divided over $n_\alpha$ and $n_\alpha u_\alpha A$ , respectively. These results are for $T_{i0} = T_{e0}$ . . . . .	80
6.9	Heat flux in the divergent MN for increasing $\tilde{v}_e$ : 0, 0.01, 0.1, 1 and 10. Units are referred to $n_0 T_{e0} c_{s0} / B_M$ . . . . .	83
6.10	(a)-(c) Direct and derived coefficients (defined in the main text) obtained fitting for three heat flux laws: combined convective-plus-diffusive law (—*—), purely-convective law (- - $\Delta$ - -) and purely-diffusive law (- - $\blacktriangle$ - -). (d)-(i) Heat flux-profiles from the three laws versus the exact profile (—) for six cases of $\tilde{v}_e$ . . . . .	83
6.11	(a) Total ion current (b) and total net current versus $\tilde{v}_e$ for two values of total potential drop $\hat{\phi}_D$ : $-3$ (— $\blacksquare$ —) and $-3.5$ (— $\blacktriangle$ —). . . . .	84
6.12	Simulation results with two different temporal laws for $\phi_D$ : $\phi_D^{(1)}$ (—) and $\phi_D^{(2)}$ (- - -), which are defined in the main text. Both of the cases are run with e-e collisions for $\tilde{v}_e = 0.1$ . Results shown are: (a) spatial profile of $n_t/n_e$ at $t_s$ and steady state, and (b) temporal evolution of $\phi$ and $T_{\parallel e}$ at $\hat{z} = 300$ . . . . .	85
6.B.1	Simulation results of some plasma spatial profiles for a spatially dependent e-e collision frequency $\tilde{v}_e = 0.1 n_e(z)/n_0$ (—), and a constant one $\tilde{v}_e = 0.1$ (- - -). . . . .	87
A.1	Structure of HYPHEN with W-module. . . . .	95
A.2	Sketch of the simulation domains for HPT05M. . . . .	96

A.3	Applied magnetic field . . . . .	98
A.4	2D maps of plasma-wave interaction magnitudes for HPT05M . . . . .	98
A.5	2D maps of plasma transport magnitudes for HPT05M . . . . .	99
A.6	Applied magnetic field . . . . .	100
A.7	2D maps of plasma-wave interaction magnitudes for HPT03 . . . . .	100
A.8	2D maps of plasma transport magnitudes for HPT03 . . . . .	101
B.1	Sketch of the simulation domains for the ECRT prototype developed by ONERA. . . . .	103
B.2	2D maps of plasma transport magnitudes obtained with HYPHEN for the ECRT prototype developed by ONERA. . . . .	104

# List of Tables

2.1	Performance indicators. The two terms in the sums of the last column are the contributions of walls W1 (first term) and W2 (second one).	17
3.1	Performance indicators of different HPT05M configurations.	41
3.2	Total thrust breakdown: pressure force/magnetic force, and vessel force/plume increment. Contributions to the magnetic term from source and plume, and to the pressure term from back wall and lateral wall. The forces are in $mN$ .	43
4.1	Type of collisions considered when simulating for diatomic molecules.	48
4.2	Threshold energy [ $eV$ ] of reactions for air substances, $Xe$ is shown for comparison.	49
4.3	Performance indicators of a particular HPT05M configuration operated with $N_2$ , $O$ and $Xe$ .	56
6.1	Comparison of results between VLASMAN (case $\tilde{v}_e = 0.1$ ) and the SSK model of Ref. [4]. Species currents are defined in Eq. (6.19), $I_0 = en_0c_{s0}A_M$ and $I = I_e + I_i$ . Species energies are defined in Eq. (6.21).	79
A.1	Simulation parameters	98
A.2	Performance indicators of HPT05M	98
A.3	Simulation parameters	100
A.4	Performance indicators of HPT03	100



## Chapter 1

# Introduction

Electric propulsion (EP) for space missions was proposed in the early 20th century, and independently by Goddard in 1906 [36] and Tsiolkovsky in 1911 [66]. However, only after 1950s, the space exploration was impulsed in the context of the space race between US and USSR, and the first EP systems were introduced. The Gridded Ion Thruster (GIT) and Hall Effect Thruster (HET), two of the most common mature EP systems nowadays, were first launched, respectively, by US in 1962 and USSR in 1971 [37]. Since then, EP has been developing continuously, and currently it is substituting the traditional chemical propulsion (CP). There are initiatives such as the All-Electric Propulsion Satellite by Boeing, the Eurostar Series satellite platforms with the option of full EP by Airbus, and the Starlink satellite internet constellation by SpaceX, which contribute to full EP implementation for satellites in the near future.

The EP systems use the on-board electric power of the spacecraft, usually supplied by solar panels, to ionize the propellant and accelerate the resulting plasma with electromagnetic fields to generate thrust [46, 37]. In principle, EP systems have no limitations on the specific impulse, i.e. the exhaust velocity of the propellant. Conversely, in CP systems, the specific impulse obtained from combustion is limited by the fuel specific chemical energy, a property intrinsic to the type of fuel. The rocket equation, or Tsiolkovsky's equation, relates the total impulse and the propellant mass needed for a mission as

$$\Delta V = I_{sp} g_0 \ln \frac{m_{dry} + m_{prop}}{m_{dry}} \rightarrow \frac{m_{prop}}{m_{dry}} = \exp \frac{\Delta V}{I_{sp} g_0} - 1, \quad (1.1)$$

where:  $\Delta V$  is the total impulse;  $m_{dry}$  is the dry mass of the spacecraft,  $m_{prop}$  the propellant mass; and  $I_{sp}$  is the specific impulse of the propulsion system with  $g_0 = 9.8 m/s^2$ . We see that the higher the specific impulse is the lower the required mass of propellant is, and typical values of  $I_{sp}$  for EP are around 1000-5000s, while for CP are in the range 100-500s. Then, EP allows significant savings in propellant mass, and therefore in mission costs since the weight during the launch is usually the main contribution to the mission budget. The main drawback of EP is that the available power on-board is limited, and the thrust produced is much smaller (thrust-to-weight  $10^{-6}$ - $10^{-4}$ , for GIT and HET) than in CP (thrust-to-weight  $10^{-2}$ - $10^2$ ). The time for a manoeuvre is prolonged with EP, and is used mainly for in-space manoeuvres such as station keeping, drag compensation, orbit transfers, orbit adjustments, etc.

EP systems are commonly classified based on the thrust mechanism, which can be electrothermal, electrostatic or electromagnetic [47]:

- **Electrothermal.** The thrust is due to the pressure of the plasma on the thruster walls. The plasma is heated with electric power and expanded in a solid nozzle, in a similar way as in chemical thrusters.
- **Electrostatic.** The thrust is produced by the electric force of plasma on electrodes. The plasma is accelerated by the electrodes biased to different electric potentials.
- **Electromagnetic.** The thrust is generated by the interaction between the plasma currents and the currents of the thruster magnetic circuit (created by a set of coils or magnets for an applied magnetic field).

Two of the mature technologies, GIT and HET, belong, respectively, to the second and third group. GIT ionizes the propellant with bombardment of high-energy electrons emitted by a hollow cathode. The ions are accelerated with an electric field created by biased grids, and the ejected ion beam is neutralized by the electrons of a second external hollow cathode. GIT is the EP thruster with best performances: specific impulse  $\sim 3000$ s and thrust efficiency  $\sim 70\%$ . HET has an internal anode and an external hollow cathode. The hollow cathode emits electrons: part of them goes to the anode, collide with the propellant and produces ionization; and another part goes to neutralize the ejected ion beam. The magnetic field is applied in-between the electrodes and makes the electrons drift azimuthally, which prevents from short circuiting the discharge and generate the thrust. HET performances are a bit worse: specific impulse  $\sim 1500$ s and thrust efficiency  $\sim 50\%$ . The main drawback of GIT and HET is that the operational lifetime is limited by the erosion of the electrodes. GIT has a lifetime about 30000hours (3 year) and HET has about 10000hours (1 year), but the modern satellites are designed, usually, to last for more than 20 years on average.

Commercial EP thrusters use mostly xenon as propellant [37]. Xenon has a very good trade-off of properties: low energy threshold for ionization, which means less power losses; heavy element, good for thrust generation; and chemically inert, so that reactions with the electrodes, which modify their properties, are avoided. However, xenon is a scarce element on Earth, the supply is poor and will not satisfy the foreseen demand in the near future [77, 42]. Propellants alternative to xenon have been searched, and currently there are many candidates. Traditionally, other noble gases, e.g argon and krypton, have been proposed [35]. These are more abundant than xenon in the atmosphere, but are still rare gases. On the other hand, non-noble substances have been investigated as well. Iodine is advantageous from a system point of view, which allows compact storage in solid state and does not need high pressure tanks, and has similar performances compared to xenon [99, 114]. Water, which is abundant in the solar system, would make feasible the concept of in-situ resources utilisation for propellant replenishment [75, 74, 94]. New thrust concepts have also appeared in this context, such as the air-breathing thrusters, which have potential use in low Earth orbits for drag compensation. Since no large propellant storage is needed, this concept would allow long-term missions at low altitudes [28, 29, 87, 8]. The problem is that the non-noble substances, although versatile, are reactive, and will further reduce the lifetime for HET and GIT.

The Electron Cyclotron Resonance Thruster (ECRT) and the Helicon Plasma Thruster (HPT) are novel thrusters [11, 93, 2, 105], which have an electrothermal/electromagnetic character. The plasma, mainly the electrons, is heated via interaction with electromagnetic waves emitted by an antenna. Once energized, the electrons collide with the propellant and are able to ionize. The magnetic field applied in conventional designs, is quasi-axial inside and divergent outside the thruster. Inside, the field screens

the plasma from the walls to reduce the losses, and outside operates as a magnetic nozzle: it channels and accelerates the plasma to generate thrust, in an analogous way to a solid nozzle but being contactless. The main difference between ECRT and HPT is in the way the plasma is produced and heated. In ECRT, the frequency of the electromagnetic waves excites the electron cyclotron resonance, and typically is within the microwave range of GHz. The electron cyclotron frequency is proportional to the applied magnetic field, and the resonance happens usually around a localized surface since the field strength is spatially dependent. In HPT, the radiofrequency range of MHz is used to get a helicon plasma source, and heating is generally less localized.

The ECRT and HPT are electrodeless and, in principle, should have a longer lifetime than GIT and HET. Being electrodeless makes them also tolerant to a wide range of propellants, even non-noble substances [122, 123, 17]. They have a specific impulse around 1000s, and could substitute HET and GIT in several scenarios. However, they are still under research, with a Technology Readiness Level (TRL) of 4-5 [25]. The existing prototypes report still low performances and results of direct measurements from thrust balances show that the thrust efficiency is below 10% [116, 81, 96, 106], which is still not competitive with respect to GIT and HET. Research is being conducted extensively for ECRT and HPT in order to increase their TRL and thrust efficiency. In Europe, there is a Strategic Research Cluster on in-space EP, within the program Horizon 2020 promoted by the European Commission, to conduct research on new disruptive EP technologies and concepts. Among them, there is the MINOTOR project for ECRT, and the HIPATIA project for HPT.

The physics behind the operation of ECRT and HPT is not fully understood yet, which makes difficult to optimize their design, and further research is required. The theoretical models have flexibility to perform fast parametric studies, and can estimate certain properties which experiments cannot measure easily. Thus, the models, if reliable, are useful to guide the future designs. The methods for modeling (with a decreasing level of complexity are):

- Kinetic approach [89, 121]. This describes the species with their distribution functions in phase-space (i.e. physics-velocity space), which are obtained solving the Boltzmann equation. It is the most accurate level for modeling. However, the application to full simulations of the plasma discharge in thrusters means to simulate 6 dimensions, which is very costly from a computational point of view.
- Particle-in-cell (PIC) approach [40, 115, 100, 104, 22, 26]. This is actually an alternative Lagrangian-Eulerian form of the kinetic approach. The species distribution functions are discretized in macroparticles, which are followed considering the forces applied to each of them. The level of accuracy is similar to the kinetic approach, but there is noise in the results associated to the statistics of the macroparticles. The smallest spatial and temporal scales, which are determined by the electrons, need to be solved. Due to the large disparity in mass with respect to the heavy species, this approach is not proper for full simulations either.
- Fluid approach [49, 71]. This characterizes directly the macroscopic properties of the species (e.g. density, velocity and temperature), which are obtained solving a macroscopic model: a set of equations from the velocity moments of the Boltzmann equation. This approach is much faster than the kinetic and PIC ones but needs assumptions to close the model, which may reduce its

physical consistency. At each step of the hierarchy of moments to the Boltzmann equation, macroscopic terms of next order appears. The equations need to be truncated at some point and closures for the higher order terms are needed, which usually are energy equation and heat flux.

Aside from the pure approaches above, the hybrid approach using PIC for heavy species and fluid for electrons is viewed as an excellent trade-off between accuracy and computational costs. The accepted standards of this approach was introduced by Fife, Parra and coworkers in Refs. [33, 78], with the development of the codes HPHALL and HPHALL-2 for HET. Similar formulations afterwards were used by other authors [39, 53]. In these codes, the PIC subcode is two-dimensional axisymmetric, and the fluid subcode is partially 2D. Only ‘regular’ magnetic field topologies can be solved, i.e. with magnetic streamlines connecting inner and outer walls of an annular HET chamber and without singular magnetic points. The electrons in HETs are confined within magnetic field lines, and those lines are considered isothermal and equations are formulated for averaged electron magnitudes along them. Nowadays, most new thrusters present more complex magnetic topologies [41, 50], which do not fit within the capabilities of these codes. In particular: modern HET designs tend to implement magnetic shielding of chamber walls [72, 73]; an alternative version of the HET, the High Efficient Multistage Plasma Thruster, relies on magnetic topologies with several singular points and cusp-type topologies [52]; and the HPT and the ECRT present magnetic nozzles with magnetic lines closing far away from the thruster main chamber.

Our research group, Equipo de Propulsion Espacial y Plasmas (EP2) [32], is devoted to theoretical modeling in EP (with also extensive experimental activities), and is involved in many EP research projects for the mature technologies and also for the novels ones ECRT and HPT, e.g. the projects MINOTOR and HIPATIA mentioned above. Following the advantages of hybrid approaches, and as continuation of the codes HPHALL and HPHALL-2, EP2 is developing HYPHEN [79, 31]: a multi-thruster simulation platform to be applied for many types of electromagnetic thrusters, which was initiated for HET and is extensible to ECRT and HPT. The code is 2D axisymmetric for heavy species and electrons, with improvements to the previous ones. In the PIC subcode, a population control algorithm is implemented to reduce the noise in the results, and dedicated computational lists are used for each species to have the flexibility to handle mixtures of as many species as possible and the interactions between them. In the fluid subcode, a fully 2D magnetized electron model is implemented. Since magnetized electrons have anisotropic transport properties, the use of a magnetic field aligned mesh (MFAM) avoids numerical diffusion [9, 80]. However, for realistic and complex magnetic topologies, the use of a MFAM face many challenges such as the selection of schemes for numerical derivatives, and the solution around the highly irregular boundary cells for this non-Cartesian mesh and an anisotropic fluid.

As long as the Debye length is the smallest length of the plasma, and plasma quasineutrality holds except in thin Debye sheaths around surfaces, hybrid codes benefit from quasineutrality being easily implemented. HYPHEN is organized in three main modules: the Ion(I)-module, solving the dynamics of the various ions and neutral species, the Electron(E)-module solving the electron response, and the Sheath(S)-module solving the plasma interaction with different types of surfaces (dielectric, metallic,...) [3, 79]. A fourth Wave(W)-module, solving the plasma-wave interaction and energy deposition, would be necessary for electrodeless thrusters such as the HPT and the ECRT.

Furthermore, the plasma expansion along magnetic nozzle needs deeper analyses with a separate



code. The plasma becomes very rarefied, and one-dimensional kinetic steady-state models [64, 4] have been used. However, these models cannot solve self-consistently a subpopulation of electrons trapped along the expansion, which are generated via transient processes or infrequent collisions, and are shown to have a significant role on the properties of the expansion [86].

## 1.1 Thesis scope and objectives

In the framework of this thesis, HYPHEN is extended to HPT and ECRT plasmas. As already shown, the modeling of these thrusters has two distinguished parts: plasma transport and plasma-wave interaction. The first part shares synergies with HETs, since in all these thrusters the plasma dynamics is under an applied magnetic field. The main changes are associated to the different magnetic topologies and their functions, and the different plasma heating mechanism. The second part is exclusive of HPTs and ECRTs, and requires an additional model. This thesis is focused mainly on the plasma transport, while the plasma-wave interaction is the objective of other related PhD theses [112, 48].

HYPHEN is improved in the numerical and modeling aspects. In the former, the electron fluid model was not solved correctly due to the numerical problems on a MFAM. The numerical treatment of the model is investigated thoroughly to find proper algorithms that assure the accuracy of the results. In the latter, the collisions of diatomic molecules are implemented so that simulations of complex alternative propellants can be conducted.

The code, once assured the accuracy of the results, is applied to solve self-consistently the main aspects of the plasma discharge and the plasma temperature given a known power deposition map, and thus understand the physical phenomena in electrodeless thrusters with magnetic nozzles. The main design parameters are studied, the main reasons of the low performances are identified, and improvements are proposed. Furthermore, the code is used to assess the air-breathing concept for this type of thrusters by studying air as alternative propellant. The discussions in this thesis are focused mainly on HPTs, in particular on the prototype HPT05M [76], which is being developed within EP2 in collaboration with SENER (see Fig. 1.1).

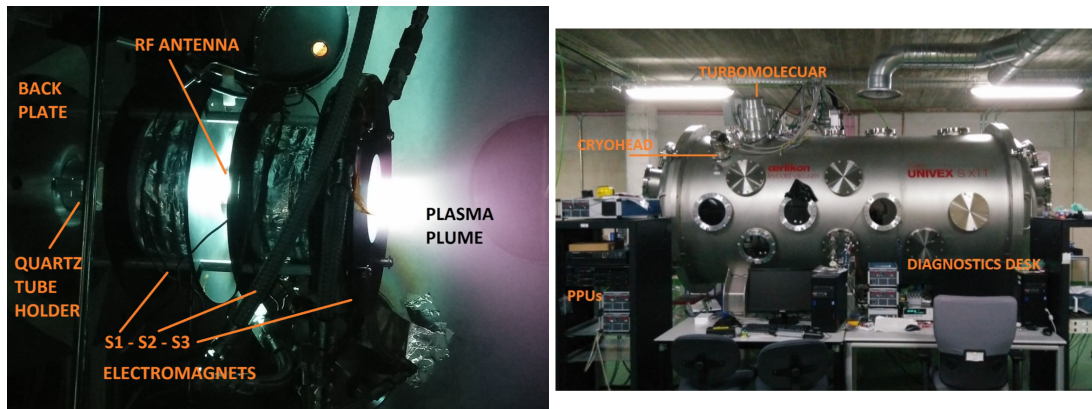


**Figure 1.1:** Pictures of (left) the HPT prototype HPT05M and (right) the vacuum chamber in the facilities of EP2.

Apart from HYPHEN, an 1D time-dependent and weakly-collisional kinetic code VLASMAN is used for deeper analyses of the plasma expansion along magnetic nozzle. This code was developed by Sánchez-Arriaga, and within the framework of this thesis some support was given for the development [89]. The code implements a Boltzmann-Poisson system and the model improves a previous one in Ref. [64, 4] allowing to study the unsteady evolution of the plasma and the collisional processes and, solving self-consistently the subpopulation of trapped electrons. The properties of the expansion are better characterized and the macroscopic behaviour of the plasma is discussed.

## 1.2 Thesis outline

The core of the thesis is organized as follows:

- Chapter 2 discusses the numerical treatment for the continuity and momentum equations of the magnetized electron fluid model within HYPHEN on a MFAM. The main numerical problems are identified and numerical algorithms to handle those problems are proposed. Closing the fluid model with a polytropic electron temperature, simulations with HYPHEN are run for mini-HPT to test the algorithms. The solution from the fluid model is studied together with thruster performances. This chapter adapts the contents of the peer-reviewed journal article [120].
- Chapter 3 completes the electron fluid model with the energy and heat flux equations, and extends the numerical treatment discussion in Chapter 2. Simulations with HYPHEN for HPT05M are run solving the electron temperature from the energy equation for a given power deposition map. Two design parameters, magnetic topology and thruster length, are studied, for the impact on the plasma discharge profiles and performances. The main inefficiencies of the discharge are analyzed, and thrust mechanisms are identified. The current configuration of HPT05M is partially optimized and further improvements are proposed.
- Chapter 4 describes the modeling of collisions in HYPHEN and the implementation of those for diatomic molecules. HYPHEN is used to evaluate the air-breathing concept for a particular configuration of HPT05M. Results of plasma profiles and performances are obtained, and are compared with Xe. Proper operation conditions with air are discussed. This chapter was partially completed during a research stay at the Consiglio Nazionale delle Ricerche in Italy, under the supervision of Taccogna.
- Chapters 5 and 6 show the analyses of the plasma expansion along magnetic nozzle with VLASMAN. Chapter 5 is focused on the transient process, and Chapter 6 on the collisions. Chapter 5 adapts partially the contents of the peer-reviewed journal article [89], and Chapter 6 the contents of an article in process of revision for a peer-reviewed journal [121].
- Chapter 7 summarizes the main conclusions, and lists issues interesting for future research.
- Appendix A shows the simulation results with HYPHEN solving also the plasma-wave interaction, which therefore produces a self-consistent power deposition map. The results are for HPT prototypes.
- Appendix B shows the simulation results with HYPHEN for a ECRT prototype.

## Chapter 2

# Hybrid simulation model: numerical treatment (i)

*This chapter adapts the published contents from a peer-reviewed journal article: "Numerical treatment of a magnetized electron fluid model within an electromagnetic plasma thruster simulation code", Plasma Sources Science and Technology 28 (2019) 115004.*

### 2.1 Introduction

The goal of this chapter is to analyze the numerical algorithms used to solve the electron continuity and momentum equations on a given magnetic field aligned mesh (MFAM) of the Electron(E)-module within the code HYPHEN. The strategies for the generation of a suitable 2D magnetic mesh, based on geometric quality indicators, were already discussed in Ref. [80, 79]. The challenges here to obtain accurate numerical algorithms come from several sides: (1) the high irregularity of the cells; (2) the large anisotropy in electron conductivity caused by the magnetic field; (3) the treatment of non-magnetically aligned boundary cells, and (4) the presence of null singular points. Finite volume, finite difference, and least square methods will be proposed for each specific case.

The electron continuity and momentum equations are here closed with a polytropic state equation relating pressure and density. To illustrate the electron response with the proposed numerical algorithms a HPT configuration will be used. This will allow to compare the present approach with the simpler one by Ahedo and Navarro [7], where local current ambipolarity is imposed (and ions are treated as a fluid).

The rest of the chapter is organized as follows. Sec. 2.2 presents the thruster and magnetic geometries that will be simulated and the electron fluid model. Sec. 2.3 discusses the numerical treatment of these equations. Sec. 2.4 assesses the previous numerical algorithms treatment with simulations of an HPT plasma discharge. Sec. 2.5 summarizes the conclusions of this chapter.

## 2.2 Problem formulation

### 2.2.1 Geometric and magnetic topologies

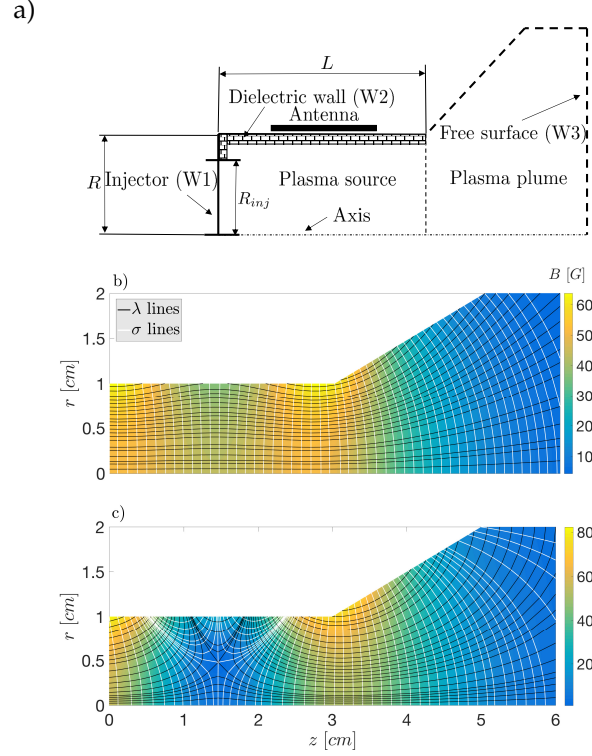


**Figure 2.1:** (a) Scheme of the mini-HPT plasma domain to be simulated. The vessel length and radius are 3 cm and 1 cm, respectively. The injector radius is 0.75cm. (b) Conventional magnetic field to be used in cases C1A (and in case C1B with double strength). (c) Magnetic field with a null point used in case C2.

Figure 1(a) presents a sketch of the plasma domain to be simulated, which is similar (but shorter) to the one used in previous HPT studies [112, 7]. The vessel length and radius are  $L=3\text{cm}$  and  $R=1\text{cm}$ . The injector of xenon occupies a circle of radius  $R_{inj}=0.75\text{cm}$  at the back of the chamber. The rest of the vessel wall is made of a dielectric material. An external helical antenna around the vessel emits radiofrequency energy inside, which is absorbed by the plasma. External coils with independent electric currents generate an applied magnetic field  $B$ . Magnetic topology and strength depend on the values and directions of these currents.

Figure 1(b) and 1(c) depict the streamlines and the equipotential lines (surfaces of revolution, indeed) for two magnetic topologies. Figure 1(b) shows the conventional one for a HPT, with quasi-axial magnetic lines inside the vessel (to accomplish good magnetic confinement at the lateral walls), and divergent magnetic lines outside (to form the magnetic nozzle that accelerates supersonically the plasma beam and generates magnetic thrust [109, 76]). The topology of Fig. 1(c), bearing a singular magnetic point, has been used in some prototypes [113] and has been selected here mainly to assess the capability of the numerical scheme to deal with a null point.

Two coordinates systems are used: first, the natural cylindrical reference frame  $\{\mathbf{1}_z, \mathbf{1}_r, \mathbf{1}_\theta\}$ , with coordinates  $(z, r, \theta)$ ; and, second, the ‘magnetic’ reference frame constituted by  $\{\mathbf{1}_\perp, \mathbf{1}_\parallel, \mathbf{1}_\theta\}$ , with  $\mathbf{1}_\parallel = \mathbf{B}/B$  and  $\mathbf{1}_\perp = \mathbf{1}_\parallel \times \mathbf{1}_\theta$  and coordinates  $(\lambda, \sigma, \theta)$ . The orthogonal magnetic coordinates  $\lambda(z, r)$  and  $\sigma(z, r)$  arise from the solenoidal and irrotational equations for the axisymmetric magnetic field,  $\nabla \cdot \mathbf{B} = 0$  and  $\nabla \times \mathbf{B} = 0$ , in an axisymmetric geometry:

$$\frac{\partial \lambda}{\partial z} = r B_r, \quad \frac{\partial \lambda}{\partial r} = -r B_z, \quad (2.1)$$

$$\frac{\partial \sigma}{\partial z} = B_z, \quad \frac{\partial \sigma}{\partial r} = B_r. \quad (2.2)$$

The isolines are obtained by numerical integration of these equations and the unit derivatives satisfy

$$\frac{\partial}{\partial \mathbf{1}_\perp} = r B \frac{\partial}{\partial \lambda}, \quad \frac{\partial}{\partial \mathbf{1}_\parallel} \equiv B \frac{\partial}{\partial \sigma}. \quad (2.3)$$

The selection of a magnetic mesh with a suitable distribution of isolines is a hard task, since the rates of change of  $\lambda$  and  $\sigma$  depend on the local strength of the magnetic field. Hence, the distances between the surfaces defined by two given values of one curvilinear coordinate depend on the field intensity, and can vary widely over the simulation domain. Ref. [80] discussed strategies for meshing definition with a given number of isolines.

### 2.2.2 Electron fluid model

According to the sequential and time-marching solving of the models for heavy species and electrons, at each timestep iteration, the Ion(I)-module delivers 2D maps of densities and fluxes of the different heavy species. This data is implemented into the electron fluid model we describe next, which delivers back the 2D maps of electric potential  $\phi$ , electron current density  $j_e$ , and electron temperature  $T_e$ .

Let  $n_s$ ,  $Z_s$ , and  $\mathbf{u}_s$  be the density, charge number, and macroscopic velocity of any independent species  $s$  (i.e. electrons and different heavy species). Since the plasma is quasineutral, the electron density satisfies

$$n_e \simeq \sum_{s \neq e} Z_s n_s, \quad (2.4)$$

and is thus known from the I-module. The ion and electron current densities are  $j_i = e \sum_{s \neq e} Z_s n_s \mathbf{u}_s$  and  $j_e = -e n_e \mathbf{u}_e$ . The first one is computed by the I-module, the second one will be obtained from the continuity equation

$$\nabla \cdot \mathbf{j} = 0, \quad (2.5)$$

for the electric current density,  $\mathbf{j} = \mathbf{j}_i + \mathbf{j}_e$ . For these current density vectors, we will distinguish between the azimuthal and meridional current densities, that is, for instance,  $j_{\theta e} = \mathbf{j}_e \cdot \mathbf{1}_\theta$  and  $\tilde{j}_e = \mathbf{j}_e - j_{\theta e} \mathbf{1}_\theta$ .

The electron momentum equation is expressed as

$$\mathbf{0} = -\nabla(n_e T_e) + e n_e \nabla \phi + \mathbf{j}_e \times \mathbf{B} + \mathbf{F}_{res}, \quad (2.6)$$

where the total resistive force,  $\mathbf{F}_{res}$ , is modelled as

$$\mathbf{F}_{res} = - \sum_{s \neq e} \nu_{es} m_e n_e (\mathbf{u}_e - \mathbf{u}_s) \equiv \frac{en_e}{\sigma_e} (\mathbf{j}_e + \mathbf{j}_c), \quad (2.7)$$

with:  $\nu_{es}$  the collision frequency with species  $s$ ;  $\sigma_e = e^2 n_e / m_e \nu_e$  the scalar (or parallel) conductivity;  $\nu_e = \sum_{s \neq e} \nu_{es}$  the effective electron momentum collision frequency; and

$$\mathbf{j}_c = en_e \sum_{s \neq e} (\nu_{es} / \nu_e) \mathbf{u}_s \quad (2.8)$$

the heavy species contribution to electron resistivity, expressed, for convenience, in terms of an equivalent current. Just for illustration, if the heavy species in the plasma are reduced to neutrals and singly-charged ions, it is  $\mathbf{j}_c \simeq \mathbf{j}_i$  for  $\nu_{ei} \gg \nu_{en}$ , and  $\mathbf{j}_c - \mathbf{j}_i \simeq en_e (\mathbf{u}_n - \mathbf{u}_i)$  for  $\nu_{ei} \ll \nu_{en}$ .

Finally a polytropic state equation is postulated for  $T_e$ :

$$T_e = T_{e0} (n_e / n_{e0})^{\gamma-1}, \quad (2.9)$$

where  $\gamma$  is the polytropic coefficient and  $n_{e0}$  and  $T_{e0}$  are two constants. This allows to define the barotropy function

$$h_e = \frac{\gamma(T_e - T_{e0})}{e(\gamma - 1)}, \quad (2.10)$$

(expressed in the units of  $\phi$ ), which satisfies  $\nabla h_e = \nabla(n_e T_e) / en_e = \gamma(T_e / e) \nabla \ln n_e$ . [For the isothermal case  $\gamma = 1$ , it is  $h_e = (T_{e0} / e) \ln(n_e / n_{e0})$ .]

Hence, the momentum equation reads

$$\mathbf{0} = en_e (\nabla \phi - \nabla h_e) + \mathbf{j}_e \times \mathbf{B} + (en_e / \sigma_e) (\mathbf{j}_e + \mathbf{j}_c). \quad (2.11)$$

which is indeed a tensorial Ohm's law for  $\mathbf{j}_e$ . Defining the Hall parameter  $\chi = \omega_{ce} / \nu_e$  and setting  $\partial / \partial \theta = 0$ , the three scalar momentum equations in the magnetic frame can be written as

$$j_{\parallel e} = \sigma_e \left( \frac{\partial h_e}{\partial \mathbf{1}_{\parallel}} - \frac{\partial \phi}{\partial \mathbf{1}_{\parallel}} \right) - j_{\parallel c} \quad (2.12)$$

$$j_{\perp e} = \frac{\sigma_e}{1 + \chi^2} \left( \frac{\partial h_e}{\partial \mathbf{1}_{\perp}} - \frac{\partial \phi}{\partial \mathbf{1}_{\perp}} \right) - \frac{j_{\perp c} + j_{\theta c} \chi}{1 + \chi^2} \quad (2.13)$$

$$j_{\theta e} = -j_{\perp e} \chi - j_{\theta c}. \quad (2.14)$$

Equations (2.12) and (2.13) set relation between the electron current density components and  $\phi$ ; the rest of contributions are known from the I-module. Equation (2.14) does not include  $\phi$  and thus is uncoupled of the other two.

In general it is  $L \nu_e (m_e / m_i) \ll \sqrt{T_e / m_i}$  with  $L$  the typical chamber dimension. This implies that

$$\frac{\partial \phi}{\partial \mathbf{1}_{\parallel}} \approx \frac{\partial h_e}{\partial \mathbf{1}_{\parallel}} \gg \frac{j_{\parallel e} + j_{\parallel c}}{\sigma_e} \quad (2.15)$$

and Eq. (2.12) is ill-conditioned numerically to determine  $j_{\parallel e}$ . This issue is ameliorated by using, instead

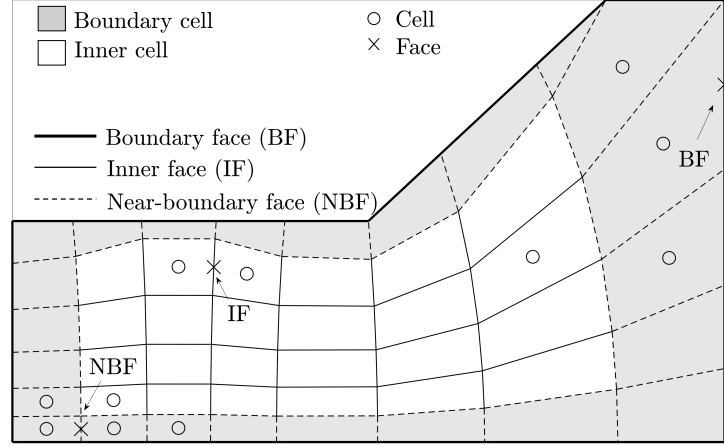


**Figure 2.2:** Sketch of cells and faces in a MFAM. The three crosses ( $\times$ ) are examples of the three types of faces. For each one, the circles surrounding them constitute the stencil considered for gradient reconstruction. The FDM is considered for an inner face. The WLSM is used for the non-inner faces with stencils constituted by two levels of adjacency.

of  $\phi$ , the thermalized potential  $\Phi$ , defined as the correction to the polytropic Boltzmann relation for electrons:

$$\Phi = \phi - h_e(n_e). \quad (2.16)$$

[Ref. [21] used the Bernoulli function  $H_e = -e\Phi$  instead of  $\Phi$ .] However, in Eq. (2.13) and for  $\chi \gg 1$ , we expect

$$\frac{\partial \phi}{\partial \mathbf{1}_\perp} \sim \frac{\partial h_e}{\partial \mathbf{1}_\perp} \leq O\left(\frac{j_{\perp e} \chi^2}{\sigma_e}\right), \quad (2.17)$$

so operating with  $\Phi$  or  $\phi$  is indifferent when solving for  $j_{\perp e}$ .

Regarding boundary conditions for the electron model, in general, they are set on the current perpendicular to the wall,  $j_n = \mathbf{j} \cdot \mathbf{n}$ , where  $\mathbf{n}$  is the boundary normal unit vector pointing outwards. In particular  $j_n = 0$  is imposed at the chamber dielectric walls and at the axis. Since there are no sources of electric current inside the domain, the total current through the free-space boundary is zero. Two limit cases to accomplish this condition are either to take the free-space boundary as ‘dielectric’ (i.e.  $j_n = 0$ ) or as ‘conductor’ (i.e.  $\phi = \text{const}$ ). In addition,  $\phi = 0$  is set at an arbitrary reference point.

## 2.3 Numerical treatment

### 2.3.1 Problem discretization

The electron fluid equations will be solved in the magnetic meshes of Fig. 2.1. A Finite Volume Method (FVM) is chosen to solve the current continuity equation while a Gradient Reconstruction Method (GRM) is used to discretize the Ohm’s law for electrons. The cells of the magnetic mesh are divided in two types, sketched in Fig. 2.2: *inner cells*, enclosed by two pairs of faces that are magnetic lines, and *boundary cells*, with at least one face corresponding to a domain boundary which is not a magnetic line;

boundary cells can have a number of faces different from 4. The *cell center* is the magnetic center for the inner cells and the geometric center for the rest of cells. The faces of the magnetic mesh are classified in three types: *inner faces*, separating two inner cells; *boundary faces*, corresponding to the plasma domain boundary; and *near-boundary faces*, which correspond to boundary cells and are not boundary faces. The *face center* is determined by the magnetic center or the geometric center when the former one is not available.

Applying the FVM to the electric current continuity equation on any cell yields

$$0 = \int_{\Omega} d\Omega \nabla \cdot \mathbf{j} \approx \sum_m S_m j_{nm}, \quad j_{nm} \equiv \mathbf{j}_m \cdot \mathbf{n}_m, \quad (2.18)$$

where  $\Omega$  is the cell volume, index  $m$  applies to all the cell faces,  $\mathbf{n}_m$  is the face unit normal pointing outwards,  $S_m$  is the area of the cone frustum face (in the 3D axisymmetric space), and  $\mathbf{j}_m$  is computed at the center of the face. Except for boundary faces,  $j_{nm}$  is either  $\pm j_{\parallel}$  or  $\pm j_{\perp}$  at the face, while for boundary faces  $j_{nm}$  is assumed known (the extension of the numerical method to other boundary conditions is not treated in this work).

GRMs, which are discussed in detail in the next subsection, discretize the derivatives at a face center  $m$  of a given function, say the thermalized potential  $\Phi$ , along a generic direction  $\mathbf{1}$ , as a linear combination of the function at several centers of surrounding cells. That is

$$\left. \frac{\partial \Phi}{\partial \mathbf{1}} \right|_m = \sum_l g_{ml} \Phi_l, \quad (2.19)$$

where  $l$  is the index of the cell centers involved,  $\Phi_l$  are the values at those points, and  $g_{ml}$  are the geometric factors of cell  $l$  with respect to face  $m$ . Using Eqs. (2.12) and (2.13) and GRMs, the parallel electric current density at the center of a  $\sigma=\text{const}$  face  $m$  satisfies

$$j_{\parallel m} = -\sigma_{em} \sum_l g_{ml} \Phi_l + j'_{\parallel m}, \quad j'_{\parallel m} = j_{\parallel im} - j_{\parallel cm}, \quad (2.20)$$

and the perpendicular electric current density at the center of a  $\lambda=\text{const}$  face  $m$  is

$$j_{\perp m} = -\frac{\sigma_e}{1+\chi^2} \left|_m \sum_l g_{ml} \Phi_l + j'_{\perp m}, \quad j'_{\perp m} = \left( j_{\perp i} - \frac{j_{\perp c} + j_{\theta c} \chi}{1+\chi^2} \right) \right|_m, \quad (2.21)$$

where current densities related to heavy species and provided by the I-module are included in  $j'_m$ .

Acting on all the mesh cells, Eq. (2.18) leads to the non-square matrix relation

$$A_1 \cdot \{j_{nm^*}\} = B_1, \quad (2.22)$$

with:  $\{j_{nm^*}\}$  grouping all current densities perpendicular to non-boundary faces  $m^*$ ,  $A_1$  collecting the areas of these faces; and  $B_1$  grouping all the information at boundary faces ( $B_1 = 0$  if all electric current at the boundaries are zero). Then, applying Eqs. (2.20) and (2.21) yields

$$\{j_{nm^*}\} = A_2 \cdot \{\Phi_l\} + B_2, \quad (2.23)$$

with  $\{\Phi_l\}$  grouping  $\Phi$  for all cells,  $B_2$  collecting the information on currents  $j_i$  and  $j_c$  from the I-module,



and  $A_2$  containing plasma and geometric information at non-boundary faces. Eliminating  $\{j_{nm}^*\}$  between the two matrix equations yields

$$A \cdot \{\Phi_l\} = B, \quad (2.24)$$

with  $A = A_1 A_2$  and  $B = B_1 - A_1 B_2$ . Since  $A$  is a square matrix, Eq. (2.24) is the matrix equation to be solved for the thermalized potential. HYPHEN employs the PARDISO [83, 82] direct solver for parallelized computation of the solution, although other solvers could be implemented (e.g., LIS [54]).

If the problem was to be solved directly for  $\phi$  instead of  $\Phi$ , the equation to consider would be

$$A \cdot \{\phi_l\} = B', \quad B' \equiv B + A \cdot \{h_{el}\}, \quad (2.25)$$

with  $B'$  known from the I-module.

### 2.3.2 Gradient reconstruction methods

A Finite Difference Method (FDM) is a simple and well-known method that allows a good accuracy in the numerical evaluation of gradients. The order of accuracy achievable by the FDM and the required discrete positions at which the differentiable function must be evaluated are well-defined. The drawback is that the FDM is devised for structured meshes and is unsuitable for unstructured ones. In the present case of a MFAM, the inner cells constitute a structured mesh in the magnetic coordinates but boundary cells (with boundary faces not magnetically aligned) must be treated as in an unstructured mesh and require other GRMs.

The most extended GRMs on unstructured meshes, which are to be used here for non-inner faces, are the Weighted Least Squares Method (WLSM) and the Green-Gauss Method (GGM) [30, 95, 97]. The GGM is based on applying the divergence theorem on a finite volume to establish the relation between the gradient within the said volume with the function values at its edges. Since in our problem derivatives need to be obtained at the cell faces, the application of this method is not direct and a dual mesh of finite volumes or an interpolation scheme must be introduced. This would add unnecessary complexity and unknowns, since the definition of the numerical artifices required for the GGM is not obvious. These reasons ruled out to use the GGM here.

On the other hand, the WLSM is built on Taylor's expansions around a point (a face center here) and it relates the gradients at that point with the values of the variable at a set of surrounding points (cell centers in our case), called the stencil. The number of points of the stencil (number of Taylor's expansions and equations) is generally larger than the number of derivatives to be computed; thus a weighted linear regression is introduced to obtain the solution. The WLSM can be applied straightforwardly to our boundary cells but poses two issues. First, the optimal number and location of stencil points is case-dependent and requires some trials and estimations. Second, since derivatives at different directions are obtained simultaneously, the method is prone to cause numerical diffusion in an anisotropic problem, as it is shown in Appendix 2.A. This last issue explains that, although the WLSM could be applied to all faces within the domain, it has been limited to non-inner faces.

The first-order Taylor's expansion (say for  $\Phi$ ) around face  $m$  reads

$$\Phi_l \simeq \Phi_m + \frac{\partial \Phi}{\partial \mathbf{1}_{\parallel}} \bigg|_m \Delta s_{\parallel ml} + \frac{\partial \Phi}{\partial \mathbf{1}_{\perp}} \bigg|_m \Delta s_{\perp ml}, \quad (2.26)$$

where:  $\Phi_l$  applies to cells  $l$  adjacent to face  $m$ ,  $\Delta s_{\perp ml}$  and  $\Delta s_{\parallel ml}$  are arc lengths from face  $m$  to cell center  $l$ . In the FDM, the stencil of points is selected so that they are aligned along one magnetic coordinate, and thus arc lengths along the second coordinate are zero. Here, on an inner face  $m$ , a 2-point stencil is used by taking the two inner cells adjacent to said face. The above Taylor's expansion allows to compute  $\Phi$  and its derivative perpendicular to the face. The associated coefficients  $g_{ml}$  in Eq. (2.19) are  $\pm \Delta s_{\parallel ml}^{-1}$  or  $\pm \Delta s_{\perp ml}^{-1}$ .

On near-boundary faces the WLSM is applied on a stencil that extends until the second level of adjacency; the first level being the cells directly adjacent to the face, and the second level being the cells adjacent to those. This typically means 5-6 cells as it is illustrated in Fig. 2.2. If the above first-order Taylor expansion with 3 unknowns is considered, the set of equations for the stencil is overdetermined and the WLSM must be applied.

The linear system in Eq. (2.26) can be formally expressed as

$$\{\Phi_{l_k}\} = C \cdot \mathbf{x}_m, \quad \mathbf{x}_m = (\Phi, \partial\Phi/\partial\mathbf{1}_{\parallel}, \partial\Phi/\partial\mathbf{1}_{\perp})_m \quad (2.27)$$

with  $\{\Phi_{l_k}\}$  extended to the  $k$  adjacent cells and  $C$  a matrix of geometric coefficients. The WLSM function  $F$  to be minimized is

$$F(\mathbf{x}) = [(\{\Phi_{l_k}\} - C\mathbf{x}_m)]^T \cdot W \cdot [(\{\Phi_{l_k}\} - C\mathbf{x}_m)], \quad (2.28)$$

where superindex  $T$  is for the transposed matrix and the elements of the diagonal weighting matrix  $W$  have been chosen as  $W_{ll} = (\Delta s_{\perp ml}^2 + \Delta s_{\parallel ml}^2)^{-1}$ , i.e., the relative weight of each cell is proportional to the inverse of the squared distance to the face. Other weighting methods are possible and have been proposed in the literature; however the inverse square distance allows us to construct gradients that are biased to over-represent local information, which we have found to work best with functions in which large spatial gradients are expected. The solution of the WLSM for  $\mathbf{x}$  is

$$\mathbf{x}_m = G \cdot \{\Phi_{l_k}\}, \quad G = (C^T W C)^{-1} C^T W, \quad (2.29)$$

and one column of  $G$  includes the coefficient  $g_{ml}$  needed in Eq. (2.19).

### 2.3.3 Magnitudes at the boundary faces

The above GRM yields  $\Phi$  at all cell centers and the derivatives of  $\Phi$  at all non-boundary faces. Interpolating appropriately that data, a complete 2D picture of  $\Phi$  and  $j_e$  is obtained (for instance at the regular mesh nodes of the I-module), except for the values at the domain boundaries. There, the main difficulty is that data extrapolation in an irregular mesh can yield large errors, as we show next. [Hereafter in this subsection and for sake of illustration we assume  $j_{nm} = 0$  at any boundary.]

A first way of determining  $\mathbf{x}_m = (\Phi, \partial\Phi/\partial\mathbf{1}_{\parallel}, \partial\Phi/\partial\mathbf{1}_{\perp})_m$  at a boundary face is just applying the previous WLSM using two-adjacency level stencils, resulting of course in Eq. (2.29). Then, Eqs. (2.20) and (2.21) yield the electric current densities at the boundaries, for instance, the component normal to the boundary is

$$j_{nm} = -\sigma_{e,m} \left( \cos \alpha \frac{\partial\Phi}{\partial\mathbf{1}_{\parallel}} - \frac{\sin \alpha}{1 + \chi^2} \frac{\partial\Phi}{\partial\mathbf{1}_{\perp}} \right) \Big|_m + j'_{nm}, \quad (2.30)$$

with:  $j'_{nm} = j'_{\parallel m} \cos \alpha - j'_{\perp m} \sin \alpha$ , and  $\alpha = \text{angle}(\mathbf{n}_m, \mathbf{1}_{\parallel m})$ . The accuracy of this standard WLSM at a boundary face [called WLSM(1)] is very poor due to the combination of large magnetic anisotropy and mesh irregularity. This is illustrated in Fig. 2.3(a), which plots, for a particular simulation, the relative error  $|j_{nm}^{(1)} / j_{i,nm}|$ , where  $j_{nm}^{(1)}$  is the perpendicular current density provided by the WLSM(1) and  $j_{i,nm}$  is the perpendicular ion current density at the boundary.

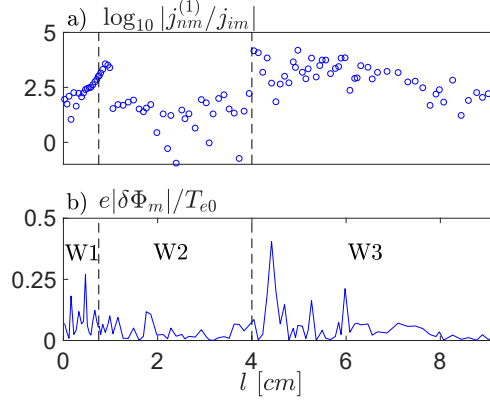


**Figure 2.3:** Relative errors in computing magnitudes at the boundary faces with WLSM(1) and WLSM(2). The coordinate  $l$  is an arc length parameter that begins at point  $(0, 0)$  and increases clockwise along the boundary walls W1, W2, and W3.

A second way of determining  $\mathbf{x}_m$  is a modified WLSM [called WLSM(2)], which assures the fulfillment of  $j_{nm} = 0$  in Eq. (2.30). The linear system from Eq. (2.27) is now expressed as

$$\{\Phi_{l_k} - \Phi_m\} = C_1 \cdot \mathbf{x}'_m, \quad \mathbf{x}'_m = (\partial\Phi/\partial\mathbf{1}_{\parallel}, \partial\Phi/\partial\mathbf{1}_{\perp})_m. \quad (2.31)$$

The solution of this WLSM(2) is

$$\mathbf{x}'_m = G_1 \cdot \{\Phi_{l_k} - \Phi_m\}, \quad G_1 = (C_1^T W C_1)^{-1} C_1^T W. \quad (2.32)$$

Substituting the derivatives of  $\Phi$  from Eq. (2.32) into Eq. (2.30) with  $j_{nm} = 0$ , yields  $\Phi$  at the boundary face,

$$\Phi_m = \frac{\mathbf{n}' \cdot G_1 \cdot \{\Phi_{l_k}\} - j'_{nm} / \sigma_{e,m}}{\mathbf{n}' \cdot G_1 \cdot \{1\}}, \quad (2.33)$$

with  $\mathbf{n}' = (\cos \alpha, -(1 + \chi_m^2)^{-1} \sin \alpha)$  and  $\{1\}$  a vector of ones.

Figure 2.3(b) plots the relative difference in  $\Phi_m$  between the two previous schemes,  $\delta\Phi_m = \Phi_m^{(1)} - \Phi_m^{(2)}$ , with superscripts (1) and (2) corresponding to WLSM(1) and WLSM(2), respectively. Since changes of  $e\Phi$  across the plasma domain are going to be  $O(T_{e0})$ , the error on  $\Phi_m^{(1)}$  is significant. Furthermore, the error becomes strongly amplified when deriving  $\Phi$  and multiplying by  $\sigma_e$ , as Fig. 2.3(a) for the electric current densities have shown.

## 2.4 Simulation results

The numerical schemes of Sec. 3 for integrating the electron fluid equations in the MFAM of the E-Module have been tested through several simulations of the mini HPT sketched at Fig. 2.1. The solutions shown here correspond to run sequentially the E-module and the I-module until a stationary discharge is reached. Simulations with three magnetic fields  $B$  are run: case C1A, with the magnetic field of Fig. 2.1(b); case C1B, identical to C1A but with double strength of  $B$ ; and case C2, with the magnetic field of Fig. 2.1(c). In the 3 cases the injector delivers a xenon mass flow rate of  $\dot{m}=0.1\text{mg/s}$  (equivalent to an electric current of  $e\dot{m}/m_i=73\text{mA}$ ) with a mean injection velocity of  $u_{inj}=300\text{m/s}$  and a temperature of  $T_{inj}=0.01\text{eV}$ . Based on experimental data [56, 60], a polytropic coefficient  $\gamma = 1.2$  is used. The reference temperature is  $T_{e0}=8\text{eV}$  and is assigned (arbitrarily) to point  $(z, r)=(1.4\text{cm}, 0.4\text{cm})$ . Chamber walls, W1 and W2, are dielectric and the condition  $j_n = 0$  is imposed at them. For magnetically guided plasmas, appropriate local boundary conditions at the downstream free-loss boundary W3, where the total electric current is zero, are a matter of present debate (see for instance [58] and references therein). For the purposes of the present chapter we will just take  $j_n = 0$  at W3. Notice that consequently the plasma plume leaving the domain downstream is current-free.

The assessment of the previous numerical algorithms on the electron fluid model is carried out in several ways. First, the thrusting performances of the three simulated cases will be briefly analyzed with the aim of understanding particle and energy balances and checking the physical consistency of the solution. Second, the 2D  $(z, r)$  maps of main plasma magnitudes will be discussed, checking again for physical reliability of results. Third, a study of the contributions of the different terms of the electron momentum equation in both magnetically-parallel and perpendicular directions will allow us to better estimate dominant and marginal contributions and thus identify the best numerical treatment. And fourth, the effects of cell size and plume extension will be assessed briefly.

### 2.4.1 Performances

Thruster performances, parametric analysis, and design optimization are not direct goals of this chapter. Nonetheless, a succinct analysis of the performances of the 3 HPT simulations is still useful for interpretation of the results. Appendix 2.B defines main thruster performance indicators and Table 1 shows them for the 3 simulation cases. A very low thrust efficiency,  $\eta_F$ , is observed in all of them, coming from the very low energy efficiency,  $\eta_{ene}$  (4-14%). Most of the absorbed power is spent in the walls (about 56-61%) and inelastic collisions (35-38%). Poor magnetic confinement explains directly wall losses but also the large inelastic collisions since neutrals are ionized twice, on average. This multiple ionization is evident when observing that the propellant utilization  $\eta_u$  is just moderate (13-60%) while the ratio of the total ion mass production rate versus the injected mass flow rate,  $\dot{m}_{i,total}/\dot{m} \equiv \eta_u/\eta_{prod}$  is 144-231%, and we remind that inelastic losses are proportional to  $\dot{m}_{i,total}$ .

The relevance of magnetic confinement is clear when comparing case C1A to C1B and C2. Doubling the magnetic field from C1A to C1B, implies a better magnetic confinement as confirmed by performances: there is a moderate reduction of energy losses at the walls and a large increase of  $\eta_u$ . This agrees with theoretical and experimental evidence [1, 7, 55, 108, 59]. Furthermore, in configurations C1A and C1B, the lateral wall is partially shielded magnetically but not the back wall. As a consequence, while the dielectric-to-injector surface ratio is 11.4 the dielectric-to-injector energy losses are

about 4.6, 2.0 and 5.8 for cases C1A, C1B, and C2, respectively. Confinement of the lateral wall improves from C2 to C1A and C1B, and this is reflected in the relative amount of energy losses at wall W2. Regarding wall W1, there is an increase on losses in case C1B, which seems to be due to the maximum plasma density being placed more upstream. Finally, plume efficiency,  $\eta_{plu}$ , is high in all cases, which means that the magnetic nozzle performs correctly. In fact, the plume divergence semi-angle defined as  $\arccos \sqrt{\eta_{plu}}$  is moderate, about 24-26 deg.

	$P_a$ [W]	$F$ [mN]	$\eta_u$	$\eta_{ene}$	$\eta_{plu}$	$\eta_F$	$\eta_{prod}$	$\epsilon_{inel}$	$\epsilon_{wall}$
<b>C1A</b>	8.36	0.166	0.25	0.07	0.83	0.016	0.14	0.37	$0.56 = 0.10 + 0.46$
<b>C1B</b>	10.57	0.365	0.60	0.14	0.83	0.063	0.26	0.38	$0.48 = 0.16 + 0.32$
<b>C2</b>	7.56	0.108	0.13	0.04	0.80	0.008	0.09	0.35	$0.61 = 0.09 + 0.52$

**Table 2.1:** Performance indicators. The two terms in the sums of the last column are the contributions of walls W1 (first term) and W2 (second one).

### 2.4.2 2D plasma profiles

Figure 2.4 shows the 2D maps of main plasma magnitudes for case C1A. The map of  $n_e$  [subplot 2.4(a)] comes from the I-module via the quasineutrality condition. Subplot 2.4(c) for the meridional current density  $\tilde{j}_i$  is provided by the I-module too. The electron current density vector and the (thermalized) electric potential are the outputs of the present electron fluid model. The reference values used for the dimensionless parameters are

$$j_0 = \frac{em}{m_i \pi R^2} = 234 \text{ A/m}^2, \quad c_{s0} = \sqrt{\frac{T_{e0}}{m_i}} = 2.43 \text{ km/s}, \quad n_0 = \frac{j_0}{ec_{s0}} = 6.02 \cdot 10^{17} \text{ m}^{-3}.$$

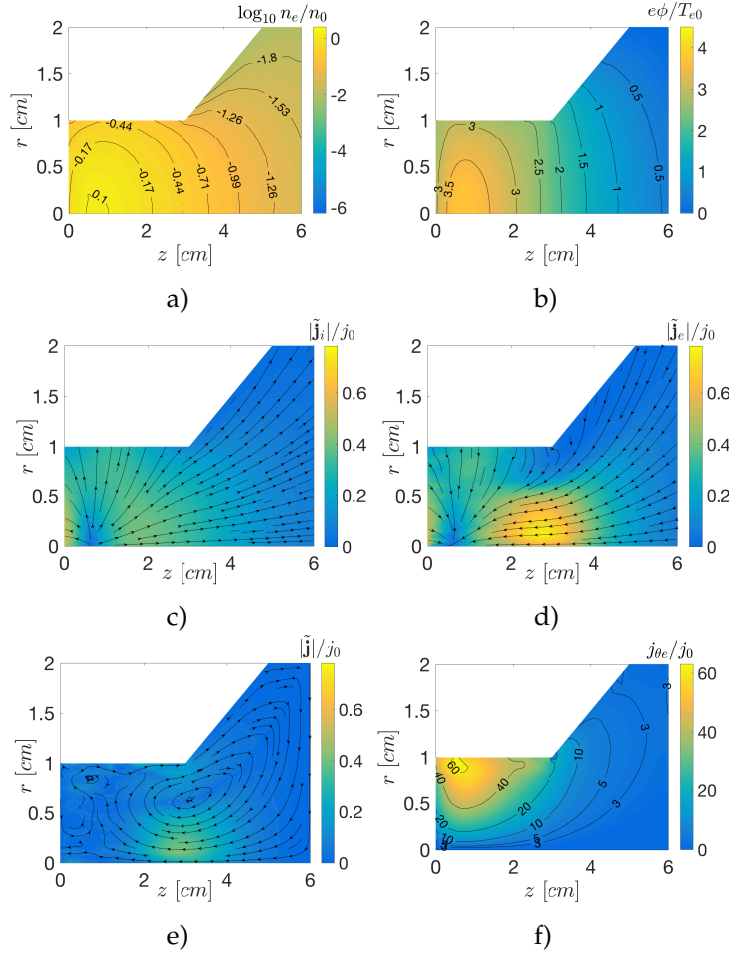
The ionization rate is maximum around the maximum of  $n_e$  (i.e. close to  $z=0.5\text{cm}$  and the axis). This explains also the behavior of the ion current streamlines  $\tilde{j}_i$ . The location of the maximum ionization rate near the back of the chamber is going to imply that many ion and electron streamlines end at the chamber walls, explaining the large energy losses and plasma recombination there. Ions move guided by the electric potential  $\phi$  [subplot 2.4(b)] which satisfies Eq. (2.16). Since the thermalized potential turns out to be much smaller than the electric potential [see Fig. 2.7(d) below],  $\phi$  satisfies approximately a ‘polytropic Boltzmann’ relation with the plasma density  $\phi \simeq h_e(n_e)$ .

The wall-normal electric current density  $j_n$  has been taken zero at all domain boundaries. This explains that the maps of  $\tilde{j}_e(z, r)$  and  $\tilde{j}_i(z, r)$  [Fig. 2.4(c) and 2.4(d)] are similar but not identical: a nonzero meridional electric current density  $\tilde{j}$  [Fig. 2.4(e)] develops. This feature will be further discussed in a later subsection.

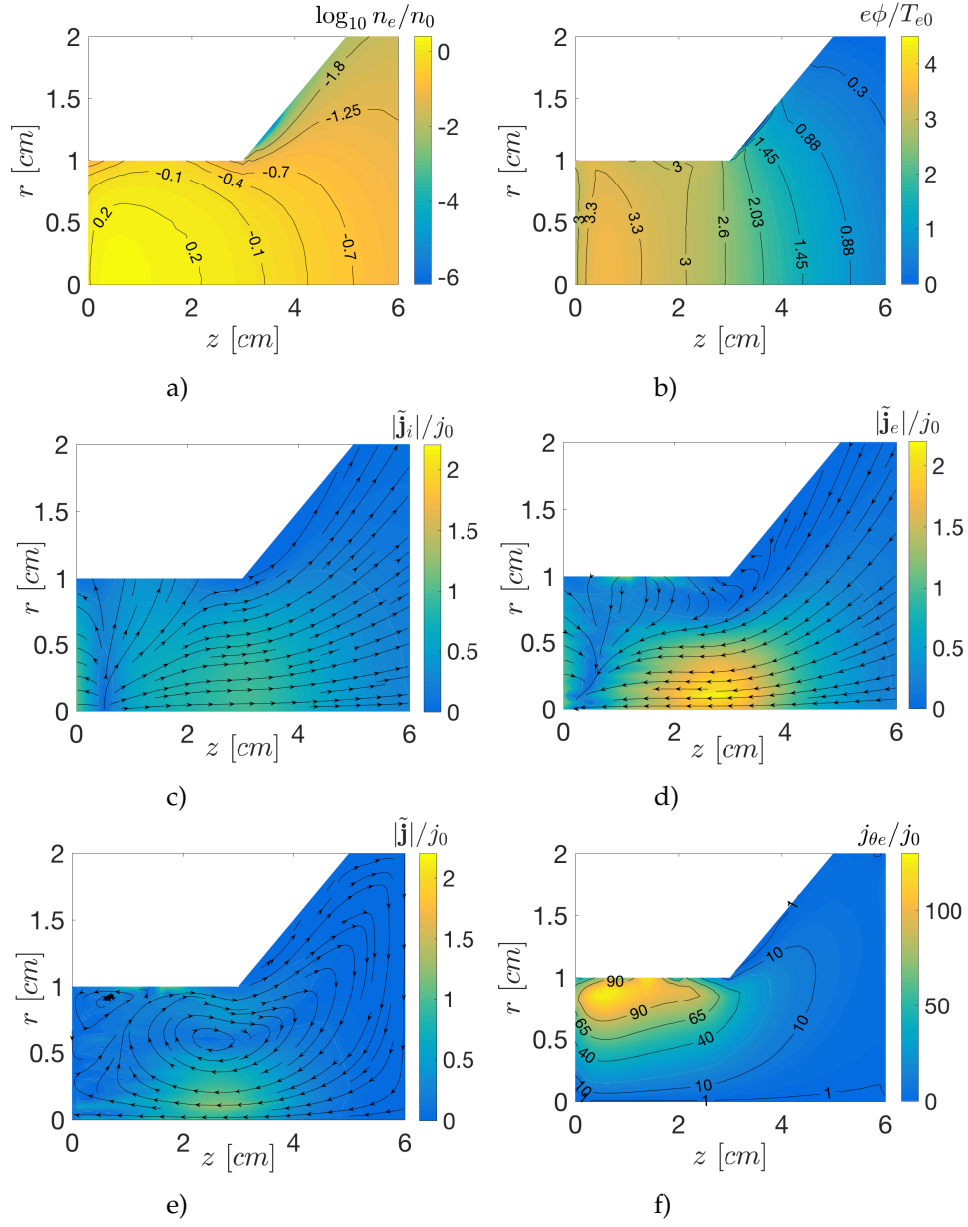
Since ions have a negligible azimuthal motion, the map of  $j_{\theta e}$  [Fig. 4(f)] corresponds to the azimuthal electric current density created in the plasma. These circular loops have an intensity proportional to the Hall parameter times  $j_{\perp e}$  and a diamagnetic character (i.e. the electric current runs in opposite direction to the coil currents creating  $B$ ) [1, 6]. Their interaction with the electric currents in the coils leads to action-reaction axial forces: the loops located in the magnetic nozzle constitute the source of magnetic thrust [6] while those inside the chamber do not contribute practically to thrust.

Figure 2.5 illustrates the electron fluid behavior for case C1B, where the magnetic strength has been doubled compared to C1A. Although performances improve much, only mild differences are appreciated in the 2D maps. Since the propellant utilization is larger, the plasma density is larger and, as a consequence, all the current densities are larger too. The maximum plasma density is shifted a bit upstream, possibly due to the higher ionization. The topology of current streamlines is very similar to C1A except for mild differences near the chamber walls due to better confinement.

Figure 2.6 corresponds to case C2. Comparing it with case C1A, the lower propellant utilization leads to a lower plasma density but its general 2D shape is similar; some differences are observed in the profiles of the electric potential inside the chamber. Current densities are naturally lower than in C1A, but the most interesting feature are the differences in the meridional currents: observe the three  $\tilde{j}$ -loops, the larger twisting of  $\tilde{j}$  lines, and the changes of signs of  $j_{\theta e}$  (around the separatrixes departing from the singular null point). In addition, the gentle behavior of the electric potential and the electron current density around the singular magnetic point (where the electron fluid becomes locally unmagnetized) confirms the capability of the numerical scheme to deal correctly with such points.



**Figure 2.4:** 2D maps of main plasma magnitudes for case C1A. The electron fluid model algorithms are responsible of determining  $\phi$  and  $j_e$ . The I-module provides  $n_e$  and  $j_i$ . Plots of plasma properties in this and subsequent figures correspond to a time average of the last 100 timesteps (which correspond to  $5\mu s$  with the time step used) of the stationary solution.



**Figure 2.5:** Same than Fig. 2.4 for case C1B.

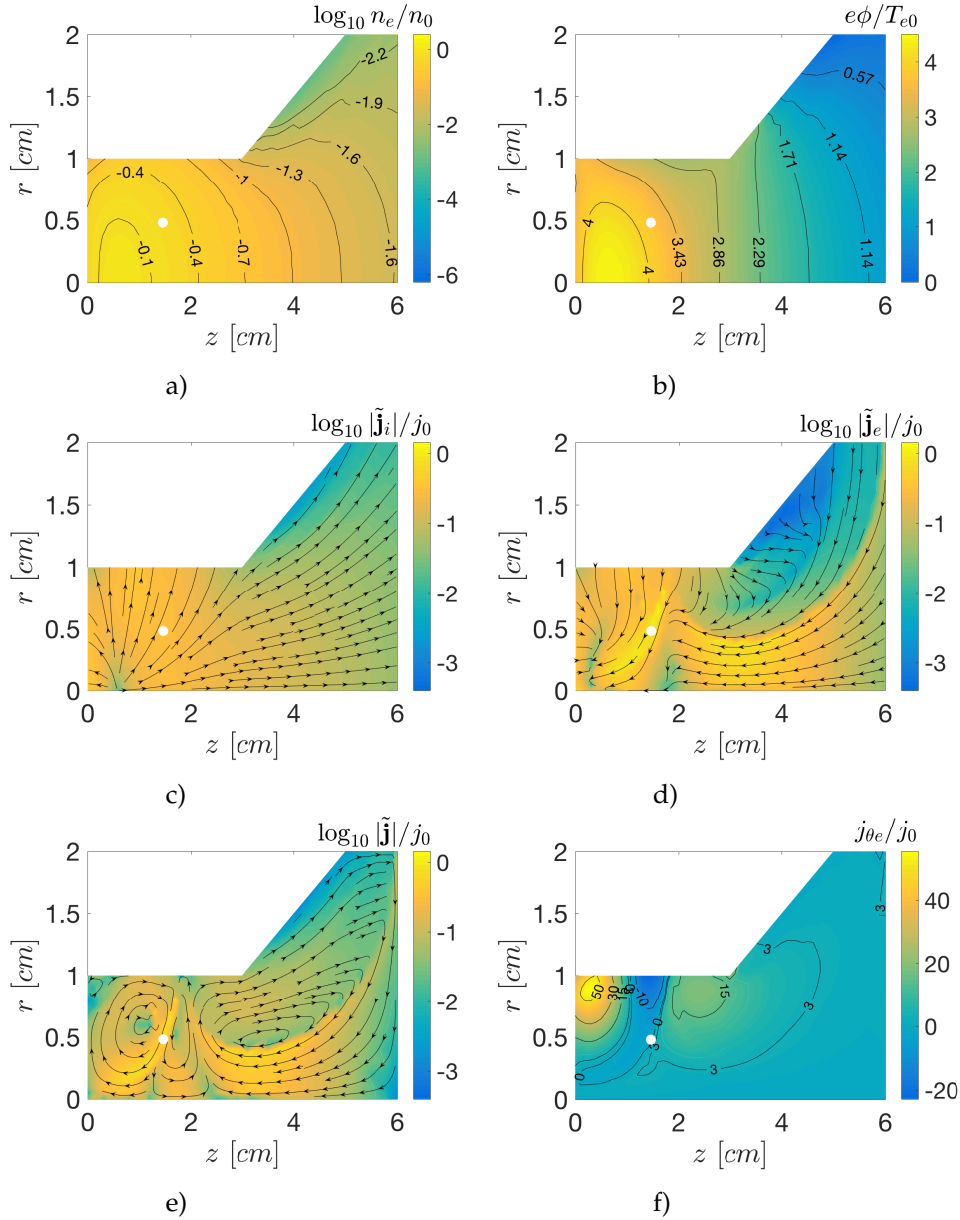


**Figure 2.6:** Same than Fig. 2.4 for case C2. The null magnetic point is indicated with a white dot.

### 2.4.3 Assessment of the momentum equation terms

The different terms of the electron momentum equations are evaluated in Fig. 2.7 for case C1A. Panel 2.7(a) shows that the contribution of heavy species to  $j_{\parallel e}$  through  $j_{\parallel c}$ , Eq. (2.12), is significant in certain regions of the plasma domain. On the contrary, the contribution of heavy species to the perpendicular electron current density, Eq. (2.13), is totally negligible:  $j_{\perp c} / [(1 + \chi^2) j_{\perp e}] < 10^{-4}$  in case C1A.

Panel 2.7(b) compares the electric current density to the ion and electron current densities, showing that  $|\vec{j}| \ll |\vec{j}_e| + |\vec{j}_i|$  in most parts of the domain, but not everywhere (specially near some boundaries). Then, panel 2.7(c) compares the parallel and perpendicular electron current densities, showing that they are of the same order inside the chamber (where boundary conditions have a stronger effect), contrary



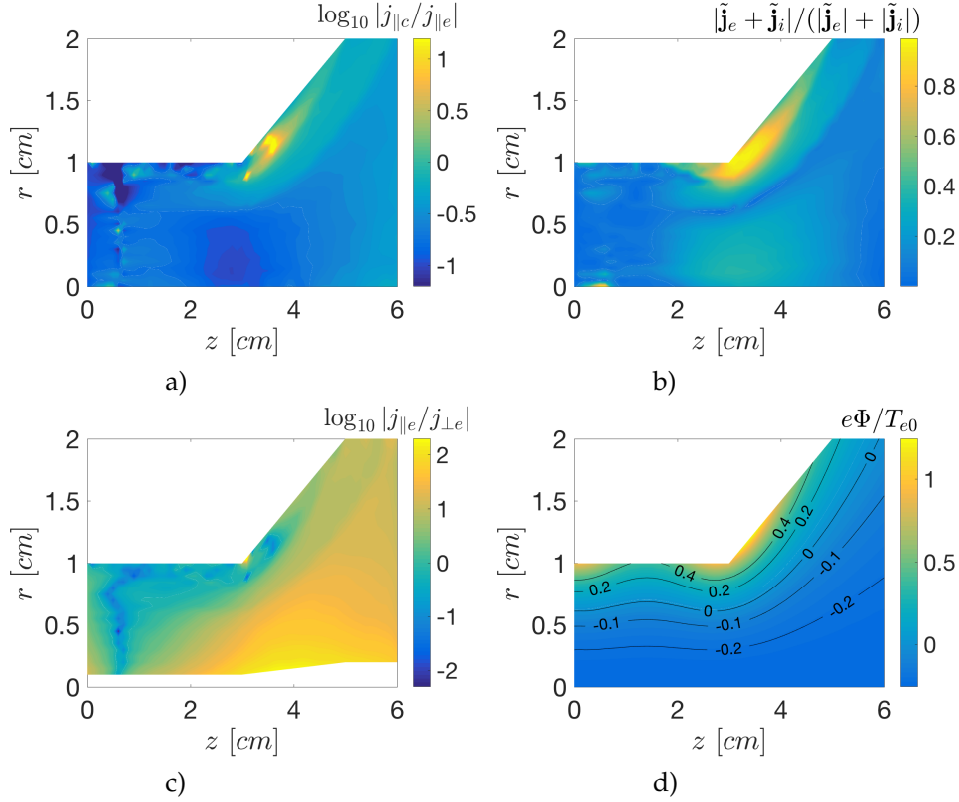


**Figure 2.7:** Additional 2D maps of case C1A for the analysis of the terms in the electron momentum equation. Upper and lower bounds have been imposed to the color scale to highlight main features.

to the naive idea that the anisotropic conductivity leads necessarily to  $j_{\perp e} \ll j_{\parallel e}$ . In the magnetic nozzle region, the higher Hall parameter and the smaller effect of domain boundaries do lead to the parallel current to dominate. Panel 2.7(d) plots the map of the thermalized potential  $\Phi$ . This has variations of about 10% of  $\phi$  variations, which confirms that the electric potential follows approximately a polytropic Boltzmann relation,  $\phi(n_e)$ . However, this small  $\Phi$  is crucial to determine the parallel electron current density in a weakly-collisional electron fluid, both in the present magnetized case and in the unmagnetized one [20]. In the magnetized case,  $\Phi$  is practically constant along the magnetic lines with  $\partial\Phi/\partial\mathbf{1}_{\parallel} \ll \partial\Phi/\partial\mathbf{1}_{\perp}$ , which makes more challenging the accurate computation of  $\Phi$  and  $j_{\parallel e}$  (this one is the product of the small  $\partial\Phi/\partial\mathbf{1}_{\parallel}$  times the very large parallel conductivity  $\sigma_e$ ).

A reliable computation of  $\Phi$  and  $j_{\parallel e}$  was the reason to work on the highly irregular MFAM and to use algorithms discretizing  $j_{\parallel e}$  and  $j_{\perp e}$  independently. Figure 2.8 compares the electric current densities inside the chamber for C2 when using for inner faces either (a) the FDM or (b) the WLSM; in both simulations, the WLSM is used in non-inner faces. The differences are very noticeable, particularly near the singular point, where the WLSM is unable to reproduce well the two current loops and yields too large values of the electric current density.

Finally, Fig. 2.9 compares results on the electric current density inside the chamber when either  $\Phi$  [Eq. (2.24)] or  $\phi$  [Eq. (2.25)] are used as main variable in the numerical algorithms. In this comparison, the differences are noticeable, the use of  $\Phi$  leads to better-defined current streamlines and lower noise in the values of the electric current. It must be mentioned that the temperature  $T_{e0}$  was doubled in this

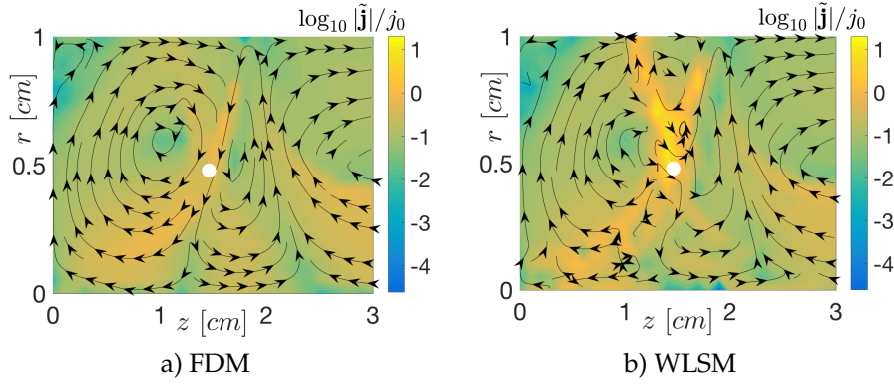


**Figure 2.8:** Electric current densities inside the chamber for case C2: (a) the FDM is used in inner faces, (b) the WLSM is used in all faces. The white dot indicates the location of the magnetic null point.

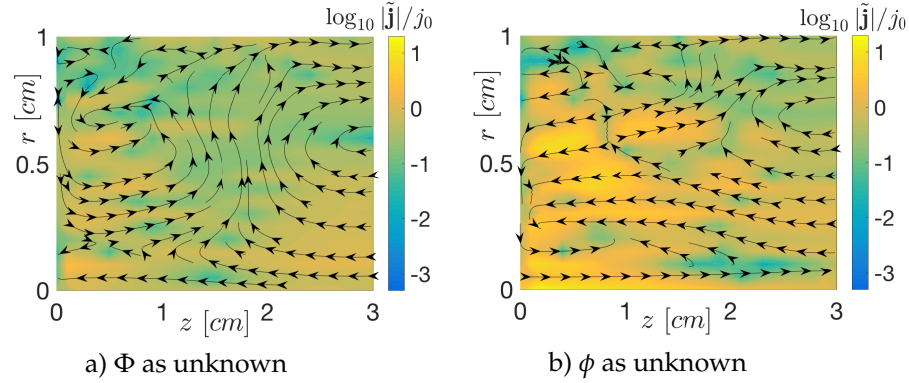


**Figure 2.9:** Electric current densities inside the chamber for same magnetic field than case C1A but with  $T_{e0} = 16\text{eV}$  (i.e. doubling the  $T_e$  map). Numerical algorithms on the electron momentum equation are applied directly on (a)  $\Phi$  or (b)  $\phi$ .

simulation to increase the effect of the electron pressure and thus the difference  $\phi - \Phi = h_e \propto T_{e0}$ .

#### 2.4.4 On current ambipolarity and plume extension

In previous subsections, we have found that meridional electric currents develop in the otherwise current-free plasma beam. These currents form several loops, which are framed by the boundaries of the simulation domain, due to the condition  $j_n = 0$  applied there.

This issue of current ambipolarity (i.e.  $\tilde{\mathbf{j}} = \mathbf{0}$ ) in a current-free plasma beam was carefully studied by Ahedo and Merino [6, 5, 68] in the context of a divergent magnetic nozzle (i.e. the plume region in the present case). They showed that fulfillment of current ambipolarity in the divergent nozzle was only achievable if ions (and thus electrons) are fully-magnetized, a too ideal case. For the case of interest of partially-magnetized (or unmagnetized) ions, current ambipolarity cannot be achieved (except at particular surfaces) and its failure is linked to the detachment of ions from magnetic lines [6]. In the present case, which includes thruster chamber and nozzle, we find that meridional current loops develop inside the chamber too. This implies that the simplified 2D fluid model (with the magnetic field purely cylindrical) of Ahedo and Navarro [7] for a helicon plasma thruster, which assumed current ambipolarity inside the thruster chamber, was incorrect in that postulate.

However, although the formation of meridional currents in the thruster chamber and nozzle is an interesting physical feature, Ahedo and Merino [6, 68] concluded that these currents have almost no relevance on the thruster performances. On the one side, these meridional currents induce an azimuthal magnetic field much smaller than the meridional field induced by the much higher azimuthal currents [Fig. 4(f) for instance], and even this last induced field is negligible for the plasma densities considered here. On the other side and more relevant for the present discussion, Ahedo and Merino found that, in the *collisionless limit*,  $u_{\parallel e}$  (and therefore  $j_{\parallel e}$ ) is a plasma variable uncoupled from the rest. As a consequence, changes of  $j_n$  at the downstream boundary, for instance, are mainly managed by  $j_{\parallel e}$ , affecting minimally the rest of the plasma response.

In order to verify that this behavior continues to apply in the present, more general model, simulations of case C1A with plume axial lengths from 3 cm (in the nominal case of Fig. 2.4) to 4.5 cm and 6 cm have been run. As the condition  $j_{n,W3} = 0$  is moved downstream with the plume length, the most downward meridional current loop changes length and topology. Figure 2.10 (a) and (b) show the ion and electric current densities for the 4.5cm-plume (i.e. 7.5 cm of total domain extension); plots have been restricted to  $z \leq 6$  cm in order to compare them easily with Fig. 2.4 (c) and (e). Differences are observed in  $\tilde{j}$ , but there are practically no changes on  $\tilde{j}_i$ , and the same is true for  $n_e$  and  $\phi$  (not shown in the figure). Also, thruster performance indicators remain basically the same for the three plume lengths, with differences about 1-2% (which, in fact, is about the level of noise of PIC simulations). Fig. 2.10(c) shows, at the mean radius for each  $z = \text{const}$  section, the 1D profiles of  $|\tilde{j}|$ ,  $j_{\perp e}$ , and  $j_{\parallel e}$  for the three plume lengths. Observe that differences are only relevant on  $j_{\parallel e}$  and even these tend to fade out if the plume is long enough. This completes the confirmation of the validity, in this more general case, of Ahedo and Merino's conclusions relative to the relevance of meridional electric currents in a magnetically guided plasma beam.

Finally, the preceding analysis allows us also to assess the effects of simulating a truncated plasma plume on the plasma/thruster response. As long as this length is not too short, the effects turn out to be rather marginal. Furthermore, Ahedo and Merino's theory and the present analysis suggest that the conditions set at the downstream boundary W3 (either  $j_n = 0$  or a different one on the electric current or potential) seem to be scarcely relevant on the plasma response, except for the parallel electron current and the related meridional electric currents.

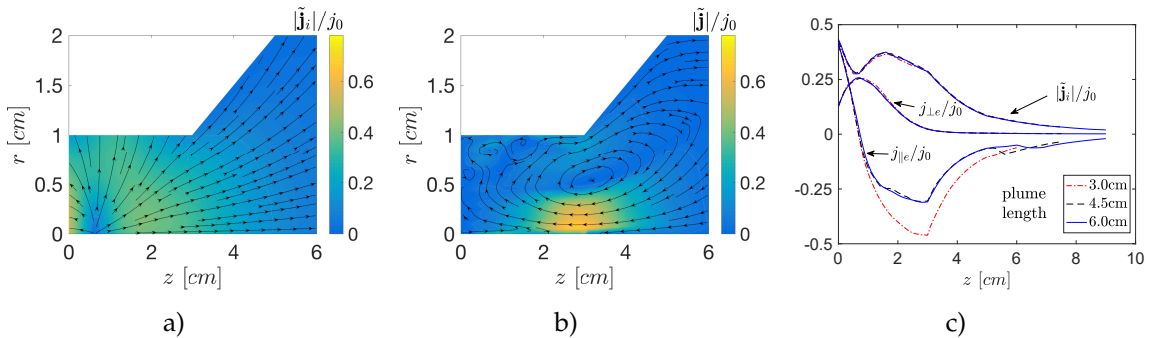


**Figure 2.10:** (a)-(b) Ion and electric current densities for a case identical to C1A except that the plume axial length is 4.5cm instead of 3cm. For easier comparison with same currents in Fig. 2.4, plots have been restricted to  $z \leq 6$  cm. (c) Ion and electron currents for plume axial lengths of 3cm, 4.5cm and 6cm, at the mean  $r$  of each  $z = \text{const}$  section.

### 2.4.5 Effects of mesh refinement

Simulations so far have been run on a MFAM (for the electrons) and a structured mesh (for the I-Module) of about 1200 cells each. To assess the solution sensitivity to mesh spacing, the case C1A with  $T_{e0} = 16\text{eV}$  has been calculated with about 1200, 2400, and 4800 cells in each mesh. Increasing the number of cells is a costly process, since the time step has to be reduced as well to fulfill numerical stability; this makes the simulation time to increase nearly quadratically. To have an idea of the computational cost here, the base simulation of Fig. 2.4 with 1200 cells takes already about 12 hours in a machine with 12 cores (i.e. 6 days-core) to simulate 2.5ms.

Results of the mesh size sensitivity analysis are shown in Fig. 2.11. Figures 2.11(a) and 2.11(b) plot the electric current density in the case of 4800 cells for the two numerical choices on computing  $\phi$  and must be compared with those of Fig. 2.9. As expected, smoother 2D maps are obtained as the mesh is refined. When algorithms work directly with  $\Phi$  [subplot 2.11(a)], the differences on the current lines are small but the spatial irregularities on  $|\tilde{j}|$  of Fig. 2.9(a) have nearly disappeared. On the other hand, when working directly with  $\phi$  [subplot 2.11(b)], irregularities decrease but still persist and there are still differences with subplot 2.11(a).

Figure 2.11(c) provides a more detailed evaluation of these results. It plots  $|\tilde{j}|$  at the exit section of the thruster ( $z=3\text{cm}$ ) for the three mesh sizes and the two numerical strategies on computing  $\phi$ . The convergence with the mesh size is observable and also the larger noise found when working directly with  $\phi$ . A quantitative assessment of the differences among the curves is obtained taking first the case with 4800 cells and  $\Phi$  as unknown as our ‘best (numerical) solution’. Then, calling  $|\tilde{j}|^{ref}(r)$  the curve for that case, the mean deviation of the rest of curves is defined as  $\delta = 1/R \int_0^R \left| |\tilde{j}| / |\tilde{j}|^{ref} - 1 \right| dr$  with  $R = 1\text{ cm}$ . Values of this deviation (or apparent error) are given in the inserts of the two panels of Fig. 2.11(c). It is worth to notice that there is still a deviation of 9.3% with 4800 cells when working with  $\phi$ , larger than in the case of 2400 cells and working with  $\Phi$ .

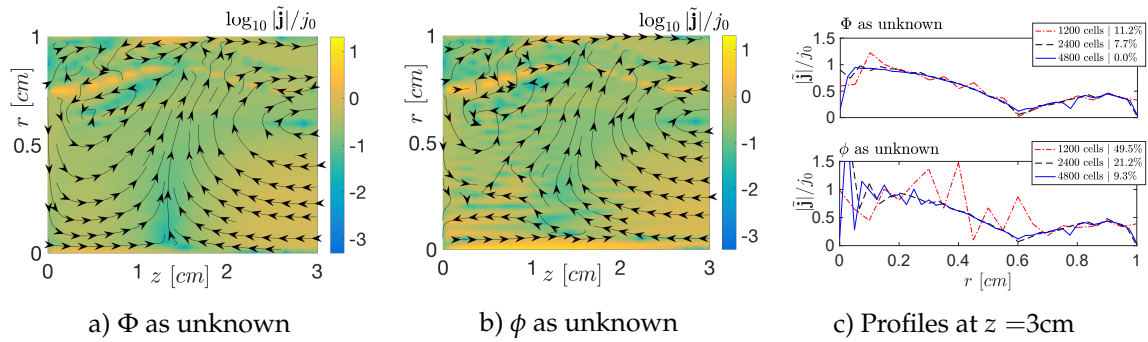


**Figure 2.11:** Panels (a) and (b) correspond to the same cases than Fig. 2.9 but using 4800 cells/mesh instead of 1200 in the simulations. Panel (c) plots the cuts of the electric current density at the chamber exit section,  $z = 3\text{cm}$ , for the 1200, 2400 and 4800 cells/mesh cases and the two numerical strategies followed to compute  $\phi$ . The percentages shown in the inserts of panel (c) correspond to the mean deviation  $\delta$  (defined in the main text) with respect to  $|\tilde{j}|$  for 4800 cells and  $\Phi$  as unknown.

## 2.5 Conclusions

The solution of a weakly-collisional, magnetized electron fluid model in a 2D axisymmetric geometry presents important challenges on magnitudes such as the electron current density, the ambipolar electric field, and the resulting electric potential map. These are caused by the large anisotropy between the directions parallel and perpendicular to the magnetic field, which can cause strong numerical diffusion ruining the accuracy of the results.

The first action for designing a reliable numerical treatment of that model is to operate on a magnetically aligned mesh, although this yields a large cell inhomogeneity in terms of size and aspect ratio. The second main action is to use a finite difference method for gradient reconstruction, whenever possible, which here means in all inner faces (i.e. those unrelated to boundary cells). It has been proven that weighted least squares methods, beyond presenting some arbitrariness on stencil and weight selection, can lead to numerical diffusion. Therefore, their use must be limited to the faces of the irregular boundary cells. Still, the computation of magnitudes in the boundary faces have required special modalities of the WLSM and there is still room for further improvements. Additionally, the use of a finite volume method for the electric current conservation equation has allowed to deal easily with the cells around singular null-points of the magnetic field.

The numerical methods on the electron model have been tested successfully by implementing them into the E-module of the HYPHEN code and simulating the plasma discharge in a HPT. The numerical benefits of using the thermalized potential instead of the natural electric potential, when solving the parallel Ohm's law under large magnetization and low collisionality, have been assessed too. Variations of the thermalized potential are much lower than those of the electric potential, which allows to conclude (when a barotropy function exists) that the electric potential follows approximately a Boltzmann-type relation with the plasma density. However, those variations are crucial in determining the parallel electron current density. Indeed, this current component has a central role in the formation of meridional electric current loops but these are shown to have a marginal effect on the rest of the plasma response. Related to this, it is also shown that the response is rather insensitive to the plume axial extension included in the simulation. Finally, the reliability of the solution against the number of cells used in the simulation, specially important in the case of an irregular magnetic mesh, has been checked positively.

The finite volume and gradient reconstruction methods on a MFAM have been analyzed here on a simplified polytropic electron model. The first next step is to add the electron energy and heat flux equations and to apply the algorithms developed here to them, done in Chapter 3. The second next step is to match this electron transport model to the wave-plasma model and thus have a physically complete discharge in a HPT, done in Appendix A.

## 2.A Testing gradient reconstruction methods

The accuracy of the FDM and the WLSM for gradient reconstruction of  $\Phi$  is tested here using the simple trial function

$$\psi(x_{\parallel}, x_{\perp}) = \exp(-x_{\parallel}/\bar{\chi}^2) \exp(-x_{\perp}), \quad (2.34)$$

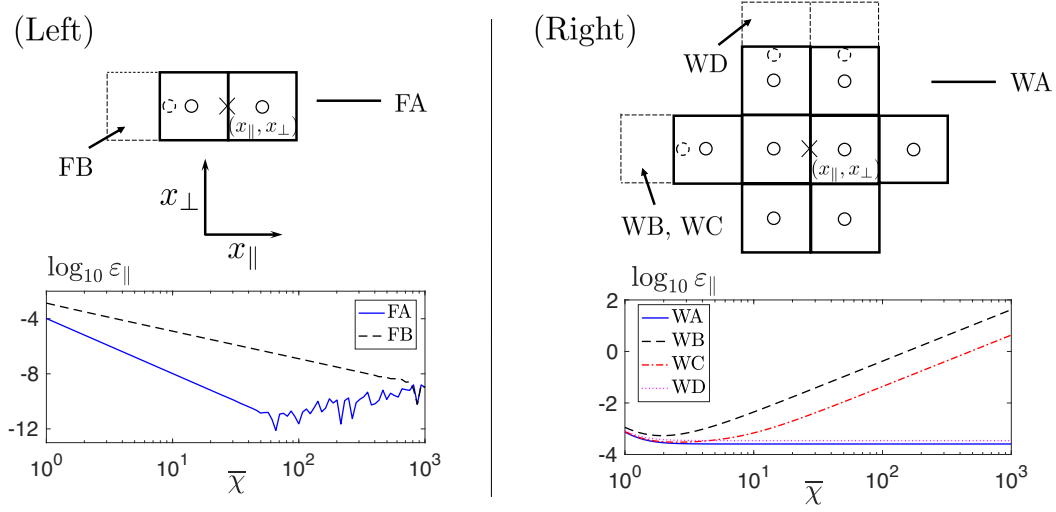


**Figure 2.12:** Scheme of the stencils used by each GRM when testing with an analytical function. Panel (left) corresponds to FDM and (right) to WLSM. GRM is done for a particular face of a hypothetical MFAM, which is represented by a cross and located at  $(x_{\parallel}, x_{\perp})$ . The surrounding cells, whose centers are marked by a circle, constitute the stencils. The main text defines the trial function and explains the different configurations of the stencils.

where  $x_{\parallel}$  and  $x_{\perp}$  replicate the coordinates parallel and perpendicular to the magnetic field, the constant  $\bar{\chi}$  replicates the Hall parameter and therefore controls the anisotropy level. The tests are performed at  $x_{\parallel} = x_{\perp} = 0$  on the vertical face shown in Fig. 2.12 and compare the numerical and analytical values of  $\partial\psi/\partial x_{\parallel}$  there. Left and right sketches in Fig. 2.12 show the stencils used for the FDM and the WLSM, respectively. The error on the numerical derivative (with subscript *num*) is

$$\varepsilon_{\parallel} = \left| \bar{\chi}^2 (\partial\psi/\partial x_{\parallel})_{num} + 1 \right|. \quad (2.35)$$

For the FDM two configurations of a 2-point stencil are used. In scheme FA, the cells are squares and identical with length  $\Delta x_{\parallel} = \Delta x_{\perp} = 0.5$ . In scheme FB, the left cell increases  $\Delta x_{\parallel}$  by a 10% compared to FA. The relative error  $\varepsilon_{\parallel}$  is shown in Fig. 2.12(left). Both in schemes FA and FB, the error decreases as  $\sim \bar{\chi}^{-2}$  with  $\bar{\chi}$  increasing. This means an excellent performance of the FDM, with the error being proportional to the second derivative of  $\psi$ . The higher error with the nonuniform FB is natural too. At very large  $\bar{\chi}$  the error on FA reaches the machine precision.

Four schemes are used for assessing the relative error when using the WLSM. In scheme WA, an 8-point stencil with identical cells is used. In schemes WB and WC, the left cell changes  $\Delta x_{\parallel}$  by a 10% and a 1%, respectively. In scheme WD, the two upper cells change  $\Delta x_{\perp}$  by a 10%. The relative error  $\varepsilon_{\parallel}$  is shown in Fig. 2.12(right). Scheme WA behaves very well for any  $\bar{\chi}$ , but not as well as scheme FA. Scheme WD behaves exactly as WA, meaning that nonuniformities in the perpendicular direction do not matter. However, schemes WB and WC warn that nonuniformities in the parallel direction can lead to large errors at large  $\bar{\chi}$ . This is the numerical diffusion effect. Since the MFAM of our problem is highly nonuniform, it is concluded that the FDM must be used whenever it is possible.

## 2.B Performance indicators

The thrust produced by the plasma beam satisfies

$$F = \int_{W3} \sum_s (n_s m_s u_{zs} \mathbf{u}_s \cdot \mathbf{n} + n_s T_s \mathbf{1}_z \cdot \mathbf{n}) dS \quad (2.36)$$

with  $\mathbf{n}$  the external normal to surface W3. This thrust, with dynamic and static components, includes the contribution of both the heavy species (obtained through the I-module) and the electrons. The heavy species contribution to thrust is obtained from the I-module and is computed directly with the particle formulation and not with the above fluid one. Notice that if the simulated plume length is too short, the plasma beam acceleration would be incomplete and the thrust would be slightly underestimated.

The overall thrust efficiency is defined as

$$\eta_F = \frac{F^2}{2\dot{m}P_a}, \quad (2.37)$$

where  $P_a$  is the power absorbed by the plasma. There are several partial contributions to  $\eta_F$ , that are defined next. A steady-state discharge is assumed implicitly.

Let  $\dot{m}_{i,W1}$ ,  $\dot{m}_{i,W2}$ , and  $\dot{m}_{i,W3}$  be the mass flows of ions (of different electric charges) toward the surfaces W1, W2 and W3 of Fig. 2.1, and  $\dot{m}_{i,total} = \dot{m}_{i,W1} + \dot{m}_{i,W2} + \dot{m}_{i,W3}$  the total ion flow produced by the thruster. The downstream ion flow  $\dot{m}_{i,W3}$  is considered the useful one for thrust. The quality of the plasma production in the chamber is characterized by the propellant utilization and the production efficiency, defined respectively as, [7]

$$\eta_u = \frac{\dot{m}_{i,W3}}{\dot{m}}, \quad \eta_{prod} = \frac{\dot{m}_{i,W3}}{\dot{m}_{i,total}}. \quad (2.38)$$

The production efficiency measures the percentage of the total plasma production useful for thrust; the rest of plasma production is just recombined at the walls.

In order to estimate a power budget and the power efficiency for this discharge, the energy balance of the whole plasma must be considered. Adding for all plasma species, the total energy equation can be expressed as

$$\nabla \cdot \sum_s \left[ \left( \frac{5}{2} n_s T_s + \frac{1}{2} n_s m_s u_s^2 \right) \mathbf{u}_s + \mathbf{q}_s \right] = -\nabla \phi \cdot \mathbf{j} + Q_a - Q_{ion} - Q_{exc}, \quad (2.39)$$

where:  $Q_a$  is the density of power deposited; and  $Q_{ion}$  and  $Q_{exc}$  the power spent in ionization and excitation (inelastic collisions) per unit volume. Integrating the equation over the whole domain, the power balance is

$$P_a = P_{ion} + P_{exc} + P_{W1} + P_{W2} + P_{W3}, \quad (2.40)$$

where  $P_a$ ,  $P_{ion}$  and  $P_{exc}$  are the volumetric integrals of  $Q_a$ ,  $Q_{ion}$  and  $Q_{exc}$ , respectively, and the three other integrals are energy flows through the different domain boundaries,

$$P_{W1} = \int_{W1} \sum_s \left[ \left( \frac{5}{2} T_s + \frac{1}{2} m_s u_s^2 \right) n_s \mathbf{u}_s + \mathbf{q}_s \right] \cdot \mathbf{n} dS, \quad (2.41)$$



and identical expressions for walls W2 and W3. Equation (2.40) does not include the total work of the electric field on the domain since it is zero. This comes out from

$$\int_V \nabla \phi \cdot j dV \equiv \int_{W1+W2+W3} \phi j \cdot n dS - \int_V \phi \nabla \cdot j dV, \quad (2.42)$$

where: the first term at the right-hand side is zero if  $j_n = 0$  at all surfaces, and the second term is zero since there are no sources of current inside the domain [Eq. (2.5)].

In the complete model of a HPT discharge,  $Q_a(z, r)$  will be determined from a wave-plasma sub-model, such as the one developed in [112]. Then, Eq. (2.39) would determine the 2D map of electron temperature. Here, since  $T_e(z, r)$  has been prescribed through a polytropic relation with  $n_e$ , Eq. (2.39) is not used and, indeed, the power  $P_a$  required to sustain that  $T_e(z, r)$  is derived from Eq. (2.40).

Based on the useful power  $P_{W3}$ , the energy (or power) efficiency is defined as

$$\eta_{ene} = P_{W3} / P_a. \quad (2.43)$$

The energy 'inefficiency' is evaluated through

$$\epsilon_{inel} = \frac{P_{ion} + P_{exc}}{P_a}, \quad \epsilon_{wall} = \frac{P_{W1} + P_{W2}}{P_a}, \quad (2.44)$$

which measure inelastic and wall losses, respectively.

Finally, there is the plume efficiency, measuring the effect of plume divergence. Here, this is defined as

$$\eta_{plu} = \frac{P_{zi, W3}}{P_{i, W3}}, \quad (2.45)$$

where  $P_{zi, W3}$  and  $P_{i, W3}$  are the flows of, respectively, axial and total energy of ions. Combining partial efficiencies, one has  $\eta_F \approx \eta_u \eta_{ene} \eta_{plu}$ .



## Chapter 3

# Hybrid simulation model: numerical treatment (ii) and parametric analysis for HPTs

### 3.1 Introduction

The goal of this chapter is to complete the electron fluid model with the energy and heat flux equations for the E-module within HYPHEN. Here, the complete model, repeating some contents in Chapter 2, is described for an easier discussion. In addition, the model is completed with turbulence, which is not considered in Chapter 2. The model is discussed featuring the analogy of the energy and heat flux equations to the continuity and momentum equations. In the drift-diffusive approach, the structure of both systems of equations are similar: a conservation equation for current or energy, and a equation for the fluxes of current or energy (generalized Ohm's law or Fourier's law). The numerical treatment of the energy and heat flux system of equations is discussed. The spatial derivatives of the system, by analogy, can be solved with an extension of the numerical algorithms found in Chapter 2. Furthermore, this system has a temporal character, and thus a scheme is needed for temporal derivatives as well. Finally, simulation results are obtained for HPT05M with HYPHEN solving the electron temperature distribution for a given known power deposition map. The current configuration of HPT05M used in the experimental settings, and the role of two design parameters, magnetic field topology and vessel length, are studied. The performances, both overall and partial efficiencies, are investigated. The balance of the thrust and the physical mechanisms of the thrust generation are looked into.

The rest of the chapter is organized as follows. Section 3.2 describes the configurations of HPT05M, and the interaction between the modules within HYPHEN focused on the E-module. Section 3.3 discusses the numerical treatment of the E-module's energy and heat flux equations. Section 3.4 shows the results obtained for HPT05M. Section 3.5 summarizes the conclusions of the chapter.

## 3.2 Model formulation

### 3.2.1 General aspects

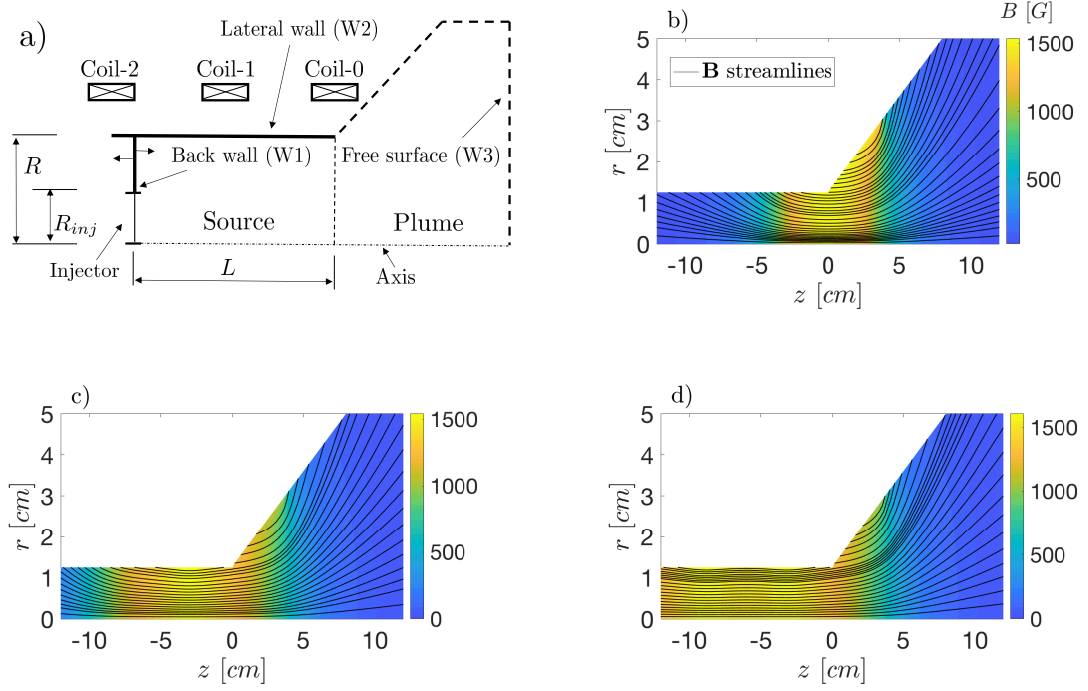


**Figure 3.1:** (a) Sketch of the thruster and (b)-(d) 3 possible applied magnetic fields generated by the set of coils.

Figure 3.1 (a) is a sketch of the HPT05M prototype. The thruster vessel is made of ceramic material and has radius  $R = 1.25\text{cm}$  and length  $L$ . The back wall of the vessel is movable to change the length, and 3 lengths of  $L_0 = 12\text{cm}$ ,  $L_1 = 6\text{cm}$ , and  $L_2 = 3\text{cm}$  are considered. An injector is placed in that wall occupying a circle of radius  $R_{inj} = 0.4\text{cm}$ , which delivers a mass flow  $\dot{m}$  with mean injection velocity  $u_{inj}$  and temperature  $T_{inj}$ . A set of 3 external coils are placed along the vessel to generate a stationary magnetic field  $\mathbf{B}$ . Figure 3.1 (b)-(d) show 3 fields: Field-0, Field-1 and Field-2, corresponding to switch on progressively Coil-0, Coil-1 and Coil-2. With only Coil-0 on, the field has a convergent-divergent geometry with a throat at the vessel exit, while switching on also Coil-1 and Coil-2 make the topology inside the vessel tend to axial. The thruster has been operating in a configuration C0 with  $L_0$ /Field-0 and has reported very poor performances [118]. In this chapter, four alternative configurations are tested exploring separately: (i) magnetic field topology, C1A ( $L_0$ /Field-1) and C1B ( $L_0$ /Field-2); and (ii) vessel length, C2A ( $L_1$ /Field-0) and C2B ( $L_2$ /Field-0).

The plasma transport modules of HYPHEN are shown in Fig. 3.2 (a). The I-module and E-module are run sequentially. Let us denote  $n_s$  and  $\mathbf{u}_s$  as, respectively, the density and velocity of species  $s$  (electrons  $e$ , ions  $i$  or neutrals  $n$ );  $\phi$  and  $T_e$  as, respectively, the electric potential and electron temperature. The I-module gives, as outputs,  $n_s$  and  $\mathbf{u}_s$  for heavy species. These outputs are taken by the E-module together with the power deposition map. The E-module, and the S-module for wall magnitudes, give

a complete solution of  $\phi$  and  $T_e$ , which are necessary for a new time advancement of the I-module. Fig. 3.2 (b) shows the given power deposition map  $Q_a$  (for a self-consistent deposition map see Appendix A). The deposition is uniformly distributed inside the vessel to obtain a fixed total deposited power  $P_a$ . (Notice that as  $P_a$  is fixed, if the vessel length is changed then  $Q_a$  needs also to be changed accordingly.)

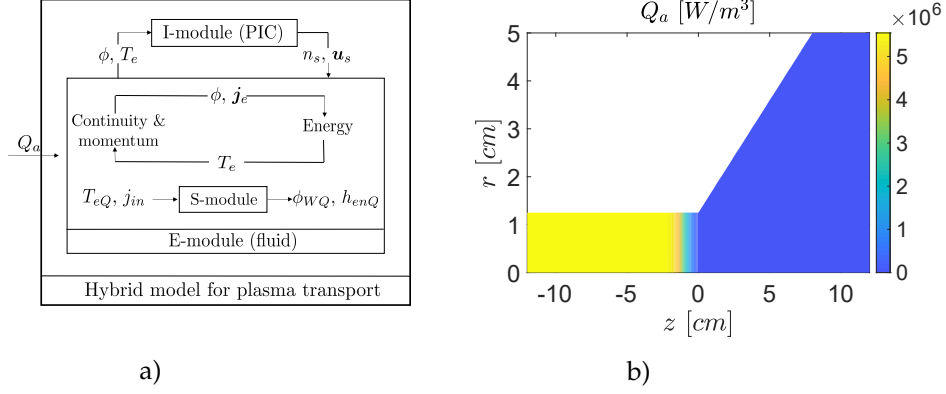


**Figure 3.2:** Structure of the code.

The I-module uses a Cartesian mesh defined on the natural cylindrical reference frame  $\{\mathbf{1}_z, \mathbf{1}_r, \mathbf{1}_\theta\}$ , with coordinates  $(z, r, \theta)$ , as seen in Fig. 3.3 (a). This mesh is selected non-uniform in both radial and axial directions based on the expected gradient of plasma properties. In the radial one, the mesh starts coarse from the symmetry axis and concentrates cells close to the vessel walls. In the axial one, the cell size increases from vessel to plume according to the expansion. The E-module uses a MFAM mesh due the anisotropic character of the magnetized electron fluid as seen in Fig. 3.3 (b), and the details of this mesh is explained in Chapter 2. As the meshes used by I-module and E-module are different, interpolation of the plasma properties between them are required and linear methods are used. For an accurate interpolation, it is tried to keep the MFAM cells with the same sizes as the I-module mesh ones when possible.

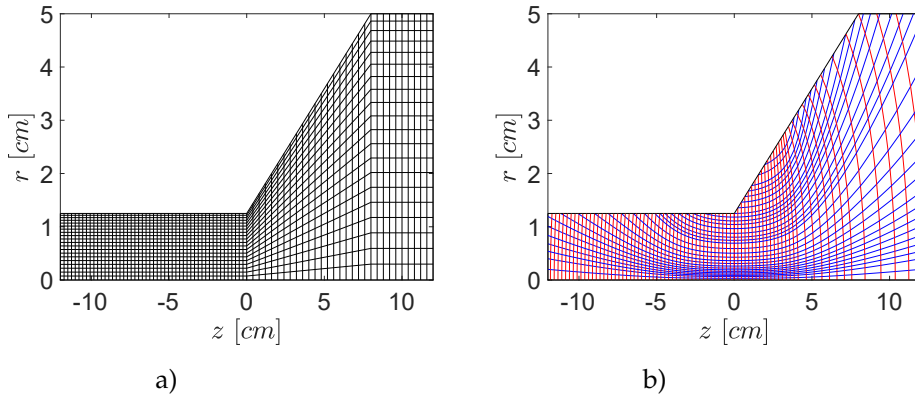


**Figure 3.3:** (a) Cartesian mesh of I-module and (b) MFAM mesh of E-module for a particular simulation case.

### 3.2.2 Electron module

The electron fluid is described with a magnetized, weakly-collisional and drift-diffusive (inertialess) model [79, 31]:

$$n_e = \sum_{s \neq e} Z_s n_s, \quad (3.1)$$

$$\nabla \cdot \mathbf{j} = \nabla \cdot (\mathbf{j}_e + \mathbf{j}_i) = 0, \quad (3.2)$$

$$0 = -\nabla(n_e T_e) + en_e \nabla \phi + \mathbf{j}_e \times \mathbf{B} + \mathbf{F}_{res} + \mathbf{F}_{turb}, \quad (3.3)$$

$$\frac{\partial}{\partial t} \left( \frac{3}{2} n_e T_e \right) + \nabla \cdot \mathbf{h}_e = -\nabla \phi \cdot \mathbf{j}_e + Q_e + Q_a, \quad (3.4)$$

$$0 = -\frac{5n_e T_e}{2e} \nabla T_e - \mathbf{q}_e \times \mathbf{B} - \frac{5T_e}{2e} (\mathbf{F}_{res} + \mathbf{F}_{turb}) - en_e \sigma_e^{-1} \mathbf{q}_e + \mathbf{Y}_{turb}. \quad (3.5)$$

Equation (3.1) is the quasi-neutrality condition and allows to obtain density of electrons through the densities of heavy species, where  $Z_s$  is the charge number of species  $s$ . Equation (3.2) is the conservation of current density  $\mathbf{j} = \mathbf{j}_e + \mathbf{j}_i$ , where  $\mathbf{j}_e = -en_e \mathbf{u}_e$  is the electron current density and  $\mathbf{j}_i = e \sum_{s \neq e} Z_s n_s \mathbf{u}_s$  is the ion current density, and the plasma beam is current-free since no current source exists. [The current density vectors can be divided in the azimuthal and meridional current densities, i.e.  $j_{\theta s} = \mathbf{j}_s \cdot \mathbf{1}_\theta$  and  $\tilde{\mathbf{j}}_s = \mathbf{j}_s - j_{\theta s} \mathbf{1}_\theta$ .] Equation (3.4) is the energy conservation. On the left-hand side, there is total variation of energy: temporal derivative and total energy flux, which is  $\mathbf{h}_e = \frac{5}{2} T_e n_e \mathbf{u}_e + \mathbf{q}_e$  with  $\mathbf{q}_e$  the heat flux. On the right-hand side, the energy changes with: work of electric field  $-\nabla \phi \cdot \mathbf{j}_e$ ; inelastic collisions  $Q_e = -Q_{ion} - Q_{exc}$ , where  $Q_{ion}$  and  $Q_{exc}$  are, respectively, power losses for ionization and excitation (see Chapter 4).

Equation (3.3) is for momentum and there is a balance among: pressure gradient  $-\nabla(n_e T_e)$ ; electric field  $en_e \nabla \phi$ ; magnetic force  $\mathbf{j}_e \times \mathbf{B}$ ; collisional resistive force  $\mathbf{F}_{res} = -\sum_{s \neq e} \nu_{es} m_e n_e (\mathbf{u}_e - \mathbf{u}_s) = en_e \sigma_e^{-1} (\mathbf{j}_e + \mathbf{j}_c)$ ,  $\nu_{es}$  the collision frequency with species  $s$ ,  $\sigma_e = e^2 n_e / m_e \nu_e$  the conductivity,  $\nu_e = \sum_{s \neq e} \nu_{es}$  the total collision frequency, and  $\mathbf{j}_c = en_e \sum_{s \neq e} (\nu_{es} / \nu_e) \mathbf{u}_s$  an equivalent current density representing collisional effects of heavy species; and an anomalous transport force due to turbulence  $\mathbf{F}_{turb}$ . Equation (3.5) is for heat flux and has dual terms compared with the momentum equation. Here, two collision terms are present,  $-\mathbf{F}_{res} 5T_e / 2e$  corresponds to the resistive force from the momentum equation, and  $en_e \sigma_e^{-1} \mathbf{q}_e$  is the direct effect of collisions on the heat flux; and contributions of turbulence are also included,  $-\mathbf{F}_{turb} 5T_e / 2e$  and  $\mathbf{Y}_{turb}$ . The turbulence terms are modeled with phenomenological models [33, 78] as  $\mathbf{F}_{turb} = \alpha_t j_{\theta e} B \mathbf{1}_\theta$  and  $\mathbf{Y}_{turb} = -\alpha_t q_{\theta e} B \mathbf{1}_\theta$ , which enhance, respectively, the electron current and heat flux across the magnetic field lines. The parameter  $\alpha_t$  has to be selected and, based on typical values in the literature, is taken as  $\alpha_t = 0.01$ .

Equations (3.3) and (3.5) relate, as shown below, respectively,  $\mathbf{j}_e$  with  $\phi$  and  $\mathbf{q}_e$  with  $T_e$ . Introducing them into the conservation equations,  $\mathbf{j}_e$  in Eq. (3.2) and  $\mathbf{q}_e$  in Eq. (3.4) gives, respectively, an elliptic type equation for  $\phi$  and a parabolic type equation for  $T_e$ .

#### Generalized Ohm's and Fourier's laws

The Eqs. (3.3) and (3.5) can be rearranged, respectively, as generalized Ohm's and Fourier's laws,

$$\mathbf{j}_e = \sigma_e \tilde{\mathcal{K}} \cdot \left[ -\nabla \phi + \frac{\nabla p_e}{en_e} \right] + \mathbf{j}'_e, \quad \mathbf{j}'_e = -\tilde{\mathcal{K}} \cdot \mathbf{j}_c, \quad (3.6)$$

and

$$\mathbf{q}_e = -\frac{5}{2} \frac{T_e}{e^2} \sigma_e \tilde{\mathcal{K}} \cdot \nabla T_e - \frac{5}{2} \frac{T_e}{e} \tilde{\mathcal{K}} \cdot \left( \mathbf{j}_e + \mathbf{j}_c + \frac{\sigma_e}{en_e} \mathbf{F}_{turb} \right). \quad (3.7)$$

In these expressions, the normalized conductivity tensor is defined, on the magnetic reference frame, as

$$\tilde{\mathcal{K}} = \begin{bmatrix} \frac{1}{1+\chi\chi'} & 0 & \frac{\chi'}{1+\chi\chi'} \\ 0 & 1 & 0 \\ -\frac{\chi'}{1+\chi\chi'} & 0 & \frac{\chi'}{\chi} \frac{1}{1+\chi\chi'} \end{bmatrix}, \quad (3.8)$$

where the Hall parameters are

$$\chi = \frac{\omega_{ce}}{\nu_e}, \quad \chi' = \frac{\omega_{ce}}{\nu_e + \alpha_t \omega_{ce}}, \quad (3.9)$$

with  $\omega_{ce} = eB/m_e$  the electron gyrofrequency.

The separate components of the Ohm's law are

$$j_{\parallel e} = \sigma_e \left[ \frac{1}{en_e} \frac{\partial (n_e T_e)}{\partial \mathbf{1}_{\parallel}} - \frac{\partial \phi}{\partial \mathbf{1}_{\parallel}} \right] + j'_{\parallel e}, \quad (3.10)$$

$$j_{\perp e} = \frac{\sigma_e}{1+\chi\chi'} \left[ \frac{1}{en_e} \frac{\partial (n_e T_e)}{\partial \mathbf{1}_{\perp}} - \frac{\partial \phi}{\partial \mathbf{1}_{\perp}} \right] + j'_{\perp e}, \quad (3.11)$$

$$j_{\theta e} = -\chi' j_{\perp e} + \chi' j'_{\perp e} + j'_{\theta e}. \quad (3.12)$$

In a similar way, the components of the Fourier's law are

$$q_{\parallel e} = -\sigma_e \frac{5}{2} \frac{T_e}{e^2} \frac{\partial T_e}{\partial \mathbf{1}_{\parallel}} - \frac{5}{2} \frac{T_e}{e} (j_{\parallel e} + j_{\parallel c}), \quad (3.13)$$

$$q_{\perp e} = -\frac{\sigma_e}{1+\chi\chi'} \frac{5}{2} \frac{T_e}{e^2} \frac{\partial T_e}{\partial \mathbf{1}_{\perp}} - \frac{5}{2} \frac{T_e}{e} \frac{j_{\perp e} + j_{\perp c} + \chi (j_{\theta e} + j_{\theta c} \chi' / \chi)}{1+\chi\chi'}, \quad (3.14)$$

$$q_{\theta e} = -q_{\perp e} \chi' - \frac{5}{2} \frac{T_e}{e} \left( j_{\theta e} + j_{\theta c} \frac{\chi'}{\chi} \right). \quad (3.15)$$

The dynamics in the perpendicular components are determined by the magnetic field, whose information is contained within the Hall parameters  $\chi$  and  $\chi'$ , and limits the transport across the magnetic field lines. The first is the natural one and the second accounts for turbulence, which adds an additional collisionality  $\alpha_t \omega_{ce}$  and enhances the limited transport.

The dynamics in the parallel components is characterized by the weakly-collisional condition and thus high conductivity ( $\sigma_e \propto \nu_e^{-1}$ ). In Eqs. (3.10) and (3.13), it happens that

$$\frac{\partial \phi}{\partial \mathbf{1}_{\parallel}} \approx \frac{1}{en_e} \frac{\partial (n_e T_e)}{\partial \mathbf{1}_{\parallel}} \gg \frac{j_{\parallel e}}{\sigma_e}, \quad \frac{\partial T_e / \partial \mathbf{1}_{\parallel}}{T_e} \approx 0. \quad (3.16)$$

Thus, along magnetic field lines there is mainly a balance between pressure gradient and electric field, and temperature remains isothermal. A Boltzmann relation can be established as

$$\Phi = \phi - \frac{T_e}{e} \ln \frac{n_e}{n_{e0}}, \quad \frac{\partial \Phi / \partial \mathbf{1}_{\parallel}}{\Phi} \approx 0, \quad (3.17)$$

where  $\Phi$  is the thermalized potential with a reference density  $n_{e0}$ . The condition in Eq. (3.10) makes the computation of  $j_{\parallel e}$  ill-conditioned numerically, since it is not a dominant term but needs to be solved. As solution, Chapter 2 proposed to solve with  $\Phi$  as unknown instead of  $\phi$ . Introducing  $\Phi$ , Eq. (3.10) becomes

$$j_{\parallel e} = \sigma_e \left[ \frac{1}{e} \left( 1 - \ln \frac{n_e}{n_{e0}} \right) \frac{\partial T_e}{\partial \mathbf{1}_{\parallel}} - \frac{\partial \Phi}{\partial \mathbf{1}_{\parallel}} \right] + j'_{\parallel e}, \quad (3.18)$$

and now  $j_{\parallel e}/\sigma_e \sim \partial \Phi / \partial \mathbf{1}_{\parallel} \sim e^{-1} \partial T_e / \partial \mathbf{1}_{\parallel}$ .

### Boundary conditions and plasma-wall interaction (S-module)

The boundary conditions, when solving Eqs. (3.2) and (3.4), are set on the currents and total energy fluxes normal to the surfaces:  $j_n = \mathbf{j} \cdot \mathbf{n}$  and  $h_{en} = \mathbf{h}_e \cdot \mathbf{n}$  with  $\mathbf{n}$  the outward unit normal. On the axis, symmetry implies that  $j_n = 0$  and  $h_{en} = 0$ . On the ceramic walls, the dielectric condition  $j_n = 0$  is applied and  $h_{en}$  comes from the sheath model. On the free surface, the current-free condition states that  $\int_{W3} j_n dS = 0$ . The condition can be fulfilled simply as  $j_n = 0$  without significant influences on the simulation results if the free surface is far enough as seen in Chapter 2. Regarding the total energy flux, kinetic studies [4] suggest that  $h_{en} = cn_e T_e u_{en}$  with  $c$  a constant taken as  $c = 9/2$ .

The S-module relates plasma magnitudes at the quasi-neutral edge  $Q$  and the ceramic walls of the vessel  $W$ . The model implemented is from Ref. [3], which: is collisionless and unmagnetized, i.e. Debye length is much smaller than the mean free path and Larmor radius, and accounts for two populations of electrons: (i) primary electrons from the plasma bulk and (ii) secondary electrons emitted from the ceramic material. In addition, for primary electrons, the elastically reflected and repletion of high energy tail particles are considered as well. The outputs of the model are the potential drop and the total energy flux through the sheath,

$$\frac{e\phi_{WQ}}{T_{eQ}} = \ln \left[ \frac{en_e \sqrt{\frac{8T_e}{\pi m_e}}}{4j_{in}} \right]_Q \sigma_t (1 - \delta_{wr}) (1 - \delta_{ws}), \quad (3.19)$$

and

$$h_{enQ} = 2T_{eQ} \frac{j_{in}/e}{1 - \delta_{ws}} - 2T_s \delta_{ws} \frac{j_{in}/e}{1 - \delta_{ws}} + \phi_{WQ} j_{in}, \quad (3.20)$$

respectively. In these expressions,  $\delta_{ws}$  is the fraction of secondary electrons emitted from the wall with a temperature  $T_s$ , which is taken as  $T_s = 2eV$ ; and  $\delta_{wr}$  is the same but for elastically reflected primary electrons. These yields depend on  $T_e$  and are modeled as

$$\delta_{wr} = \delta_{r0} \frac{E_r^2}{(T_{eQ} + E_r)^2}, \quad \delta_{ws} = \frac{2T_{eQ}}{E_s}, \quad (3.21)$$

where the parameters  $\delta_{r0}$ ,  $E_s$  and  $E_r$  depend on the type of ceramic material. Taking the common Boron Nitride, we have that  $\delta_{r0} = 0.4$ ,  $E_s = 50eV$  and  $E_r = 20eV$  [3, 103]. Finally,  $\sigma_t$  is the replenishment fraction of the primary electron high energy tail, which changes usually in the range  $\sigma_t \sim 0.1-0.3$  and is taken as  $\sigma_t = 0.1$ .

### 3.3 Numerical treatment for E-module

Inside the E-module, the elliptic equation from the current conservation and Ohm's law for  $\phi$  and  $j_e$ , and the parabolic equation from the energy conservation for  $T_e$  are solved sequentially. The numerical procedure used for the former was explained in Chapter 2, and the novelties are for the latter. In the parabolic equation, the I-module provides heavy species densities and velocities; the quasi-neutrality condition gives  $n_e$ ; and  $Q_a$  is a known input. The numerical treatment requires first a temporal discretization. The implicit temporal schemes are preferable for a robust convergence, however, these schemes are costly since the equation is non-linear in  $T_e$ . Thus, as trade-off a semi-implicit scheme is used to select the terms implicit (at  $t + \Delta t_e$ ) and explicit (at  $t$ ) conveniently and linearize the equation in  $T_e$ . Applying the scheme to advance a time step  $\Delta t_e$ , from time  $t$  to  $t + \Delta t_e$ , yields

$$\frac{3}{2} n_e \frac{T_e^{t+\Delta t_e} - T_e^t}{\Delta t_e} + \frac{3}{2} \frac{\partial n_e}{\partial t} T_e^{t+\Delta t_e} = -\nabla \cdot \mathbf{h}_e - \nabla \phi \cdot \mathbf{j}_e + Q_e + Q_a, \quad (3.22)$$

$$\mathbf{h}_e = \frac{5}{2} n_e \mathbf{u}_e T_e^{t+\Delta t_e} + \mathbf{q}_e, \quad \mathbf{q}_e = -\frac{5}{2} \frac{T_e^t}{e^2} \sigma_e \tilde{\mathcal{K}} \cdot \nabla T_e^{t+\Delta t_e} - \frac{5}{2} \frac{T_e^{t+\Delta t_e}}{e} \tilde{\mathcal{K}} \cdot \left( \mathbf{j}_e + \mathbf{j}_c + \frac{\sigma_e}{en_e} \mathbf{F}_{turb} \right). \quad (3.23)$$

On the left-hand side of Eq. (3.22), the temporal derivative of the energy is simply transformed to a numerical form. On the right-hand side of Eq. (3.22),  $T_e$  appears in the total energy flux of Eq. (3.23), the convective fluxes (including the ones of  $\mathbf{q}_e$ ) are  $\propto T_e$ , i.e. linear in  $T_e$ , and the diffusive fluxes are  $\propto T_e \nabla T_e$ , i.e. nonlinear in  $T_e$ . The scheme takes  $T_e$  implicit for the convective fluxes;  $T_e$  explicit and  $\nabla T_e$  implicit for the diffusive fluxes. The terms without superscript come either from other modules or have an internal non-linear dependence on  $T_e$  and are taken at  $t$ . Other terms without superscript are  $\phi$  and  $\mathbf{u}_e$  (or  $\mathbf{j}_e$ ), which are taken from the solution of the elliptic equation at  $t$  so as to allow the method of sequential time marching.

Once applied the temporal scheme, a spatial discretization is needed. Given the analogy with the current conservation and Ohm's law, the numerical procedure is similar as in Chapter 2. The equations are solved on a MFAM such as the one of Fig. 3.3 (b). A finite volume method (FVM) is used to solve the conservation, Eq. (3.22), and a gradient reconstruction method (GRM) is used for the flux, Eq. (3.23).

Applying the FVM to Eq. (3.22) for a generic cell yields

$$\frac{3}{2} n_e \frac{T_{el}^{t+\Delta t_e} - T_{el}^t}{\Delta t_e} \Omega_l + \frac{3}{2} \frac{\partial n_e}{\partial t} T_{el}^{t+\Delta t_e} \Omega_l + \sum_m h_{nm} S_m = (-\nabla \phi \cdot \mathbf{j}_e + Q_e + Q_a)|_l \Omega_l, \quad h_{nm} = \mathbf{h}_{em} \cdot \mathbf{n}_m, \quad (3.24)$$

where subscript  $l$  refers to a cell, with volume  $\Omega_l$ , and  $m$  to its faces, with area  $S_m$  and outward unit normal  $\mathbf{n}_m$ . The volumetric terms are computed at cell centers, and the total energy flux at the face centers. Apart from boundary faces,  $h_{nm}$  is either  $h_{\parallel e}$  or  $h_{\perp e}$ , and for boundary faces  $h_{nm}$  is known from boundary conditions. A GRM is used to discretize  $T_e^{t+\Delta t_e}$  in  $h_{nm}$ . In inner faces (those out of the boundary), named as  $m^*$ , the function value or the derivatives of  $T_e$  in  $h_{em^*}$ , say  $x_{m^*}$ , are obtained as

$$x_{m^*} = \sum_l g_{m^*l} T_{el}^{t+\Delta t_e}, \quad (3.25)$$

where  $g_{m^*l}$  are geometric coefficients dependent on the mesh and the specific GRM used.

The Eq. (3.24) applied to all the cells yields the matrix system

$$A_1\{T_{el}^{t+\Delta t_e}\} + A_2\{h_{nm^*}\} = B_1, \quad (3.26)$$

where  $A_1$  contains the coefficients of the temporal terms,  $A_2$  the areas of the cell faces, and  $B_1$  the source terms and the total energy fluxes to the boundary.

Then, applying Eq. (3.25) to fluxes in inner faces, we obtain

$$\{h_{nm^*}\} = A_3\{T_{el}^{t+\Delta t_e}\}, \quad (3.27)$$

where  $A_3$  collects information on plasma and geometric properties (including the GRM coefficients). Eliminating  $\{h_{nm}\}$  from the two systems, we obtain

$$A\{T_{el}^{t+\Delta t_e}\} = B \quad (3.28)$$

with  $A = A_1 + A_2A_3$  and  $B = B_1$ , which allows to solve  $T_e$  in the cells.

In order to have the complete solution in the whole domain, we need to compute  $T_e$  in the boundary. The heat flux at the boundary faces,  $h_{nm}$ , is known from the boundary conditions, and the solution of  $T_e$  has to be such that Eq. (3.23) gives the same value as the boundary conditions. In order to force the constraint, we need a modification of the GRM,

$$x_m = \sum_l g_{ml}T_{el}^{t+\Delta t_e} + g_{mm}T_{em}^{t+\Delta t_e}, \quad (3.29)$$

which introduces  $T_e$  at the boundary face  $m$  so that it becomes an unknown. Using this form of the GRM in the constraint, we get an equation for each  $m$ ,

$$\sum_l a_{ml}T_{el}^{t+\Delta t_e} + a_{mm}T_{em}^{t+\Delta t_e} = h_{em}, \quad T_{em}^{t+\Delta t_e} = \frac{h_{em} - \sum_l a_{ml}T_{el}^{t+\Delta t_e}}{a_{mm}}. \quad (3.30)$$

Here,  $a_{ml}$  and  $a_{mm}$  are analogous terms to the matrices shown above.

The specific GRMs used were discussed in Chapter 2. The methods for the Ohm's law were based on the anisotropic character of the thermalized potential gradient, which has small variations along  $\mathbf{1}_{\parallel}$  and large variations along  $\mathbf{1}_{\perp}$ . The weighted least square methods were found versatile, however they compute derivatives along different directions at the same time and are prone to producing numerical diffusion, and were used only for the highly irregular cells near the boundary. Inside the domain, finite difference methods, which separate the computation of the derivatives, were used. Since the behaviour of the thermalized potential in the Ohm's law is the same for the electron temperature in the Fourier's law, here the same GRMs are used for the total energy fluxes.

### 3.4 Results

Simulations are run for the configurations C0, C1A/B, and C2A/B of HPT05M described in Sec. 3.2. The operation conditions are the same for all the configurations. The injector delivers a mass flow



$\dot{m} = 1\text{mg/s}$  of xenon with a temperature of  $T_{inj} = 0.02\text{eV}$  and a mean velocity of  $u_{inj} = 300\text{m/s}$ . The total power deposited is  $P_a = 300\text{W}$ .

### 3.4.1 2D plasma profiles

Figure 3.4 shows the 2D maps of main plasma transport magnitudes for the configuration C0. The same profiles for configurations C1A/B, with different magnetic field topologies, and for C2A/B, with shorter vessel lengths, are displayed, respectively, in Figs. 3.5-3.6 and Figs. 3.7-3.8. The results in all these figures are extracted once steady states are reached in the simulations.

In the configuration C0, the electron temperature [Fig. 3.4 (a)], inside the vessel, is homogeneous, and we see that the heating is rather poor with a mean volumetric value of  $\langle T_e \rangle = 3.45\text{eV}$ . Besides, the electrons are near isothermal along the magnetic field lines (see Fig. 3.1). This is expected from the closure for the electron heat flux: the low collisionality makes the parallel conductivity huge, and the gradient of temperature tends to zero to keep a finite heat flow in Eq. (3.13). The experiments confirms this result inside the source [105]. However, also from experiments, a cooling is expected outside in the plume [60], where a Fourier-type closure may be unsuitable once the plasma gets very rarefied along the expansion.

The electrons, once heated, collide with neutrals to produce ionization. We see that, along the discharge, the neutrals [Fig. 3.4 (b)] deplete, and the plasma [Fig. 3.4 (c)] is produced. The maximum of the plasma density is around the section  $z = -2.5\text{cm}$ , where most of the ionization is produced. High plasma densities up to  $n_e \sim 10^{19}\text{m}^{-3}$  are obtained, but, full ionization is not found in the plume, where  $n_e \sim n_n$ .

The thermal energy of the plasma, stored mainly within electrons, is transformed into kinetic energy of ions to generate thrust through potential falls along the discharge. The potential [Fig. 3.4 (d)] peaks near the vessel exit, and decays in all directions driving the ions [Fig. 3.4 (e)-(f)],  $|\Delta\phi| \sim 2\langle T_e \rangle / e$  to the vessel and  $|\Delta\phi| \sim 6\langle T_e \rangle / e$  to the plume. The streamlines of ions stem from the section  $z = -2.5\text{cm}$ , where the plasma density is maximum, and travel to two regions: the backward-flow region  $z < -2.5\text{cm}$ , where ions hit the walls and are recombined; and the forward-flow region  $z > -2.5\text{cm}$ , where ions are accelerated for thrust generation. Since the backward-flow region occupies most of the vessel, the amount of wall recombination, mostly in the lateral wall, is significant.

In configurations C1A/B, the magnetic field lines inside the vessel become axial when progressively switching on the Coil-1 and Coil-2 (see Fig. 3.1). The backward-flow region gets smaller, with the location of maximum ionization shifted to  $z = -9\text{cm}$  (C1A) and  $z = -12\text{cm}$  (C1B) [Fig. 3.5-3.6 (c) and (f)], once the lateral wall is better shielded magnetically. The electron temperature isolines [Fig. 3.5-3.6 (a)] change accordingly with the magnetic field topology, and the heating is improved to  $\langle T_e \rangle = 5.13\text{eV}$  (C1A) and  $\langle T_e \rangle = 14.49\text{eV}$  (C1B). The plasma, with similar maximum densities inside the vessel, is now close to full ionization in the plume, where  $n_e \gg n_n$  [Fig. 3.5-3.6 (b) and (c)]; and the potential falls and therefore the ion acceleration are larger [Fig. 3.5-3.6 (d) and (e)].

In configurations C2A/B, the rear side of the vessel is cut, which removes the backward-flow region and reduces the wall recombination. Once the wall recombination is reduced, again as for C1A/B, the electron heating is improved to  $\langle T_e \rangle = 8.71\text{eV}$  (C2A) and  $\langle T_e \rangle = 25.35\text{eV}$  (C2B), which are higher

than for C1A/B though. Given, the analogous behaviour for  $T_e$ , the influence on the other plasma profiles is also similar.

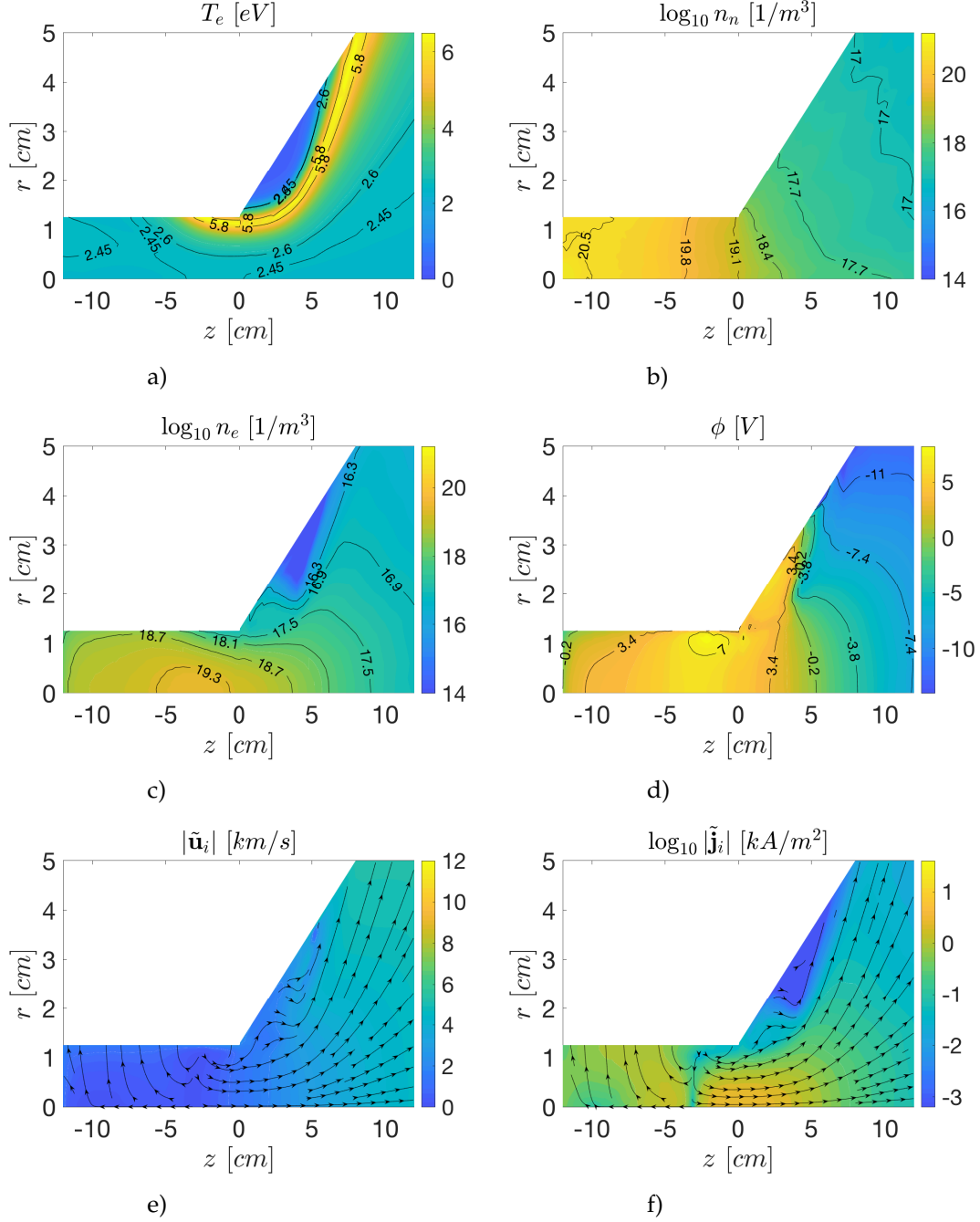


**Figure 3.4:** 2D maps of plasma magnitudes for C0.

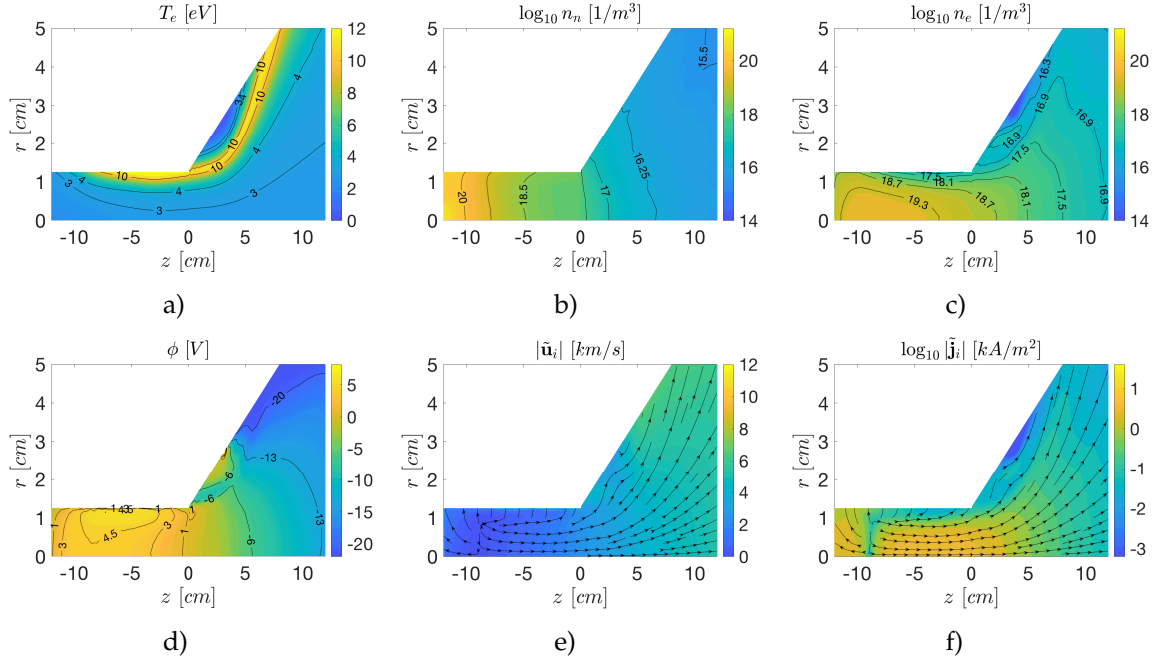


Figure 3.5: 2D maps of plasma magnitudes for C1A.

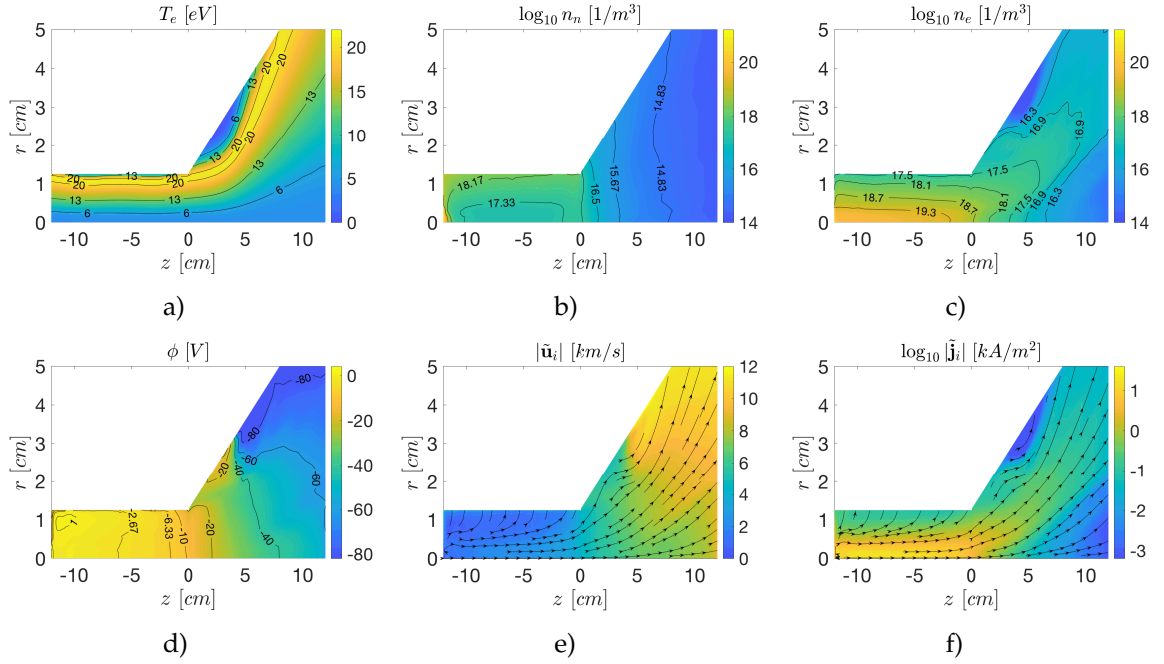


Figure 3.6: 2D maps of plasma magnitudes for C1B.

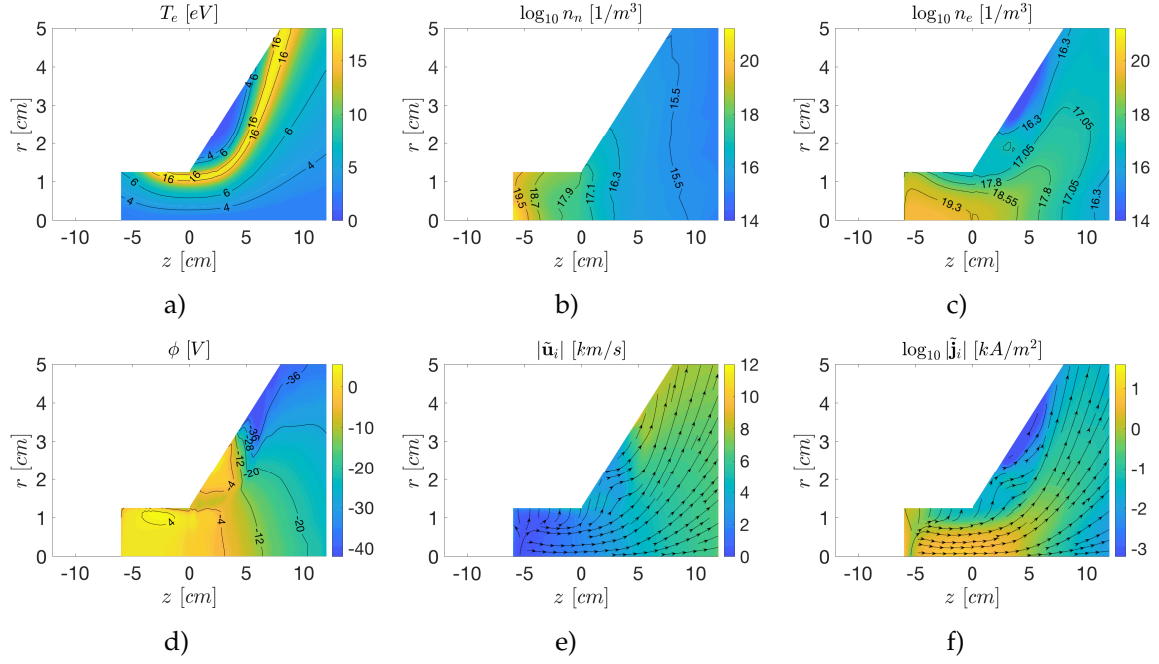


Figure 3.7: 2D maps of plasma magnitudes for C2A.

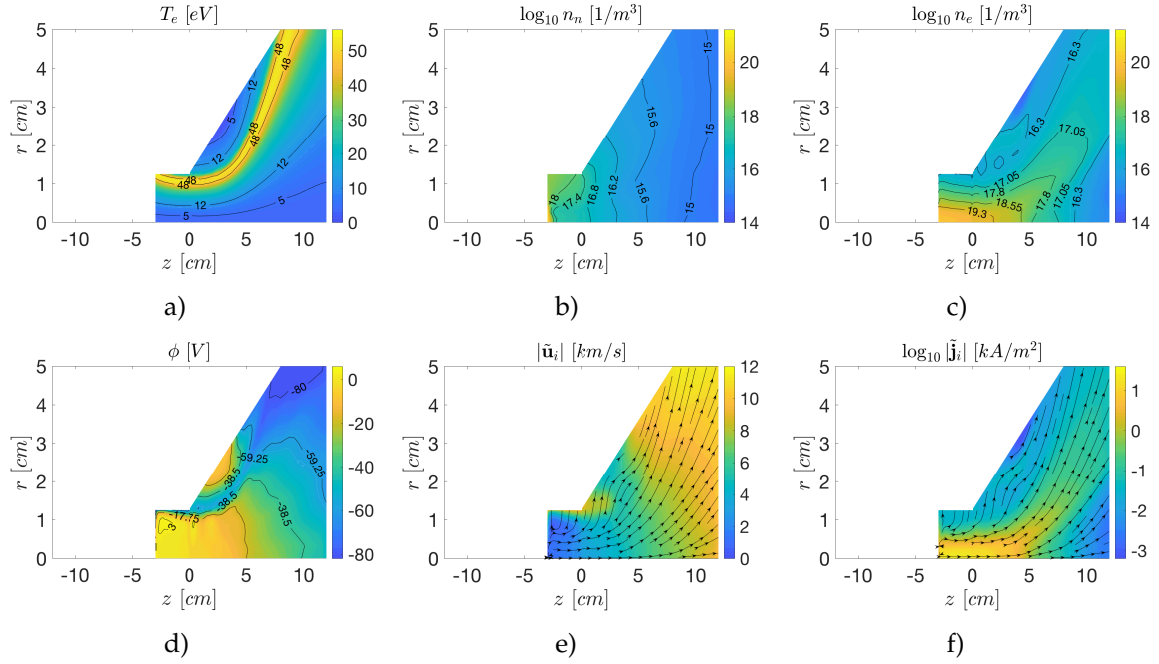


Figure 3.8: 2D maps of plasma magnitudes for C2B.

### 3.4.2 Performances

Table 3.1 shows the performance indicators for C0, C1A/B and C2A/B. The indicators are defined in Chapter 2, and the difference is the introduction of the dispersion efficiency

$$\eta_{disp} = \frac{F^2}{2\dot{m}_{i,W3}P_{W3}}. \quad (3.31)$$

This efficiency accounts for the velocity dispersion of plasma in the free loss surface W3, which comes from two contributions: divergence of the plume and degree of thermal-to-kinetic energy conversion. (Notice that  $\eta_F = \eta_u \eta_{ene} \eta_{disp}$ .) In the configuration C0, we see a poor thrust efficiency of only  $\eta_F = 1.3\%$ . This is mainly due to the very low energy efficiency of  $\eta_{ene} = 5.3\%$ , meaning that the power losses are significant in: inelastic collisions losses,  $\eta_{inel} = 67\%$ , dominated by excitation due to the low electron temperature ( $\langle T_e \rangle = 3.45eV$ ), and wall losses,  $\eta_{wall} = 27.7\%$ . The propellant utilization is of  $\eta_u = 66\%$ , and the plasma in the plume is not fully ionized. The total plasma production,  $\dot{m}_i / \dot{m} = \eta_u / \eta_{prod} = 8.25$ , is much larger than the propellant mass flow, and for steady conditions, most of the ionized propellant must be recombined to the walls,  $\dot{m}_{wall} / \dot{m} = \eta_u / \eta_{prod} - \eta_u = 7.59$ . These results on the mass balance suggest that the propellant is ionized and recombined over and over along the vessel, which is a consequence of the bad magnetic shielding of the walls. The velocity dispersion of the plasma in the plume is noticeable, with a efficiency of  $\eta_{disp} = 37.1\%$ .

	$\langle T_e \rangle [eV]$	$F [mN]$	$\eta_u$	$\eta_{ene}$	$\eta_{disp}$	$\eta_F$	$\eta_{prod}$	$\epsilon_{wall}$ (W1/W2)	$\epsilon_{inel}$ (ion/exc)
<b>C0</b>	3.45	2.85	0.66	0.053	0.371	0.013	0.08	0.010+0.267	0.241+0.429
<b>C1A</b>	5.13	4.01	0.92	0.116	0.253	0.027	0.13	0.040+0.326	0.205+0.313
<b>C1B</b>	14.49	7.49	0.98	0.341	0.278	0.093	0.24	0.252+0.196	0.116+0.095
<b>C2A</b>	8.71	5.37	0.97	0.181	0.273	0.048	0.16	0.118+0.314	0.178+0.209
<b>C2B</b>	25.35	8.02	0.97	0.449	0.239	0.104	0.36	0.249+0.158	0.073+0.071

**Table 3.1:** Performance indicators of different HPT05M configurations.

In the configurations C1A/B, the thrust efficiency increases about a factor of 2 for C1A,  $\eta_F = 2.7\%$ , and a factor of 7 for C1B,  $\eta_F = 9.3\%$ . Given the better magnetic shielding, the plasma recombination to the walls is reduced to  $\dot{m}_{wall} / \dot{m} = 6.16-3.10$ , and unnecessary plasma production is also reduced, which is closer to the 100%,  $\dot{m}_i / \dot{m} = 7.08-4.08$ . The power losses are proportional to  $\dot{m}_{wall} T_e$ , and since the total deposited power is fixed, the lower  $\dot{m}_{wall}$ , the higher  $T_e$ . Indeed, we have that electron temperature is higher than for C0, with  $\langle T_e \rangle = 5.13-14.49eV$ . The energy efficiency is improved to  $\eta_{ene} = 11.6-34.1\%$  due to the lower inelastic losses. The ionization losses, proportional to  $\dot{m}_i$ , and also the excitation losses, important at low  $T_e$ , are reduced accordingly giving  $\epsilon_{inel} = 51.8-21.1\%$ . The losses to the walls worsen to  $\epsilon_{wall} = 36.6-44.8\%$  however, plasma recombination is smaller but the plasma reaching the walls is more energetic. The propellant utilisation improves to  $\eta_u = 92-98\%$ , and the dispersion efficiency remains similar. In the configurations C2A/B, the plasma recombination concentrated at the rear side of the vessel is removed, and analogous tendencies are observed as for C1A/B. The thrust efficiency increases to  $\eta_F = 4.8-10.4\%$  and some more noticeable improvements are obtained.

From C0 to C1B and C2B, we have improved significantly the thrust efficiency. However, the performances of C1B and C2B are still within the current state-of-art of HPT prototypes [96, 106], and

coincide with the highest ones reported from reliable measurements. We see that there is still room for improvement of the energy efficiency, with significant power losses to the walls. Once the lateral wall (W2) is better shielded, from  $\epsilon_{W2} = 26.7\%$  (C0) to  $\epsilon_{W2} = 19.6\%$  (C1B) and  $\epsilon_{W2} = 15.8\%$  (C2B), the losses are directed to the back wall (W1), from  $\epsilon_{W1} = 1.0\%$  (C0) to  $\epsilon_{W1} = 25.2\%$  (C1B) and  $\epsilon_{W1} = 24.9\%$  (C2B), where the magnetic field lines cut almost perpendicularly. Furthermore, the magnetic nozzle operation is poor, something also observed in recent experiments [23], and needs to be improved.

### 3.4.3 On the thrust generation

The momentum equation, after adding all species, is

$$\nabla \cdot \sum_s (m_s n_s \mathbf{u}_s \mathbf{u}_s + n_s T_s \mathcal{I}) = \mathbf{j} \times \mathbf{B}, \quad (3.32)$$

where  $\mathcal{I}$  is the unit tensor. The electric field does not appear due to quasi-neutrality, nor the collisions since they are internal to the plasma. Physically the thrust is the force exerted by the plasma on the thruster, and integrating the momentum equation along the axial direction for the whole domain, we obtain the thrust balance

$$F = F_p + F_m, \quad (3.33)$$

with two contributions to thrust

$$F_p = - \int_{W1+W2} \sum_s (n_s m_s u_{zs} \mathbf{u}_s \cdot \mathbf{n} + n_s T_s \mathbf{1}_z \cdot \mathbf{n}) dS \quad (3.34)$$

and

$$F_m = - \int_V j_\theta B \sin \gamma dV, \quad \gamma = \arctan(B_z / B_r). \quad (3.35)$$

In the case of  $F_p$ , it represents the pressure thrust of the plasma (both static and dynamic) on the vessel walls, and can be separated as  $F_p = F_{p,W1} + F_{p,W2}$ , with  $F_{p,W1}$  for back wall and  $F_{p,W2}$  for lateral wall. (Notice that  $F_{p,W2}$  is actually a tangential force to the lateral wall.) Regarding  $F_m$ , the azimuthal current  $j_\theta$ , which is mainly due to the electrons, with a diamagnetic character reacts on the coils with a force  $j_\theta B \mathbf{1}_\perp$ , and the proper deflection of the magnetic field lines,  $\gamma$  ( $\gamma < 0$  convergent,  $\gamma > 0$  divergent), produces a magnetic thrust. This force has a volumetric character, and can be divided into  $F_m = F_{m,vess} + F_{m,plu}$ , where  $F_{m,vess}$  accounts for the vessel and  $F_{m,plu}$  for the plume.

An alternative form of the thrust balance is

$$F = F_{vess}(1 + \kappa_F), \quad \kappa_F = F_{m,plume} / F_{vess}, \quad (3.36)$$

where  $F_{vess} = F_p + F_{m,vess}$  is the thrust generated inside the source, and  $\kappa_F$  is the increment of the vessel thrust achieved along the magnetic nozzle.

	$F_p$	$F_m$	$F_{vess}$	$\kappa_F$	$F_{m,vess}$	$F_{m,plu}$	$F_{p,W1}$	$F_{p,W2}$
<b>C0</b>	4.84	-1.99	2.08	37%	-2.76	0.77	2.60	2.24
<b>C1B</b>	6.82	0.67	6.35	18%	-0.47	1.14	8.18	-1.36
<b>C2B</b>	6.82	1.20	5.57	44%	-1.25	2.45	7.01	-0.19

**Table 3.2:** Total thrust breakdown: pressure force/magnetic force, and vessel force/plume increment. Contributions to the magnetic term from source and plume, and to the pressure term from back wall and lateral wall. The forces are in  $mN$ .

Table 3.2 shows the thrust balance for the configurations C0, C1B and C2B. First, in the form of  $F_p$  and  $F_m$ , we see that  $F_p$  is the main mechanism of thrust, and gets larger from C0 to C1B and C2B, where higher densities and temperatures are achieved. We also see that  $F_m$  is even a drag force instead of a propelling force for C0, and small for C1B and C2B. In the form of  $F_{vess}$  and  $\kappa_F$ ,  $F_{vess}$  differs from  $F_p$  being smaller, and is increased along the plume with  $\kappa_F = 18\text{--}44\%$ , which coincides with the range obtained in experiments [107]. Thus, the magnetic nozzle can provide an important increment to thrust.

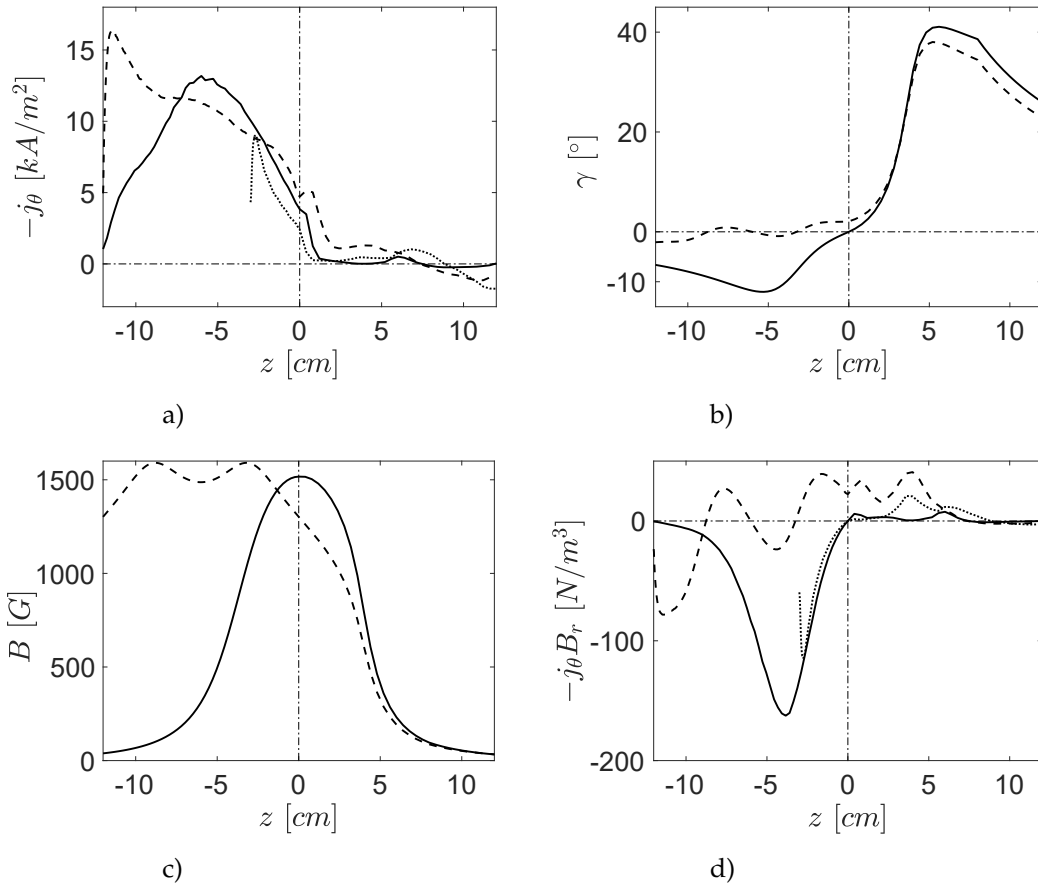


**Figure 3.9:** 1D  $z$ -profiles at a mean  $r$ , about 75% of domain radius at each  $z = \text{constant}$  section, of (a) azimuthal current density, (b) magnetic field angle, (c) magnetic field strength and (d) magnetic thrust per unit volume for C0 (—), C1B (---) and C2B (.....).

The splitting of the magnetic force indicates that in the plume,  $F_{m,plu}$  is a propelling force as expected, but inside the vessel,  $F_{m,vess}$  is a drag force. This is an interesting result, since the theoretical and experimental studies for this mechanism of thrust have been focused on the magnetic nozzle, and do not discuss about the source [6, 34, 7, 106]. Figure 3.9 shows the magnetic force per unit volume and its separate terms for the configurations C0, C1B and C2B. The 1D profiles at a mean  $r$ , about the 75% of the maximum radius for each  $z = \text{constant}$  section are shown. The azimuthal current density [panel (a)] is dominant inside the vessel and decays outside in the plume. In the vessel, the geometry is convergent ( $\gamma < 0$ ) at least in some regions [panel (b)]. Although  $\gamma$  is small, due to the large magnetic field strength [panel (c)] and azimuthal current, a drag force, which could be significant, is generated [panel (d)]. We see that the drag force is the largest for C0, and then is reduced for C1B and for C2B, where the convergent geometry is either reduced or removed. In the plume, with a divergent magnetic field geometry ( $\gamma > 0$ ), a propelling force is generated.

Regarding the pressure force, the splitting indicates that for C0, both  $F_{p,W1}$  and  $F_{p,W2}$  are comparable, and for C1B and C2B,  $F_{p,W1}$  dominates over  $F_{p,W2}$ , which becomes a drag force. Figure 3.10 shows the pressure force per unit area on the vessel walls for the three configurations. In the back wall [panel (a)], the pressure force is concentrated on the injection surface,  $r = 0-0.4\text{cm}$ . In the lateral wall [panel (b)], the pressure force, which is much smaller, starts positive and turns to negative at some point along the vessel. Remembering that the pressure force is the opposite of the plasma momentum flux to the walls, the behaviour of the profiles, when changing the configurations, is explained with the shifts of the location of maximum ionization. Since it shifts to the rear side when going from C0 to C1B and C2B, the flux to that wall increases, and more plasma hits the lateral wall when travelling to the plume generating a drag force.

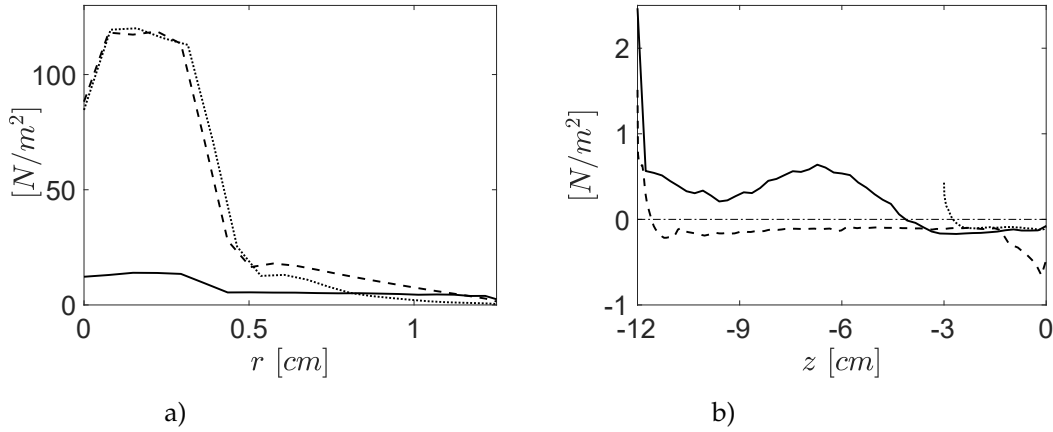


**Figure 3.10:** (a) Pressure force per unit area of the plasma on (a) back wall and (b) lateral wall of the vessel for C0 (—), C1B (---) and C2B (.....).

### 3.5 Conclusions

The magnetized and drift-diffusive electron fluid model within HYPHEN is completed with the energy conservation equation and a Fourier's law as closure for the heat flux, so that the spatial profile of electron temperature can be obtained for a given arbitrary known power deposition map. A parabolic differential equation is found for  $T_e$  combining the energy conservation and the Fourier's law. The



numerical procedure for the equation requires a temporal discretization, and a semi-implicit scheme is proposed as a trade-off between convergence and simplicity. The scheme takes implicit the linear terms and explicit the non-linear terms of the equation. Among the explicit terms, we have also the electric potential and electron velocity, which are solved from the current conservation and Ohm's law system sequentially in time within the electron fluid module. The spatial discretization of the equation is by analogy similar to the one for the current conservation and Ohm's law system, which was introduced in Chapter 2. The discretization is done on a MFAM, a FVM is applied to discretize the energy conservation on the cells of the mesh while GRMs are used to discretize the Fourier's law on the cells' faces. The GRMs found in Chapter 2 for the derivatives of the thermalized potential in the Ohm's law to avoid numerical diffusion must be extended to the derivatives of the electron temperature in the Fourier's law, since the gradient of both have the same anisotropic character (small and large variations, respectively, parallel and perpendicular to the magnetic field).

HYPHEN is used to study the prototype HPT05M, for which experimental results reported very poor performances. Alternative configurations have been searched looking into two key design parameters, magnetic topology and vessel length. 2D maps of the main plasma transport magnitudes, and performance indicators (plasma production, power balance and magnetic nozzle operation) are obtained. Furthermore, the thrust mechanisms, pressure and magnetic contributions, are studied.

In the current configuration of HPT05M, with a coil at the long vessel exit, the magnetic field is maximum there and decays fast. The magnetic shielding of the walls is bad and a region of backward-flow plasma occupying most of the vessel is formed, which results in a huge wall recombination concentrated mainly in the lateral wall. Two options have been found to mitigate this problem: the first option is to have a better magnetic shielding of the walls by placing more coils along the vessel; and the second option is to shorten the vessel. The region of backward-flow and therefore the wall recombination are significantly reduced or removed with these actions. The thrust efficiency, for the current configuration, is very poor, 1.3%, as already suggested by the experiments, and the improved configurations optimize the thrust efficiency to 9.3%-10.4%. The optimization, although significant, is partial, since the performances achieved are still within the current state-of-art. The main reasons limiting higher performances, are the power losses to the back wall, which conventional quasi-axial magnetic topology cannot handle, and the operation of the magnetic nozzle, which has a significant velocity dispersion of the plasma.

The thrust assessment suggests that the pressure contribution is the main mechanism of thrust. Regarding the magnetic contribution, the magnetic force generated by the magnetic nozzle, gives an increment of the thrust that can be significant. However, it is found that the magnetic force generated by the source, if a convergent geometry exists inside the vessel, counteracts the one by the magnetic nozzle canceling the overall magnetic contribution.

In view of the results, further optimization is required for HPT05M to become competitive. The next step will be to find a non-conventional magnetic topology that can shield both back and lateral walls, something that can be achieved with ring-cusps topologies [52, 15]. The operation of the magnetic nozzle needs to be improved as well. Although the typical values of efficiencies obtained are observed in experiments, the modeling of the plume expansion needs to be revised. The electron cooling, which is observed also in experiments, is not reproduced in our model. This is due to the diffusive (Fourier-type) closure for the electron heat flux, commonly used in the literature, is not suitable once

the plasma becomes very rarefied, and the electron heat transport in the plume requires further investigation. Chapters 5 and 6 have deeper studies of the plasma expansion along magnetic nozzle with kinetic simulations.

## Chapter 4

# Hybrid simulation model: modeling of chemistry and alternative propellants for HPTs

### 4.1 Introduction

The modeling of thruster operations with complex chemistry, which is necessary for many of the candidates for alternative propellants, is not very advanced. The existing thruster models are rather simple ones that are not able to handle mixtures of several substances or molecular collisions such as dissociation, vibrational and rotational excitation, etc. Recently, Sheppard and Little [94] progressed partially on this issue: they developed a one-dimensional model for electrodeless thrusters to characterize properly the complex chemistry and obtained results for operation with water. Being one-dimensional, details such as realistic magnetic topologies, different from a purely axial one, and wall losses are not considered. Furthermore, electric potential and electron temperature are not solved self-consistently, but are related through a phenomenological relation.

This chapter presents the modeling with HYPHEN, which can handle multiple species and is implemented with the collisions typical of diatomic molecules. Simulations are run for the HPT prototype HPT05M using air as propellant, and plasma profiles and operation performances are studied and compared with xenon.

The rest of the chapter is organized as follows: Section 4.2 explains the implementation of collisions, Section 4.3 discusses the simulation results, and Section 4.4 summarizes the conclusions.

### 4.2 Modeling of collisions

#### 4.2.1 Type of collisions

In low altitudes, where the air-breathing concept can be applied, the main components of air are  $N_2$  and  $O$  [16]. From sea level until 200km, the composition is dominated by  $N_2$ , and from 200km until 400km, by  $O$ . The modeling of atomic substances are common and well-known, and the discussion is focused on diatomic substances, which is the novel part implemented in HYPHEN.

Table 4.1 shows collisions for simulations with diatomic substances. The formula of each collision is given for a generic substance, where  $A_2$  stands for a diatomic molecule and  $A$  for an atom, and superscript  $+$  refers to positive ions and  $e$  to electrons. Only electron-heavy species collisions are considered, while the heavy-heavy species and photon-driven ones are negligible within the normal operation conditions in EP. The electrons, if energetic enough, can ionize and also dissociate the diatomic molecules through collisions, thus producing molecular ions  $A_2^+$  and atoms  $A$ . Instead, the electrons without enough energy excite  $A_2$ , and the excitation accounts for the transitions between electronic states, and also for those between vibrational and rotational states. Apart from the inelastic collisions, the electrons can collide elastically with  $A_2$  and through Coulomb interaction with  $A_2^+$ . The derived species  $A$  from dissociation suffers collisions as well being possible again the ionization to produce  $A^+$ , the excitation, and the elastic collisions.

Type of collision	Formula
Elastic	$A_2 + e \rightarrow A_2 + e$
Coulomb	$A_2^+ + e \rightarrow A_2^+ + e$
Excitation	$A_2 + e \rightarrow A_2^* + e$
Ionization	$A_2 + e \rightarrow A_2^+ + 2e$
Dissociation	$A_2 + e \rightarrow 2A + e$
Elastic	$A + e \rightarrow A + e$
Coulomb	$A^+ + e \rightarrow A^+ + e$
Excitation	$A + e \rightarrow A^* + e$
Ionization	$A + e \rightarrow A^+ + 2e$

**Table 4.1:** Type of collisions considered when simulating for diatomic molecules.

The collision  $i$  is characterized with a reaction rate  $R_i$ , which is, for negligible heavy species velocity and an electron Maxwellian distribution of temperature  $T_e$ ,

$$R_i = \sqrt{\frac{8}{\pi m_e T_e^3}} \int_{\varepsilon_{th,i}}^{\infty} \varepsilon_e \sigma_i(\varepsilon_e) \exp(-\varepsilon_e / T_e) d\varepsilon_e. \quad (4.1)$$

Here:  $\varepsilon_e$  is the electron impact energy,  $\varepsilon_{th,i}$  is the threshold energy of the reaction, and  $\sigma_i$  is the cross section. The threshold energy is the one needed each time a collision of the reaction happens. The elastic and Coulomb reactions have  $\varepsilon_{th,i} = 0$ , and the rest (ionization, excitation and dissociation) are inelastic reactions, with  $\varepsilon_{th,i} > 0$ , which involve energy losses. The cross section of the reaction,  $\sigma_i$ , is a function of  $\varepsilon_e$ , and data determined experimentally or theoretically is available in the literature. The rate measures the likelihood for a reaction to happen, and physically represents the volume swept by an electron in its trajectory. The rate multiplied by the density of the collision target, the heavy species, give the collision frequency, i.e. the number of collisions which an electron suffers per unit time. The collision frequency multiplied by the density of electrons is the number of collisions which the electrons suffer per unit time and unit volume within a location.

Data of cross sections for low-temperature plasmas have been collected for  $N_2$ ,  $N$  and  $O$ . There are data from journal articles specific for the topic [45, 44, 101, 102], where compilations are done; detailed quantum mechanics computations [117, 110], and the online database LXCAT [62, 84]. The information

is repeated over the different sources, and is postprocessed with a benchmark before being used in HYPHEN.

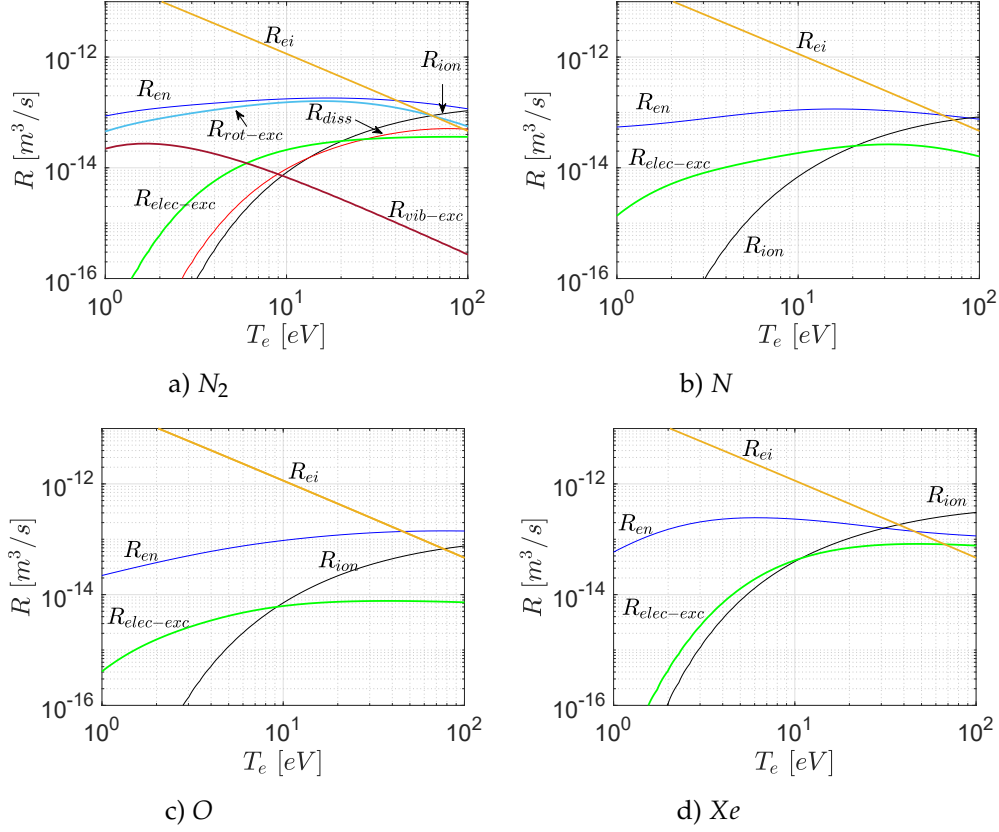


**Figure 4.1:** Reaction rates of air substances, Xe is shown for comparison.

	$N_2$	$N$	$O$	$Xe$
$\varepsilon_{th,ion}$	15.6	14.8	13.6	12.1
$\varepsilon_{th,elec-exc}$	$\sim 10$	$\sim 8$	$\sim 8$	$\sim 8$
$\varepsilon_{th,vib-exc}$	$\approx 0$	-	-	-
$\varepsilon_{th,rot-exc}$	$\approx 0$	-	-	-
$\varepsilon_{th,diss}$	9.8	-	-	-

**Table 4.2:** Threshold energy [eV] of reactions for air substances, Xe is shown for comparison.

Figure 4.1 and Table 4.2 shows, respectively, the rates versus  $T_e$  and the energy thresholds, for air substances and Xe. The notation used for the collisions are: elastic collision (*en*), Coulomb collision (*ei*), ionization (*ion*), electronic excitation (*elec – exc*), vibrational excitation (*vib – exc*), rotational excitation (*rot – exc*), and dissociation (*diss*). The rate for Coulomb collision does not come from the sources mentioned above, but from a general analytical formula known from plasma theory [13]. The excitation rates include the transitions from ground state to the relevant states that have been identified. Notice that each transition from ground state to a higher energy state has a different threshold, and the values

shown are averaged ones for the temperature range of interest ( $\sim 10\text{eV}$ ) in EP. One of the main objectives in an EP device is to try to fully ionize the propellant.  $\text{Xe}$  has a  $\varepsilon_{ion}$  slightly smaller, and  $R_{ion}$  2-3 times larger than  $\text{N}_2$  and  $\text{O}$ . In  $\text{N}_2$ , the ionization can happen as separate dissociation-ionization, but this indirect way is more costly in terms of energy. The excitations imply energy losses and have to be minimized: the electronic excitation thresholds are comparable to the ionization ones. In  $\text{N}_2$ , there are vibrational and rotational excitations additionally, which however have  $\varepsilon_i \approx 0$  and are basically elastic collisions. The dominance of  $R_{ion}$  over  $R_{exc}$ , happens if electron temperature is high enough: about  $10\text{eV}$  for  $\text{Xe}$  and  $\text{O}$ , and  $20\text{eV}$  for  $\text{N}_2$ .

## 4.2.2 Implementation in HYPHEN

The plasma properties change along the discharge while their species collide between them. The collisions modify the plasma via species production, momentum transfer and power losses. In the hybrid formulation and quasi-neutral plasma approach of HYPHEN, the I-module is in charge of the generation of species. The momentum transfer and power losses are assigned to the E-module for electrons due to the large mass disparity with respect to heavy species.

### I-module

The collisions that generate species are ionization and dissociation. The former, as obvious, was already implemented in HYPHEN, and here the algorithms are generalized to handle also the latter.

The generation is done for each mesh cell and per each time step of the I-module. First, the total mass of the new species to be generated is obtained as

$$\Delta m = m_s n_s n_e R_{es}(T_e) V \Delta t, \quad (4.2)$$

where:  $V$  is the cell volume and  $\Delta t$  the time step;  $m_s$  and  $n_s$  are, respectively, the mass and density of the input species  $s$ , and  $n_e$  the electron density;  $R_{es}$  is the generation rate. Second, the amount of macroparticles to be generated is given by

$$N_p = \frac{\Delta m}{m_s W_{gen}}, \quad (4.3)$$

with  $W_{gen}$  the generation weight selected, i.e. the number of elementary particles within one macroparticle. In ionization,  $N_p$  is exactly the number of new macroparticles, but in dissociation, there are  $N_p$  pair of macroparticles.

The new generated macroparticles, apart from their weights, need to be assigned a position and a velocity. The position of the macroparticles is allocated randomly with an uniform probability inside the cell where they are generated. Regarding the velocity, the procedure is different for ionization and dissociation. For ionization and each of the  $N_p$  new macroparticles, we sample a velocity of the original species from a Maxwellian distribution defined with the local properties, namely  $v_s$ , and which is allocated directly. For dissociation, the same sampling is done for each  $N_p$  pair of new macroparticles, but now  $v_s$  has to be distributed over the pair. The distribution is done in a way so that the output

species conserved the energy of the input ones. The output velocities have modules

$$|v_1| = \sqrt{2(1-x)}|v_s|, \quad |v_2| = \sqrt{2x}|v_s|, \quad (4.4)$$

where  $x$  is a random number chosen uniformly between 0-1, and directions also uniformly distributed over the space.

## E-module

In the fluid model of E-module in Chapter 3, the collisions contribute to momentum (Eq. 3.3) and energy (Eq. 3.4), and more specifically to, respectively, the collision resistive force and power losses:

$$F_{res} = -n_e \sum_{s \neq e} v_{es} m_e (\mathbf{u}_e - \mathbf{u}_s), \quad (4.5)$$

and

$$Q_e = -n_e \sum_{s \neq e} v_{es} \varepsilon_{th,es}. \quad (4.6)$$

The collision frequency is defined as

$$v_{es} = n_s R_{es}, \quad (4.7)$$

and the sum in the two terms is extended over all types of collisions of  $e$  with species  $s$ .

## 4.3 Results

Simulations are run separately for  $N_2$  and  $O$ . The configuration C2B of HPT05M defined in Chapter 3 is used, i.e. vessel length  $L = 3cm$  and only Coil-0 turned on. The propellants are evaluated for the same operation parameters as in Chapter 3, i.e. a mass flow of propellant  $\dot{m} = 1mg/s$  and a known uniform power density map with total power deposited  $P_a = 300W$ .

### 4.3.1 2D plasma profiles

The 2D plasma profiles for  $N_2$  and  $O$  are displayed in Figs. 4.2 and 4.3. Panels (a) show the electron temperature, and profiles isothermal along the magnetic field lines and radially decaying are found. Panels (b)-(c) show the neutral and plasma densities: the propellant is partially depleted, and the ionization is poor ( $n_e \ll n_{N_2}, n_O$ ). In the case of  $N_2$ , there is also dissociation, which is important since we have  $n_{N_2} \sim n_N$  as seen in panel (g). The generation of electrons come from ionization of both  $N_2$  and  $N$ , panels (h) and (i) show the densities of  $n_{N_2}^+$  and  $n_N^+$ , and they are comparable. Panels (d) show the potential, with a peak inside the vessel around  $(z, r) = (1.5, 0.8)cm$ , and decays in all directions. Panels (e)-(f) show the meridional ion velocity and current density. We see that ions follow the potential fall: a part of the ions hit and are recombined in the vessel walls, and another part exit the vessel and are accelerated to supersonic conditions to generate thrust.

The analogous plots for  $Xe$  are shown in Fig. 4.4. The comparison reveals that the general physics for  $N_2$  and  $O$  are similar to that of  $Xe$ . The main difference is that the electron temperature is larger for  $Xe$  [panels (a)] and, with a higher level of ionization, the propellant is ionised nearly in totality [panels (b)-(c)]. The potential falls are accordingly higher [panels (d)], and the ion acceleration is milder [panels

(e)] since Xe is heavier. As discussed in Chapter 3, the electron heating is less effective if there are more wall losses, which can be proved indeed in the ion fluxes of panels (f), and therefore it is related to the magnetic confinement. The electron azimuthal current density,  $j_{\theta e}$ , produces a force  $-j_{\theta e} B \mathbf{1}_{\perp}$ , which, inside the vessel ( $\mathbf{1}_{\perp} \approx \mathbf{1}_r$ ), screens the plasma from the walls. There is worse confinement for  $N_2$  and O due to the larger level of collisionality: given the same amount of propellant mass flow, more particles for  $N_2$  and O are present since they are lighter [panels (b)-(c)], and thus more collisions take place. Fig. 4.5 compares  $j_{\theta e}$  and electron collision frequency  $\nu_e$  for the propellants, and corroborate the argument.

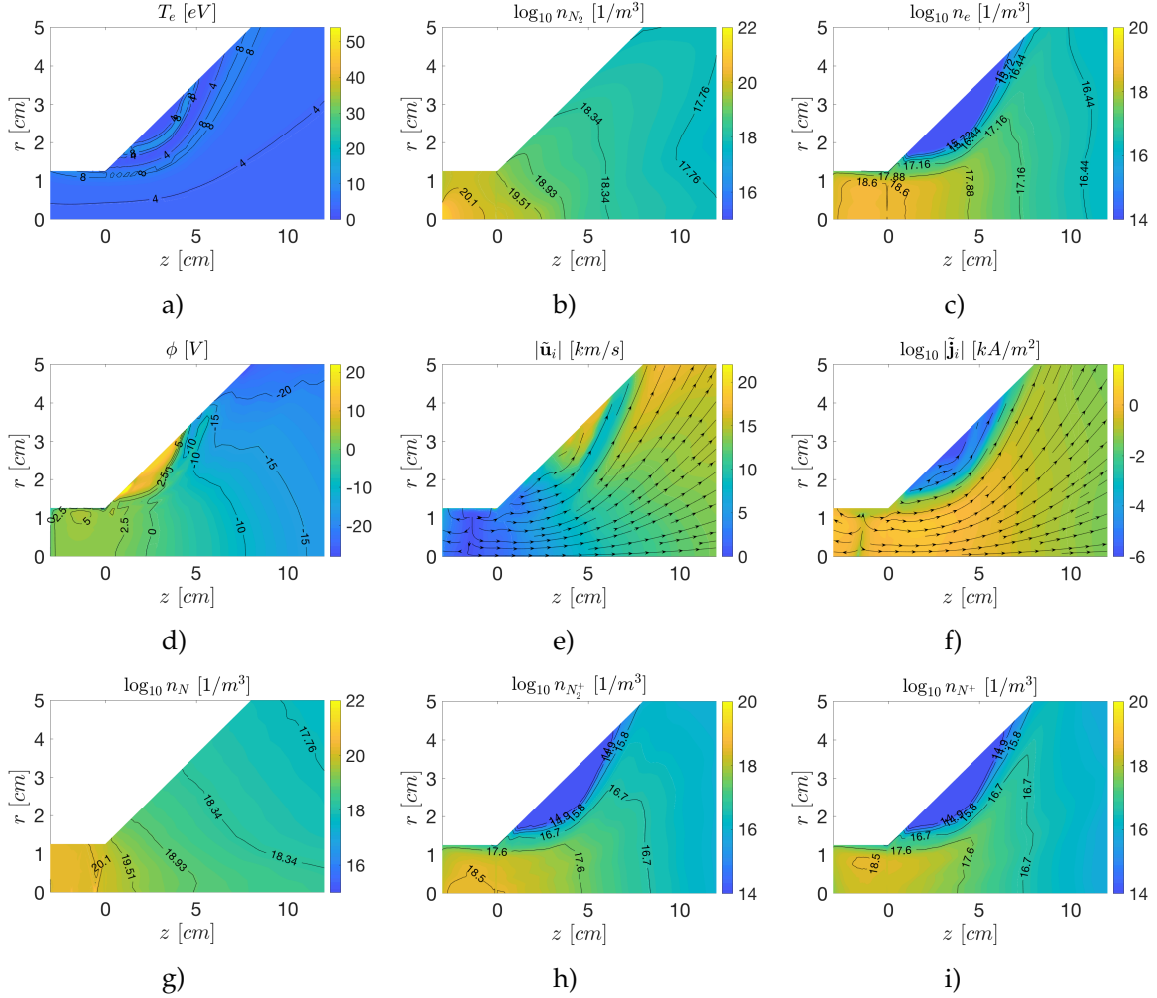


Figure 4.2: 2D maps of plasma magnitudes for  $N_2$ .



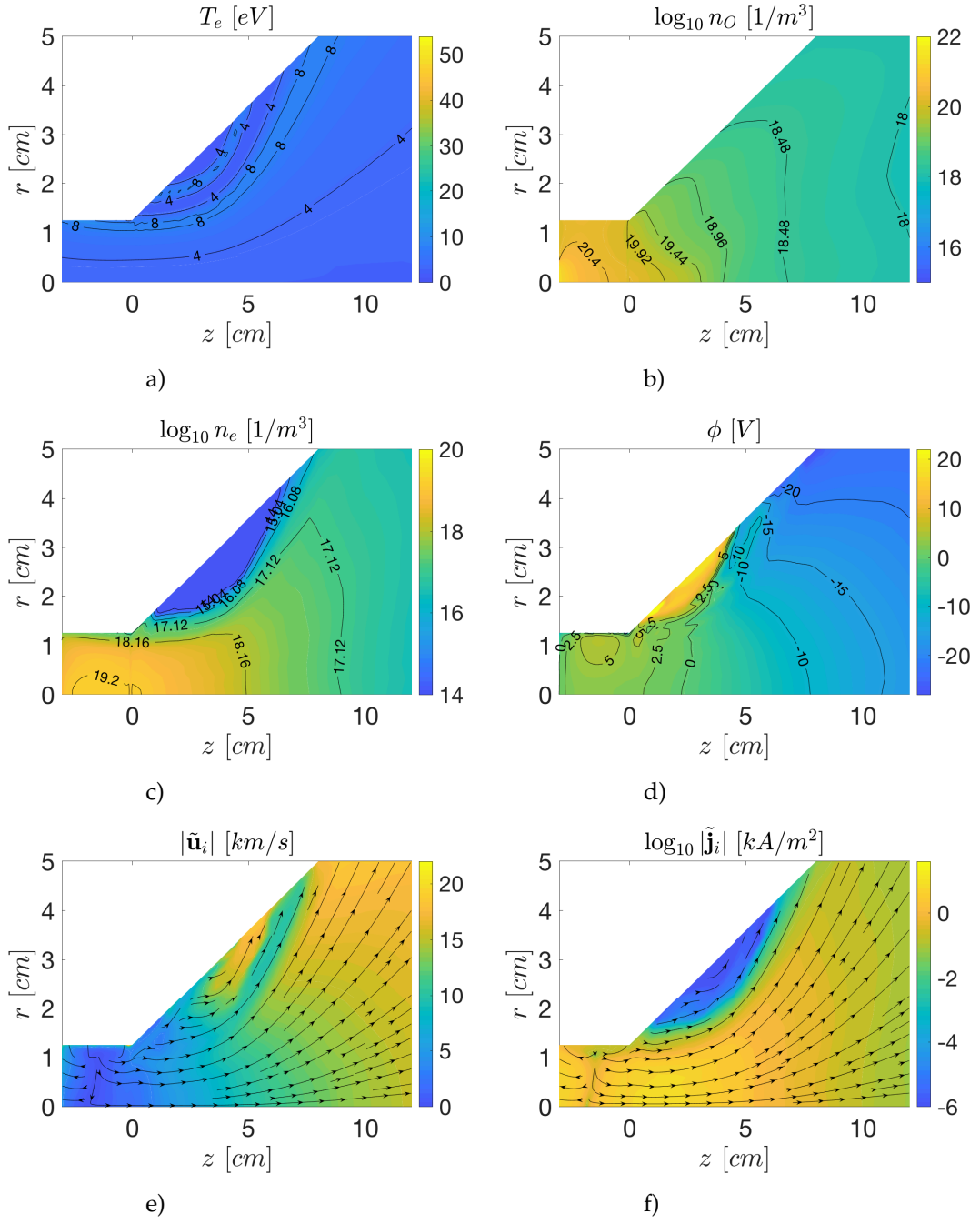


Figure 4.3: 2D maps of plasma magnitudes for O.

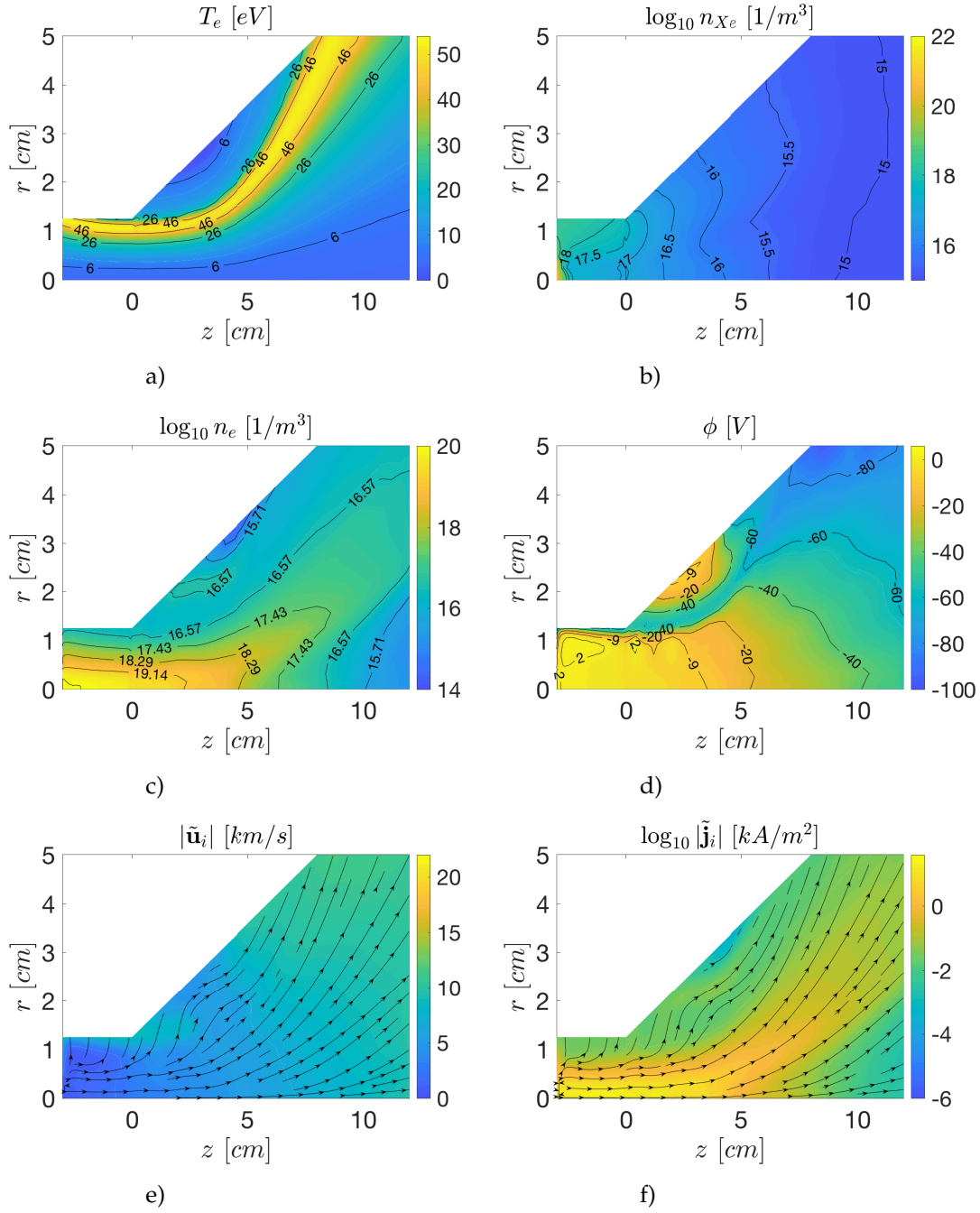
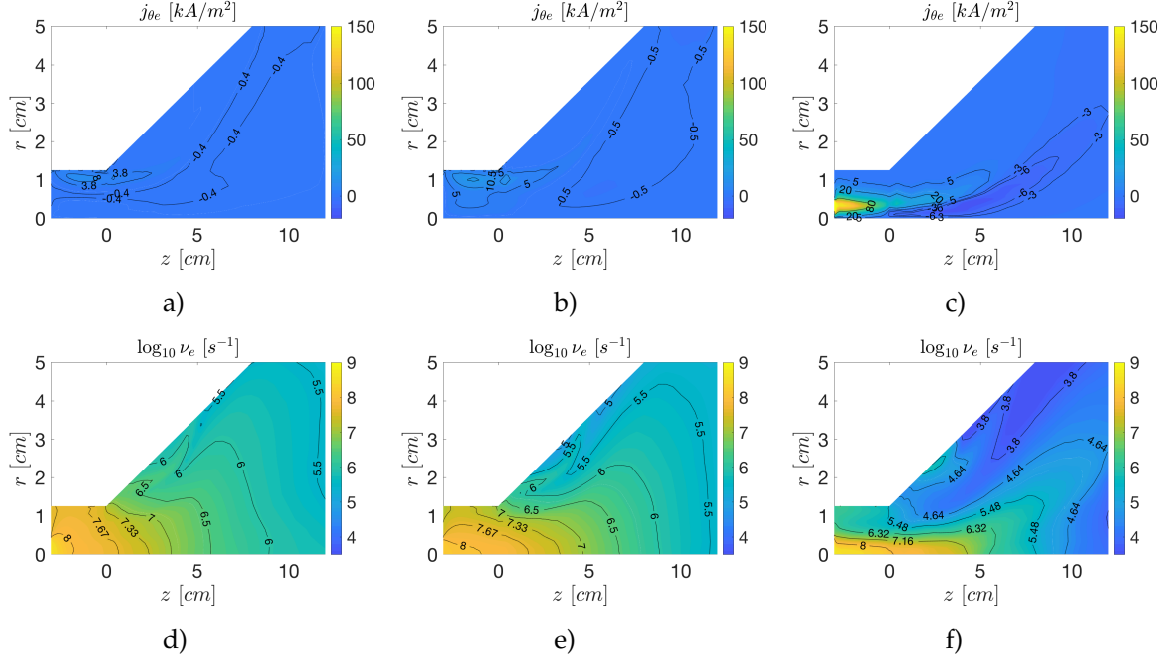


Figure 4.4: 2D maps of plasma magnitudes for Xe.



**Figure 4.5:** Electron azimuthal current density and total collision frequency for  $\text{N}_2$  (first column),  $\text{O}$  (second column), and  $\text{Xe}$  (third column).

### 4.3.2 Performances

Table 4.3 shows the performance indicators (which are defined in Chapter 3) of the HPT operated with  $\text{N}_2$  and  $\text{O}$ . The analogous results for  $\text{Xe}$  are shown for comparison. Apart from the deposited power  $P_a = 300\text{W}$ , we also show the results for  $P_a = 600\text{W}$ .  $\text{Xe}$  offers better overall efficiency,  $\eta_F$  (notice that  $\eta_F = \eta_m \eta_{ene} \eta_{disp}$ ), than  $\text{N}_2$  and  $\text{O}$  as expected. Operating with  $P_a = 300\text{W}$ ,  $\text{N}_2$  and  $\text{O}$  have a  $\eta_F$  of 1.3-4.5%, which are noticeably worse than the 10.4% of  $\text{Xe}$ . The poor performance is due to the poor electron heating: the volumetric mean temperature,  $\langle T_e \rangle$ , is 4.84-5.19eV for  $\text{N}_2$  and  $\text{O}$ , while  $\text{Xe}$  has 25.35eV. In consequence, there is a low propellant utilization,  $\text{N}_2$  and  $\text{O}$  have a plume partially ionized,  $\eta_m = 20\text{-}34\%$ . Furthermore, the portion of power carried by the plume (useful for thrust) is worse as well,  $\eta_{ene} = 16\text{-}35\%$ . The energy balance suggests that the larger power losses are due to inelastic collisions,  $\epsilon_{inel} = 44\text{-}69\%$ , which are dominated by the excitation.

Introducing more power,  $P_a = 600\text{W}$ ,  $\langle T_e \rangle$  grows accordingly. The increment is noticeable for  $\text{Xe}$ , and small for  $\text{N}_2$  and  $\text{O}$ . In  $\text{Xe}$ , the efficiencies remain similar and thrust is increased. In  $\text{N}_2$  and  $\text{O}$ , the propellant utilization is nearly double, and the portion of beam power is slightly improved. The overall efficiency follows  $\eta_m$  and is increased to  $\eta_F = 2.4\text{-}7.6\%$ . If further power is deposited and  $\langle T_e \rangle$  is high enough to have full ionization ( $\eta_m \approx 1$ ), we can expect, based on the tendency observed, to achieve  $\eta_F \sim 5\text{-}10\%$ . Then for high powers, air would have efficiencies comparable to those of  $\text{Xe}$ .

Since the simulations have been run separately for  $\text{N}_2$  and  $\text{O}$ , the performances of air as mixture, within the first 400km of the atmosphere, are expected to be a kind of average between them. Results suggest that  $\text{O}$  presents a better performance than  $\text{N}_2$ , thus thrust efficiency would increase with altitude.

	$\langle T_e \rangle$ [eV]	$F$ [mN]	$\eta_m$	$\eta_{ene}$	$\eta_{disp}$	$\eta_F$	$\eta_p$	$\epsilon_{wall}$	$\epsilon_{inel} (\epsilon_{ion} + \epsilon_{exc} + \epsilon_{diss})$
$N_2$ -300W	4.84	2.82	0.20	0.16	0.40	0.013	0.40	0.15	0.11+0.53+0.05
$O$ -300W	5.19	5.23	0.34	0.35	0.38	0.045	0.44	0.21	0.21+0.23
$Xe$ -300W	25.35	8.02	0.97	0.45	0.24	0.104	0.36	0.41	0.07+0.07
$N_2$ -600W	5.37	5.38	0.38	0.20	0.32	0.024	0.42	0.16	0.10+0.50+0.04
$O$ -600W	7.00	9.64	0.62	0.41	0.30	0.076	0.45	0.24	0.18+0.17
$Xe$ -600W	46.98	11.34	0.98	0.45	0.24	0.108	0.37	0.50	0.03+0.02

**Table 4.3:** Performance indicators of a particular HPT05M configuration operated with  $N_2$ ,  $O$  and  $Xe$ .

## 4.4 Conclusions

The search of alternative propellants for EP is a current topic due to the scarce supply for  $Xe$  and the foreseen growth of EP. Several candidates have been proposed with potential advantages. However, many of them have molecular structures, and there was no simulation tool that, at the same time, reproduces self-consistently the physics of the plasma discharge and models complex chemistry. The simulation code HYPHEN fills that gap and contributes to a progress. The code has been extended to include collisions typical of diatomic molecules, which already allows to assess a wide variety of propellants. The tool is used to evaluate air as alternative propellant, which is the basis for air-breathing concepts. The HPT05M prototype is used for the simulations.

Simulations are run considering low altitudes, where the air is still dense enough. Within the first 400km, the air is dominated by  $N_2$  (0-200km) and  $O$  (200-400km), and  $N_2$  and  $O$  are evaluated separately. The results of 2D maps and performances are shown and compared with  $Xe$ . Studies reveal that the main 2D profiles and physical mechanisms of the discharge are similar. The main difference is that the electron heating is less effective for  $N_2$  and  $O$  given the same amount of deposited power. This is due to a worse confinement for them: for the same mass flow of propellant and being less massive, their particle densities are larger and therefore they are more collisional. At low power ( $\sim 100W$ ), the low electron temperature, makes the plume poorly ionised and they have a thrust efficiency far from that of  $Xe$ . At high power ( $\sim 1000W$ ) however, for which the temperature is enough, they could be competitive with respect to  $Xe$ . Furthermore,  $O$  is found to have better efficiency than  $N_2$ , and then higher altitudes of flight are better in terms of propulsive performance.

## Chapter 5

# Kinetic study of magnetic nozzles: transient process

*This chapter adapts partially the published contents from a peer-reviewed journal article: "Kinetic features and non-stationary electron trapping in paraxial magnetic nozzles", Plasma Sources Science and Technology 27 (2018) 035002.*

### 5.1 Introduction

The modeling of magnetic nozzles has attracted great attention. One [19], two [10, 6, 69, 67] and three [61] dimensional fluid models have been developed, and the transformation of the internal energy of the plasma into directed kinetic energy, the plasma detachment, and the role played by the plasma-induced magnetic field have been discussed. However, since plasma flows are generally weakly collisional, simple closures of the fluid equation hierarchy for the pressure tensor and the heat fluxes are doubtful. A self-consistent determination of these magnitudes needs inevitably a kinetic description of the plasma.

Stationary solutions of the Vlasov equation in a magnetized plasma expansion have been obtained recently [64]. After assuming steady conditions, a slender nozzle geometry, and a fully magnetized plasma, the conservation of the total energy and the magnetic moment were used to write rigorously the densities of the particles connecting with the source as functions of the electrostatic potential and to compute the latter. It was then found that there exist regions in phase space not connected with either the source or the downstream region, where doubly-trapped bouncing particles can exist. Since in collisionless plasmas the filling of those regions happens during the transient, a stationary model cannot characterize rigorously the trapped particles. The plasma spatial solution and its numerical convergence turned out to be very sensitive to the distribution of trapped particles on the divergent side of the nozzle. After adding an heuristic population of trapped electrons, the authors found numerical solutions with the electron density dominated by the confined electrons over most of the divergent jet.

Discussions on whether or not trapped population of electrons are an essential component of the solutions and how they are determined also arise in other areas of plasma physics. For instance, for an electron-attracting Langmuir probe in flowing plasma, it was argued that a population of electrons should exist at the ram side of the probe [91]. The formation of such a trapped population during the transient phase, which is an adiabatic process, has been observed recently in non-stationary direct (eulerian) Vlasov simulations [88]. Adiabatic trapping in slowly varying time-dependent electric fields

[38] has been considered in analytical studies of magnetized plasma expansion [85]. Particles can also be trapped due to collisional effects. Particle collisions, which can also produce trapped particles, have been included in non-stationary particle-in-cell (PIC) simulations [65].

This chapter studies plasma expansions in magnetic nozzles by using a non-stationary direct Vlasov code. As compared to stationary fluid models, this technique computes the pressure tensor, the heat fluxes and the population of trapped electrons self-consistently. PIC codes do also exhibit these two features. However, due to the numerical noise, they do not give an accurate description if the number of macroparticles per cell is small, a circumstance that is unavoidable in non-stationary simulations of a plasma expansion into vacuum. Direct Vlasov codes, which are more demanding from a computational point of view because they discretize the distribution function in real and velocity spaces instead of using macroparticles, provide a better accuracy and degree of detail of the distribution functions.

The contents of this chapter comes from Ref. [89]. This chapter shows only the results related to the macroscopic response of the steady-state plasma. The kinetic features such as distribution functions, the dependency of the steady-state solution on the transient history, and the transient trapping mechanism of the electrons are not shown. (The latter was done mainly by Sánchez-Arriaga, with the support of the rest of the authors, and can be found in Ref. [89].) The rest of the chapter is organized as follows: Section 5.2 presents the mathematical model and describes briefly the numerical algorithm. The effects of fixing in the code the size of the nozzle (finite simulation domain) and the electrostatic potential value at the exit, two parameters that do not appear or are not externally imposed in a real infinite plasma expansion, are shown in Sec. 5.3. The correct selection of these two parameters allows to reproduce with the code the conditions of a real nozzle with zero net current. Section 5.3 also presents the particle densities, momentum balances, temperature, and heat fluxes. Section 5.4 summarizes the conclusions of the chapter.

## 5.2 Magnetic nozzle model based on guiding center theory

### 5.2.1 Plasma model

Let us consider a tank placed at  $z < z_0 < 0$  and filled with an electron-ion plasma. We are interested in the time-dependent, magnetically-channeled plasma expansion that is produced when a hole of radius  $R_0$  at  $z = z_0$  is opened at the plasma-vacuum wall. For the sake of illustration, the geometry of the magnetic nozzle is the one corresponding to a current loop of radius  $R_L$  ( $R_L > R_0$ ) placed at the plane  $z = 0$ . It generates a stationary and non-uniform magnetic field in the vacuum region that reaches its maximum value  $B_T$  at  $z = 0$  (the nozzle throat T). The forward distribution functions of ions and electrons entering the nozzle are assumed semi-Maxwellian,

$$f_\alpha(t, z = z_0, v_\parallel > 0, v_\perp) = N^* \left( \frac{m_\alpha}{2\pi k_B T_\alpha^*} \right)^{3/2} \exp \left( -\frac{m_\alpha v^2}{2k_B T_\alpha^*} \right), \quad \alpha = i, e, \quad (5.1)$$

while the backward distribution functions will be determined self-consistently by the expansion characteristics. Here  $N^*$  and  $T_\alpha^*$  are reference parameters (not the actual densities and temperatures at  $z = z_0$  that also involve the backward distribution function),  $v = \sqrt{v_\parallel^2 + v_\perp^2}$  is the velocity, and  $v_\parallel$  and  $v_\perp$  the velocity components parallel and normal to the magnetic field lines. For convenience, hereafter

the axial coordinate, time, velocities, magnetic field, electrostatic potential, particle distribution functions, and densities, are all normalized and we will write  $z/\lambda_{De}^* \rightarrow z$ ,  $t\omega_{pe}^* \rightarrow t$ ,  $v_{\parallel,\perp}/\lambda_{De}^*\omega_{pe}^* \rightarrow v_{\parallel,\perp}$ ,  $B/B_T \rightarrow B$ ,  $e\phi/k_B T_e^* \rightarrow \phi$ ,  $f_\alpha/N^*(m_e/k_B T_e^*)^{3/2} \rightarrow f_\alpha$ , where  $\lambda_{De}^* = \sqrt{\epsilon_0 k_B T_e^*/N^* e^2}$  is the Debye length,  $\omega_{pe}^* = \sqrt{N^* e^2/m_e \epsilon_0}$  the electron plasma frequency,  $k_B$  the Boltzmann constant,  $m_e$  the electron mass,  $e$  the elementary charge, and  $\epsilon_0$  the vacuum permittivity. As shown below, the plasma dynamics depends on the following dimensionless parameters in our model

$$r_L \equiv \frac{R_L}{\lambda_{De}^*}, \quad \delta_\alpha \equiv \frac{T_\alpha^*}{T_e^*}, \quad \beta_\alpha \equiv \frac{m_\alpha}{m_e}, \quad Z_\alpha, \quad (5.2)$$

where the subscript  $\alpha = e, i$  denotes electrons and ions, and  $m_\alpha$  and  $Z_\alpha$  are the mass and the charge number of the  $\alpha$ -species.

We follow a paraxial approximation and assume a slender and slowly-varying magnetic field, i.e. we take  $R_L/R_0 \gg 1$ , and just look at the center line of the magnetic nozzle. Under this hypothesis, the parameter  $R_0$  does not appear anymore in the model and one just needs the normalized magnetic field at the center line. It reads

$$\mathbf{B}(z) = \frac{r_L^3}{(r_L^2 + z^2)^{3/2}} \mathbf{1}_z, \quad (5.3)$$

where  $\mathbf{1}_z$  is a unit vector along the  $z$ -axis. Therefore, we are having a convergent-divergent nozzle with the maximum of the magnetic field  $B = 1$  at  $z = 0$  and  $B \rightarrow 0$  as  $z \rightarrow \pm\infty$ ; the analysis here will be focussed at the divergent side of the nozzle. The model also assumes that the magnetic field is very strong and the normalized Larmor radii satisfies  $\rho_{L\alpha} \equiv \beta v_\perp / |Z_\alpha| B \ll r_L$ . In the limit  $\rho_{L\alpha}/r_L \rightarrow 0$ , the slow drift motion of the particles across the field lines can be ignored and the normalized magnetic moment

$$\mu_\alpha = \frac{\beta_\alpha v_\perp^2}{2B} \quad (5.4)$$

is conserved (for brevity, we will generally write  $\mu_\alpha \rightarrow \mu$ ). Hereafter, we will work with the gyrocenter variables  $(z, v_\parallel, \mu, \gamma)$ , and will also average the distribution functions of the particles  $f_\alpha$  over the fast gyrophase  $\gamma$

$$\bar{f}_\alpha(t, z, v_\parallel; \mu) = \frac{1}{2\pi} \int_0^{2\pi} f_\alpha(t, z, v_\parallel, \mu, \gamma) d\gamma. \quad (5.5)$$

The evolution of the gyrocenter distribution function  $\bar{f}_\alpha$  is governed by the Vlasov equation

$$\frac{\partial \bar{f}_\alpha}{\partial t} + v_\parallel \frac{\partial \bar{f}_\alpha}{\partial z} + a_\alpha \frac{\partial \bar{f}_\alpha}{\partial v_\parallel} = 0, \quad (5.6)$$

where we ignored the induced magnetic field and introduced the parallel dimensionless acceleration

$$a_\alpha = -\frac{1}{\beta_\alpha} \left( Z_\alpha \frac{\partial \phi(t, z)}{\partial z} + \mu \frac{dB(z)}{dz} \right). \quad (5.7)$$

The normalized electric field  $\mathbf{E} = E_\parallel \mathbf{B}/B = -\partial\phi/\partial z$  is given by the paraxial Poisson's equation

$$B \frac{\partial}{\partial z} \left( \frac{E_\parallel}{B} \right) = \sum_{\alpha=e,i} Z_\alpha n_\alpha \quad (5.8)$$

with the particle densities computed from the distribution functions as

$$n_\alpha(z) = \int f_\alpha d\mathbf{v} = \frac{2\pi B}{\beta_\alpha} \int_{-\infty}^{+\infty} \int_0^{+\infty} \bar{f}_\alpha dv_\parallel d\mu. \quad (5.9)$$

Therefore, the dynamics of the electrons and the ions governed by the two Vlasov equations in Eq. (5.6) are nonlinearly coupled through the electrostatic potential. This set of equations must be integrated with appropriate boundary and initial conditions, discussed in Subsec. 5.2.3.

## 5.2.2 Evolution of macroscopic quantities

The evolution equations of the main macroscopic quantities are helpful in the analysis of the simulations. The average or mean value of any quantity  $\psi$  is computed as

$$\langle \psi \rangle_\alpha = \frac{1}{n_\alpha} \int \psi f_\alpha d\mathbf{v} = \frac{2\pi B}{\beta_\alpha n_\alpha} \int_{-\infty}^{+\infty} \int_0^{+\infty} \psi \bar{f}_\alpha dv_\parallel d\mu. \quad (5.10)$$

Interesting quantities are: densities  $n_\alpha = \langle 1 \rangle_\alpha$ , Eq. (5.9); macroscopic velocities parallel to the magnetic field  $u_\alpha = \langle v_\parallel \rangle_\alpha$ ; current densities  $j_\alpha = Z_\alpha n_\alpha u_\alpha$ ; temperatures  $T_{\parallel\alpha} = \beta_\alpha \langle c_{\parallel\alpha}^2 \rangle_\alpha$  and  $T_{\perp\alpha} = B \langle \mu \rangle_\alpha$ , where we introduced the peculiar velocities  $c_{\parallel\alpha} = v_\parallel - u_\alpha$ ; pressures  $P_{\parallel\alpha} = n_\alpha T_{\parallel\alpha}$  and  $P_{\perp\alpha} = n_\alpha T_{\perp\alpha}$ ; and (parallel) heat fluxes of parallel and perpendicular energy,  $Q_{\parallel\alpha} = \frac{1}{2} \beta_\alpha n_\alpha \langle c_{\parallel\alpha}^3 \rangle_\alpha$  and  $Q_{\perp\alpha} = B n_\alpha \langle \mu c_{\parallel\alpha} \rangle_\alpha$ , respectively. According to Sec. 5.2, the normalization has been done with characteristic variables involving the electron mass.

The evolution equations of these quantities are obtained straightforwardly by taking velocity moments in Eq. (5.6). In the paraxial case, the equations for continuity, axial momentum, total energy, and perpendicular energy are, respectively,

$$\frac{\partial n_\alpha}{\partial t} + B \frac{\partial}{\partial z} \left( \frac{n_\alpha u_\alpha}{B} \right) = 0, \quad (5.11)$$

$$\begin{aligned} \frac{\partial}{\partial t} (\beta_\alpha n_\alpha u_\alpha) + B \frac{\partial}{\partial z} \left( \frac{\beta_\alpha n_\alpha u_\alpha^2}{B} \right) &= -Z_\alpha n_\alpha \frac{\partial \phi}{\partial z} \\ &+ \left[ (P_{\parallel\alpha} - P_{\perp\alpha}) \frac{\partial \ln B}{\partial z} - \frac{\partial P_{\parallel\alpha}}{\partial z} \right], \end{aligned} \quad (5.12)$$

$$\begin{aligned} &\frac{\partial}{\partial t} \left[ n_\alpha \left( \frac{\beta_\alpha}{2} u_\alpha^2 + \frac{T_{\parallel\alpha}}{2} + T_{\perp\alpha} \right) \right] + \\ B \frac{\partial}{\partial z} \left[ \frac{n_\alpha u_\alpha}{B} \left( \frac{\beta_\alpha}{2} u_\alpha^2 + \frac{3}{2} T_{\parallel\alpha} + T_{\perp\alpha} \right) + \frac{Q_{\parallel\alpha} + Q_{\perp\alpha}}{B} \right] &+ j_\alpha \frac{\partial \phi}{\partial z} = 0, \end{aligned} \quad (5.13)$$

$$\frac{\partial}{\partial t} (n_\alpha T_{\perp\alpha}) + B^2 \frac{\partial}{\partial z} \left[ \frac{1}{B^2} (n_\alpha u_\alpha T_{\perp\alpha} + Q_{\perp\alpha}) \right] = 0. \quad (5.14)$$

This set of macroscopic equations is incomplete, unless equations for the parallel heat fluxes  $Q_{\parallel\alpha}$  and  $Q_{\perp\alpha}$  are added, which will introduce higher order magnitudes. A closure of the set of the fluid equations is not simple in a collisionless plasma.



Here, the consistent kinetic solution is obtained directly, so the fluid equations are used to interpret the results, mainly the steady-state ones in Section 5.3. In this respect, in the above equations,  $1/B$  plays the role of the effective beam area [furthermore, it is in fact the natural spatial variable (instead of  $z$ ) in the divergent paraxial nozzle]. Thus, in Eq. (5.11),  $n_\alpha u_\alpha/B$  is the species flow (i.e. the flux area integrated), which is constant spatially in steady-state. The species current,  $j_\alpha/B$ , and the total plasma current,  $I = (j_e + j_i)/B$ , are constant in steady-state too. In Eq. (5.12), the two last terms on the right-hand side are the contribution of the divergence of the pressure tensor (i.e. the net pressure force). Then, the steady-state limit of Eq. (5.13) yields that the total enthalpy flow,  $\dot{H}_\alpha$ , is constant spatially,

$$\dot{H}_\alpha \equiv \frac{n_\alpha u_\alpha}{B} \left( \frac{\beta_\alpha}{2} u_\alpha^2 + \frac{3}{2} T_{\parallel\alpha} + T_{\perp\alpha} + Z_\alpha \phi \right) + \frac{Q_{\parallel\alpha} + Q_{\perp\alpha}}{B} = \text{const}. \quad (5.15)$$

Here,  $(Q_{\parallel\alpha} + Q_{\perp\alpha})/B$  is the total heat conduction flow. The steady state limit of Eq. (5.14) yields that the (convection plus conduction) flow of perpendicular energy evolves proportional to  $B^{-1}$

$$\frac{n_\alpha u_\alpha T_{\perp\alpha} + Q_{\perp\alpha}}{B^2} = \text{const}, \quad (5.16)$$

which is the direct consequence of the conservation of the magnetic moment of the species. These conservation laws were already used in Ref. [63] to analyze the plasma response in a convergent magnetic field. Finally, if the mean kinetic energy is eliminated from Eq. (5.13) by using Eqs. (5.11) and (5.12), the evolution equation for the internal energy is obtained,

$$\begin{aligned} \frac{\partial}{\partial t} \left( \frac{P_{\parallel\alpha}}{2} + P_{\perp\alpha} \right) + B \frac{\partial}{\partial z} \left\{ \frac{1}{B} \left[ u_\alpha \left( \frac{3}{2} P_{\parallel\alpha} + P_{\perp\alpha} \right) + (Q_{\parallel\alpha} + Q_{\perp\alpha}) \right] \right\} \\ - u_\alpha \left[ \frac{\partial P_{\parallel\alpha}}{\partial z} + (P_{\perp\alpha} - P_{\parallel\alpha}) \frac{\partial \ln B}{\partial z} \right] = 0, \end{aligned} \quad (5.17)$$

which can substitute for Eq. (5.13).

### 5.2.3 Simulation domain and boundary conditions

We are interested in the time-dependent plasma expansion along the (semi-infinite) divergent nozzle, extending from  $z = 0$  (the throat  $T$ ) to  $z = \infty$ . However, since the numerical simulation requires to work with a finite domain, the downstream end of the domain (point M) will be placed at a certain  $z_M \gg 1$ , with  $B_M \ll 1$ . A parametric analysis of the combined influence of  $z_M$  and  $r_L$  on the solution is carried out below. Furthermore, it turns out that, in spite of applying quasineutrality at the upstream end of the simulation domain, a non-desirable Debye sheath, extending a few Debye lengths develops there. In order to eliminate its spurious influence, the upstream end of the domain has been placed at the convergent side of the nozzle, in particular, at  $z_0 = -r_L/2$ .

At the domain entrance, we set Maxwellian functions for the injected particles,

$$\bar{f}_\alpha(t, z = z_0, v_{\parallel} > 0; \mu) = \chi_\alpha(t) \bar{f}_{M\alpha} \quad (5.18)$$

with

$$\bar{f}_{M\alpha} = \left( \frac{\beta_\alpha}{2\pi\delta_\alpha} \right)^{3/2} \exp \left( -\frac{\beta_\alpha v_{\parallel}^2}{2\delta_\alpha} - \frac{B\mu}{\delta_\alpha} \right) \quad (5.19)$$

and  $\chi_e = 1$ . The parameter  $\chi_i(t)$  is dynamically varied to accomplish quasineutrality at entrance section  $z = z_0$ , once reflected-back particles are taken into account there. [For instance, if no ions are reflected back and all electrons are, then  $\chi_i = 2$ .] At the domain downstream end, in order to simulate the vacuum at infinity, we impose no incoming particles into the domain,

$$\bar{f}_\alpha(t, z = z_M, v_\parallel < 0; \mu) = 0. \quad (5.20)$$

Regarding initial conditions, one would initially set  $\bar{f}_\alpha(t = 0, z > z_0, v_\parallel; \mu) = 0$ . However, since such a hard transition can lead to numerical issues, our simulations used

$$\bar{f}_\alpha(t = 0, z > z_0, v_\parallel; \mu) = \bar{f}_{M\alpha} \times \exp\left(-\frac{z - z_0}{L_0}\right) \quad (5.21)$$

with  $L_0$  a dimensionless parameter that controls the density gradient of the initial plasma profile. A value  $L_0 = 2$ , which yields a profile with width about a few Debye lengths, is enough to provide a smooth transition at  $t = 0$  in the simulations.

Finally, Poisson's equation requires two boundary conditions on the electrostatic potential. Clearly, there is the freedom to take  $\phi(z = z_0) = 0$ . With respect to the boundary condition at the downstream end, the studies of the semi-infinite, stationary nozzle with a simple plasma have shown two things. First, the potential decays monotonically to an asymptotic value  $\phi = \phi_\infty < 0$  (i.e. yielding  $d\phi/dz|_\infty \rightarrow 0$ ). Second, the net electric current of the plasma beam  $I$  is not a parameter independent of  $\phi_\infty$ : a parametric current-voltage curve  $I(\phi_M)$  with  $\partial I / \partial |\phi_\infty| > 0$  exists. This behavior of the current-voltage curve is simple to explain: for normalized distribution functions at injection, the more negative  $\phi_\infty$  is, a larger fraction of electrons injected into the nozzle is reflected back to the reservoir while (near) all ions cross freely the nozzle, and thus the more positive becomes  $I$ . Therefore, in the downstream end of our finite simulation box we can impose either  $\phi_M = \phi(z_M)$  or  $I$ . The first choice is the natural one for the numerical scheme. Notice then, that the case of most practical interest,  $I = 0$ , which corresponds to a current-free plasma beam, requires to iterate on  $\phi_M$ .

#### 5.2.4 Direct Vlasov solver

This section discusses briefly the main features of the novel direct Vlasov code VLASMAN (VLASov Simulator for MAGnetic Nozzles), that has been developed for the numerical integration of Eq. (5.6). A mesh of points  $z_i$  with  $i = 1, \dots, N_z$  is defined within the interval  $z_0 \leq z \leq z_M$ . These points are distributed non-uniformly in order to keep constant the ratio between the resolution of the mesh and the local Debye length, which is expected to vary as  $\lambda_{De} \sim n^{-1/2} \sim B^{-1/2}$ . The velocity space, involving  $v_\parallel$  and  $\mu$ , was truncated as  $-v_{max}^\alpha \leq v_\parallel \leq v_{max}^\alpha$  and  $0 \leq \mu \leq \mu_{max}^\alpha$  and discretized with  $N_{v_\parallel} \times N_\mu$  points. Unlike the spatial mesh, which is common for both species, different maximum velocities and magnetic moments are chosen for electrons and ions. For both species, the velocity mesh is uniform. The unknowns of the code are the values of the distribution functions at the points of the mesh and at discrete times  $t_m, \bar{f}_\alpha(t_m, s_i, v_{\parallel j}, \mu_k)$ .

Since  $\mu$  appears as a parameter in Eq. (5.6), the algorithm just needs to solve a one dimensional equation  $N_\mu$  times. Given the distribution function  $\bar{f}_\alpha(t_m, s_i, v_{\parallel j}, \mu_k)$ , the value at  $t_m + \Delta t$  is found by using a splitting algorithm that treats the convective terms in the  $z$  and  $v_\parallel$  directions separately, and

gives a scheme of second order in  $\Delta t$  [18]. A short summary of the splitting algorithm and a description of the numerical schemes implemented for the interpolation and the numerical integration are given in [89].

In the simulations, we took the physical parameters  $\delta_i = 1$ ,  $\beta_i = 100$ ,  $Z_i = 1$ , and considered several values of  $r_L$ . The value of  $\beta_i$  is not realistic for an electron-ion plasma but it still separates significantly the electron and ion response times and helped us save computational resources. Regarding the geometry of the nozzle, we set  $z_0 = -r_L/2$ , i.e. the divergent and convergent segments have lengths equal to  $r_L/2$  and  $z_M$ , respectively. The most relevant numerical parameters are  $N_{v_{\parallel}} = 77$ ,  $N_{\mu} = 101$ ,  $v_{\max}^e = 5$ ,  $v_{\max}^i = 0.5$ ,  $\mu_{\max}^e = \mu_{\max}^i = 12.5$ , and  $\Delta t = 0.03$ . Tradeoffs analysis varying the numerical parameters  $z_M$  and  $\phi_M$  are shown in Sec. 5.3.

### 5.3 Stationary solution and parametric analysis

The effect of the truncation of the computational box up to a length  $z_M$  and the setting of the electrostatic potential value  $\phi_M$  at that position have been investigated by running a large number of simulations. After taking an expansion rate of  $r_L = 50$ , the physical and numerical parameters explained in Sec. 5.2.4, and several values of  $z_M$  and  $\phi_M$ , we integrate the Vlasov-Poisson system forward in time until the plasma reached the corresponding stationary state. For each simulation, the latter was verified by monitoring the time evolution of the most important variables, such as density and potential, and the  $z$ -profiles of  $n_{\alpha}u_{\alpha}/B$ , which becomes uniform at stationary conditions.

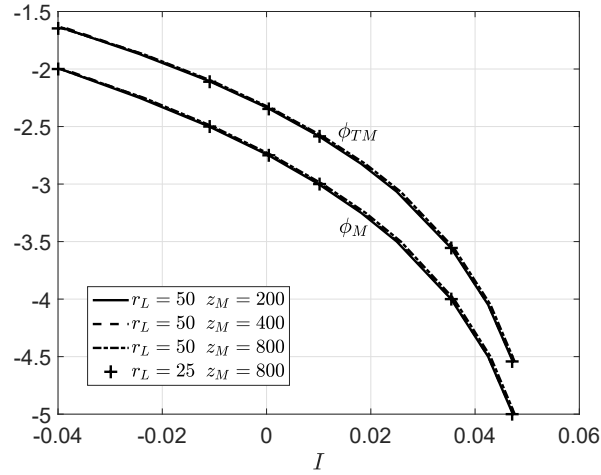


**Figure 5.1:** Net current-to-magnetic field ratio  $j/B$  versus the total potential drop ( $\phi_M$ ) and the one between the throat and  $z_M$  ( $\phi_{TM}$ ) for several expansion rates and box sizes. The curves practically overlap, also for the case  $r_L = 100$  (not shown).

First of all, Fig. 1 shows the results of investigating the influence of the total potential fall  $\phi_M$  on the electric current  $I$  across the nozzle in steady-state. As expected and known from previous models, the current  $I$  (abscissa) is positive for large, negative values of  $\phi_M$  (ordinate), and negative otherwise. The most relevant result here is the universal character of the curve  $\phi_M(I)$ : it is practically independent of  $r_L$  and  $z_M$  (as long as  $B_M \ll 1$ ), which allows to infer that this curve reproduces the behavior of the semi-infinite nozzle too. Furthermore, Fig. 5.1 shows that the curve  $\phi_{TM}(I)$  for the potential fall

along the divergent part of the nozzle is (near) universal too. The principal, current-free beam case has potential falls of  $\phi_M \approx -2.75$  and  $\phi_{TM} \approx -2.34$ . Such potential drops are consistent with previous calculations from stationary kinetic models (extrapolate to  $m_i/m_e = 100$  the results in Fig. 4(c) of Ref. [64]). Hereafter, we focus the analysis at discussing the (approximate) 'current-free case'  $\phi_M = -2.75$ . The steady states values of the normalized species current are  $I_i = -I_e \simeq 0.074$ .

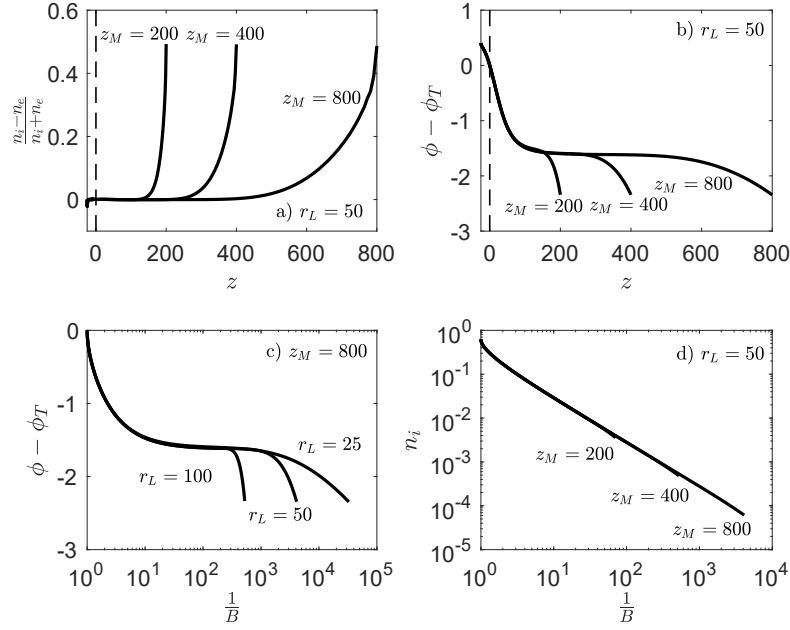


**Figure 5.2:** (a), (b) and (d) Respectively, the normalized space charge,  $\phi$  versus  $z$  and  $n_i$  versus  $1/B$  for  $r_L = 50$  and several  $z_M$ . (c)  $\phi$  versus  $1/B$  for  $z_M = 800$  and several expansion rates.

Figure 5.2 shows (near) stationary axial profiles for different  $r_L$  and  $z_M$ . Panel (a) plots the relative space charge for  $r_L = 50$  and several lengths of the simulation box; panels (b) and (c) plot the electric potential profile versus  $z$  and  $B^{-1}$ , and panel (d) the ion density versus  $B^{-1}$ . Three different spatial regions can be distinguished in panels (a)-(c). First, a small sheath (with a relative space charge  $< 5\%$  and extending a few Debye lengths) forms at the entrance of the simulation domain, in spite of having forced quasineutrality locally at  $z = z_0$ . This 'numerical' sheath is caused by the need of the electric field to adapt the entrance distribution functions of ions and electrons and it was the reason to include a small convergent part of the nozzle, even though the work is focused on the divergent nozzle behavior. Second, there is the large quasineutral region, with a decreasing electric field as we move downstream. Third, there is a second Debye sheath at the downstream end of the simulation. Since the Debye length is proportional to  $n_\alpha^{-1/2}$  [and thus nearly proportional to  $B^{-1/2}$ , according to panel (d)], it increases by 1-2 orders of magnitude along the discharge, thus giving the impression that the downstream sheath is thick. Just for reporting, the relative space-charge and the potential fall in the downstream sheath are nearly constant, because of the low electric field at the sheath entrance and the need to adjust the total potential fall to  $\phi_M$ . Panel (c) shows that  $\phi$  depends more naturally on  $B^{-1}$  in the quasineutral region. In panel (d), we see that  $n_i$  is near proportional to  $B$ , indicating a much gentler dependence of  $u_i$  on  $B$  (to have  $n_i u_i / B = \text{const}$ ). The electron density  $n_e$  behaves as  $n_i$  except at the downstream sheath where it decreases more sharply. Normalized plasma densities at the entrance and the throat are

$n_{e0} = 0.97$  and  $n_{eT} = 0.62$ , the difference indicating the jet acceleration in the small convergent region of the nozzle. Finally, at the simulation box entrance, the ratio of ion-to-electron densities for forward moving particles, that is,  $\chi_i$  in Eq. (5.18) is 1.53: this ratio would be close to 2 and 1 if the entrance would be, respectively, at the throat and further upstream in the convergent magnetic nozzle.

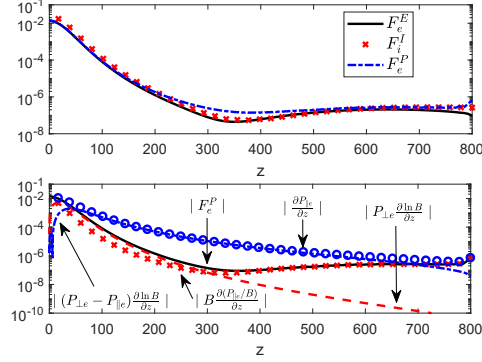


**Figure 5.3:** Stationary, spatial profiles of inertial, pressure, and electric forces of ions and electrons for  $r_L = 50$  and  $z_M = 800$ .

The stationary momentum equation of ions and electrons, Eq. (5.12), states the balance

$$F_\alpha^I = F_\alpha^P + F_\alpha^E, \quad (5.22)$$

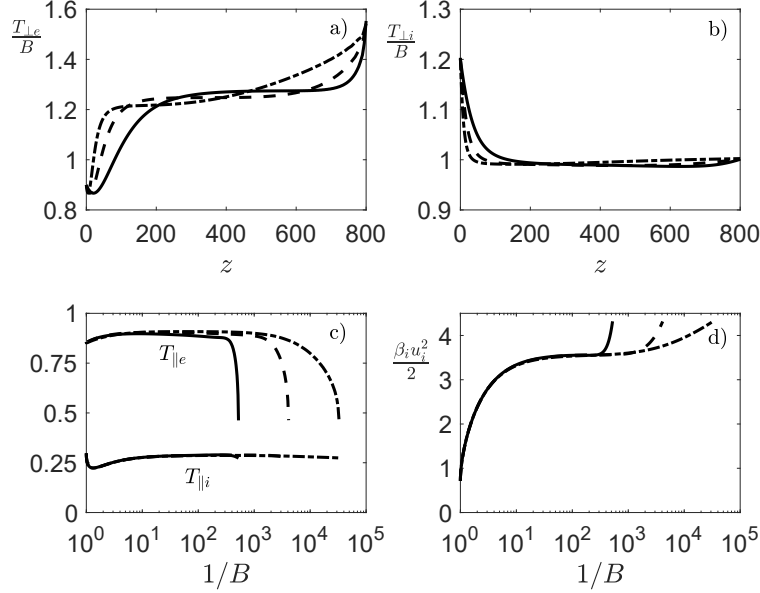
between the inertial force (or flow of species momentum)  $F_\alpha^I$ , the pressure force  $F_\alpha^P$ , and the electric force  $F_\alpha^E$ . Both  $F_\alpha^I$  are positive, both  $F_\alpha^P$  are expected to be positive, while  $F_i^E > 0$  and  $F_e^E < 0$ . Furthermore, one has:  $F_e^E \simeq F_i^E$  in the quasineutral region; and  $F_e^I/F_i^I \sim m_e/m_i \ll 1$  for the current-free and ‘small current’ cases. The combination of these two facts implies that the electron inertia is negligible, and the electric and electron pressure forces balance each other, i.e.  $F_e^P \simeq -F_e^E \gg F_e^I$ . For ions, the inertial force is dominant, and the relevance of the ion pressure depends on upstream conditions for  $T_i/T_e$ . These trends are confirmed by Figure 5.3(a), which plots  $F_e^E$ ,  $F_e^P$ , and  $F_i^I$ ; the two other forces are obtained by just applying Eq. (5.22). In this case, the ion flow is supersonic and thus is accelerated freely by the electric force.

Figure 5.3(b) assesses the different contribution to the net electron pressure force, that is, the pressure tensor divergence. This can be expressed in two different ways:

$$\nabla \cdot \bar{P}_\alpha = \frac{\partial P_{\parallel\alpha}}{\partial z} + (P_{\perp\alpha} - P_{\parallel\alpha}) \frac{\partial \ln B}{\partial z} \equiv B \frac{\partial}{\partial z} \left( \frac{P_{\parallel\alpha}}{B} \right) + P_{\perp\alpha} \frac{\partial \ln B}{\partial z}. \quad (5.23)$$

The first division is based on the parallel pressure gradient and the magnetic mirror effect, and the second is based on the  $P_{\parallel\alpha}$  and  $P_{\perp\alpha}$  contributions. The panel shows, interestingly, that the parallel pressure gradient and the magnetic mirror effect are individually much larger as their difference (i.e. they compensate practically each other). This makes them not very suitable to characterize the total pressure contribution. On the contrary, the  $P_{\parallel\alpha}$  and  $P_{\perp\alpha}$  contributions are of the same order as their difference. For this particular case, the  $P_{\perp\alpha}$ -contribution dominates mildly upstream, while the  $P_{\parallel\alpha}$ -contribution dominates totally downstream. The milder behavior of the  $z$ -derivative of  $P_{\parallel\alpha}/B$  compared to that of  $P_{\parallel\alpha}$ , and the drop of the  $P_{\perp\alpha}$ -contribution, are due to  $n_\alpha \propto B$  approximately and the behaviors of  $T_{\parallel\alpha}$

and  $T_{\perp\alpha}$  shown below. Although not shown, the ion pressure contributions behave in the same way than the electron ones.



**Figure 5.4:** (a), (b) The perpendicular temperature of the electrons and the ions, respectively. (c) Their parallel temperatures and (d) the mean kinetic energy of the ions.  $z_M = 800$  and solid, dashed, and dot-dash lines correspond to  $r_L = 100, 50$ , and  $25$ , respectively.

Figure 5.4(a)-(c) displays the stationary spatial profiles of the parallel and perpendicular temperatures of ions and electrons for  $z_M = 800$  and  $r_L = 25, 50$ , and  $100$ . In this collisionless plasma, these kinetic temperatures simply express the dispersion of particle velocities. The first interesting feature is that both perpendicular temperatures decrease with  $B^{-1}$ , a behavior related to the conservation of magnetic moment. On the contrary, the parallel temperatures are rather constant spatially, except for the decrease of  $T_{\parallel e}$  at the downstream sheath. Therefore, the plasma expansion along the divergent nozzle implies both anisotropy and cooling [the average temperature is  $(T_{\parallel\alpha} + 2T_{\perp\alpha})/3$ ]. This behavior agrees qualitatively with stationary, kinetic, fully-quasineutral models (see Fig. 7 in Ref. [64]). Apparently, the main difference of the non-stationary model, which computes the population of trapped electrons self-consistently, is a softer decay of the parallel temperature. Values of normalized temperatures at the throat are  $T_{\parallel iT} \simeq 0.30$ ,  $T_{\perp iT} \simeq 1.20$ ,  $T_{\parallel eT} \simeq 0.86$ ,  $T_{\perp eT} \simeq 0.90$ , and they are explained by the analysis of Ref. [63] for a convergent magnetic geometry: there the ion distribution function is determined by the combination of the magnetic mirror and the free extraction at the throat, while electrons remain near Maxwellian. Figure 5.4(d) displays the ion axial kinetic energy, which increases downstream thanks to the electric potential energy. For this current-free case, the electron axial energy behaves exactly the same in the quasineutral region (but it is  $m_e/m_i$  times lower).

Figure 5.5 analyzes the  $z$ -profiles of the heat (or internal energy conduction) flows. We recall that  $Q_{\parallel}$  and  $Q_{\perp}$  represent parallel fluxes of the parallel and perpendicular thermal energies (perpendicular fluxes are zero in our model). Notice that, since this is a collisionless plasma, no Fourier-type law is expected to apply for these heat flows. Panel (a) shows that: the area-integrated parallel heat flows,  $Q_{\parallel\alpha}/B$ , are approximately constant (except, as often, near the ends of the simulations) while the parallel

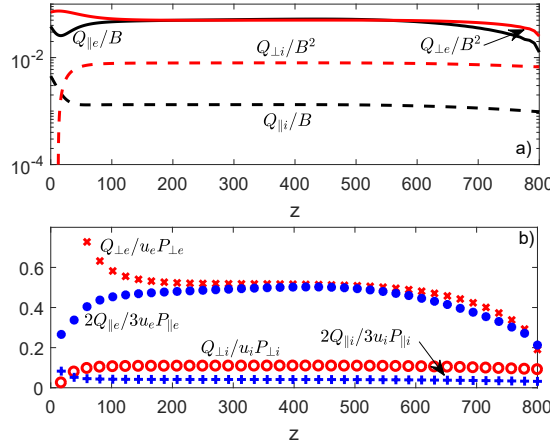


**Figure 5.5:** Axial profiles of the heat fluxes [panel (a)] and their relative rates versus the pressure fluxes [panel (b)]  $r_L = 50$  and  $z_M = 800$ .

flows of perpendicular thermal energy,  $Q_{\perp\alpha}/B$ , decrease proportional to  $B^2$ . The same dependence with  $B$  was found for the internal energy convection flows,  $n_\alpha u_\alpha (3T_{\parallel\alpha}/2)$  and  $n_\alpha u_\alpha T_{\perp\alpha}$ . To complete this, panel (b) determines the relative rates of internal energy conduction versus the pressure flux for ions and electrons. Focusing on the main quasineutral region, conduction of parallel and perpendicular internal energies of electrons is about 50-52% of its convection; for ions conduction represents 4% and 11% in the parallel and perpendicular cases; more parametric analyses are needed to ascertain how these values depend on the upstream plasma conditions. In spite of this, it seems clear that, both for ions and electrons, the internal energy perpendicular flow decreases in proportion to  $B$ , Eq. (5.16), and becomes negligible downstream. Then, since the total enthalpy flow is conserved, Eq. (5.15), that loss of perpendicular energy goes mainly into increasing the axial kinetic energy, which is the macroscopic equivalence of the classical particle mirror effect, for ions, and the electric potential energy for electrons.

## 5.4 Conclusions

In this chapter, the steady-state behaviour of the plasma expansion, from the Vlasov-Poisson solver, is discussed. The parametric analysis shows how the electrostatic potential drop and the size of the simulation box should be selected to reproduce relevant physical conditions in the simulations. Along the expansion, a non-neutral region is found downstream, which is a consequence of the semi-infinite expansion truncation. However, the results are robust with respect to the simulation domain length, for a larger length, the quasineutral solution upstream does not change, and the overall potential drop and final relative space-charge are the same along the downstream sheath. The cooling of both ions and electrons are observed, with the perpendicular temperatures tending to zero due to the magnetic mirror while the parallel ones tend to a non-zero values. The parallel and perpendicular heat fluxes are found to scale with the respective convective fluxes of internal parallel and perpendicular energies.

The analysis of kinetic features, which is not shown in this chapter but is found in Ref. [89], provides quantitative information about the relative importance of the different electron populations. Reflected electrons are the dominant population in the quasineutral region, followed by the free and the trapped electrons. The latter represents about 20% of the total. This figure is much smaller than the one

needed to make stationary Vlasov-Poisson solver converge in previous studies. Therefore, a population of trapped electrons seems to be a fundamental component of the expansion but it is not as large as considered earlier. Moreover, it is shown that the exact amount of trapped electrons depends on the particular history of the system and several steady states are possible.

## 5.A Effect of the convergent segment

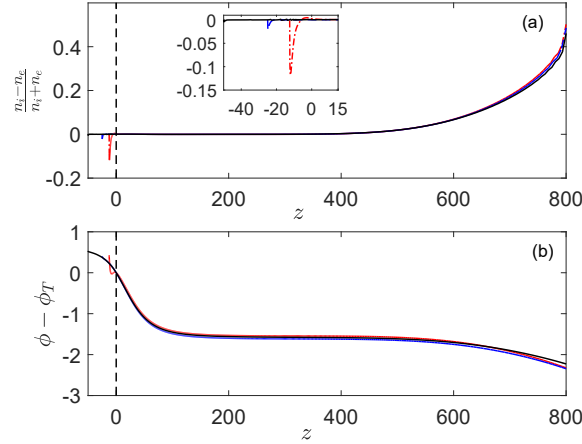


**Figure 5.6:** (a), (b) The charge densities and potential profiles for simulations with lengths of the convergent segment equal to  $z_0 = -50$  (solid black),  $z_0 = -25$  (dashed blue) and  $z_0 = -12.5$  (red dashed-dotted). The curves practically overlap.

Although this work is focused on the divergent segment of the nozzle, we here explain briefly why it is convenient to add a small convergent segment in the simulation domain, and the impact of its length,  $|z_0|$ , in the results of the expansion in the divergent region. A short parametric analysis for  $z_0 = -50, -25, -12.5$  and  $r_L = 50$ , is presented next.

Panel (a) of Fig. 5.6 displays the normalized charge density profiles in stationary conditions. The sheath forms always at the left edge of the simulation box and its strength mitigates as the length of the convergent segment is increased [see inset in panel (a)]. Eventually the sheath would disappear if the whole plasma source were included, as it is the case in the stationary model of Ref. [64]. Panels (a) and (b) show that both the charge density and the electric potential (when referenced to the throat) are almost unaltered by the segment length (if this is larger than a few Debye lengths). The same conclusion was reached for other plasma properties in the divergent nozzle, like for instance the temperature profiles. In this respect, the results of our work are robust. If the left edge of the simulation were placed at the throat, a non-negligible sheath would appear next to the throat affecting significantly the potential fall along the divergent nozzle. It is clear that there are distribution functions that avoid the development of a sheath at the left edge, but we do not see a way to characterize them. The presence of this *spurious* sheath has been reported also in full particle-in-cell simulations of unmagnetized and magnetized plumes too [43, 57].



## Chapter 6

# Kinetic study of magnetic nozzles: collisions

*This chapter adapts the contents of the article titled "Time-dependent expansion of a weakly-collisional plasma beam in a paraxial magnetic nozzle", which has been submitted to Plasma Sources Science and Technology and is under revision [121]. Although this is a continuation of Chapter 5, some notation changes were found convenient.*

### 6.1 Introduction

As continuation of Chapter 5, this chapter extends VLASMAN into the weakly-collisional regime. The occasional electron-electron collisions can alter (and presumably increase) the occupancy level of the trapped-electron region, and thus verify if the full occupancy postulated by the quasineutral, steady-state kinetic (SSK) model of Martínez-Sánchez et al. is achieved [64]. A Bhatnagar-Gross-Krook (BGK) intraspecies collision operator [12] is used. This attempts to relax the local velocity distribution function (VDF) towards a drifted Maxwellian VDF with the same density, drift and temperature. Recently, Ahedo et al. [4] came back to the SSK model to characterize the total potential drop and other downstream plasma magnitudes; analyze the mass, momentum and energy balances; and discuss closures for electron heat flux. The kinetic and macroscopic solutions from VLASMAN will be compared to the ones of Ref. [4].

Section 6.2 explains the physical model and the simulation setup. Most of this section has been already described in Chapter 5, but as the notation has changed, it is repeated with the new notation for consistency in this chapter. Section 6.3 presents the main kinetic features and the role of the collisions. Section 6.4 presents the spatial profiles of macroscopic magnitudes and the balances of macroscopic equations. Section 6.5 discusses on closure laws for electron heat flux. Section 6.6 discusses on the total potential drop as boundary condition. Section 6.7 summarizes the conclusions.

### 6.2 Magnetic nozzle model

#### 6.2.1 Physical model and boundary conditions

A paraxial convergent-divergent MN defined by a stationary magnetic field  $B$  is considered. If the plasma beam is fully magnetized, it is contained within a magnetic surface of area  $A(z) = \pi R^2(z)$ .

Although the results are far more general, for sake of illustration, the simulations here consider the particular magnetic field generated by a current loop of radius  $R_L$ . The paraxial approximation requires that  $R \ll R_L$ . Then, the axial magnetic field on the plasma beam is the one at the axis

$$\mathbf{B}(z) \simeq \frac{B_M}{[1 + (z/R_L)^2]^{3/2}} \mathbf{1}_z, \quad (6.1)$$

and the condition  $\nabla \cdot \mathbf{B} = 0$  yields  $A(z)B(z) = \text{const}$ . In fact, the larger  $R_L$  is, the lower the nozzle divergence rate is:  $d \ln A/dz \propto 1/R_L$ . Figure 6.1 sketches the magnetic field and the simulation domain. The nozzle throat M is located at  $z = 0$ ,  $B_M$  is the maximum field and  $A_M$  is the minimum area. The simulation domain, which is initially empty, extends from a plasma source at  $z_0 < 0$  to a downstream boundary  $z_D > 0$ . The source ejects a fully-ionized Maxwellian-like plasma constituted of electrons and singly-charged ions. Electrons and ions reaching the downstream boundary  $z_D$  leave the domain.

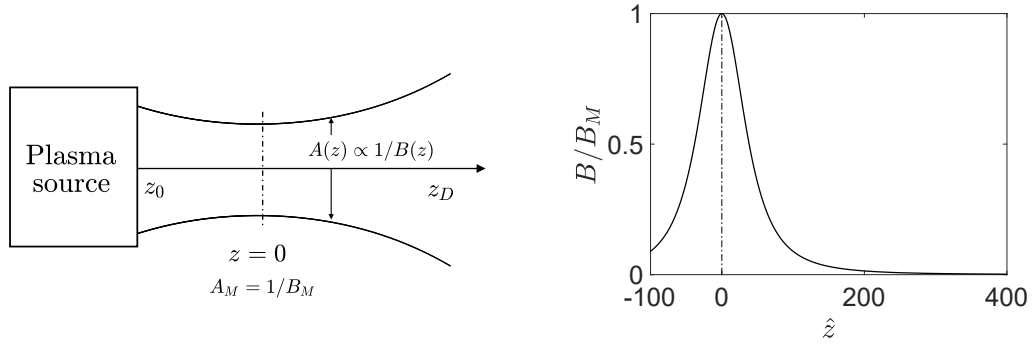


**Figure 6.1:** Sketch of the magnetic nozzle (left) and the external magnetic field  $B$  (right). Plasma is injected from a source and expands from  $z_0$  to  $z_D$  with the nozzle throat M at  $z = 0$ .

Let  $\alpha = e, i$  denote electrons and ions, respectively, with mass  $m_\alpha$  and charge number  $Z_\alpha$ . The distribution function of the species  $\alpha$ ,  $f_\alpha(t, z, v_\parallel, v_\perp, \varphi)$ , depends on time  $t$ , axial coordinate  $z$  and species velocity  $\mathbf{v} = v_\parallel \mathbf{B}/B + v_\perp$ . For convenience, the latter is split in the parallel ( $v_\parallel$ ) and perpendicular ( $v_\perp$ ) components to  $\mathbf{B}$ , and in turn, the perpendicular one is given by its module  $v_\perp$  and the gyrophase  $\varphi$ . The high-magnetization limit considered here means that the Larmor radius,  $\rho_{L\alpha} \equiv m_\alpha v_\perp / eB$  (with  $e$  the elementary charge), of any species is small compared to the scale length of the variation of the magnetic field, i.e.  $\rho_{L\alpha}/R_L \ll 1$ . In addition, the low collisionality limit means that the species collision frequency  $\nu_\alpha$  is much smaller than the gyrofrequency,  $\omega_{c\alpha} = eB/m_\alpha$ , and the inverse of the transit time in the MN. Under these conditions, the plasma is attached to the magnetic field lines, and the guiding center theory can be applied [14]. The details of the gyromotion are not important and, instead of using  $f_\alpha$ , the evolution of its average value in the gyrophase  $\varphi$  can be followed. This gyrocenter VDF is of the form  $\bar{f}_\alpha(t, z, v_\parallel, \mu)$ , where the magnetic moment  $\mu = m_\alpha v_\perp^2 / 2B$  substitutes to  $v_\perp$  as independent variable.

Ignoring any self-induced magnetic field and in the limit of small Larmor radius and large gyrofrequency, the Boltzmann equation for the gyrocenter VDF is [98, 14]

$$\frac{\partial \bar{f}_\alpha}{\partial t} + v_\parallel \frac{\partial \bar{f}_\alpha}{\partial z} + a_\alpha \frac{\partial \bar{f}_\alpha}{\partial v_\parallel} = \frac{\delta \bar{f}_\alpha}{\delta t}, \quad (6.2)$$

where the species acceleration,

$$a_\alpha = -\frac{1}{m_\alpha} \left[ Z_\alpha e \frac{\partial \phi(t, z)}{\partial z} + \mu \frac{dB(z)}{dz} \right], \quad (6.3)$$

is due to both electric and magnetic mirror forces. Finally, the paraxial Poisson equation for the electrostatic potential  $\phi$  is

$$B \frac{\partial}{\partial z} \left( \frac{1}{B} \frac{\partial \phi}{\partial z} \right) = -\frac{e}{\epsilon_0} \sum_{\alpha=e,i} Z_\alpha n_\alpha, \quad (6.4)$$

with  $\epsilon_0$  the vacuum permittivity, and the condition  $AB = \text{const}$  was applied. The collisionless case of this model was used in the study of Ref. [89].

Macroscopic magnitudes such as density ( $n_\alpha$ ), mean axial velocity ( $u_\alpha$ ), parallel and perpendicular temperatures and pressures ( $T_{\parallel\alpha}$  and  $T_{\perp\alpha}$ ,  $p_{\parallel\alpha}$  and  $p_{\perp\alpha}$ ) and axial heat flux ( $q_\alpha$ ) are obtained from velocity moments of  $\bar{f}_\alpha$ :

$$\begin{aligned} n_\alpha &= \langle 1 \rangle_\alpha, & n_\alpha u_\alpha &= \langle v_\parallel \rangle_\alpha, & p_{\parallel\alpha} &= n_\alpha T_{\parallel\alpha} = m_\alpha \langle c_\parallel^2 \rangle_\alpha, \\ p_{\perp\alpha} &= n_\alpha T_{\perp\alpha} = B \langle \mu \rangle_\alpha, & q_\alpha &= \frac{m_\alpha}{2} \langle c_\parallel^3 \rangle_\alpha + B \langle \mu c_\parallel \rangle_\alpha, \end{aligned} \quad (6.5)$$

where  $c_\parallel = v_\parallel - u_\alpha$  and

$$\langle \psi \rangle_\alpha = \frac{2\pi B}{m_\alpha} \int \int \psi \bar{f}_\alpha dv_\parallel d\mu. \quad (6.6)$$

The mean temperature and pressure are, respectively,  $T_\alpha = (T_{\parallel\alpha} + 2T_{\perp\alpha})/3$  and  $p_\alpha = n_\alpha T_\alpha$ .

Internal collisions within a particular species are modeled with the BGK operator [12]

$$\frac{\delta \bar{f}_\alpha}{\delta t} = \nu_\alpha (\bar{f}_{M\alpha} - \bar{f}_\alpha), \quad (6.7)$$

where  $\nu_\alpha$  represents an intraspecies collision frequency. This operator drives each plasma species towards local thermodynamic equilibrium by relaxing the local VDF  $\bar{f}_\alpha$  towards the Maxwellian VDF with the same local and instantaneous  $n_\alpha$ ,  $u_\alpha$  and  $T_\alpha$ , i.e.

$$\bar{f}_{M\alpha}(t, z, v_\parallel, \mu) \equiv n_\alpha \left( \frac{m_\alpha}{2\pi T_\alpha} \right)^{3/2} \exp \left[ -\frac{m_\alpha (v_\parallel - u_\alpha)^2}{2T_\alpha} - \frac{B\mu}{T_\alpha} \right]. \quad (6.8)$$

For a weakly-collisional plasma beam in a MN, the transit times (between  $z_0$  and  $z_D$ ) of ions and electrons are small compared to the mean collision times  $\nu_\alpha^{-1}$ . Thus, only trapped electrons, bouncing back and forth within the MN, are really affected by collisions. Therefore, ion collision frequency  $\nu_i$  will be neglected and only the electron collision frequency  $\nu_e$  appears in the model. Furthermore, for the elementary parametric study on collisional effects to be attempted here,  $\nu_e$  will be taken constant, i.e. representing an average value along the expansion. Only Appendix 6.B explores briefly a variable  $\nu_e$ .

The Boltzmann equation needs boundary conditions at  $z_0$  and  $z_D$ . At  $z_0$  the injected species ( $v_{\parallel} > 0$ ) are taken to follow the semi-Maxwellian VDFs

$$\bar{f}_{\alpha}(t, z_0, v_{\parallel} > 0, \mu) = n_{\alpha\star}(t) \left( \frac{m_{\alpha}}{2\pi T_{\alpha\star}} \right)^{3/2} \exp \left( -\frac{m_{\alpha} v_{\parallel}^2}{2T_{\alpha\star}} - \frac{B\mu}{T_{\alpha\star}} \right), \quad (6.9)$$

where  $T_{e\star}$  and  $T_{i\star}$  are constant. Regarding  $n_{\alpha\star}$ ,  $n_{e\star}$  is also constant while  $n_{i\star}(t)$  is such that the plasma is quasineutral at any time at  $z_0$ , i.e.  $n_0 \simeq n_{e0} \simeq n_{i0}$ . If  $z_0$  is far away from the MN throat, into the convergent segment (as it will be the case here),  $n_{e\star}$ ,  $n_{i\star}$ ,  $T_{e\star}$  and  $T_{i\star}$  correspond at steady state, to the densities and temperatures of the species at  $z_0$ , i.e.  $n_0$ ,  $T_{e0}$ , and  $T_{i0}$ ; hereafter, only these last symbols will be used. At  $z_D$  no species return once it reaches the domain exit and it gives the condition

$$\bar{f}_{\alpha}(t, z_D, v_{\parallel} < 0, \mu) = 0. \quad (6.10)$$

The boundary conditions for the Poisson equation are  $\phi(z_0) = 0$  and  $\phi(z_D) = \phi_D$ , where  $\phi_D$  is the total potential drop and it regulates the total net current in the plume.

The solutions of the Boltzmann-Poisson model are found with VLASMAN. A detailed explanation of the numerical scheme without collisions is in Ref. [89] and the implementation of the novel collision operator is described in Appendix 6.A.

Variables are non-dimensionalized with  $n_0$ ,  $T_{e0}$ ,  $\lambda_{De0} = \sqrt{\epsilon_0 T_{e0} / n_0 e^2}$  and  $c_{e0} = \sqrt{T_{e0} / m_e}$ . Dimensionless variables are represented with hat on the top:

$$\hat{z} = \frac{z}{\lambda_{De0}}, \quad \hat{t} = t \frac{c_{e0}}{\lambda_{De0}}, \quad \hat{v}_{\parallel} = \frac{v_{\parallel}}{c_{e0}}, \quad \hat{\mu} = \mu \frac{B_M}{T_{e0}}, \quad \hat{f}_{\alpha} \equiv \bar{f}_{\alpha} \frac{c_{e0}^{3/2}}{n_0}, \quad \hat{\phi} = \frac{e\phi}{T_{e0}}.$$

The typical electron and ion transit times are  $\tau_{te} = (z_D - z_0) / c_{e0}$  and  $\tau_{ti} = (z_D - z_0) / c_{s0}$ , with  $c_{s0} = \sqrt{T_{e0} / m_i}$ , while the typical electron collision time is  $\nu_e^{-1}$ . In order to reach a stationary behavior for both ions and electrons, the total simulation time  $\tau_{sim}$  must be larger than both  $\tau_{ti}$  and  $\nu_e^{-1}$ . The criterion followed here is  $\tau_{sim} \geq 2.0 \max(\tau_{ti}, \nu_e^{-1})$ , which assures a change of results below 1% in the last fourth of the simulation.

The level of e-e collisionality will be measured with the dimensionless parameter

$$\tilde{\nu}_e = \nu_e \tau_{te},$$

which is small in the weakly-collisional regime. This will be the central parameter of the present investigation. The other dimensionless parameters of the model are  $\hat{\phi}_D$ ,  $\hat{z}_0$ ,  $\hat{z}_D$ ,  $R_L / \lambda_{De0}$ ,  $m_i / m_e$  and  $T_{i0} / T_{e0}$ ; and most of them were already discussed in Ref. [89].

The baseline configuration of the simulations here takes

$$\hat{\phi}_D = -3, \quad \hat{z}_0 = -100, \quad \hat{z}_D = 400, \quad R_L / \lambda_{De0} = 50, \quad m_i / m_e = 100, \quad T_{i0} / T_{e0} = 1.$$

Thus, the computational domain includes a significant portion of the convergent segment ( $B(z_0) / B_M = 0.09$ ) and a nearly complete expansion ( $B(z_D) / B_M = 0.002$ ). The total potential drop selected corresponds approximately to a current-free plume in the weakly-collisional regime as discussed in Sec.

6.6. The unrealistically low mass ratio  $m_i/m_e = 100$  allows us saving computational resources while keeping the electron and ion time scales well-separated. The large convergent segment, not included in Ref. [89], allows to have plasma sonic conditions in a natural way around the MN throat and a better comparison with the SSK model of Ref. [4].

## 6.3 Kinetic features

### 6.3.1 Basic concepts

The formulation followed here determines the distribution function  $\bar{f}_\alpha$  in the four-dimensional phase-space  $(t, z, v_\parallel, \mu)$ . In our continuum approach and for each species  $\alpha$ , the characteristic lines  $C : [z(t), v_\parallel(t), \mu(t)]$  of the Boltzmann equation (6.2) are defined in the phase-space as satisfying

$$\frac{dz}{dt}|_C = v_\parallel, \quad \frac{dv_\parallel}{dt}|_C = a_\alpha, \quad \frac{d\mu}{dt}|_C = 0. \quad (6.11)$$

Along these lines, the variation of the distribution function is exclusively due to collisions

$$\frac{d\bar{f}_\alpha}{dt}|_C = \frac{\delta \bar{f}_\alpha}{\delta t}, \quad (6.12)$$

where the collision operator is a function in the phase-space representing the collective collisional effects. Furthermore, the energy function can be defined in the phase-space as

$$E(t, z, v_\parallel, \mu) = \frac{1}{2}m_\alpha v_\parallel^2 + B(z)\mu + Z_\alpha e\phi(t, z), \quad (6.13)$$

which satisfies

$$\frac{dE}{dt}|_C = Z_\alpha e \frac{\partial \phi}{\partial t}. \quad (6.14)$$

Therefore, the energy is constant along the characteristic lines in the steady state.

As a consequence, only in the absence of collisions and the steady state,  $\bar{f}_\alpha$  is conserved along the characteristic lines together with  $E$  and  $\mu$ . Besides, in the collisionless plasma, the trajectory of individual particles coincide with the characteristic lines being  $E$  and  $\mu$  the conserved particle energy and magnetic moment. These facts were used in Ref. [64] to take  $E$  instead of  $v_\parallel$  as a more convenient independent variable to determine  $\bar{f}_\alpha$ . Since

$$v_\parallel^\pm(z, E, \mu) = \pm \sqrt{2 \frac{E - B(z)\mu - Z_\alpha e\phi(z)}{m_\alpha}}, \quad (6.15)$$

the sign discrimination requires to split the VDF as

$$\bar{f}_\alpha(z, E, \mu) = \bar{f}_\alpha^+(z, E, \mu) + \bar{f}_\alpha^-(z, E, \mu),$$

with  $\bar{f}_\alpha^+(z, E, \mu)$  and  $\bar{f}_\alpha^-(z, E, \mu)$  the downstream ( $v_\parallel = v_\parallel^+$ ) and upstream ( $v_\parallel = v_\parallel^-$ ) parts, respectively. Applying the change of variable  $v_\parallel \rightarrow E$ , Eq. (6.12) is reduced, in the collisionless steady-state case to [86]

$$v_\parallel^\pm \frac{\partial \bar{f}_\alpha^\pm(z, E, \mu)}{\partial z} = 0, \quad (6.16)$$

i.e.  $\tilde{f}_\alpha^\pm$  are  $z$ -independent piecewise functions for a given set of  $(E, \mu)$ .

The condition  $v_\parallel = 0$  defines a maximum magnetic moment, which, for electrons, is

$$\mu_m(z, E) = \frac{E + e\phi(z)}{B(z)}, \quad (6.17)$$

such that there are no electrons with  $\mu > \mu_m(z, E)$ . Then, two critical energies are defined:  $E = e|\phi_D|$  and  $E = E^*$ , where  $E^*$  satisfies

$$\frac{\partial^2 \mu_m(z, E^*)}{\partial z^2} = 0,$$

dividing the phase-space  $(z, E, \mu)$  in three electron subpopulation regions sketched in Fig. 6.2. Examples of trajectory of individual electrons, without collisions, are plotted within the regions. For  $E < E^*$  [panel (a)], there is only one subpopulation: all electrons from the source are reflected back, at the location  $z$  where  $\mu = \mu_m(z, E)$ . For  $E^* < E < e|\phi_D|$  [panel (b)], there are two subpopulations separated by  $(z, \mu) = [z_T(E), \mu_T(E)]$  (where point T corresponds to the minimum of  $\mu_m$ ): those with  $z > z_T$  and  $\mu > \mu_T$  are trapped electrons and the rest of them are reflected ones. For  $E > e|\phi_D|$  [panel (c)], there are also two subpopulations: those with  $\mu < \mu_T$  are free electrons and those with  $\mu > \mu_T$  and  $z < z_T$  are reflected ones.

In the steady-state, collisional problem of interest here, the above three regions in the phase-space  $(z, E, \mu)$  continue to be perfectly defined and are named as free-, reflected-, and trapped-electron regions. In the particle approach, collisions will make individual electrons go in and out of these regions. In our continuum approach, the collision operator determines the flows in and out of these regions, which are balanced in the steady state.

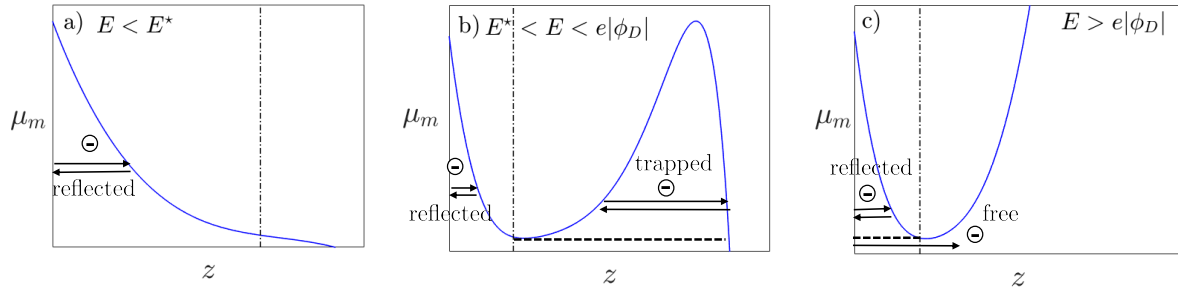


**Figure 6.2:** Cases of maximum magnetic moment  $\mu_m$  curves for electrons. Each panel represents a specific energy. The vertical dash-dot lines represent the position of the MN throat, and the horizontal dashed lines separate the subpopulation regions. Examples of trajectory of individual electrons shown are for the absence of collisions.

### 6.3.2 Effect of collisions on trapped-electron subpopulation

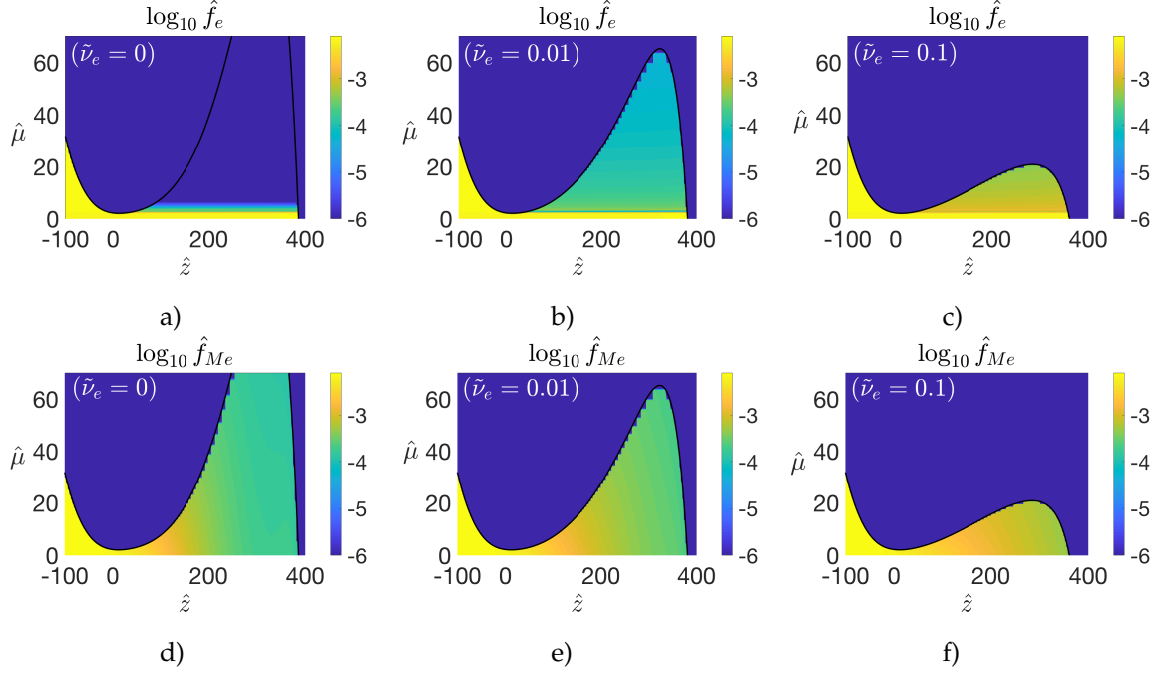


**Figure 6.3:** Steady-state electron VDF  $\hat{f}_e$  and target Maxwellian VDF  $\hat{f}_{Me}$  in the  $\mu$ - $z$  plane for the cases of  $\tilde{v}_e = 0, 0.01$  and  $0.1$ . Results are for  $E/T_{e0} = 2.85$ .

The effect of collisions on trapped-electron subpopulation is studied with the simulation settings of Sec. 6.2. Figure 6.3 (a)-(c) show the steady-state electron VDF in the  $\mu$ - $z$  plane together with  $\mu_m(z)$  curves for  $E/T_{e0} = 2.85$ . This energy satisfies  $E^* < E < e|\phi_D|$  and is convenient for analyzing the trapped-electron subpopulation. From left to right, the panels correspond to different e-e collisionalities going from collisionless case to weakly-collisional cases with  $\tilde{v}_e = 0, 0.01$  and  $0.1$ . The reflected-electron region includes the entire convergent segment and a low- $\mu$  band in the divergent one, and is practically unaffected by collisions. On the contrary, the trapped-electron region is nearly empty in the collisionless case,  $\tilde{v}_e = 0$ , and increasingly populated for larger  $\tilde{v}_e$ . In the collisionless case, only a narrow magnetic moment band above  $\mu_T$  is populated, which is filled during the transient period [89]. The BGK collision operator drives the electron VDF to a local Maxwellian VDF. Figure 6.3 (d)-(f) plot the steady-state Maxwellian VDF for the respective electron VDF shown above them. The larger the collisionality is, the more electrons are trapped, but at the same time the extension of their  $(z, \mu)$ -region gets smaller.

Figure 6.4 plots 1D vertical and horizontal cuts for the case  $\tilde{v}_e = 0.1$  of Fig. 6.3 (c) and (f). Figure 6.4 (a) plots  $\mu$ -profiles of  $\hat{f}_e^\pm$  and  $\hat{f}_{Me}^\pm$  at  $\hat{z} = 300$ , i.e. near the maximum of  $\mu_m(z)$  curve. Two  $\mu$ -regions are identified: (i)  $\mu < \mu_T$ , populated with reflected electrons, and zoomed in Fig. 6.4 (b); and (ii)  $\mu > \mu_T$ , populated with trapped electrons. Since reflected and trapped electrons are confined subpopulations and do not contribute to the macroscopic transport of magnitudes (e.g. charge or energy), one has  $\hat{f}_e^+(\mu) \approx \hat{f}_e^-(\mu)$  in spite of having  $\hat{f}_{Me}^+(\mu) \neq \hat{f}_{Me}^-(\mu)$ . On the contrary, both regions differ in the positions of  $\hat{f}_e^\pm$  relative to  $\hat{f}_{Me}^\pm$ . For trapped-electron region, collisions make  $\hat{f}_e^\pm$  to lie between  $\hat{f}_M^+$  and  $\hat{f}_M^-$ , while this is not the case for reflected-electron region, nearly unaffected by collisions.

Figure 6.4 (c) displays the  $z$ -profiles of  $\hat{f}_e^\pm$  and  $\hat{f}_{Me}^\pm$  at  $\hat{\mu} = 3$ . This line cuts the  $\mu_m(z)$  curve at  $z_r$ ,  $z_{t1}$  and  $z_{t2}$ . The region  $0 < z < z_r$  is filled with reflected electrons, and the region  $z_{t1} < z < z_{t2}$  with trapped electrons; the interval  $z_r < z < z_{t1}$  is void because  $\mu > \mu_m$ . The reflected-electron region covers nearly the entire convergent segment and is zoomed in Fig. 6.4 (d). There, the electron VDFs inherit the Maxwellian properties at the upstream source, i.e.  $\hat{f}_e^\pm \approx \hat{f}_e^\pm(z_0)$ . In the trapped-electron region,  $\hat{f}_e^\pm$  lie between  $\hat{f}_{Me}^+$  and  $\hat{f}_{Me}^-$  just as in the  $\mu$ -profiles, and we have that  $\partial \hat{f}_e / \partial \hat{z} \approx 0$  in spite of the varying  $\hat{f}_{Me}^\pm(\hat{z})$ .

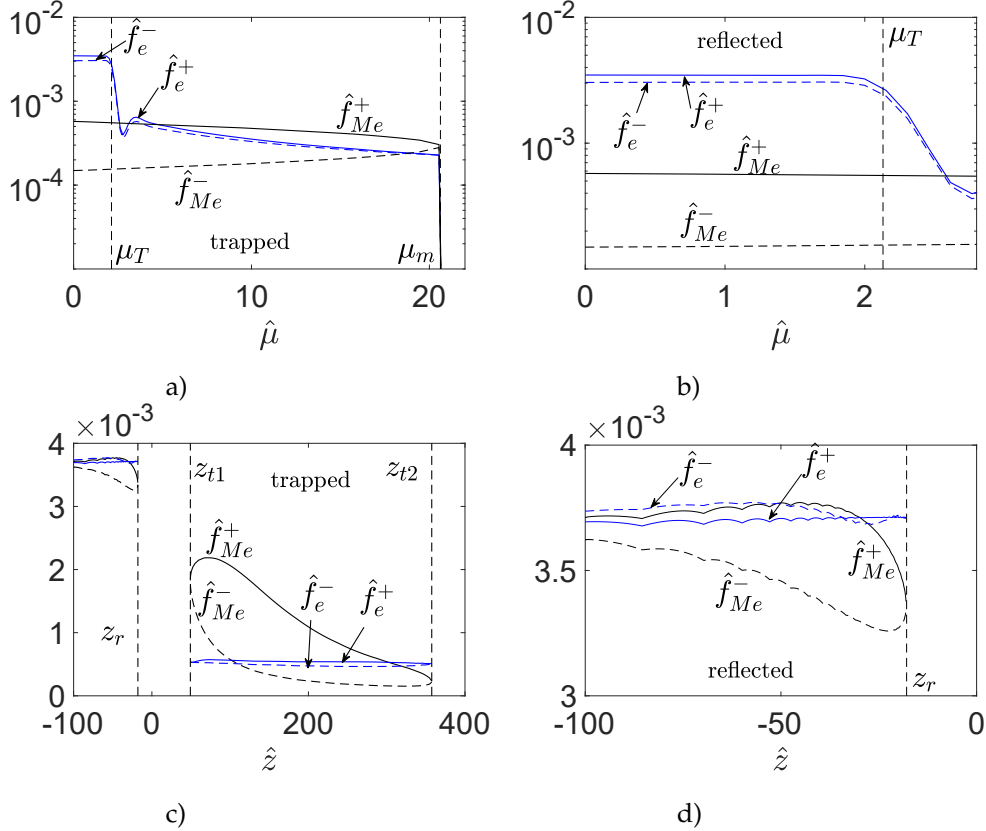


**Figure 6.4:** 1D profiles of  $\hat{f}_e^\pm$  and  $\hat{f}_{Me}^\pm$  extracted from 2D profiles of Fig. 6.3 (c) and (f) [case  $\tilde{v}_e = 0.1$  and  $E/T_{e0} = 2.85$ ]: (a)  $\mu$ -profiles at  $\hat{z} = 300$ , and (c)  $z$ -profiles at  $\hat{\mu} = 3$ ; (b) and (d) are zooms of (a) and (c), respectively.

The SSK model of Refs. [64, 4] postulates that the functional form of  $\hat{f}_e$  in trapped region was identical to the one in reflected region, which was Maxwellian-like, thus indicating that the occupancy level of trapped region was maximum. Let us define  $\langle \hat{f}_t(E) \rangle$  and  $\langle \hat{f}_r(E) \rangle$  as the average values of the VDFs in trapped and reflected regions, respectively. For  $E/T_{e0} = 2.85$ , the ratio  $\langle \hat{f}_t \rangle / \langle \hat{f}_r \rangle$  is 0.6%, 2.5% and 12.7%, for  $\tilde{v}_e = 0, 0.01$  and  $0.1$ , respectively. Similar values are obtained for other energies within  $E^* < E < e|\phi_D|$ , which implies, roughly

$$\langle \hat{f}_t \rangle / \langle \hat{f}_r \rangle \sim \tilde{v}_e \quad \text{for} \quad \tilde{v}_e \ll 1. \quad (6.18)$$

The SSK model postulates  $\langle \hat{f}_t \rangle / \langle \hat{f}_r \rangle = 100\%$  and therefore, overestimates greatly the trapped region in the weakly-collisional regime.



As seen, when collisionality increases, the trapped region is more populated but such region shrinks too, so the contribution of trapped electrons to the electron density does not necessarily increase. Figure 6.5 shows the relative contributions of the three subpopulations to  $n_e(z)$  for  $\tilde{\nu}_e = 0$  and 0.1. In the figure,  $n_t$ ,  $n_r$  and  $n_f$  correspond to trapped, reflected and free densities, respectively. The contribution of the trapped electrons increases, but much less than  $\langle \hat{f}_t \rangle / \langle \hat{f}_r \rangle$ : the maximum percentage of trapped electrons just increases from 25% to 40% for the two plotted cases. This moderate behavior of trapped electrons differs with the one in the SSK model, where  $n_t$  is, by large, the main contribution to electron density in an ample region of the divergent segment. Finally, the simulations are with the constant- $\nu_e$  BGK model, and Appendix 6.B shows one with  $\nu_e$  not constant, but varying spatially with the electron density.

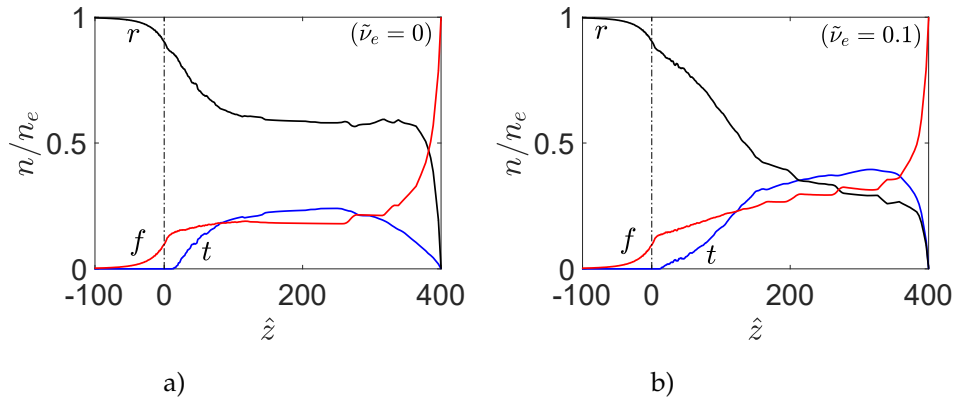


**Figure 6.5:** Steady-state density percentages of the three electron subpopulations for two cases of  $\tilde{\nu}_e$ .

## 6.4 Macroscopic response

This section analyzes the steady-state response of macroscopic magnitudes and the momentum and energy balances for each species. Results here will be compared with the collisionless case of Ref. [89] and the alternative SSK model of Ref. [4].

### 6.4.1 Spatial profiles

Figure 6.6 shows the spatial profiles of main macroscopic plasma magnitudes. Results are presented again for the collisionless and weakly-collisional cases with  $\tilde{\nu}_e = 0, 0.01$  and 0.1. The inclusion here of a large convergent segment facilitates the comparison with Ref. [4] and differs from Ref. [89], where (practically) just the divergent segment was considered. In particular, conditions at the MN throat differ substantially. With the e-e collisionality changing, the potential, Fig. 6.6 (a), shows differences in the divergent segment caused by the different amount of trapped electrons. Collisionality favors a smoother potential drop and reduces the extension of the non-neutral region next to the downstream boundary  $z_D$ , Fig. 6.6 (c). (As pointed out in Ref. [89], the non-neutral region is somehow ‘artificial’, a result of bringing the final potential at infinity to  $z_D$ . The further downstream  $z_D$  is located, the plasma solution in quasineutral region does not change, and extends further downstream.) Collisionless ions are closely driven by the potential as  $n_i$  and  $u_i$  show, Fig. 6.6 (b) and (d). Thanks to the convergent segment, ion macroscopic velocity becomes sonic around the throat; to this respect, notice that the

macroscopic model of the next subsection is not complete enough to define an exact sound velocity for the ion collisionless fluid. Potential and plasma density at the throat are similar to those obtained in Ref. [4],  $e\phi_M/T_{e0} = -0.6$  and  $n_{iM}/n_0 = 0.52$ , and corresponds approximately to a Maxwell-Boltzmann relation,  $n_i/n_0 \approx \exp(e\phi/T_{e0})$ , in the convergent segment.

The initially temperature-isotropic ions, Fig. 6.6 (e), become strongly anisotropic along the convergent segment due to the magnetic mirror as in Ref. [4], having  $T_{\parallel iM}/T_{e0} = 0.3$  and  $T_{\perp iM}/T_{e0} = 1.29$  at the throat. The behaviour in the divergent segment is also equivalent to the one found in Ref. [4], with a near-constant  $T_{\parallel i}$  ( $T_{\parallel iD}/T_{e0} = 0.19$ ) and a rapidly decaying  $T_{\perp i}$ . The profiles of the electron temperature, Fig. 6.6 (f), follow the main trends of those in Ref. [4], being near-isothermal and near-isotropic in the convergent segment ( $T_{\parallel eM}/T_{e0} = 0.84$  and  $T_{\perp eM}/T_{e0} = 0.9$ ). In the divergent segment, strong anisotropy is developed,  $T_{\parallel e}$  decays to a non-zero value ( $T_{\parallel eD}/T_{e0} = 0.43$ ), while  $T_{\perp e}$  decays to zero. Interestingly, larger collisionality means more trapped electrons, and these tend to decrease noticeably  $T_{\parallel e}$  and increase slightly  $T_{\perp e}$  resulting in less anisotropy and a smaller mean temperature  $T_e$ . Indeed, the electron temperature is much less anisotropic and  $T_e$  is much smaller in Ref. [4], where more trapped electrons are found.

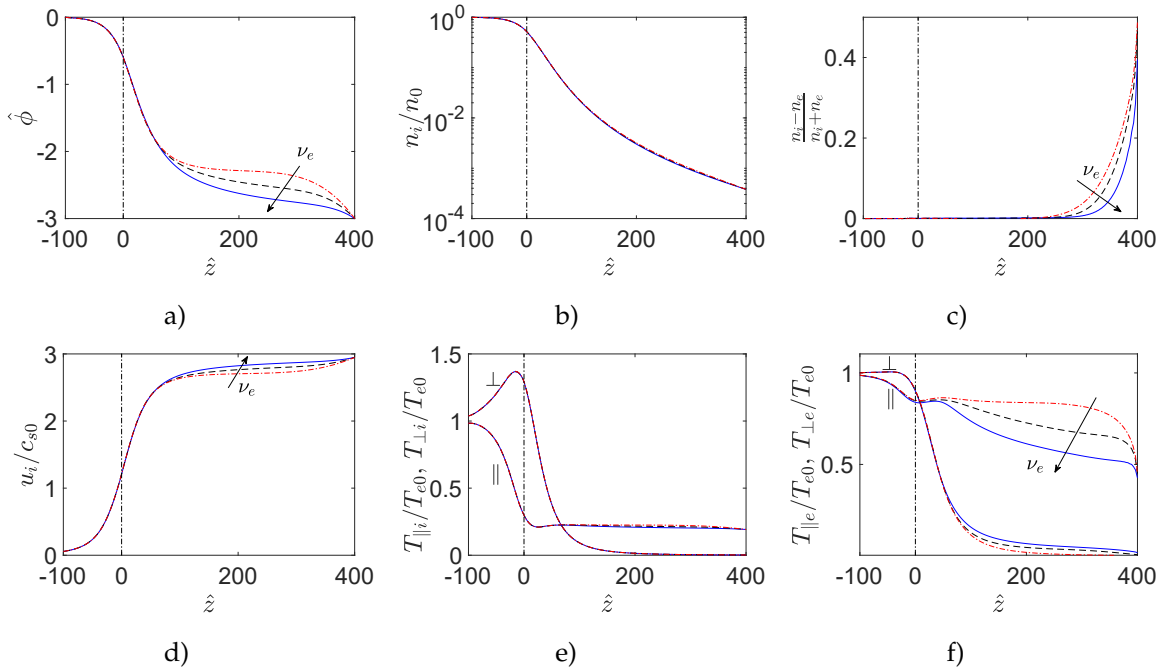


**Figure 6.6:** Steady-state spatial profiles of macroscopic plasma magnitudes. Curves correspond to three cases of  $\tilde{\nu}_e$ : 0 (---), 0.01 (-.-.-) and 0.1 (—).

Figure 6.7 shows, for the case  $\tilde{\nu}_e = 0.1$ , the temperatures of the three electron subpopulations treated as independent species. Different behaviors are observed for each one. Interestingly, the trapped subpopulation is nearly isotropic, while the free and reflected ones are anisotropic. Besides, the free subpopulation has a larger velocity dispersion than the two confined subpopulations. The temperature of the whole electron species is determined by the dominant subpopulation. Here, only free electrons reach  $z_D$  and which explains that  $T_{eD} \simeq T_{fD}$ . Since the free electrons are nearly unaffected by collisions, the values of the temperature at  $z_D$  are independent of collisionality [Fig. 6.6 (f)]. On the other hand,

in Ref. [4], where the trapped electrons still dominates downstream, the electrons have that  $T_{eD} \simeq T_{tD}$  being much more isotropic and cooler.

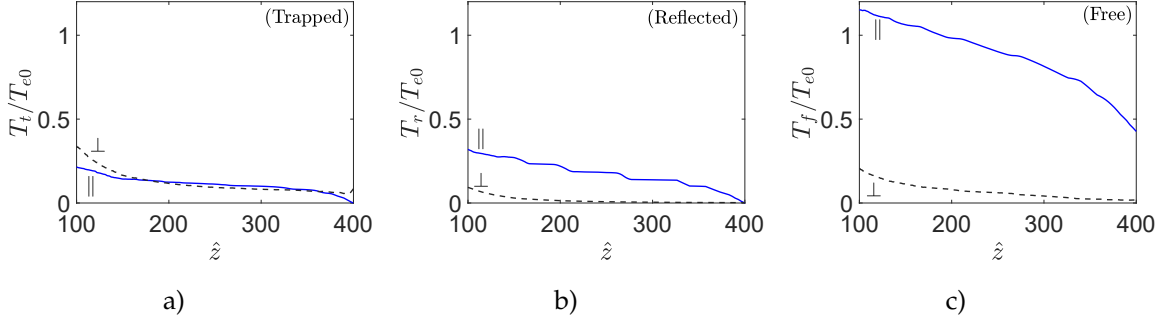


**Figure 6.7:** Parallel and perpendicular electron temperatures for each electron subpopulation [case  $\tilde{v}_e = 0.1$ ]. Notice that, locally, free and reflected electrons have practically the same ratio  $T_{\perp}/T_{\parallel}$ .

As a summary, Table 6.1 compares downstream results from the present study (case  $\tilde{v}_e = 0.1$ ) with those of the SSK model in Ref. [4], for identical upstream plasma sources and near-zero net current. The just commented difference on  $T_{eD}$ , caused by different amounts of trapped electrons, is the main discrepancy and, as it will be seen below, explains the difference in  $q_{eD}$ . The SSK model was compared with experimental data of MNs for particular thrusters in Ref. [24]. The main plasma profiles showed good agreement except for the electron cooling, which was too large in the SSK model. The more moderate electron cooling obtained with VLASMAN fits better with the experimental trends.

Variable	VLASMAN	SSK model
$\hat{\phi}_D$	-3.0	-3.2
$I/I_0$	-0.05	0
$I_i/I_0$	0.61	0.59
$u_{iD}/c_{s0}$	2.9	3.0
$\varepsilon_e/T_{e0}$	4.2	4.5
$\varepsilon_i/T_{e0}$	1.6	1.7
$T_{\parallel eD}/T_{e0}$	0.43	0.07
$T_{\parallel iD}/T_{e0}$	0.19	0.11
$T_{\perp eD}/T_{e0}$	$\sim 0$	$\sim 0$
$T_{\perp iD}/T_{e0}$	$\sim 0$	$\sim 0$
$q_{eD}/n_{eD}u_{eD}T_{e0}$	0.2	1.2
$q_{iD}/n_{iD}u_{iD}T_{e0}$	$\sim 0$	$\sim 0$

**Table 6.1:** Comparison of results between VLASMAN (case  $\tilde{v}_e = 0.1$ ) and the SSK model of Ref. [4]. Species currents are defined in Eq. (6.19),  $I_0 = en_0c_{s0}A_M$  and  $I = I_e + I_i$ . Species energies are defined in Eq. (6.21).

#### 6.4.2 Momentum and energy balances

The macroscopic plasma equations are obtained from Boltzmann equation's integral velocity moments. For the present BGK collision operator (intraspecies collisions), no sources are introduced for charge,

momentum and energy. The resulting equations are the same collisionless ones of Ref. [89], which in the steady state for species  $\alpha = i, e$  are

$$I_\alpha = eZ_\alpha n_\alpha u_\alpha A = \text{const}, \quad (6.19)$$

$$m_\alpha n_\alpha u_\alpha \frac{\partial u_\alpha}{\partial z} + Z_\alpha e n_\alpha \frac{\partial \phi}{\partial z} + \frac{\partial p_{\parallel\alpha}}{\partial z} + (p_{\perp\alpha} - p_{\parallel\alpha}) \frac{d \ln B}{dz} = 0, \quad (6.20)$$

$$\left( Z_\alpha e \phi + \frac{m_\alpha}{2} u_\alpha^2 + \frac{3}{2} T_{\parallel\alpha} + T_{\perp\alpha} + \frac{q_\alpha}{n_\alpha u_\alpha} \right) n_\alpha u_\alpha A = \text{const} = \varepsilon_\alpha n_\alpha u_\alpha A. \quad (6.21)$$

Equation (6.19) expresses the conservation of the species current. The momentum equation (6.20), which cannot be reduced to a first integral, includes the axial components of  $\nabla \cdot \bar{\bar{p}}_\alpha$ :  $\partial p_{\parallel\alpha} / \partial z$  and  $(p_{\perp\alpha} - p_{\parallel\alpha}) d \ln B / dz$ , the latter is the macroscopic magnetic mirror force and is relevant only if the pressure is anisotropic. Equation (6.21) is the conservation of the total energy flow, which includes: the flow of kinetic energy, the convective flow of internal energy and the heat flow (or diffusive flow of internal energy), and also the flow of potential energy. Naturally, the total energy ‘per particle’  $\varepsilon_\alpha$  is conserved too. (The energy per particle,  $\varepsilon_\alpha - Z_\alpha e \phi$  (excluding the potential energy), is not conserved however.)

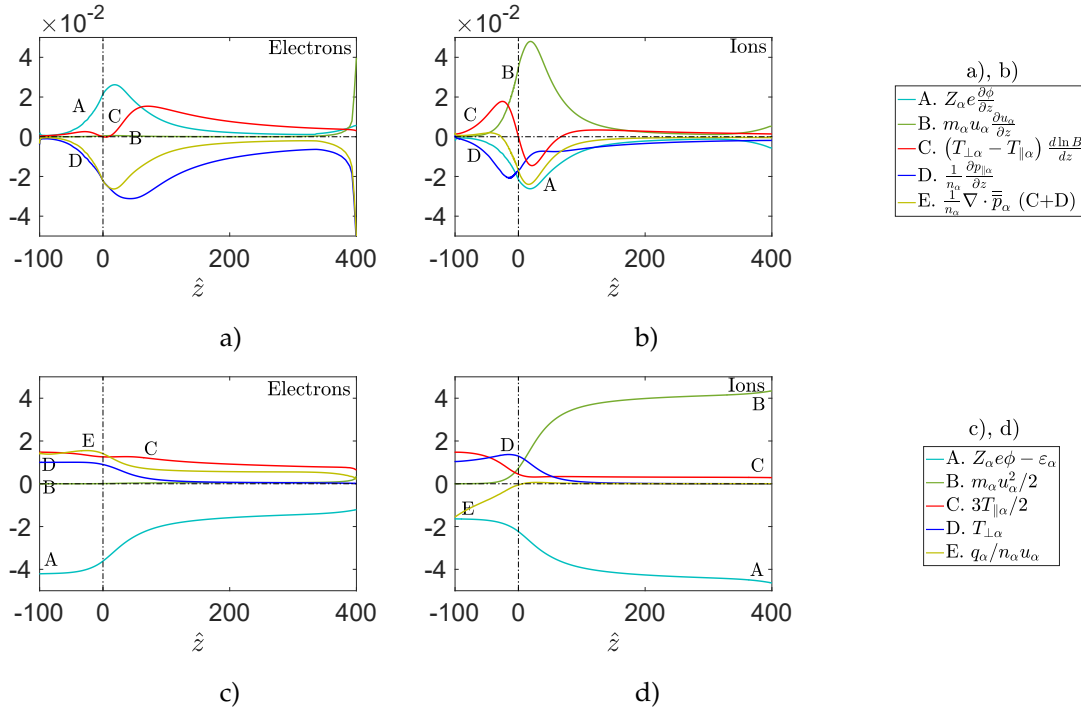


**Figure 6.8:** Balances of (a)-(b) momentum and (c)-(d) energy ‘per particle’ for  $\tilde{v}_e = 0.1$ . Units in (a)-(b) are referred to  $T_{e0}/\lambda_{De0}$  and in (c)-(d) to  $T_{e0}$ . Momentum and energy corresponds to Eqs. (6.20) and (6.21), divided over  $n_\alpha$  and  $n_\alpha u_\alpha A$ , respectively. These results are for  $T_{i0} = T_{e0}$ .

Figure 6.8 analyzes the contributions (per particle) of the different terms in momentum and energy equations for both species and case  $\tilde{v}_e = 0.1$ . Notice that for the energy equation of each species, the magnitude  $Z_\alpha e \phi - \varepsilon_\alpha$  is used so that the sum of the plotted contributions is zero. The electron momentum, panel (a), shows a balance between the electric force and the pressure tensor divergence. The two

contributions to this last force have different signs. The macroscopic magnetic mirror force, which is proportional to the temperature anisotropy, is here larger than in Ref. [4]. The downstream electric force is small compared with the individual contributions of the pressure tensor. With respect to ions, panel (b), the individual contributions to the ion pressure tensor divergence dominate in the convergent segment. In the divergent segment, both the electric force and the total pressure force contribute similarly to the increase of ion momentum.

For the plotted case in panels (c) and (d), since  $\phi(z_0) = 0$  and kinetic energies are negligible upstream, the average energies per ion and electron are  $\varepsilon_i = 1.6T_{e0}$  and  $\varepsilon_e = 4.2T_{e0}$ , which represent the thermal energies of ions and electrons upstream. As  $T_{i0} = T_{e0}$ , the differences between the values is due to the 'diffusive' contributions per flowing particle,  $q_\alpha/n_\alpha u_\alpha$ , negative for ions and positive for electrons. Along the expansion, the variation of potential energy reduces the thermal energy of electrons to a final non-zero value  $\varepsilon_e + e\phi_D = 1.2T_{e0}$ , while the MN transforms both the upstream thermal energy of ions and the thermal energy lost by electrons into kinetic energy, until the downstream value  $\varepsilon_i - e\phi_D = 4.6T_{e0}$  (i.e about 1/3 and 2/3 coming from, respectively, ion and electron thermal energy). The potential energy terms vanish when an electron/ion pair is considered. The upstream plasma thermal energy is  $5.8 T_{e0}$ , and downstream, still  $1.2 T_{e0}$  (about 20%) is thermal. Table 6.1 compares these results with the ones of Ref. [4] showing similar general trends. The main difference is that, given a similar total energy flow for electrons downstream, those flows are distributed in a different way. Here, a much higher  $T_{eD}$  (smaller electron cooling) implies a larger convective flow and consequently a lower diffusive flow.

## 6.5 On closure laws for electron heat flux

As it is well-known, the successive macroscopic equations derived from velocity moments of the Boltzmann equation include terms of next-order. In the case of the set of Eqs. (6.19)-(6.21), these are the heat fluxes for ions and electrons, which turn out to be important contributions in certain regions of the MN. The main concern is with the electron heat flux in the divergent MN, due to its relevance in the far expansion of plasma plumes. In order to assess the strong influence of the collisionality on the heat flux, the condition  $\tilde{\nu}_e \ll 1$  is relaxed in the analysis here, although the high-magnetization condition  $\nu_e \ll \omega_{ce}$  is formally maintained. Fig. 6.9 shows the spatial variation of the heat flow for different  $\tilde{\nu}_e$ . The heat flux changes little while in the weakly-collisional regime, but then decreases much (since the VDF evolves to a Maxwellian, which has  $q_e = 0$ ).

The need of postulating a closure relation of the energy equation, external to the Boltzmann equation, was already discussed in Ref. [4]. It was concluded that a Fourier type law was not adequate, while a convective law, with  $q_e \propto n_e u_e T_e$ , could fit well with the exact solution 'on average' but not locally. Furthermore, it was shown that this type of law was equivalent to a polytropic electron behavior. Here, a combined convective-plus-diffusive law of the form

$$q_e = \bar{\alpha} n_e T_e u_e - \bar{\beta} \frac{5n_e T_e}{2m_e \nu_e} \frac{dT_e}{dz} \quad (6.22)$$

is investigated, where coefficients  $\bar{\alpha}$  and  $\bar{\beta}$  are fitted with a least-square method applied only on the divergent MN profiles. This law is compared with two others: a purely-convective one with  $\bar{\beta} = 0$  and fitting only for  $\bar{\alpha}$ ; and a purely-diffusive one with  $\bar{\alpha} = 0$  and fitting only for  $\bar{\beta}$ .

Figure 6.10 shows the results of the three approximate heat flux laws for different collisionalities. Figure 6.10 (a)-(b) depict  $\bar{\alpha}$  and  $\bar{\beta}$ , while Fig. 6.10 (d)-(i) show the three fitting heat flux-profiles compared to the exact profile. The combined heat flux law yields, of course, the best fitting. In the weakly-collisional regime, one has  $\bar{\alpha} \approx 2.1$  and  $\bar{\beta} \ll 1$ . Parameter  $\bar{\beta}$  remains negligible up to  $\tilde{v}_e \sim 1$ , while  $\bar{\alpha}$  decreases moderately to  $\bar{\alpha} \approx 1.4$ . For  $\tilde{v}_e > 1$ ,  $\bar{\beta}$  starts to increase from near-zero and reaches  $\bar{\beta} \approx 1$  at  $\tilde{v}_e \sim 100$ , when  $\bar{\alpha}$  has decreased to near-zero.

Observing in Fig. 6.10 (d)-(i) the profiles for the three fittings, we conclude that a purely-convective law (i.e. with  $\bar{\beta} = 0$ ) is a suitable choice from  $\tilde{v}_e \ll 1$  to up, say,  $\tilde{v}_e \sim 10$ . A crude collision-dependent law for  $\bar{\alpha}$  would be

$$\bar{\alpha} \approx \begin{cases} 1.9 & \text{for } \log_{10} \tilde{v}_e < -1 \\ 1.3 - 0.6 \log_{10} \tilde{v}_e & \text{for } -1 < \log_{10} \tilde{v}_e < 1 \end{cases}. \quad (6.23)$$

For  $\tilde{v}_e \geq 10$ , and into the highly-collisional regime, a purely-diffusive law (i.e. with  $\bar{\alpha} = 0$ ) seems adequate with  $\bar{\beta}$  following, roughly,

$$\bar{\beta} \approx \begin{cases} 0.5 \log_{10} \tilde{v}_e & \text{for } 1 < \log_{10} \tilde{v}_e < 2 \\ 1 & \text{for } \log_{10} \tilde{v}_e > 2 \end{cases}. \quad (6.24)$$

These two fittings, valid for the crude constant- $\nu_e$  BGK model, are just illustrative of the tendencies of  $\bar{\alpha}$  and  $\bar{\beta}$  with the collisionality.

The double-parameter fitting has confirmed the proposal from Ref. [4] of a convective law in the weakly-collisional regime, while showing the transition to a diffusive law as collisionality increases. Reference [4] also pointed out that the convective law is equivalent to assuming an electron state law  $p_e \propto n_e^{\bar{\gamma}}$  with a polytropic coefficient

$$\bar{\gamma} = \frac{5 + 2\bar{\alpha}}{3 + 2\bar{\alpha}}. \quad (6.25)$$

In fact, a more appealing interpretation of the electron gas behavior, well aligned with classical thermodynamics, is that the electron gas has an specific enthalpy  $h_e = T_e \bar{\gamma} / (\bar{\gamma} - 1)$  such that Eq. (6.21), ignoring the small kinetic energy, can be expressed as

$$\left[ \left( -e\phi + \frac{\bar{\gamma}}{\bar{\gamma} - 1} T_e \right) n_e u_e - \bar{\kappa} \frac{\partial T_e}{\partial z} \right] A \simeq \text{const} = \varepsilon_e n_e u_e A, \quad (6.26)$$

where  $\bar{\kappa} = \bar{\beta} 5 n_e T_e / 2 m_e \nu_e$  represents the thermal conductivity. This interpretation considers that the monoatomic gas does not behave like a collisional monoatomic one (with  $\bar{\gamma} = 5/3$ ) but as a gas mixture, which indeed is the case: a mixture of the free, reflected and trapped subpopulations. The effective specific heat ratio  $\bar{\gamma}$  is shown in Fig. 6.10 (c). In the weakly-collisional limit, the electron gas expands near-adiabatically with  $\bar{\gamma} \approx 1.28$ , a value slightly larger than experimental estimates [24, 60, 51] because of the artificially low mass ratio; the studies of Refs. [4, 70] with a polytropic index  $\bar{\gamma}$  show this to depend on the propellant mass ratio and upstream plasma conditions. As the electron gas becomes collisional,  $\bar{\gamma}$  increases (with an evolution towards  $5/3$ ) and a diffusive heat flux appears to accompany the specific enthalpy, with the effective collision frequency given in  $\bar{\kappa}$  by  $\nu_e / \bar{\beta}$ .

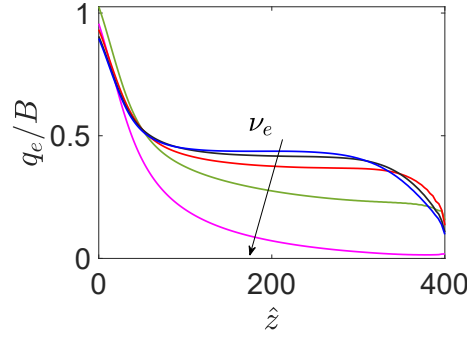


**Figure 6.9:** Heat flux in the divergent MN for increasing  $\tilde{\nu}_e$ : 0, 0.01, 0.1, 1 and 10. Units are referred to  $n_0 T_{e0} c_{s0} / B_M$ .

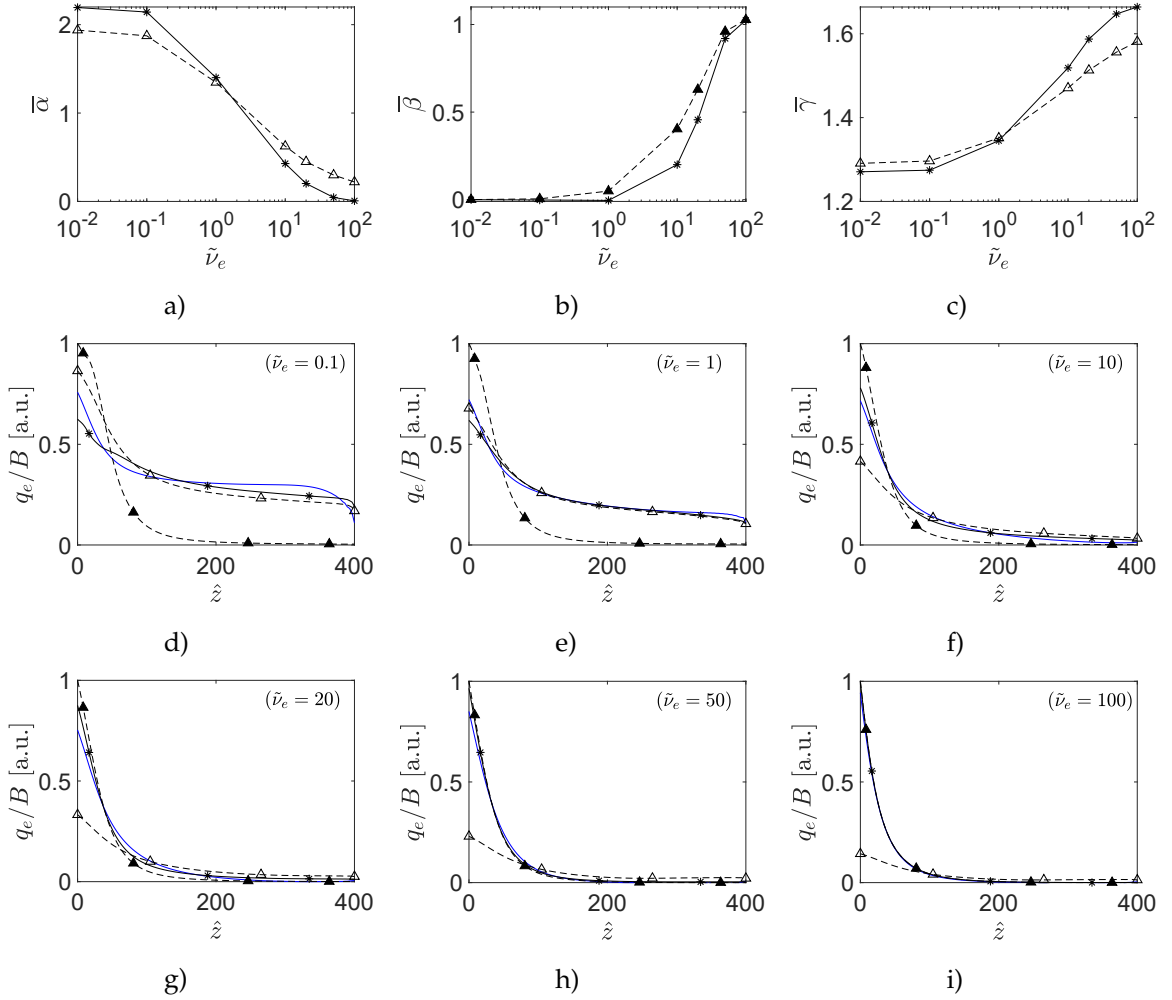


**Figure 6.10:** (a)-(c) Direct and derived coefficients (defined in the main text) obtained fitting for three heat flux laws: combined convective-plus-diffusive law (—\*—), purely-convective law (- -  $\triangle$  - -) and purely-diffusive law (- -  $\blacktriangle$  - -). (d)-(i) Heat flux-profiles from the three laws versus the exact profile (—) for six cases of  $\tilde{\nu}_e$ .

## 6.6 On the total potential drop

In the most natural formulation of the problem, the total potential drop  $|\hat{\phi}_D|$  is a boundary condition, while the ion and electron currents,  $I_i$  and  $I_e$ , are outputs. Once the steady state is reached, these two currents and the net current,  $I = I_i + I_e$ , are constant along the expansion as stated by Eq. (6.19). Figure 6.11 plots the currents  $I_i$  and  $I$ , which have been non-dimensionalized with  $I_0 = en_0 c_{s0} A_M$ , versus e-e collisionality and two different  $|\hat{\phi}_D|$ . The ion current in panel (a) is, quite obviously, independent of  $\tilde{\nu}_e$ , but it is also independent of  $|\hat{\phi}_D|$ : ions are freely accelerated within the divergent MN so the potential drop does not control their flow. However, the potential drop regulates tightly the electron current, by reflecting back a certain (large) fraction of electrons and letting a certain (small) fraction of free electrons to reach the end of the domain. This flow control is clearly observed in panel (b), where  $|I_e| = |I - I_i|$  decreases with  $|\hat{\phi}_D|$ . For  $|\hat{\phi}_D|$  fixed, the rate of variation of  $I_e$  with collisionality is practically negligible in the weakly-collisional regime, and starts to be significant once in the collisional regime.

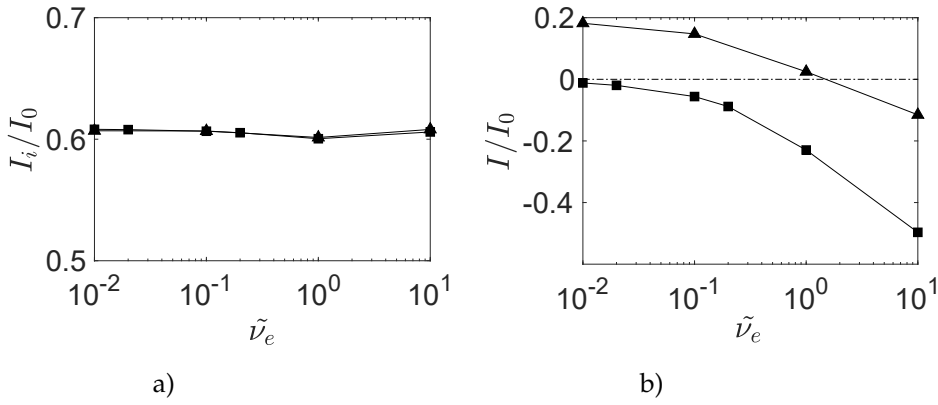


**Figure 6.11:** (a) Total ion current (b) and total net current versus  $\tilde{\nu}_e$  for two values of total potential drop  $\hat{\phi}_D$ :  $-3$  (—■—) and  $-3.5$  (—▲—).

In most cases of interest, plasma plumes are current-free, i.e.  $I = 0$ . To set this as a boundary condition implies  $|\hat{\phi}_D|$  to become an eigenvalue of the problem. For instance, a current-free plume has  $|\hat{\phi}_D| \approx 3, 3.1, 3.5$  and  $3.7$  for, respectively,  $\tilde{\nu}_e \sim 0.01, 0.1, 1$  and  $10$  in the cases shown above in Fig. 6.11. Then, an efficient way to proceed would be to adjust  $\phi_D(t)$  dynamically along the simulation, but there were concerns that this dynamical adaptation could modify the amount of trapped subpopulation and thus the steady-state solution. In fact this was the case in the collisionless simulations of Ref. [89]. In order to assess this issue when collisions are present, we proceed as in Ref. [89] and run the same case with two different temporal laws for the total potential drop:  $\phi_D^{(1)}(t) = \phi_{Df}$  and

$$\phi_D^{(2)}(t) = \phi_{Di} + \frac{\phi_{Df} - \phi_{Di}}{2} \left( 1 + \frac{2}{\pi} \arctan \frac{t - t_s}{\tau_s} \right). \quad (6.27)$$

If an appropriate value of  $\tau_s$  is used,  $\phi_D^{(2)}$  is almost equal to  $\phi_{Di}$  until time  $t_s$ . Afterwards,  $\phi_D^{(2)}$  transits smoothly to  $\phi_{Df}$ . This test has been carried out with similar values to those in Ref. [89]:  $t_s = 4\tau_{te}$ ,  $\tau_s = 0.02\tau_{te}$ ,  $e\phi_{Di} = -T_{e0}$  and  $e\phi_{Df} = -3T_{e0}$ , and a collisionality of  $\tilde{\nu}_e = 0.1$  within the weakly-collisional regime. The plasma evolution in the two simulations are different but both converged to the same steady state, as shown in Fig. 6.12. Panel (a) depicts the  $z$ -profile of the relative density ratio of



trapped electrons at two different instants,  $t_s$  and steady state. Panel (b) shows the evolution of some macroscopic magnitudes at  $\hat{z} = 300$ : parallel electron temperature and potential. Simulations with other temporal laws for  $\phi_D$  have been tried with similar conclusions. Thus, collisions, even if scarce, erase the transient response and lead to a unique steady-state solution.

After we have confirmed this uniqueness, there is more freedom in setting the downstream boundary condition. One case of clear practical interest is to impose a current-free condition to the plasma beam and to iterate on a varying  $\phi_D(t)$  until convergence at steady state. Furthermore, alternative ways to implement the downstream boundary condition, such as the one proposed in Ref. [58] (in a different but assimilable context), can be attempted too.

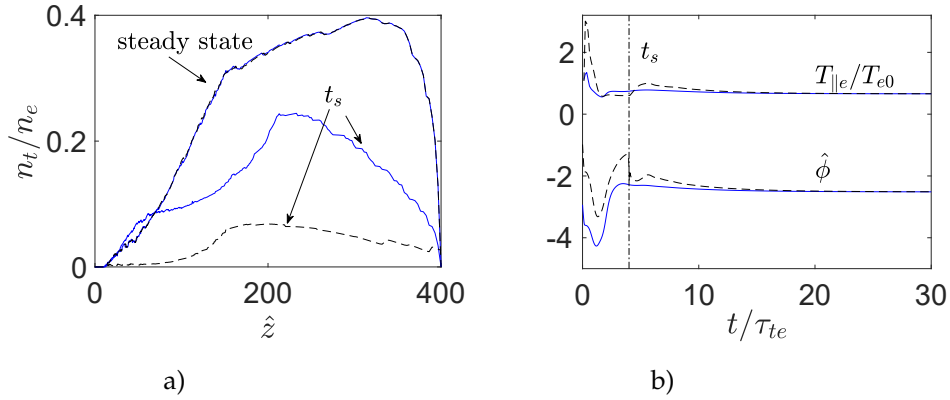


**Figure 6.12:** Simulation results with two different temporal laws for  $\phi_D$ :  $\phi_D^{(1)}$  (—) and  $\phi_D^{(2)}$  (- - -), which are defined in the main text. Both of the cases are run with e-e collisions for  $\tilde{\nu}_e = 0.1$ . Results shown are: (a) spatial profile of  $n_t/n_e$  at  $t_s$  and steady state, and (b) temporal evolution of  $\phi$  and  $T_{\parallel e}$  at  $\hat{z} = 300$ .

## 6.7 Conclusions

Direct kinetic simulations of the Boltzmann-Poisson problem with a BGK collision operator have been used to study the transient and steady-state expansion in a paraxial magnetic nozzle of a plasma with weak intraspecies electron collisions. A central goal has been to determine the relative density ratio of trapped electrons contained in a phase-space region isolated from the upstream plasma source and the downstream vacuum and to compare it with: (i) the very low occupancy obtained in the collisionless, time-dependent model of Sánchez-Arriaga et al. and; (ii) the full occupancy postulated in the SSK model of Martínez-Sánchez, Ahedo and coworkers. Simulations show that the maximum density ratio increases moderately from 25% to 35-45% within the weakly-collisional regime, with occupancy levels of the trapped region from 0.6% to 10-20%. These numbers are far from the full occupancy and the dominance of trapped electrons of the SSK model in the divergent MN.

Simulations have been run to show that collisions erase the transient history, and thus, in contrast to the collisionless case, the steady-state solution is unique. This will allow in future work to set the steady-state net current of the plasma beam (for instance, to zero), by adapting in a transient period the total potential drop.

Spatial profiles of plasma macroscopic magnitudes show that the effect of occasional collisions is felt only through the density of trapped electrons in the divergent MN. Consequently the convergent MN is unaffected, while the potential drop in the divergent MN moves upstream. The parallel and perpendicular temperatures of ions and electrons follow similar general trends to the SSK model. Interestingly, the electron subpopulations present different velocity dispersions: trapped electrons are rather isotropic and cold, reflected electrons are anisotropic and cold, while free electrons are anisotropic and hotter. The resulting temperatures of the whole electron species reflect these features, weighed with their partial densities. This explains that here, with free electrons dominating downstream, the electron temperature is much more anisotropic and the cooling is much milder than in the SSK model.

The macroscopic balances of momentum and energy are also similar in general lines to those from the SSK model. The main differences come from the different electron temperature anisotropy and cooling. In electron momentum, here the macroscopic magnetic mirror force is larger. In electron energy, here since the convective flux of thermal energy is larger, the diffusive flux is necessarily smaller.

Finally, the issue of a closure law for the heat flux has been revisited investigating the electron gas response for different collisionalities. The conclusion is that electrons behave as a ‘gas mixture’ (of free, reflected, and trapped subpopulations) with an effective specific heat ratio, and follow a Fourier heat flux law defined with an effective collision frequency. In the weakly-collisional limit, the gas mixture is near-adiabatic. In the highly-collisional limit, the gas behaves as monoatomic and the classical Fourier heat flux law is recovered.

## 6.A Numerical scheme

The simulations have been carried out with an updated version of the code VLASMAN. The numerical scheme from Ref. [89] is extended to implement the collision operator defined in Eq. (6.7), and the main changes are shortly explained. The Boltzmann equation (6.2) is solved with a second-order splitting method [18, 92]. This method, given the VDFs at time  $t$ , advances them to  $t + \Delta t$ , for each  $\mu$  as

$$\bar{f}_\alpha(t + \Delta t, z, v_\parallel) = \mathcal{C}^{1/2} \mathcal{S}^{1/2} \mathcal{F}^1 \mathcal{S}^{1/2} \mathcal{C}^{1/2} \bar{f}_\alpha(t, z, v_\parallel). \quad (6.A.1)$$

The operators  $\mathcal{C}$ ,  $\mathcal{S}$  and  $\mathcal{F}$  solve, respectively, for  $\nu_\alpha(\bar{f}_{M\alpha} - \bar{f}_\alpha)$ ,  $-v_\parallel \partial \bar{f}_\alpha / \partial z$  and  $-a_\alpha \partial \bar{f}_\alpha / \partial v_\parallel$ . Super-scripts in the operators, 1/2 and 1, indicate time steps of, respectively,  $\Delta t/2$  and  $\Delta t$ .

The collisional part of Eq. (6.A.1) is the novel one and the collision operator is defined with a Crank-Nicolson method following Ref. [27],

$$\mathcal{C}^{1/2} \bar{f}_\alpha(t, z, v_\parallel) = \bar{f}_\alpha(t, z, v_\parallel) + \frac{\nu_\alpha \Delta t}{2 + \nu_\alpha \Delta t} \left[ \bar{f}_{M\alpha}(t, z, v_\parallel) - \bar{f}_\alpha(t, z, v_\parallel) \right]. \quad (6.A.2)$$

Notice that if  $\nu_\alpha = 0$  then the operator is consistent since  $\bar{f}_\alpha$  is not modified.

The streaming and force operators ( $\mathcal{S}^{1/2} \mathcal{F}^1 \mathcal{S}^{1/2}$ ) are the same as in Ref. [89] with

$$\mathcal{S}^{1/2} \bar{f}_\alpha(t, z, v_\parallel) = \bar{f}_\alpha(t, z - v_\parallel \Delta t/2, v_\parallel), \quad (6.A.3)$$

$$\mathcal{F}^1 \bar{f}_\alpha(t, z, v_\parallel) = \bar{f}_\alpha(t, z, v_\parallel - a_\alpha \Delta t). \quad (6.A.4)$$

The electric field in  $a_\alpha$  of the force operator is found by solving Poisson equation with the densities computed from  $S^{1/2}C^{1/2}\bar{f}_\alpha$ .

The operators above are applied on the phase-space defined by  $z$ ,  $v_\parallel$  and  $\mu$ . As explained in Ref. [89], a non-uniform mesh of  $N_z$  points between  $z_0 \leq z \leq z_D$  that keeps constant the ratio mesh resolution-local Debye length is used, and an uniform one of size  $N_{v_\parallel} \times N_\mu$  is used for velocity space. The latter mesh is truncated with  $-v_{max}^\alpha \leq v_\parallel \leq v_{max}^\alpha$  and  $0 \leq \mu \leq \mu_{max}^\alpha$ , where the limits  $v_{max}^\alpha$  and  $\mu_{max}^\alpha$  are selected large enough. Here, after including the convergent MN and with the addition of collisions, high- $\mu$  reflected and trapped subpopulations are, respectively, injected and generated. Since they coexist with the low- $\mu$  free subpopulations, an uniform  $\mu$ -mesh with enough points that reproduce correctly the dynamics of all subpopulations is not computationally feasible. Thus, as alternative we use a grid with a uniform part from  $0 \leq \mu \leq \mu_{max1}^\alpha$  for free subpopulations and a non-uniform one from  $\mu_{max1}^\alpha \leq \mu \leq \mu_{max}^\alpha$  for reflected and trapped subpopulations, where an intermediate limit  $\mu_{max1}^\alpha$  is introduced and selected properly.

## 6.B A density-dependent collision frequency

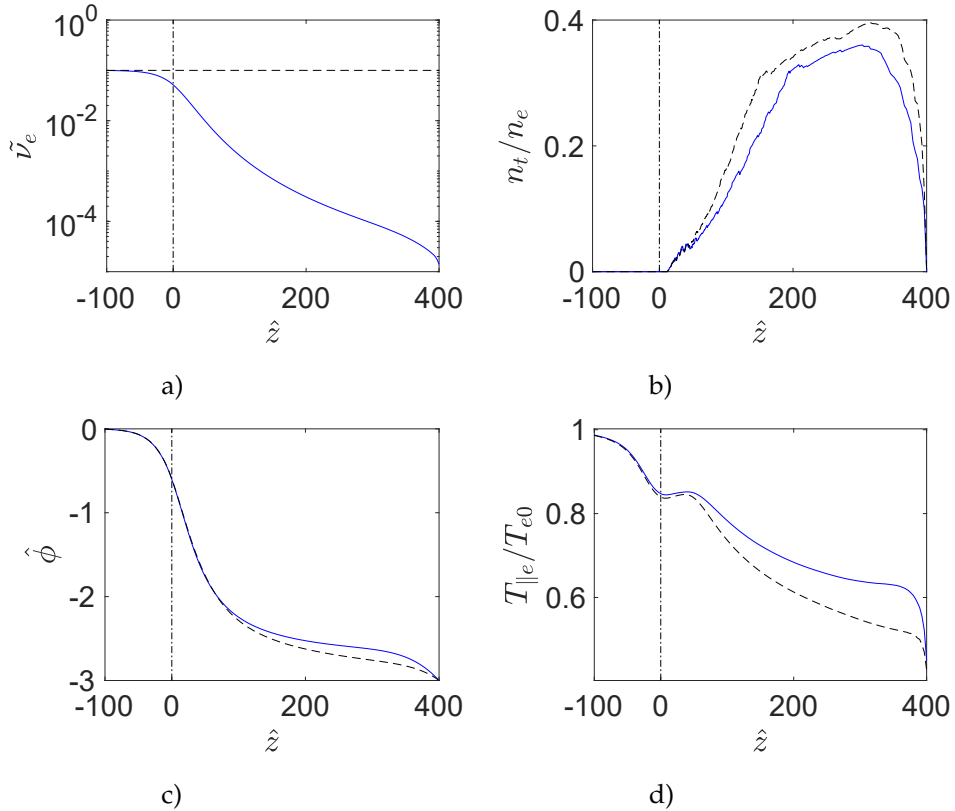


**Figure 6.B.1:** Simulation results of some plasma spatial profiles for a spatially dependent e-e collision frequency  $\tilde{v}_e = 0.1n_e(z)/n_0$  (—), and a constant one  $\tilde{v}_e = 0.1$  (- - -).

In this work, the simplest BGK collisional operator with a constant e-e collision frequency has been used. In order to validate the robustness of the results, and without aiming to enter into the full complexity, a simulation with  $\tilde{v}_e$  proportional to the local electron density is presented here. Figure 6.B.1

shows some results for  $\tilde{\nu}_e = 0.1n_e(z)/n_{e0}$  and compared them to those with  $\tilde{\nu}_e = 0.1$ . In spite of the quick decay of  $\tilde{\nu}_e$  with the density, the subpopulation of trapped electrons [panel (b)] and therefore, the macroscopic magnitudes [panels (c) and (d)] are modified slightly. The trends are similar with the ones in Figs. 6.5 and 6.6 when varying  $\tilde{\nu}_e$ .

## Chapter 7

# Conclusions and future work

This thesis has progressed on the modeling and understanding of the plasma discharge in electrodeless thrusters with magnetic nozzles. The main topics of the thesis are divided in full simulations of the plasma discharge with HYPHEN, a 2D axisymmetric PIC-fluid hybrid code with application to many electromagnetic thrusters; and simulations of the plasma expansion along magnetic nozzle with VLASMAN, an 1D Boltzmann-Poisson kinetic code. The use of VLASMAN is motivated since the expanding plasma along the magnetic nozzle becomes very rarified and far from thermodynamic equilibrium, and deeper studies are required with a kinetic code.

On the side of full simulations, first the thesis has contributed to the development of HYPHEN. The bases of the PIC model for heavy species and the fluid model for electrons were established, respectively, by Domínguez-Vázquez [31] and Pérez-Grande [79]. However, the code was used only for simulations in HETs. Besides, several numerical problems were found due to the anisotropic character of the strongly magnetized electrons, specially if magnetic field topologies were complex. For the present research, the code has been extended for simulations in electrodeless thrusters. The numerical treatment for the fluid model has been investigated thoroughly, and solid numerical algorithms have been found for the problems. Besides, the code (originally with the capability of simulating only atomic propellants) is implemented with the main collisions of diatomic propellants. Many of the alternative propellants for Xe, an issue of increasing interest in EP, are diatomic and in this way the code is able to evaluate them. Second, the thesis, with the extended and improved HYPHEN, has contributed to study the HPT prototype HPT05M revealing details of the plasma discharge and guidelines on the design, and to evaluate air-breathing concepts in HPTs by running simulations with air substances as propellants. Although the studies are focused mainly on HPTs, the efforts on HYPHEN have allowed to produce results for ECRTs in the framework of another thesis as shown in Appendix B.

On the side of kinetic simulations for magnetic nozzle, VLASMAN is used to model the transient processes and rare collisions and characterize self-consistently a subpopulation of electrons trapped along the expansion, which previous steady state kinetic models cannot solve. The kinetic trapping process of the electrons is revealed, and the macroscopic behaviour of the plasma is studied.

## 7.1 Conclusions

### 7.1.1 Full simulations with HYPHEN

The numerical treatment of the electron fluid model in HYPHEN is discussed for the continuity equation and the Ohm's law from the momentum equation. Closing the fluid model with a polytropic relation for the electron temperature, simulations are run for a mini-HPT to test the numerical algorithms proposed. Chapter 2 contains the discussion and the following conclusions are obtained.

- The main numerical difficulties are caused by the anisotropic character of the strongly magnetized electron fluid. The numerical algorithms have to treat properly the strongly different transport properties between the directions parallel and perpendicular to the magnetic field, and avoid numerical diffusion.
- A magnetic field aligned mesh, which separates the parallel and perpendicular transport properties, is required. However, this mesh has irregular cells and specially close to boundary for realistic spatially varying magnetic fields.
- The continuity equation is solved with a finite volume method. This allows to have flexibility on irregular meshes such as magnetic field aligned meshes.
- The Ohm's law is discretized with gradient reconstruction methods. Finite difference methods and weighted least squares methods are compared. It is found that finite difference methods avoid numerical diffusion problems, since they select stencils of cells in a way that mixture of information from different directions are avoided. Weighted least squares methods, although versatile, are very arbitrary in the selection of stencils of cells and can lead to numerical diffusion. The former is used everywhere except near the boundaries, where the cells are highly irregular and the latter needs to be applied.
- The numerical computation of the parallel electron current density requires to introduce the thermalized potential as unknown instead of the potential. In the model used for the electron momentum, the information of the electron current density is present through collisions and, within the weakly-collisional and highly magnetized regime, the parallel component is a negligible term. The use of the thermalized potential allows to group the other dominant terms so that they become of the same order as the current density.
- The numerical algorithms for the electron fluid model are tested within HYPHEN for simulations of a mini-HPT being able to produce accurate results even for non-conventional magnetic topologies with null points. The thruster performances and the 2D profiles of electron related magnitudes are obtained, and the analysis on them concludes that the physical response is consistent.
- Sensitivity analyses on the domain truncation and number of cells are performed. Both of them have confirmed the reliability of the results, and also provides numerical convergence information useful for future simulations.

The electron fluid model in HYPHEN from Chapter 2 is completed with the energy equation and a Fourier's law as closure for the heat flux. The numerical treatment for the added equations to the model

is discussed. Given a power deposition map, the profile of the electron temperature is solved and simulations are run for the prototype HPT05M. The 2D profiles of main plasma transport magnitudes, and performances are obtained for the current and other alternative configurations of the thruster. Chapter 3 contains the discussion and the following conclusions are obtained.

- The system of the energy equation and the Fourier's law is shown to be equivalent to the one of continuity equation and Ohm's law in the drift-diffusive approach of the electron fluid model. Both of the systems have the conservation of a magnitude (current or energy), and are complemented with an equation relating the flux of the magnitude with the gradient of the field to be solved (electric potential or electron temperature). The main difference is that the energy equation, contrary to the continuity equation, has a temporal character, and requires temporal discretization apart from spatial discretization.
- A semi-implicit temporal scheme is used for the energy equation selecting conveniently the terms explicit and implicit. This scheme, within the numerical convergence of the results, simplifies the numerical procedure to solve the electron fluid model. First, it allows to solve the energy equation sequentially with respect to the continuity equation. Second, it linearizes the discretized equations. Once applied the temporal discretization, the spatial discretization is virtually the same as the one for the continuity equation and Ohm's law.
- The current configuration of HPT05M has a coil at the vessel exit to generate the applied magnetic field, which is maximum at the exit and decays fast, and as the vessel is long, the magnetic shielding of the walls is bad in most of the vessel. A region of backward-flow plasma occupying most of the vessel is formed, which results in a significant plasma recombination to the walls.
- Alternative configurations are proposed to mitigate the problem, ones with more coils along the vessel to improve the magnetic shielding, and others with shorter vessels. These configurations either reduces (first ones) or directly removes (second ones) portions of the backward-flow region.
- The current configuration has a very poor thrust efficiency (1.3%) caused by the huge wall recombination. The alternative configurations improve the thrust efficiency (9.3-10.4%) by reducing the wall recombination.
- The optimization with the alternative configurations, although significant, is partial. The performances achieved are still within the current state-of-art. The main reasons limiting for higher performances, are the power losses to the back wall, which conventional quasi-axial magnetic topology cannot handle, and the operation of the magnetic nozzle, which has a significant velocity dispersion in the plume.
- The balance of thrust is studied distinguishing between pressure force and magnetic force. The pressure contribution is found as the main mechanism of thrust. Regarding the magnetic contribution, the magnetic force generated by the divergent magnetic nozzle gives an increment of the thrust that can be significant. However, the magnetic force generated by the source, if a convergent geometry exists inside the vessel, can counteract the one by the magnetic nozzle. The existing studies have been focused on the magnetic nozzle and do not discussed about the source.

HYPHEN is updated to handle collisions of diatomic molecules. This allows to evaluate many of the alternative propellants candidates to substitute Xe. Simulations with air substances as propellant are run for a configuration of HPT05M to test the updated code, and evaluate air-breathing concepts in

HPTs. Simulations are run separately for  $N_2$  and  $O$ , the dominant substances in the low altitudes of the atmosphere, where the concepts could be applied. Chapter 4 contains the discussion and the following conclusions are obtained.

- The results for the 2D profiles of the plasma magnitudes and the performances are shown and compared with Xe. The results reveal that the main physical phenomena of the plasma discharge are similar.
- With the same operation conditions, the magnetic confinement for  $N_2$  and  $O$  is worse than for Xe: since they have less molecular and atomic masses, higher densities are achieved and collisions are more likely to happen. The wall recombination is larger, as consequence of the worse magnetic confinement, and makes the heating of the electrons less effective.
- At low power ( $\sim 100W$ ), the low electron temperature makes the plume poorly ionized and the thrust efficiency is far from that of Xe. At high power ( $\sim 1000W$ ) however, for which the temperature is high enough, the thrust efficiency could be competitive to that of Xe.
- The comparison of the performances between  $O$  and  $N_2$  shows that  $O$  has better efficiencies. In the atmosphere  $N_2$  dominates from 0-200km and  $O$  from 200-400km, and thus for air-breathing concepts, higher altitudes of flight are better in terms of propulsive performance.

The electron temperature obtained with HYPHEN in Chapters 3 and 4 show that the electrons continue isothermal along the magnetic field lines in the plume, and the cooling found in experiments is not observed. The assumptions on the electron thermodynamics in the fluid model needs to be revisited, in particular the Fourier-type law for the electron heat flux. VLASMAN allows deeper studies with kinetic simulations for the very rarefied plasma in the plume.

### 7.1.2 Kinetic simulations of magnetic nozzle with VLASMAN

First, VLASMAN is used to study the transient process of a collisionless plasma expansion along a paraxial magnetic nozzle. A fully ionized Maxwellian plasma from a tank is injected into vacuum, which is initially empty, under the presence of a divergent magnetic field. Chapter 5 contains the discussion and the following conclusions are obtained.

- The spatial profiles of macroscopic plasma properties are obtained. A quasi-neutral region is found followed by a non-neutral region downstream to the end of the domain. An electron cooling is observed, the perpendicular electron temperature decays to zero due to the magnetic mirror effect while the parallel decays to a non-zero value developing a temperature anisotropy.
- The evolution of the distribution functions of electrons and ions during the transient process are shown, and the formation of the steady state plasma beam is observed. Once in the steady state, the distribution is anisotropic for electrons and mono-energetic for ions.
- The mechanisms for the trapping of electrons along the expansion during transient processes are identified, and trajectories of electrons getting trapped are plotted.
- The amount of trapped electrons in the steady state is proven to depend on the history of the system, and thus, also the macroscopic response of the plasma.



- The amount of trapped electrons, in the cases analyzed, is 25% of the total electron density as maximum, which is much smaller than what steady state kinetic models postulate.

Second, as continuation, VLASMAN is used to study the same plasma expansion but adding intraspecies collisions for electrons, and under a convergent-divergent magnetic field. Chapter 6 contains the discussion and the following conclusions are obtained.

- A parametric analysis is done varying the collision frequency for electrons. The rare collisions are noticed mainly for the subpopulation of trapped electrons, which have a large residence time.
- Adding collisions, the amount of trapped electrons increases, from 20% for collisionless case to 40-50% for weakly-collisional cases of maximum density ratio. In spite of the increase, the amount is still far from what steady state kinetic models postulate, which have a ratio close to 100% downstream of the expansion.
- Simulations show that collisions, even if rare, erase the transient history for the subpopulation of trapped electrons. Thus, under the presence of collisions, the macroscopic response of the plasma obtained in the steady state becomes unique.
- The subpopulation of trapped electrons is found to be cold and isotropic, compared to the other subpopulations. With more amount of trapped electrons, further electron cooling and less temperature anisotropy are observed downstream of the expansion.
- The problem for the electron heat flux closure is investigated for different collisionalities, from weakly-collisional to highly-collisional regimes. For an arbitrary collisionality, it is found that the electrons behave as a gas mixture of different subpopulations with an effective specific heat ratio, and follow a Fourier-type law for the heat flux defined with an effective collision frequency. In the weakly-collisional regime, the gas mixture is adiabatic; and in the highly-collisional regime, the gas behaves as monoatomic and the classical Fourier-type law for the heat flux is recovered.

## 7.2 Future work

The tasks interesting for future work within the topic of full simulations with HYPHEN are:

- The configurations for the prototype HPT05M that improve the thrust efficiency beyond the current state-of-art have to be searched. The problems identified in the simulations of this thesis, for partially optimized configurations of HPT05M, are the poor magnetic shielding of the back wall, where a significant amount of power losses are produced, and the operation of the magnetic nozzle. For the first problem, non-conventional magnetic topologies that can shield both the back wall and the lateral wall can be assessed, e.g. the ring-cusps ones used in other electric propulsion concepts. HYPHEN has been proved able to handle those non-conventional topologies, and the assessment is feasible. For the second problem, better understanding is required to take actions. The influence of the design and operation parameters on two of the efficiencies of a magnetic nozzle, plume divergence and internal-to-kinetic conversion efficiencies, may be studied.
- The performances of HPT05M for a wide variety of operation parameters, mass flows and input powers, can be mapped so that the operation regimes of the thruster are characterized.

- Other alternative propellants (such as Ar, Kr,  $I_2$ ...) with interesting properties, apart from air, can be assessed for HTPs. For each of them, it can be studied how the design and operation parameters need to be modified with respect to Xe in order for them to be competitive.
- The full simulations for HPTs have to be completed with the solution of plasma-wave interaction, which will reveal aspects of the radiofrequency wave propagation and the heating mechanisms of the plasma. A module solving that problem developed by other colleagues of EP2 has been integrated to HYPHEN. Some results for HTPs prototypes are shown in Appendix A.
- The simulation results for HPT05M have to be further validated against experiments. Although references to experimental evidences have been made, more detailed comparisons are necessary. For that, dedicated experiments can be set as the prototype belongs to EP2.

The tasks interesting for future work within the topic of kinetic simulations of magnetic nozzle with VLASMAN are:

- A parametric analysis on the source conditions can be done. The study of ion-electron mass and temperature ratios on the plasma response is required to complete and generalize the results obtained in this thesis. This study would allow, for example, to characterize the coefficients for the electron heat flux closure obtained, which is useful for implementation in electron fluid models such as the one of HYPHEN.
- The analyses have been based on several assumptions. Two of the most important are the paraxial and fully magnetized assumptions. Both of them are not valid downstream, once the magnetic field divergence and strength becomes, respectively, large and small. The model needs to be extended to 2D, in order to characterize these aspects.

## Appendix A

# Fully coupled simulations of two HPT prototypes

In this thesis, the simulations with HYPHEN have been focused on the plasma transport of HPTs. A W-module for the plasma-wave interaction in HPTs was developed in the doctoral work of Tian [112], and is being updated in an ongoing PhD thesis by Jiménez [48]. The W-module has been integrated in HYPHEN as part of the present research [119]. This appendix shows some simulations of HYPHEN with a W-module solving for the plasma-wave interaction.

Figure A.1 shows the structure of HYPHEN with the W-module. The plasma transport modules (E-module, I-module and S-module) have been explained in Chapter 3. The outputs of the W-module are the fast electric field  $\tilde{E}$ , which is a periodic magnitude with the high-frequency of the antenna, and the time-averaged power absorption, named  $Q_a$  as in Chapter 3, for the slow plasma transport. The W-module is called each long run (until convergence) of the modules for plasma transport, and the stationary solution of the plasma discharge is searched for.

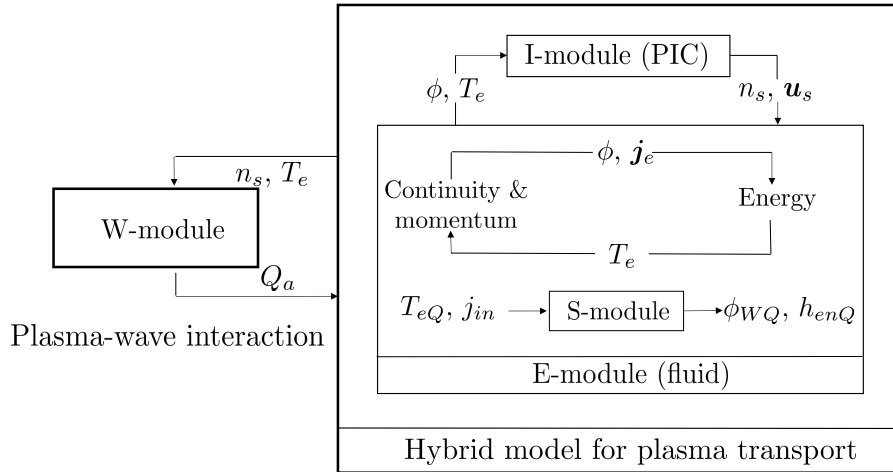


**Figure A.1:** Structure of HYPHEN with W-module.

The fully coupled simulations are run for the prototypes HPT05M and HPT03. Figure A.2 shows a generic sketch of the thrusters similar to that of Chapter 3, and the simulation domains of HYPHEN's modules. The thruster vessel has radius  $R = 1.25\text{cm}$ , and length  $L = 12\text{cm}$  for HPT05M and  $L = 6\text{cm}$  for HPT03. An injector with a circle of radius  $R_{inj} = 0.4\text{cm}$  delivers a mass flow  $\dot{m} = 1\text{mg/s}$ . The applied magnetic field is generated by a coil in the case of HPT05M, and has a convergent-divergent geometry with the throat in the vessel exit [Fig. A.3]. In the case of HPT03, it is generated by permanent magnets, and has a non-conventional topology with a null point inside the vessel [Fig. A.6]. The simulation domain for the plasma transport is delimited by the surfaces W1 and W2 (dielectric walls), and W3 (free surface).

A half-helical antenna wraps the vessel. The antenna has length  $L_a$ , mean radius  $r_a$  and thickness  $d_a$ . Its geometric center is located at an axial position  $z_a$ . The dimension and the position of the antenna is summarized in Table A.1 for HPT05M, and in Table A.3 for HPT03. The antenna emits at the frequency of  $f = 13.56\text{MHz}$ , and is regulated so that the total power deposited to the plasma is  $P_a = 300\text{W}$ . The simulation domain of the W-module is larger than for the plasma transport and ends in a perfect conductor boundary, which is the case of a vacuum chamber.

Notice that the configuration of HPT05M is the C0 described in Chapter 3, while HPT03 has not been discussed before. The operation conditions of these thrusters, mass flow and total power deposition, are the same used in Chapter 3.

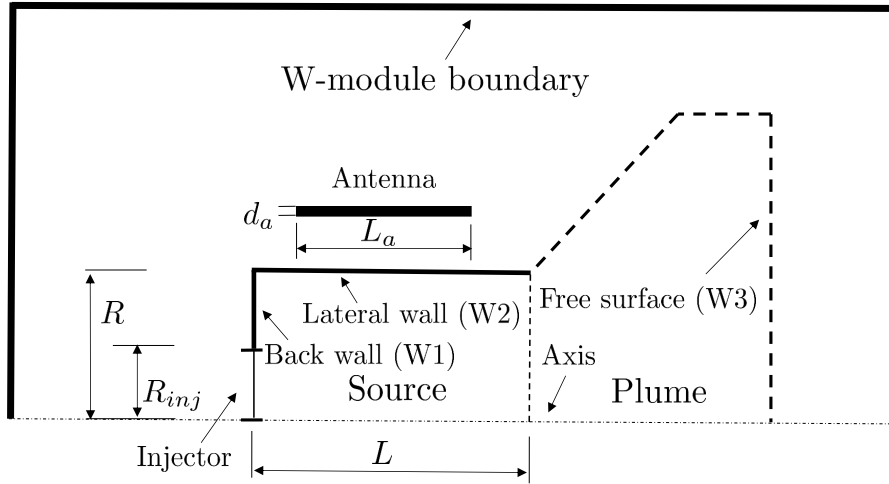


**Figure A.2:** Sketch of the simulation domains for HPT05M.

The following sections show the results for the two thrusters. Performances, in Tables A.2 and A.4, are obtained. 2D profiles of the plasma-wave interaction magnitudes are displayed in Figs. A.4 and A.7. 2D profiles of the plasma transport magnitudes are displayed in Figs. A.5 and A.8. The notation is the same as in Chapter 3.

**Discussion of results: HPT05M**

The power deposition map [Fig. A.4 (a)] obtained with the W-module differs significantly from the homogeneous one assumed in Chapter 3. Most of the power absorption is concentrated in some spots within the first half of the vessel. The module of the high-frequency electric field [Fig. A.4 (b)-(d)], compared to the magnetic topology [Fig. A.3], shows that the power absorption comes mainly from waves propagating perpendicular to the magnetic field lines, which are identified as the Trivelpiece-Gould waves [111].

Although the power deposition map is quite different, the heating is similar as seen in the electron temperature [Fig. A.5 (a)]. Similarly to Chapter 3 [see Fig. 3.4 (a)], inside the vessel, the temperature turns out to be homogeneous with a value about  $2.5eV$ . The magnetic field lines of the topology used connect the spots of the power deposition with other regions of the thruster, and thus the high parallel heat conductivity distributes efficiently the non-homogeneous power. As consequence, the other 2D profiles are also similar when comparing Fig. A.5 to Fig. 3.4. The performances obtained, comparing Table A.2 to Table 3.1, are close except for the operation of the magnetic nozzle with a better dispersion efficiency here.

**Discussion of results: HPT03**

The power absorption [Fig. A.7 (a)] is concentrated near the null point of the magnetic field [Fig. A.6]. Interestingly, near the null point the weak field makes the electron gyrofrequency (usually in the range of GHz) to decay and match with the operation frequency of the antenna (13.56 MHz), and thus electron cyclotron resonance is produced. The resonance is also observed in the module of the high-frequency electric field [Fig. A.7 (b)-(d)]. Thus, technically this prototype is working as an ECRT.

The main differences in the 2D profiles for plasma transport with respect to HPT05M are determined also by the magnetic topology. The power is distributed mainly by the magnetic field lines near the null point with noticeable higher electron temperature in those lines [Fig. A.8 (a)]. In the corners of the vessel lateral wall, given a density of power deposition (although smaller), the low density of the plasma [Fig. A.8 (c)] makes larger the temperature (energy per particle). This is again an effect of the magnetic topology, which shields better those corners, while the wall recombination is concentrated in the central region of the vessel [Fig. A.8 (f)], where the field is the weakest and with lines perpendicular to the wall.

The performances [Table A.4] show that the thrust efficiency is about 4 times larger than that of HPT05M. In terms of the partial efficiencies, except the dispersion efficiency, both the mass efficiency and the energy efficiency are larger.

## HPT05M

### Settings

Parameter	Value
Mass flow $\dot{m}$	1mg/s
Propellant	xenon
Power deposition $P_a$	300 W
Antenna type	half-helix
Antenna frequency $f$	13.56 MHz
Antenna loop radius $r_a$	1.75 cm
Antenna central position $z_a$	-6.0 cm
Antenna length $L_a$	7.5 cm
Antenna thickness $d_a$	0.3 cm

Table A.1: Simulation parameters

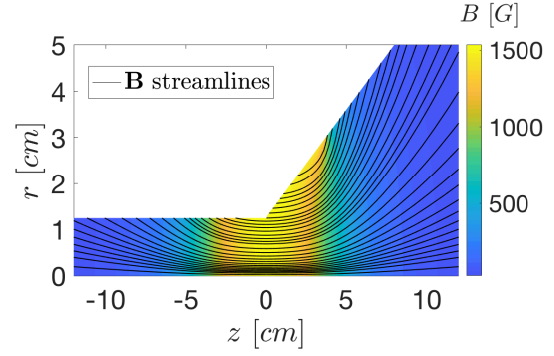


Figure A.3: Applied magnetic field

### Results

$\langle T_e \rangle$ [eV]	$F$ [mN]	$\eta_m$	$\eta_{ene}$	$\eta_{disp}$	$\eta_F$	$\eta_{prod}$	$\epsilon_{wall}$ (W1/W2)	$\epsilon_{inel}$ (ion/exc)
2.89	2.43	0.45	0.033	0.673	0.010	0.05	0.015+0.228	0.253+0.471

Table A.2: Performance indicators of HPT05M

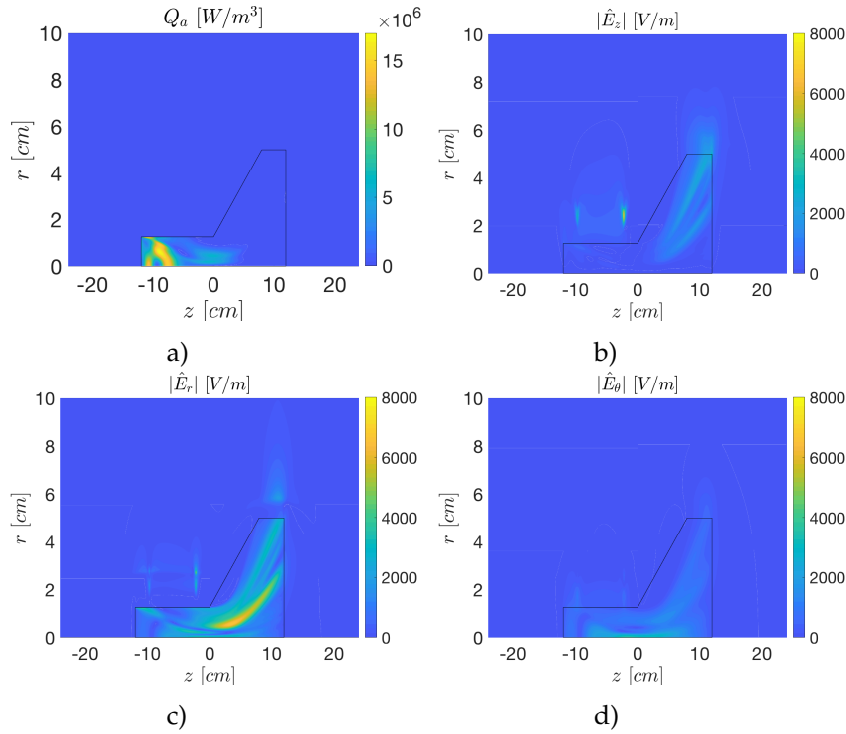


Figure A.4: 2D maps of plasma-wave interaction magnitudes for HPT05M

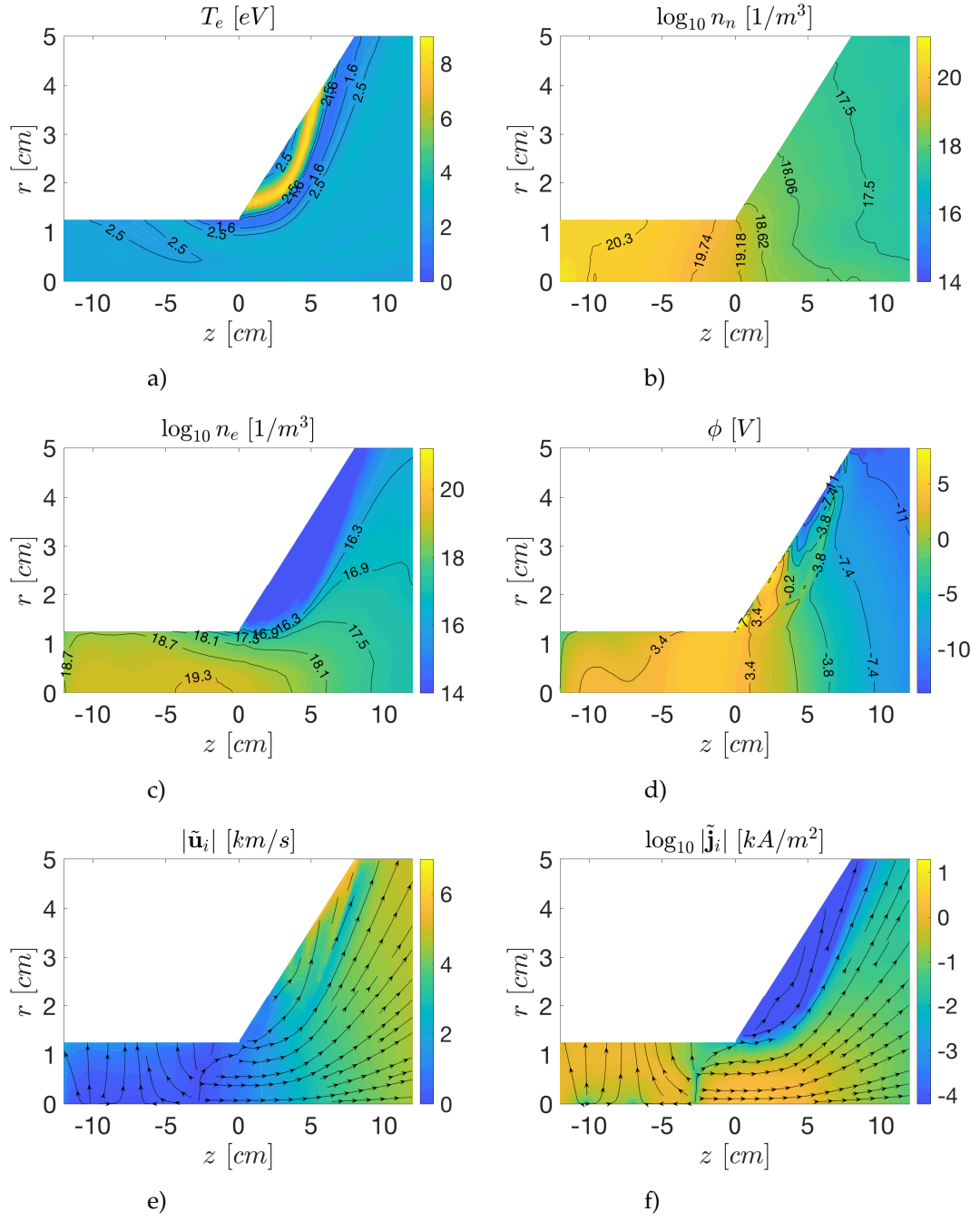


Figure A.5: 2D maps of plasma transport magnitudes for HPT05M

## HPT03

### Settings

Parameter	Value
Mass flow $\dot{m}$	1mg/s
Propellant	xenon
Power deposition $P_a$	300 W
Antenna type	half-helix
Antenna frequency $f$	13.56 MHz
Antenna loop radius $r_a$	1.9 cm
Antenna central position $z_a$	-3.25 cm
Antenna length $L_a$	4.5 cm
Antenna thickness $d_a$	0.4 cm

Table A.3: Simulation parameters

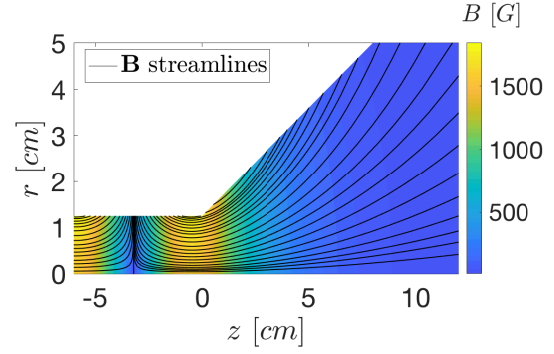


Figure A.6: Applied magnetic field

### Results

$\langle T_e \rangle$ [eV]	$F$ [mN]	$\eta_m$	$\eta_{ene}$	$\eta_{disp}$	$\eta_F$	$\eta_{prod}$	$\epsilon_{wall}$ (W1/W2)	$\epsilon_{inel}$ (ion/exc)
3.96	5.07	0.72	0.098	0.609	0.043	0.11	0.140+0.379	0.187+0.196

Table A.4: Performance indicators of HPT03

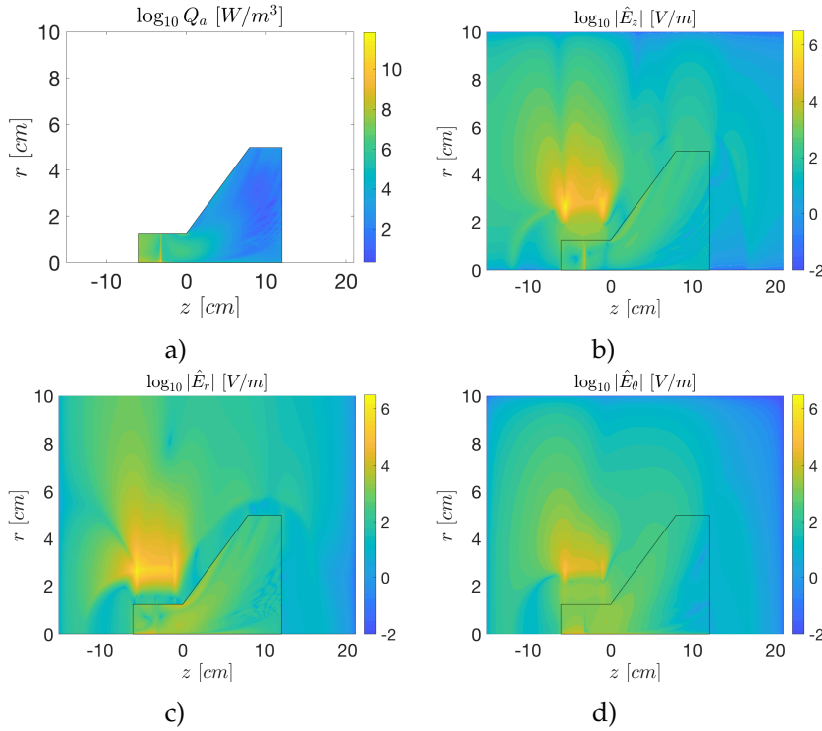


Figure A.7: 2D maps of plasma-wave interaction magnitudes for HPT03



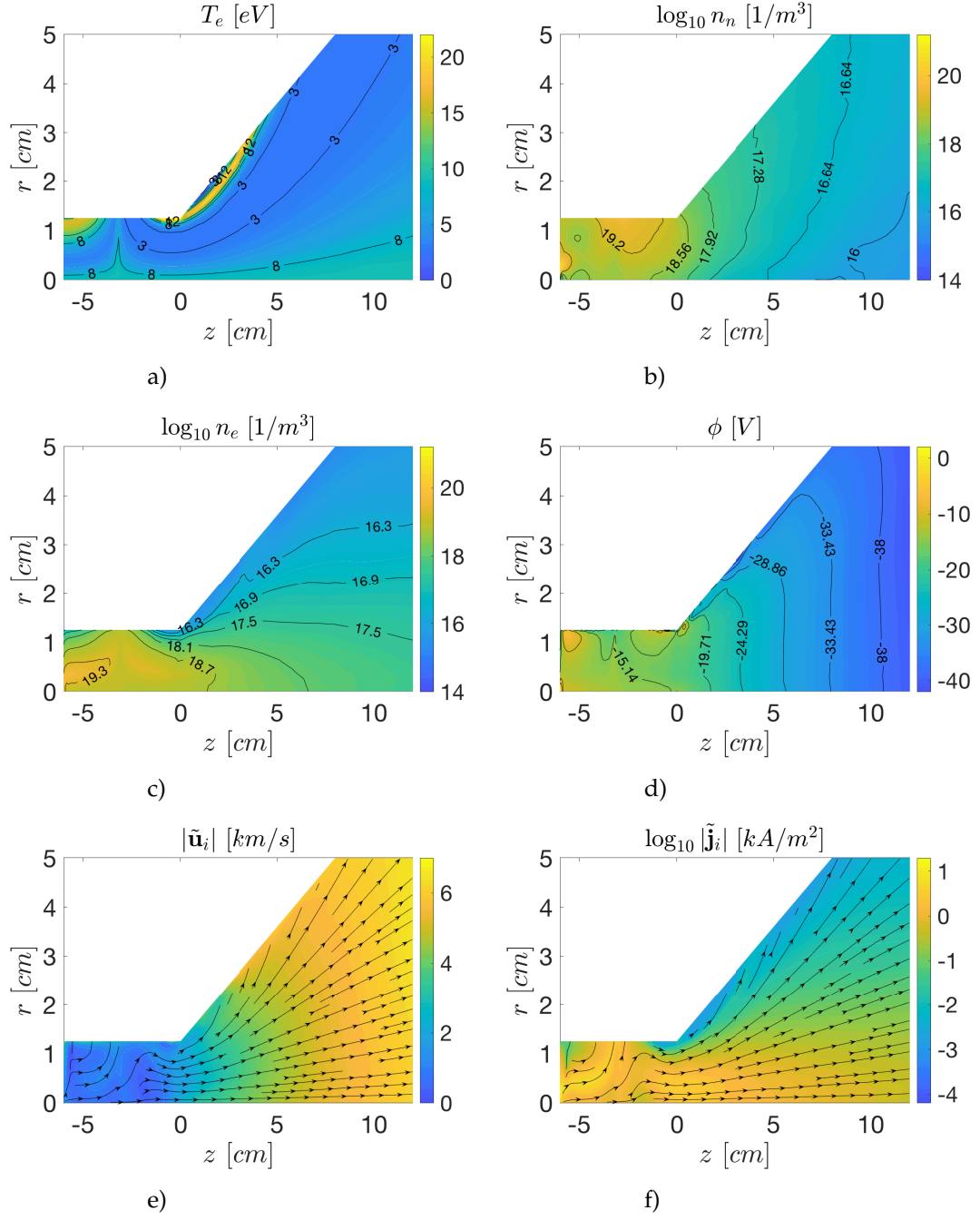


Figure A.8: 2D maps of plasma transport magnitudes for HPT03



## Appendix B

# Fully coupled simulations of an ECRT prototype

In this thesis, HYPHEN has been extended to analyze the plasma transport and performances in HPT prototypes. ECRTs share the same plasma transport model than HPTs and differ on the plasma-wave regime and the required numerical techniques to solve the plasma-wave model. Sánchez-Villar is carrying out a PhD thesis within EP2 centered on developing a specific W-module for ECRTs (based on finite element methods instead of finite difference methods of Tian [112]) and its application to an ECRT prototype [116, 81] developed by the Office National d'Etudes et de Recherches Aéronautiques (ONERA) in France. In a joint effort, we have published an article [90] with full simulations of that prototype coupling the W-module of Sánchez-Villar to the transport modules of HYPHEN described within this thesis.

Just as an illustration of the simulations and results on the article [90], Fig. B.1 shows a sketch of the thruster and the simulation domains. This thruster has an annular injector of xenon placed at the back wall. In magenta some applied magnetic field lines are shown, which in this prototype are completely divergent within the simulation domains. A coaxial cable feeds electromagnetic power through a cavity located at the back wall. Figure B.2 shows the main 2D profiles for plasma transport magnitudes, which have qualitative similarities to the ones for HPTs in Chapter 3 and Appendix A.

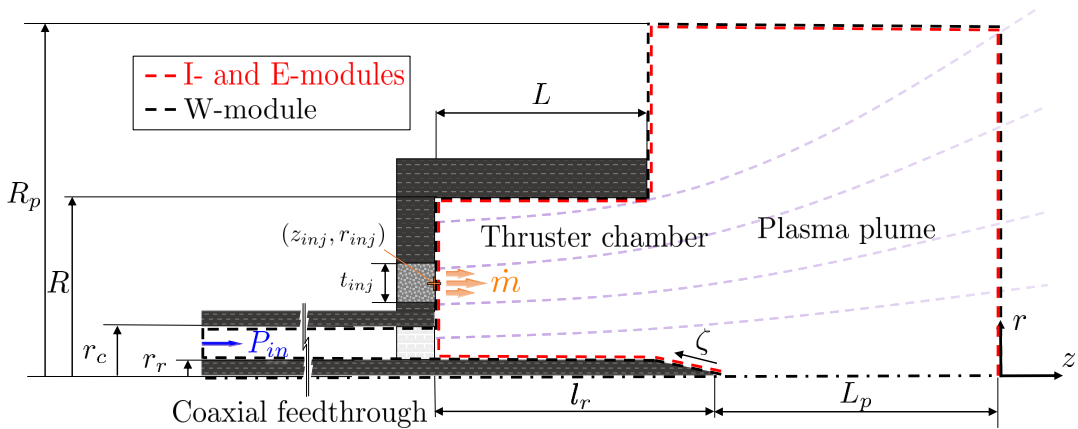


**Figure B.1:** Sketch of the simulation domains for the ECRT prototype developed by ONERA.

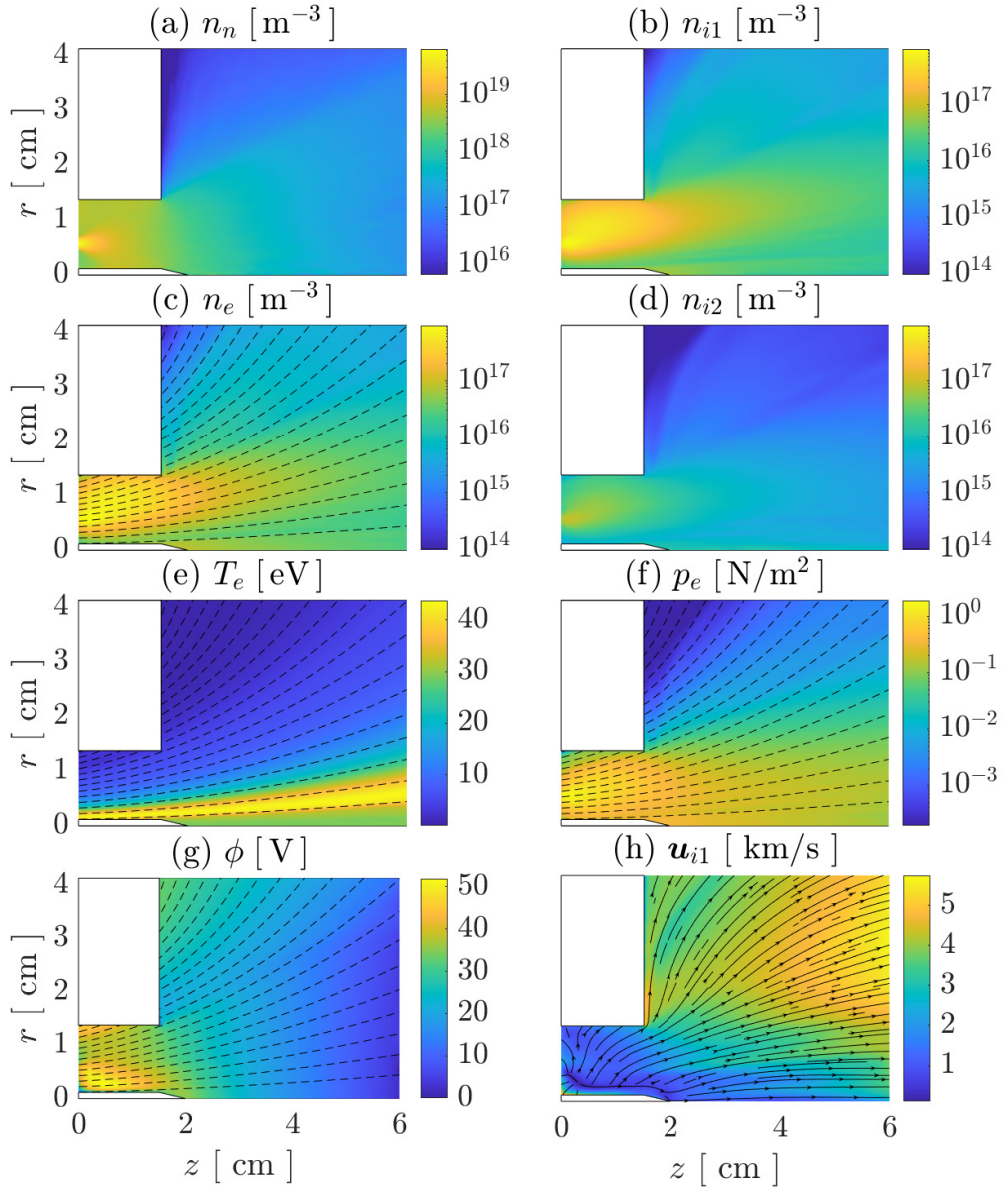


**Figure B.2:** 2D maps of plasma transport magnitudes obtained with HYPHEN for the ECRT prototype developed by ONERA.

# Bibliography

- [1] E. Ahedo. "Parametric analysis of a magnetized cylindrical plasma". In: *Physics of Plasmas* 16.11 (2009), p. 113503.
- [2] E. Ahedo. "Plasma dynamics in a helicon thruster". In: *Proceedings of EUCASS 2011, 4-8 July 2011, Saint Petersburg, Russia*. paper 118. 2011.
- [3] E. Ahedo and V. d. Pablo. "Combined effects of electron partial thermalization and secondary emission in Hall thruster discharges". In: *Physics of Plasmas* 14 (2007), p. 083501.
- [4] E. Ahedo, S. Correyero, J. Navarro, and M. Merino. "Macroscopic and parametric study of a kinetic plasma expansion in a paraxial magnetic nozzle". In: *Plasma Sources Science and Technology* 29.4 (2020), p. 045017. ISSN: 1089-7674. DOI: 10.1088/1361-6595/ab7855.
- [5] E. Ahedo and M. Merino. "Two-dimensional plasma expansion in a magnetic nozzle: separation due to electron inertia". In: *Physics of Plasmas* 19.8 (2012), p. 083501. ISSN: 1089-7674.
- [6] E. Ahedo and M. Merino. "Two-dimensional supersonic plasma acceleration in a magnetic nozzle". In: *Physics of Plasmas* 17.7 (2010), p. 073501. ISSN: 1089-7674.
- [7] E. Ahedo and J. Navarro-Cavallé. "Helicon thruster plasma modeling: Two-dimensional fluid-dynamics and propulsive performances". In: *Physics of Plasmas* 20.4 (2013), p. 043512.
- [8] T. Andreussi, E. Ferrato, A. Piragino, G. Cifali, A. Rossodivita, and M. Andrenucci. "Development and experimental validation of a hall effect thruster ram-ep concept". In: *Space Propulsion Conference*. SP2018-00431. Seville, Spain: Association Aéronautique et Astronautique de France, 2018.
- [9] S. Araki and R. E. Wirz. "Magnetic Field Aligned Mesh for Ring-Cusp Discharge Chambers". In: *50th AIAA/ASME/SAE/ASEE Joint Propulsion Conference*. 2014, p. 3830.
- [10] A. V. Arefiev and B. N. Breizman. "Magnetohydrodynamic scenario of plasma detachment in a magnetic nozzle". In: *Physics of Plasmas* 12.4 (2005), p. 043504. ISSN: 1070664X. DOI: 10.1063/1.1875632. URL: <http://link.aip.org/link/PHPAEN/v12/i4/p043504/s1%5C&Agg=doi>.
- [11] G. Bethke and D. Miller. "Cyclotron resonance thruster design techniques." In: *AIAA Journal* 4.5 (1966), pp. 835–840.
- [12] P. Bhatnagar, E. Gross, and M. Krook. "A model for collision processes in gases. i. small amplitude processes in charged and neutral one-component systems". In: *Physical Review* 94 (1954), pp. 511–525.
- [13] J. Bittencourt. *Fundamentals of plasma physics*. Springer, Berlin, Germany, 2004.
- [14] A. Brizard. "A guiding-center Fokker-Planck collision operator for nonuniform magnetic fields". In: *Physics of Plasmas* 11.9 (2004).
- [15] F. Cannat, F. Guarducci, and S. B. Gabriel. "Analytical and numerical simulation of Ring Cusp Discharge Chamber". In: *36<sup>th</sup> International Electric Propulsion Conference*. IEPC-2019-905. Vienna, Austria: Electric Rocket Propulsion Society, Fairview Park, OH, 2019.

- [16] M. Capitelli, C. Ferreira, B. Gordiets, and A. Osipov. *Plasma kinetics in atmospheric gases*. Springer, Berlin, Germany, 2000.
- [17] C. Charles, R. Boswell, R. Laine, and P. MacLellan. "An experimental investigation of alternative propellants for the helicon double layer thruster". In: *Journal of Physics D: Applied Physics* 41.17 (2008), p. 175213.
- [18] C. Cheng and G. Knorr. "The integration of the vlasov equation in configuration space". In: *Journal of Computational Physics* 22 (1976), pp. 330–351.
- [19] D. Chubb. "Fully ionized quasi-one-dimensional magnetic nozzle flow". In: *AIAA Journal* 10.2 (1972), pp. 113–114.
- [20] F. Cichocki, A. Domínguez-Vázquez, M. Merino, and E. Ahedo. "Hybrid 3D model for the interaction of plasma thruster plumes with nearby objects". In: *Plasma Sources Science and Technology* 26.12 (2017), p. 125008. ISSN: 0963-0252.
- [21] F. Cichocki, M. Merino, and E. Ahedo. "A 3D electron fluid model to study magnetic field effects on an expanding plasma thruster plume". In: *Space Propulsion Conference 2018*. 00295. Seville, Spain, May 14-18: Association Aéronautique et Astronautique de France, 2018.
- [22] P. Coche and L. Garrigues. "A two-dimensional (azimuthal-axial) particle-in-cell model of a hall thruster". In: *Physics of Plasmas* 21 (2014), p. 023503.
- [23] T. Collard and B. Jorns. "Magnetic nozzle efficiency in a low power inductive plasma source". In: *Plasma Sources Science and Technology* 28.10 (2019), p. 105019.
- [24] S. Correyero, J. Jarrige, D. Packan, and E. Ahedo. "Plasma beam characterization along the magnetic nozzle of an ECR thruster". In: *Plasma Sources Science and Technology* 28.9 (2019), p. 095004. DOI: 10.1088/1361-6595/ab38e1.
- [25] S. Correyero. "Physics of plasma plumes accelerated by magnetic nozzles: an experimental and theoretical research". PhD thesis. Universidad Carlos III de Madrid, Leganés, Spain, 2020.
- [26] V. Croes, T. Lafleur, Z. Bonaventura, A. Bourdon, and P. Chabert. "2d particle-in-cell simulations of the electron drift instability and associated anomalous electron transport in hall-effect thrusters". In: *Plasma Sources Science and Technology* 26 (2017), p. 034001.
- [27] P. Dellar. "An interpretation and derivation of the lattice Boltzmann method using strang splitting". In: *Computers and Mathematics with Applications* 65 (2013), pp. 129–141.
- [28] D. Di Cara and et al. "Ram electric propulsion for low earth orbit operation: an esa study". In: *30th International Electric Propulsion Conference, Florence, Italy*. IEPC-2007-162. 2007.
- [29] k. Diamant. "A 2-stage cylindrical hall thruster for air breathing electric propulsion". In: *46th AIAA/ASME/SAE/ASEE*. 2010.
- [30] B. Diskin and J. L. Thomas. "Effects of mesh regularity on accuracy of finite-volume schemes". In: *50th AIAA Aerospace Sciences Meeting*. 2012, pp. 2012–0609.
- [31] A. Domínguez-Vázquez. "Axisymmetric simulation codes for Hall effect thrusters and plasma plumes". PhD thesis. Universidad Carlos III de Madrid, Leganés, Spain, 2019.
- [32] *Equipo de Propulsion Espacial y Plasmas*. <http://ep2.uc3m.es>.
- [33] J. Fife. "Hybrid-PIC Modeling and Electrostatic Probe Survey of Hall Thrusters". PhD thesis. Massachusetts Institute of Technology, 1998.
- [34] A. Fruchtmann, K. Takahashi, C. Charles, and R. Boswell. "A magnetic nozzle calculation of the force on a plasma". In: *Physics of Plasmas (1994-present)* 19.3 (2012), p. 033507.

- [35] V. Giannetti and et al. "Electric propulsion system trade-off analysis based on alternative propellant selection". In: *Space Propulsion Conference*. SP2016-3125194. Rome, Italy: Association Aéronautique et Astronautique de France, 2016.
- [36] R. Goddard. *The green notebooks, vol.1. The Dr. Robert H. Goddard Collection at Clark University Archives*. Clark University, 1906.
- [37] D. Goebel and I. Katz. *Fundamentals of Electric Propulsion: Ion and Hall Thrusters*. Jet Propulsion Laboratory, Pasadena, CA, 2008.
- [38] A. Gurevich. "Distribution of captured particles in a potential well in the absence of collisions". In: *Soviet Journal of Experimental and Theoretical Physics* 26 (1968), p. 575.
- [39] G. Hagelaar, J. Bareilles, L. Garrigues, and J. Boeuf. "Two-dimensional model of a stationary plasma thruster". In: *Journal of Applied Physics* 91.9 (2002), pp. 5592–5598.
- [40] R. Hockney and J. Eastwood. *Computer simulation using particles*. CRC Press, Boca Ratón, FL, 1988.
- [41] R. Hofer, P. Peterson, A. Gallimore, and R. Jankovsky. "A high specific impulse two-stage Hall thruster with plasma lens focusing". In: *7th International Electric Propulsion Conference, Pasadena, CA, USA*. IEPC-01-036. 2001.
- [42] K. Holste and et al. "In search of alternative propellants for ion thrusters". In: *34th International Electric Propulsion Conference, Hyogo-Kobe, Japan*. IEPC-2015-320. 2015.
- [43] Y. Hu and J. Wang. "Fully kinetic simulations of collisionless, mesothermal plasma emission: macroscopic plume structure and microscopic electron characteristics". In: *Physics of Plasmas* 24.3 (2017), p. 033510.
- [44] Y. Itikawa. "Cross sections for electron collisions with nitrogen molecules". In: *Journal of Physical and Chemical Reference Data* 35 (2006), pp. 31–53.
- [45] Y. Itikawa and A. Ichimura. "Cross sections for collisions of electrons and photons with atomic oxygen". In: *Journal of Physical and Chemical Reference Data* 19 (1990), pp. 637–651.
- [46] R. Jahn. *Physics of Electric Propulsion*. Dover, 2006.
- [47] R. Jahn and E. Choueiri. "Electric propulsion". In: *Encyclopedia of Physical Science and Technology*. Academic Press, 2002, pp. 125–141.
- [48] P. Jiménez. "Helicon plasma thruster full-wave simulations". MSc Thesis. Universidad Carlos III de Madrid, Leganés, Spain, 2020.
- [49] M. Keidar, I. Boyd, and I. Beilis. "Plasma flow and plasma-wall transition in Hall thruster channel". In: *Physics of Plasmas* 8.12 (2001), pp. 5315–5322.
- [50] M. Keidar and I. I. Beilis. "Sheath and boundary conditions for plasma simulations of a Hall thruster discharge with magnetic lenses". In: *Applied Physics Letters* 94.19 (2009), p. 191501.
- [51] J. Y. Kim, K. Chung, S. Kim, J. H. Ryu, K.-J. Chung, and Y. Hwang. "Thermodynamics of a magnetically expanding plasma with isothermally behaving confined electrons". In: *New Journal of Physics* 20.6 (2018), p. 063033.
- [52] N. Koch and M. Schirra. "The HEMPT Concept - A Survey on Theoretical Considerations and Experimental Evidences". In: *32nd International Electric Propulsion Conference*. paper 2011-236. Wiesbaden, Germany, September 11-15: Electric Rocket Propulsion Society, Fairview Park, OH, 2011.
- [53] J. Koo and I. Boyd. "Computational model of a Hall thruster". In: *Computer physics communications* 164 (2004), pp. 442–447.

- [54] H. Kotakemori, H. Hasegawa, and A. Nishida. "Performance evaluation of a parallel iterative method library using openmp". In: *Eighth International Conference on High-Performance Computing in Asia-Pacific Region (HPCASIA'05)*. paper 5-pp. IEEE, 2005.
- [55] T. Lafleur. "Helicon plasma thruster discharge model". In: *Physics of Plasmas* 21.4 (2014), p. 043507.
- [56] T. Lafleur, F. Cannat, J. Jarrige, P. Elias, and D. Packan. "Electron dynamics and ion acceleration in expanding-plasma thrusters". In: *Plasma Sources Science and Technology* 24.6 (2015), p. 065013.
- [57] M. Li, M. Merino, E. Ahedo, J. Ren, and H. Tang. "Full-pic code validation and comparison against fluid models on plasma plume expansion". In: *35<sup>th</sup> International Electric Propulsion Conference*. IEPC-2017-230. Atlanta, GA: Electric Rocket Propulsion Society, 2017.
- [58] M. Li, M. Merino, E. Ahedo, and H. Tang. "On electron boundary conditions in PIC plasma thruster plume simulations". In: *Plasma Sources Science and Technology* 28.03 (2019), p. 034004. ISSN: 0963-0252. DOI: 10.1088/1361-6595/ab0949.
- [59] J. Little and E. Choueiri. "Critical condition for plasma confinement in the source of a magnetic nozzle flow". In: *IEEE Transactions on Plasma Science* 43.1 (2014), pp. 277–286.
- [60] J. Little and E. Choueiri. "Electron Cooling in a Magnetically Expanding Plasma". In: *Physical Review Letters* 117.22 (2016), p. 225003.
- [61] H. Lorzel and P. G. Mikellides. "Three-Dimensional Modeling of Magnetic Nozzle Processes". In: *AIAA Journal* 48.7 (July 2010), pp. 1494–1503. ISSN: 0001-1452. DOI: 10.2514/1.J050123. URL: <http://doi.aiaa.org/10.2514/1.J050123>.
- [62] *LXCAT Database*. <https://nl.lxcat.net>. Accessed: 2019-10-21.
- [63] M. Martínez-Sánchez and E. Ahedo. "Magnetic mirror effects on a collisionless plasma in a convergent geometry". In: *Physics of Plasmas* 18.3 (2011), p. 033509.
- [64] M. Martínez-Sánchez, J. Navarro-Cavallé, and E. Ahedo. "Electron cooling and finite potential drop in a magnetized plasma expansion". In: *Physics of Plasmas* 22.5 (2015), p. 053501.
- [65] A. Meige, R. Boswell, C. Charles, and M. Turner. "One-dimensional particle-in-cell simulation of a current-free double layer in an expanding plasma". In: *Physics of Plasmas* 12 (2005), p. 052317.
- [66] T. Mel'kumov. *Pioneers of Rocket Technology: Selected Works, volume 9285*. National Aeronautics and Space Administration, 1965.
- [67] M. Merino and E. Ahedo. "Effect of the plasma-induced magnetic field on a magnetic nozzle". In: *Plasma Sources Science and Technology* 25.4 (2016), p. 045012. ISSN: 0963-0252. DOI: 10.1088/0963-0252/25/4/045012.
- [68] M. Merino and E. Ahedo. "Fully magnetized plasma flow in a magnetic nozzle". In: *Physics of Plasmas* 23.2 (2016), p. 023506. ISSN: 1089-7674. DOI: 10.1063/1.4941975.
- [69] M. Merino and E. Ahedo. "Plasma detachment in a propulsive magnetic nozzle via ion demagnetization". In: *Plasma Sources Science and Technology* 23.3 (2014), p. 032001. ISSN: 0963-0252. DOI: 10.1088/0963-0252/23/3/032001.
- [70] M. Merino, J. Mauriño, and E. Ahedo. "Kinetic electron model for plasma thruster plumes". In: *Plasma Sources Science and Technology* 27.3 (2018), p. 035013. ISSN: 0963-0252. DOI: 10.1088/1361-6595/aab3a1.
- [71] I. Mikellides and I. Katz. "Numerical simulations of Hall-effect plasma accelerators on a magnetic-field-aligned mesh". In: *Physical Review E* 86.4 (2012), p. 046703.
- [72] I. Mikellides, I. Katz, R. Hofer, D. Goebel, K. de Grys, and A. Mathers. "Magnetic shielding of the channel walls in a Hall plasma accelerator". In: *Physics of Plasmas* 18 (2011), p. 033501.



- [73] I. G. Mikellides, I. Katz, R. R. Hofer, and D. M. Goebel. "Magnetic shielding of a laboratory Hall thruster. I. Theory and validation". In: *Journal of Applied Physics* 115.4 (2014), p. 043303.
- [74] R. Moloney and et al. "Experimental validation and performance measurements of an ecr thruster operating on multiple propellants". In: *36th International Electric Propulsion Conference, Vienna, Austria*. IEPC-2019-199. 2019.
- [75] Y. Nakagawa, H. Koizumi, H. Kawahara, and K. Komurasaki. "Performance characterization of a miniature microwave discharge ion thruster operated with water". In: *Acta Astronautica* 157 (2019), pp. 294–299.
- [76] J. Navarro-Cavallé, M. Wijnen, P. Fajardo, and E. Ahedo. "Experimental characterization of a 1 kW helicon plasma thruster". In: *Vacuum* 149 (2018), pp. 69–73.
- [77] G. Parissenti, N. Koch, D. Pavarin, E. Ahedo, K. Katsonis, F. Scortecci, and M. Pessana. "Non conventional propellants for electric propulsion applications". In: *Space Propulsion 2010*. SP2010-1841086. San Sebastián, Spain, 2010.
- [78] F. Parra, E. Ahedo, M. Fife, and M. Martínez-Sánchez. "A two-dimensional hybrid model of the Hall thruster discharge". In: *Journal of Applied Physics* 100 (2006), p. 023304.
- [79] D. Pérez-Grande. "Fluid modeling and simulation of the electron population in Hall effect thrusters with complex magnetic topologies". PhD thesis. Universidad Carlos III de Madrid, Leganés, Spain, 2018.
- [80] D. Pérez-Grande, O. González-Martínez, P. Fajardo, and E. Ahedo. "Analysis of the numerical diffusion in anisotropic mediums: benchmarks for magnetic field aligned meshes in space propulsion simulations". In: *Applied Sciences* 6.11 (2016), p. 354.
- [81] S. Peterschmitt and D. Packan. "Comparison of Waveguide Coupled and Coaxial Coupled ECRA Magnetic Nozzle Thruster using a Thrust Balance". In: *Proc. of the 36th Int. Electric Propulsion Conf.(Vienna, Austria)*. 2019, pp. 2019–188.
- [82] C. G. Petra, O. Schenk, and M. Anitescu. "Real-time stochastic optimization of complex energy systems on high-performance computers". In: *Computing in Science and Engineering* 16(5) (2014), pp. 32–34.
- [83] C. G. Petra, O. Schenk, M. Lubin, and K. Gärtner. "An augmented incomplete factorization approach for computing the Schur complement in stochastic optimization". In: *SIAM Journal on Scientific Computing* 36(2) (2014), pp. C139–C162.
- [84] L. Pitchford et al. "LXCat: an Open-Access, Web-Based Platform for Data Needed for Modeling Low Temperature Plasmas". In: *Plasma Process and Polymers* 14 (2017), p. 1600098.
- [85] M. Raadu. "Expansion of a plasma injected from an electrodeless gun along a magnetic field". In: *Plasma Physics* 21 (1979), p. 331.
- [86] J. Ramos, M. Merino, and E. Ahedo. "Three dimensional fluid-kinetic model of a magnetically guided plasma jet". In: *Physics of Plasmas* 25.6 (2018), p. 061206. ISSN: 1089-7674. DOI: 10.1063/1.5026972.
- [87] F. Romano and et al. "Performance evaluation of a novel inductive atmosphere-breathing ep system". In: *35th International Electric Propulsion Conference, Atlanta, USA*. IEPC-2017-184. 2017.
- [88] G. Sánchez-Arriaga and D. Pastor-Moreno. "Direct vlasov simulations of electron-attracting cylindrical langmuir probes in flowing plasmas". In: *Physics of Plasmas* 21 (2014), p. 073504.
- [89] G. Sánchez-Arriaga, J. Zhou, E. Ahedo, M. Martínez-Sánchez, and J. J. Ramos. "Kinetic features and non-stationary electron trapping in paraxial magnetic nozzles". In: *Plasma Sources Science and Technology* 27.3 (2018), p. 035002.

- [90] A. Sánchez-Villar, J. Zhou, M. Merino, and E. Ahedo. "Coupled plasma transport and electromagnetic wave simulation of an ECR thruster". In: *Plasma Sources Science and Technology* (accepted for publication).
- [91] J. Sanmartín. "Active charging control and tethers". In: *Space environment: prevention of risk related to spacecraft charging, space technology course*. Cépadués, 2002, pp. 515–533.
- [92] U. Schiller. "A unified operator splitting approach for multi-scale fluid–particle coupling in the lattice Boltzmann method". In: *Computer Physics Communications* 185 (2014), pp. 2586–2597.
- [93] J. Sercel. "An experimental and theoretical study of the ECR plasma engine". PhD thesis. California Institute of Technology, 1993.
- [94] A. Sheppard and J. Little. "Scaling laws for electrodeless plasma propulsion with water vapor propellant". In: *Plasma Sources Science and Technology* 29 (2020), p. 045007.
- [95] E. Shima, K. Kitamura, and T. Haga. "Green-gauss/weighted-least-squares hybrid gradient reconstruction for arbitrary polyhedra unstructured grids". In: *AIAA Journal* 51.11 (2013), pp. 2740–2747.
- [96] M. U. Siddiqui, C. Cretel, J. Synowiec, A. G. Hsu, J. A. Young, and R. Spektor. "First Performance Measurements of the Phase Four RF Thruster". In: *35th International Electric Propulsion Conference, Atlanta, GA*. IEPC-2017-431. 2017.
- [97] E. Sozer, C. Brehm, and C. Kiris. "Gradient calculation methods on arbitrary polyhedral unstructured meshes for cell-centered CFD solvers". In: *52nd Aerospace Sciences Meeting*. National Harbor, Maryland, US, 2014.
- [98] H. Sugama. "Modern gyrokinetic formulation of collisional and turbulent transport in toroidally rotating plasmas". In: *Reviews of Modern Plasma Physics* 1.9 (2017).
- [99] J. Szabo, M. Robin, S. Paintal, B. Pote, V. Hruby, and C. Freeman. "Iodine propellant space propulsion". In: *33th International Electric Propulsion Conference, Washington, USA*. IEPC-2013-311. 2013.
- [100] J. Szabo. "Fully kinetic numerical modeling of a plasma thruster". PhD thesis. Massachusetts Institute of Technology, 2001.
- [101] T. Tabata, T. Shirai, M. Sataka, and H. Kubo. "Analytic cross sections for electron impact collisions with nitrogen molecules". In: *Atomic Data and Nuclear Data Tables* 92 (2006), pp. 375–406.
- [102] T. Tabata, T. Shirai, M. Sataka, and H. Kubo. "Erratum to "Analytic cross sections for electron impact collisions with nitrogen molecules" [At. Data Nucl. Data Tables 92 (2006) 375-406]". In: *Atomic Data and Nuclear Data Tables* 98 (2012), p. 74.
- [103] F. Taccogna, S. Longo, and M. Capitelli. "Plasma sheaths in Hall discharge". In: *Physics of Plasmas* 12 (2005), p. 093506.
- [104] F. Taccogna, R. Schneider, S. Longo, and M. Capitelli. "Kinetic simulations of a plasma thruster". In: *Plasma Sources Science and Technology* 17.2 (2008), p. 024003.
- [105] K. Takahashi. "Helicon-type radiofrequency plasma thrusters and magnetic plasma nozzles". In: *Reviews of Modern Plasma Physics* 3 (2019), p. 3.
- [106] K. Takahashi and A. Ando. "Enhancement of axial momentum lost to the radial wall by the upstream magnetic field in a helicon source". In: *Plasma Physics and Controlled Fusion* 59 (2017), p. 054007.
- [107] K. Takahashi, T. Lafleur, C. Charles, P. Alexander, and R. Boswell. "Electron Diamagnetic Effect on Axial Force in an Expanding Plasma: Experiments and Theory". In: *Physical Review Letters* 107.23 (2011), p. 235001.

- [108] K. Takahashi, C. Charles, and R. Boswell. "Approaching the theoretical limit of diamagnetic-induced momentum in a rapidly diverging magnetic nozzle". In: *Physical review letters* 110.19 (2013), p. 195003.
- [109] K. Takahashi, T. Lafleur, C. Charles, P. Alexander, and R. W. Boswell. "Axial force imparted by a current-free magnetically expanding plasma". In: *Physics of Plasmas* 19.8 (2012), p. 083509.
- [110] S. Tayal and O. Zatsarinny. "B-spline R-matrix-with-pseudostates approach for excitation and ionization of atomic oxygen by electron collisions". In: *Physical Review A* 94 (2016), p. 042707.
- [111] B. Tian. "Modeling of physical processes in radio-frequency plasma thrusters". PhD thesis. 2017.
- [112] B. Tian, M. Merino, and E. Ahedo. "Two-dimensional plasma-wave interaction in an helicon plasma thruster with magnetic nozzle". In: *Plasma Sources Science and Technology* 27.11 (2018), p. 114003. ISSN: 0963-0252.
- [113] F. Trezzolani, A. Lucca Fabris, D. Pavarin, et al. "Low power radio-frequency plasma thruster developement and testing". In: *33th International Electric Propulsion Conference*. IEPC 2013-153. 2013.
- [114] M. Tsay, J. Model, C. Barcroft, J. Frongillo, J. Zwahlen, and C. Feng. "Integrated testing of iodine bit-3 rf ion propulsion system for 6u cubesat applications". In: *35th International Electric Propulsion Conference, Atlanta, USA*. IEPC-2017-264. 2017.
- [115] D. Tskhakaya, K. Matyash, R. Schneider, and F. Taccogna. "The Particle-In-Cell Method". In: *Contributions to Plasma Physics* 47.8-9 (2007), pp. 563–594.
- [116] T. Vialis, J. Jarige, A. Aanesland, and D. Packan. "Direct thrust measurement of an electron cyclotron resonance plasma thruster". In: *Journal of Propulsion and Power* 34.5 (2018), pp. 1323–1333.
- [117] Y. Wang, O. Zatsarinny, and K. Bartschat. "B-spline R-matrix-with-pseudostates calculations for electron-impact excitation and ionization of nitrogen". In: *Physical Review A* 89 (2014), p. 062714.
- [118] M. Wijnen, J. Navarro-Cavallé, and P. Fajardo. "Mechanically amplified milli-newton thrust balance for direct thrust measurements of electric thrusters for space propulsion". In: *IEEE Transactions on Instrumentation and Measurement* 70 (2021), p. 3505318.
- [119] J. Zhou, P. Jiménez, M. Merino, P. Fajardo, and E. Ahedo. "Numerical Simulations of the Plasma Discharge in a Helicon Plasma Thruster". In: *36<sup>th</sup> International Electric Propulsion Conference*. IEPC-2019-330. Vienna, Austria: Electric Rocket Propulsion Society, 2019.
- [120] J. Zhou, D. Pérez-Grande, P. Fajardo, and E. Ahedo. "Numerical treatment of a magnetized electron fluid within an electromagnetic plasma thruster code". In: *Plasma Sources Science and Technology* 28.11 (2019), p. 115004.
- [121] J. Zhou, G. Sánchez-Arriaga, and E. Ahedo. "Time-dependent expansion of a weakly-collisional plasma beam in a paraxial magnetic nozzle". In: *Plasma Sources Science and Technology* (submitted for publication).
- [122] T. Ziemba, J. Carscadden, J. Slough, J. Prager, and R. Winglee. "High power helicon thruster". In: *41th AIAA/ASME/SAE/ASEE Joint Propulsion Conference & Exhibit*. AIAA 2005-4119. 2005.
- [123] T. Ziemba, P. Euripides, J. Slough, R. Winglee, L. Giersch, J. Carscadden, T. Schnackenberg, and S. Isley. "Plasma characteristics of a high power helicon discharge". In: *Plasma Sources Science and Technology* 15 (2006), p. 517.